Optimal Design of Duct Silencers in Naturally-Ventilated Buildings

by

Vivek Vasudevan Shankar

A THESIS SUBMITTED IN PARTIAL FULFILLMENT
OF THE REQUIREMENTS FOR THE DEGREE OF

Master of Applied Science

in

THE FACULTY OF GRADUATE AND POSTDOCTORAL STUDIES
(Mechanical Engineering)

The University of British Columbia
(Vancouver)

November 2015

Abstract

Natural-ventilation systems in sustainable buildings rely on wind and buoyancy effects to ensure sufficient airflow though the building. To promote airflow, these buildings have openings that connect rooms and common spaces. These openings are usually made as large as possible to maximize airflow across connected spaces. Large openings result in noise ingress between these spaces, leading to poor noise isolation and speech privacy. The performance of these openings needs to be optimized – meaning the sound isolation of these openings has to be improved, with minimal impact on the airflow performance. Previous work by Bibby investigated openings in thin partitions. This study addresses the problem of openings in thick partitions, which essentially are short ducts, as well as long ducts that deliver air-flow to different building levels. Simple surrogate models were developed from symbolic regression; they can be used as a provisional tool for predicting the sound and airflow performance of ducts with absorptive lining and baffle inserts. This tool can be used in the design phase to build optimal ducts, or for retrofit noise control. Predicted results from 2D Finite Element Analysis were used as the input data-set to build these surrogate models. Novel methods were used to extend the surrogate model into the 3D domain and to model complex duct configurations. Different configurations of sound absorbers (duct lining and baffles) were tested to identify optimal designs. The use of scale-models of ducts to study their real-life performance was also investigated. The surrogate models were validated experimentally in a 1:4-scale-model facility, by applying appropriate scaling laws, and were found to capture

the general trend of the acoustics and airflow performance within acceptable accuracy. Finally guidelines for designers were proposed based on results from the surrogate models, experiments and FEA.

Preface

This dissertation is original, unpublished, independent work by the author, Vivek Vasudevan Shankar.

Table of Contents

Abstract ii

Preface iv

Table of Contents v

List of Tables ix

List of Figures xi

Acknowledgments xxi

1 Introduction 1

1.1 Background 1

1.2 Problem statement 8

1.3 Research objectives 9

1.4 Scope and definition of audience 10

1.5 Literature review 11

1.6 Concepts and theory 15

1.6.1 Governing equations for acoustics 15

1.6.2 Sound ratings 16

1.6.3 Governing equations for fluid flow 18

1.6.4 Vena-contracta 18

1.6.5 Classification of ventilation openings 19

1.6.6 Is the flow in natural-ventilation ducts laminar or turbulent? 21
1.6.7 Surrogate modelling 22
1.7 Thesis overview 24

2 Finite-Element Modeling 26
2.1 Finite-element method 26
2.2 Finite-element method for acoustics 27
2.2.1 Modelling specifications 28
2.2.2 Domain 28
2.2.3 Boundary conditions 29
2.2.4 Mesh 31
2.2.5 Solver 33
2.2.6 Insertion loss 33
2.2.7 Sample result and verification 34
2.2.8 Comparison of plane-wave and diffuse-field sources . . 34
2.2.9 Selection and generation of data set 37
2.3 Finite-element method for airflow 39
2.3.1 Modelling specifications 40
2.3.2 Domain 40
2.3.3 Boundary conditions 42
2.3.4 Mesh 42
2.3.5 Effect of change in cross-section 43
2.3.6 Effect of addition of baffles 46
2.3.7 Mesh sensitivity analysis 47
2.3.8 Selection and generation of sample set 50
2.3.9 Finite-element modelling assumptions 51

3 Surrogate Modelling 52
3.1 Acoustic modelling 53
3.1.1 Transfer-matrix method for sound attenuation in ducts . 53
3.1.2 Surrogate-modelling considerations 55

3.1.3 Insertion loss 56
3.1.4 Analysis of model 57
3.1.5 Extension of the surrogate model 60
3.1.6 Model calculation 63
3.1.7 Estimation of flow resistivity from absorption 66
3.2 Airflow modeling 69
3.2.1 Theoretical relationships for airflow in ducts 69
3.2.2 Surrogate modelling considerations 77
3.2.3 Surrogate model 78
3.2.4 Extension of the surrogate model 85
3.2.5 Analysis of model 85
3.2.6 Model calculation 88

4 Experimental Investigation 91
4.1 Scaling 91
4.1.1 Acoustic scaling 92
4.1.2 Flow scaling 94
4.1.3 Selection of scaling factor 95
4.2 Test chamber requirements 96
4.3 Chamber construction and equipment setup 97
4.4 Measurement methodology 100
4.4.1 Equipment setup for acoustics 100
4.4.2 Sound-transmission measurement and flanking test . . . 105
4.4.3 Duct insertion loss measurement 105
4.4.4 Flow-resistivity measurement 107
4.5 Flow-rate measurement setup 108
4.5.1 Airflow measurement method 109
4.6 Duct test configurations 111
4.6.1 Configuration 1 111
4.6.2 Configuration 2 115
4.6.3 Configuration 3 117

4.6.4 Configuration 4 120
4.6.5 Configuration 5 123

5 Results and Discussion 125
5.1 Validation of surrogate models 125
5.1.1 Validation of acoustic surrogate model using TMM . . . 125
5.1.2 Comparison of airflow surrogate model with theoretical model 126
5.2 Comparison between surrogate, experimental and FEA models . 128
5.2.1 Configuration 1 128
5.2.2 Configuration 2 143
5.2.3 Configuration 3 147
5.2.4 Configuration 4 161
5.2.5 Configuration 5 172
5.2.6 Compilation of acoustic results 176
5.2.7 Compilation of performance metrics 178

6 Conclusion 184
6.1 Guidelines for designers 184
6.2 Summary of work 187
6.3 Future work 191

Bibliography 192

A Estimation of Measurement Uncertainty 197
A.1 Uncertainty in acoustic measurement 197
A.2 Uncertainty in airflow measurement 198

B MATLAB Code 200
B.1 Sample MATLAB code for surrogate model for acoustics 200
B.2 Sample MATLAB code for surrogate model for airflow 205

List of Tables

Table 2.1 Ranges of input parameters for acoustic modelling. 38
Table 2.2 Range of input parameters for airflow modelling. 50

Table 3.1 Statistics for the surrogate model for sound (Eq. (3.14)). . . . 57
Table 3.2 Statistics for surrogate model for flow-resistivity estimation. 68
Table 3.3 Statistics for airflow surrogate model for sudden contraction. 80
Table 3.4 Statistics for airflow surrogate model for flow through duct. . 81
Table 3.5 Statistics for the airflow surrogate model for a sudden expansion. 83

Table 4.1 Measured flow resistivities of different porous materials. . . . 107

Table 5.1 Performance metrics for Configuration 1a. 130
Table 5.2 Performance metrics for Configuration 1b. 131
Table 5.3 Performance metrics for Configuration 1c. 136
Table 5.4 Performance metrics for Configuration 1d. 138
Table 5.5 Performance metrics for Configuration 1e. 140
Table 5.6 Performance metrics for Configuration 1f. 142
Table 5.7 Performance metrics for Configuration 2a. 146
Table 5.8 Performance metrics for Configuration 2b. 147
Table 5.9 Performance metrics for Configuration 3a. 149
Table 5.10 Performance metrics for Configuration 3b. 152
Table 5.11 Performance metrics for Configuration 3c. 154
Table 5.12 Performance metrics for Configuration 3d. 156

Table 5.13 Performance metrics for Configuration 3e. 158
Table 5.14 Performance metrics for Configuration 3f. 161
Table 5.15 Performance metrics for Configuration 4a. 163
Table 5.16 Performance metrics for Configuration 4b. 165
Table 5.17 Performance metrics for Configuration 4c. 166
Table 5.18 Performance metrics for Configuration 4d. 170
Table 5.19 Performance metrics for Configuration 4e. 171
Table 5.20 Performance metrics for Configuration 5a. 173
Table 5.21 Performance metrics for Configuration 5b. 174
Table 5.22 Summary of the performance metrics from the surrogate model and experiments for the investigated duct configruations. . . 178
Table 5.22 Summary of the performance metrics from the surrogate model and experiments for the investigated duct configruations. . . 179
Table 5.22 Summary of the performance metrics from the surrogate model and experiments for the investigated duct configruations. . . 180
Table 5.22 Summary of the performance metrics from the surrogate model and experiments for the investigated duct configruations. . . 181

List of Figures

Figure 1.1 Examples of long purpose-provided duct-like openings in naturally-ventilated buildings. 3
Figure 1.2 Porous-absorber treatements for ducts, in the form of lining and baffles. 4
Figure 1.3 Formation of a vena-contracta due to sudden contraction. . 19
Figure 1.4 Commonly-used squashing functions used in surrogate modelling. 24
Figure 1.5 Overview of the workflow adopted in this thesis. 25

Figure 2.1 2-D illustration of the duct (top) and its equivalent 3-D extrusion (bottom). 29
Figure 2.2 Acoustic-domain geometry of the duct with lining on one side (left) and lining on both sides (right). 30
Figure 2.3 Mesh-convergence study, where x_s is the number of elements per wavelength, for width=0.2 m, thickness=0.025 mm, length=1 m and flow-resistivity=25000 Rayls/m for the lined duct. . . 32
Figure 2.4 Acoustic-pressure waves in a duct from FEA predictions for a duct with lining on two sides (w=0.8 m, l_b=l=2 m, t=0.15 m, R_f=12500 Rayls/m). 35
Figure 2.5 Insertion Loss calculated from FEA predictions for a duct with lining on two sides (w=0.8 m, l_b=l=2 m, t=0.15 m, R_f=12500 Rayls/m). 36

Figure 2.6 The geometry used to model the duct inserted between a diffuse-field source room and an anechoic receiver room 36
Figure 2.7 Comparison of IL from diffuse-field source and plane-wave source approximation, for two duct configurations. 37
Figure 2.8 Comparison of Insertion Loss between ducts having w=0.15 m and w=0.6 m, calculated from FEA predictions for a duct with lining on two sides. 39
Figure 2.9 Fluid-domain geometry of the volumes modelled. 42
Figure 2.10 Illustration of the presence of a vena-contracta, along with the streamlines. 44
Figure 2.11 Illustration of the vena-contracta, along with the pressure contours, with the sub-divisions of the duct for d_w=0.42 m, s_h=4.6 m and Re_o=34, 649. 45
Figure 2.12 Pressure drop along the length of duct x, as a percentage of l, for d_w=0.173 m, s_h=5.7 m and Re=61, 150. 45
Figure 2.13 Geometry of the duct with a baffle, as built in Comsol. . . . 46
Figure 2.14 Pressure gradient from prediction in Comsol for baf_{wx}=−0.12 m, l=1 m, s_h=6 m. 47
Figure 2.15 Mesh-convergence study for the airflow model: variation of pressure drop with velocity for different mesh densities nn (top). Zoomed view of the top plot (bottom). nn=1 is the mesh density used; nn=0.5 is half the mesh density and nn=2, double the mesh density. 48
Figure 2.16 Mesh-convergence study for the airflow model: variation of pressure drop with position in duct for different mesh densities nn (top). Zoomed view of the top plot (bottom). nn=1 is the mesh density used; nn=0.5 is half the mesh density and nn=2, double the mesh density. 49

Figure 3.1 Model showing the equivalence of a duct with lining on one side and two sides. 59

Figure 3.2 Model showing the equivalent model for a duct with baffle of twice the lining thickness, where (∗) is the logarithmic addition operator. 61
Figure 3.3 Model showing the equivalent model for a duct with baffle of any thickness, where (∗) is the logarithmic addition operator. 62
Figure 3.4 Model showing the equivalent model for a duct with lining on all sides, where (∗) is the logarithmic addition operator. . 63
Figure 3.5 Model configuration with sections named for a sample calculation. 64
Figure 3.6 Flow through aperture ignoring vena-contracta. 70
Figure 3.7 Flow through aperture including vena-contracta. 71
Figure 3.8 Flow through a sudden expansion. 73
Figure 3.9 Flow through a sudden contraction. 74
Figure 3.10 Value for K for various area ratios A_2/A_1 as suggested by various authors [1]. 75
Figure 3.11 Different regions of flow propagation of interest inside a duct. 77
Figure 3.12 Conventional symbols used in the surrogate model for a lined duct installed between two rooms. 78
Figure 3.13 Illustration showing the different regions of interest for flow propagation through a duct. 82
Figure 3.14 Different regions of interest for a lined duct installed between two rooms. 84
Figure 3.15 Approximation of change in cross-section due to presence of a baffle. 84
Figure 3.16 Variation of effect of vena contracta with source-room height s_h and duct width d_w. 87
Figure 3.17 Model configuration with sections named for a sample calculation. 88

Figure 4.1 Comparison of variation of predicted Insertion Loss with frequency at scale factors $n = 0.5, 1, 2, 4$ and 8 for a full-scale duct of dimensions $0.3\,\mathrm{m} \times 0.3\,\mathrm{m} \times 1\,\mathrm{m}$ and lining of thickness 0.00625 m, R_f=58, 176 Rayls/m. 93
Figure 4.2 Photographs of the test facility during the construction phase. 98
Figure 4.3 Photographs of the duct located between the reverberant source room *(left)* and the anechoic receiver room *(right)*. 100
Figure 4.4 Side and Top view illustrations of the test rooms (all dimensions in mm). 101
Figure 4.5 Frequency response curve for the REALISTIC 40-1377 tweeter. 102
Figure 4.6 Arrangement of tweeters in the source room. 103
Figure 4.7 Free-field responses of different Brüel & Kjaer microphones [2]. 104
Figure 4.8 Measured flanking transmission loss between source and receiver rooms when the ventilator was blocked. 104
Figure 4.9 Acoustic measurement setup. 106
Figure 4.10 Blower-door setup for airflow measurement. 110
Figure 4.11 Configuration 1a of a square duct with no porous absorbers (front and top views). 112
Figure 4.12 Configuration 1b of a square duct with felt lining (front and top views). 112
Figure 4.13 Configuration 1c of a square duct with felt lining and felt baffle near duct inlet (front and top views). 112
Figure 4.14 Configuration 1d of a square duct with felt lining and felt baffle near duct centre (front and top views). 113
Figure 4.15 Configuration 1e of a square duct with felt lining and felt baffle near duct outlet (front and top views). 113
Figure 4.16 Configuration 1f of a square duct with felt lining and two felt baffles near duct inlet (front and top views). 113
Figure 4.17 Images of 1:4 scale-model ducts built in Configuration 1. . . 114

Figure 4.18 Distortion of the baffles when inserted in the duct. 115
Figure 4.19 Configuration 2a of a rectangular duct with no porous absorbers (front and top views). 116
Figure 4.20 Configuration 2b of a rectangular duct with felt lining (front and top views). 116
Figure 4.21 Configuration 2b – modified duct with styrofoam partition used for airflow prediction of a rectangular duct. 116
Figure 4.22 Configuration 3a of a square duct with no porous absorbers (front and top views). 117
Figure 4.23 Configuration 3b of a square duct with Sonoflex lining (front and top views) 117
Figure 4.24 Configuration 3c of a square duct with Sonoflex lining and Sonoflex baffle near duct inlet (front and top views). 118
Figure 4.25 Configuration 3d of a square duct with Sonoflex lining and Sonoflex baffle near duct centre (front and top views). 118
Figure 4.26 Configuration 3e of a square duct with Sonoflex lining and Sonoflex baffle near duct outlet (front and top views). 118
Figure 4.27 Configuration 3f of a square duct with Sonoflex lining and two Sonoflex baffles near duct inlet (front and top views). . . 119
Figure 4.28 Images of ducts built in Configuration 3 with Sonoflex lining. 119
Figure 4.29 Images of ducts built in Configuration 3. 120
Figure 4.30 Configuration 4a of a rectangular duct with no porous absorbers (front and top views). 121
Figure 4.31 Configuration 4b of a rectangular duct with Sonoflex lining (front and top views) 121
Figure 4.32 Configuration 4c of a rectangular duct with Sonoflex lining and Sonoflex baffle near duct inlet (front and top views). . . 121
Figure 4.33 Configuration 4d of a rectangular duct with Sonoflex lining and Sonoflex baffle near duct centre (front and top views). . 122

Figure 4.34 Configuration 4e of a rectangular duct with Sonoflex lining and Sonoflex baffle near duct outlet (front and top views). . 122
Figure 4.35 Images of ducts built in Configuration 4. 122
Figure 4.36 Configuration 5a of a rectangular duct with bend at termination with no porous absorbers (front and top view). 123
Figure 4.37 Configuration 5b of a rectangular duct with bend at termination with Sonoflex lining (front and top view). 123
Figure 4.38 Images of ducts built in Configuration 5 showing bend at termination in the receiver room. 124

Figure 5.1 Comparison of Insertion Loss per unit length versus frequency predicted by the 2D surrogate model and the Transfer Matrix Method for two duct configurations. 126
Figure 5.2 Comparison of predicted velocity at duct inlet vs. pressure drop, between 3D surrogate model, experiments and theoretical relationships with resistance coefficient K from various authors for duct dimensions $0.15\,\mathrm{m} \times 0.15\,\mathrm{m} \times 0.8\,\mathrm{m}$. 127
Figure 5.3 Comparison of predicted velocity at duct inlet vs. pressure drop, between 2D and 3D surrogate model, 2D and 3D FEA and experiments for Configuration 1a of the scale-model duct. For the full-scale model, u_d is scaled by a factor of 1.25. . . . 129
Figure 5.4 Comparison of Insertion Loss vs. frequency between surrogate and FEA predictions, and experiments for Configuration 1b. 132
Figure 5.5 Comparison of predicted velocity at duct inlet vs. pressure drop, between 2D and 3D surrogate model, 2D FEA and experiments for Configuration 1b of the scale-model duct. For the full-scale model, u_d is scaled by a factor of 1.27. 132
Figure 5.6 Comparison of Insertion Loss vs. frequency between surrogate and FEA predictions, and experiments for Configuration 1c, 1d and 1e. 135

Figure 5.7 Comparison of predicted velocity at duct inlet vs. pressure drop, between 2D and 3D surrogate model, 2D FEA and experiments for Configuration 1c of the scale-model duct. For the full-scale model, u_d is scaled by a factor of 1.24. 135
Figure 5.8 Comparison of predicted velocity at duct inlet vs. pressure drop, between 2D and 3D surrogate model, 2D FEA and experiments for Configuration 1d of the scale-model duct. For the full-scale model, u_d is scaled by a factor of 0.98. 137
Figure 5.9 Comparison of predicted velocity at duct inlet vs. pressure drop, between 2D and 3D surrogate model, 2D FEA and experiments for Configuration 1e of the scale-model duct. For the full-scale model, u_d is scaled by a factor of 1.3212. 139
Figure 5.10 Comparison of Insertion Loss vs. frequency between surrogate and FEA predictions, and experiments for Configuration 1f. 141
Figure 5.11 Comparison of predicted velocity at duct inlet vs. pressure drop, between 2D and 3D surrogate model, 2D FEA and experiments for Configuration 1f of the scale-model duct. For the full-scale model, u_d is scaled by a factor of 1.21. 141
Figure 5.12 Comparison of predicted velocity at duct inlet vs. pressure drop, between 2D and 3D surrogate model, 2D FEA and experiments for Configuration 2a of the scale-model duct. For the full-scale model, u_d is scaled by a factor of 1.32. 143
Figure 5.13 Comparison of Insertion Loss vs. frequency between surrogate and FEA predictions, and experiments for Configuration 2b. 145
Figure 5.14 Comparison of predicted velocity at duct inlet vs. pressure drop, between 2D and 3D surrogate model, 2D FEA and experiments for Configuration 2b of the scale-model duct. For the full-scale model, u_d is scaled by a factor of 1.32. 145

Figure 5.15 Comparison of predicted velocity at duct inlet vs. pressure drop, between 2D and 3D surrogate model, 2D FEA and experiments for Configuration 3a of the scale-model duct. For the full-scale model, u_d is scaled by a factor of 1.25. 148
Figure 5.16 Comparison of Insertion Loss vs. frequency between surrogate and FEA predictions, and experiments for Configuration 3b. 151
Figure 5.17 Comparison of predicted velocity at duct inlet vs. pressure drop, between 2D and 3D surrogate model, 2D FEA and experiments for Configuration 3b of the scale-model duct. For the full-scale model, u_d is scaled by a factor of 1.31. 151
Figure 5.18 Comparison of Insertion Loss vs. frequency between surrogate and FEA predictions, and experiments for Configuration 3c. 153
Figure 5.19 Comparison of predicted velocity at duct inlet vs. pressure drop, between 2D and 3D surrogate model, 2D FEA and experiments for Configuration 3c of the scale-model duct. For the full-scale model, u_d is scaled by a factor of 1.04. 153
Figure 5.20 Comparison of predicted velocity at duct inlet vs. pressure drop, between 2D and 3D surrogate model, 2D FEA and experiments for Configuration 3d of the scale-model duct. For the full-scale model, u_d is scaled by a factor of 1.05. 155
Figure 5.21 Comparison of predicted velocity at duct inlet vs. pressure drop, between 2D and 3D surrogate model, 2D FEA and experiments for Configuration 3e of the scale-model duct. For the full-scale model, u_d is scaled by a factor of 1.06. 157
Figure 5.22 Comparison of Insertion Loss vs. frequency between surrogate and FEA predictions, and experiments for Configuration 3f. 160

Figure 5.23 Comparison of predicted velocity at duct inlet vs. pressure drop, between 2D and 3D surrogate model, 2D FEA and experiments for Configuration 3f of the scale-model duct. For the full-scale model, u_d is scaled by a factor of 1.04. 160
Figure 5.24 Comparison of predicted velocity at duct inlet vs. pressure drop, between 2D and 3D surrogate model, 2D FEA and experiments for Configuration 4a of the scale-model duct. For the full-scale model, u_d is scaled by a factor of 1.18. 162
Figure 5.25 Comparison of Insertion Loss vs. frequency between surrogate and FEA predictions, and experiments for Configuration 4b. 164
Figure 5.26 Comparison of predicted velocity at duct inlet vs. pressure drop, between 2D and 3D surrogate model, 2D FEA and experiments for Configuration 4b of the scale-model duct. For the full-scale model, u_d is scaled by a factor of 1.21. 164
Figure 5.27 Comparison of Insertion Loss vs. frequency between surrogate and FEA predictions, and experiments for Configuration 4c. 167
Figure 5.28 Comparison of predicted velocity at duct inlet vs. pressure drop, between 2D and 3D surrogate model, 2D FEA and experiments for Configuration 4c of the scale-model duct. For the full-scale model, u_d is scaled by a factor of 1.17. 167
Figure 5.29 Comparison of predicted velocity at duct inlet vs. pressure drop, between 2D and 3D surrogate model, 2D FEA and experiments for Configuration 4d of the scale-model duct. For the full-scale model, u_d is scaled by a factor of 1.10. 169
Figure 5.30 Comparison of predicted velocity at duct inlet vs. pressure drop, between 2D and 3D surrogate model, 2D FEA and experiments for Configuration 4e of the scale-model duct. For the full-scale model, u_d is scaled by a factor of 1.12. 169

Figure 5.31 Comparison of predicted velocity at duct inlet vs. pressure drop, between 2D and 3D surrogate model, 2D FEA and experiments for Configuration 5a of the scale-model duct. For the full-scale model, u_d is scaled by a factor of 1.18. 172
Figure 5.32 Comparison of Insertion Loss for 3D model from experiments , FEA and surrogate model for Configuration 5b. 175
Figure 5.33 Comparison of predicted velocity at duct inlet vs. pressure drop, between 2D and 3D surrogate model, 2D FEA and experiments for Configuration 5b of the scale-model duct. For the full-scale model, u_d is scaled by a factor ofscaled by a factor 1.26. 175
Figure 5.34 Compilation of IL curves from the surrogate model for all duct-configurations. 177
Figure 5.35 Compilation of IL curves from experiments for all duct-configurations. 177
Figure 5.36 Compilation of $SEOA_f$ from the surrogate model and experiments for selected duct-configruations. 182
Figure 5.37 Compilation of $SEOA_s$ from the surrogate model and experiments for selected duct-configruations. 182
Figure 5.38 Compilation of OAR from the surrogate model and experiments for selected duct-configruations. 183

Figure 6.1 Dependance of cross-sectional areas of the source room and the duct, on the vena-contracta 186

Acknowledgments

The last few years have been the best time of my life. My experience at UBC, and in general Vancouver, has been nothing short of amazing. Since my first day, I have felt at home at UBC. The main reason for this has been my amazing friends, my parents – far yet near and always caring, and in particular the support of my Master's supervisor Dr. Murray Hodgson. It is difficult to overstate my gratitude to Murray. Murray is the best teacher/supervisor one can possibly have. Murray has been academically and emotionally supportive through the rough road to finish this thesis. The quality of this thesis is a result of the freedom and flexibility Murray has offered, towards my research. I am grateful to have had such a knowledgable, caring, friendly and supportive supervisor. I hope that as many students as possible benefit from such a great professor, while he still teaches at UBC. Through Murray, I had the opportunity to meet some of the nicest people I have known – Bernadette Duffy, Murray's wife; Murray's family has been caring and supporting me in every possible way ever since I stepped into Canada, Margaret Gardiner, the co-ordinator of the SBSP program, but much beyond that, in terms of helping and caring for all the students in the lab, and finally Mina Samimi, who was in the lab when I first arrived.

Besides Murray Hodgson, I wish to thank my co-supervisors Fitsum Tariku and Steve Rogak for their guidance and technical support. In addition to the above stated experts, I also wish to thank Chris Waltham, for overseeing my successful thesis defence. I wish to thank Glenn Jolly from the Mechanical Engg. Instrumentation Lab for his expertise and help during the different phases of

my experiments. I also wish to thank Fitsum Tariku and BCIT for lending the blower-door for over a year which was critical to the completion of my thesis. I wish to thank all my lab-mates and in particular Mehadi Hasan, Denny Ng and Banda Logawa for all the discussions we have had. I wish you all good luck with your research. I also would like to thank James Higgins for help with redoing the airflow-measurements.

I wish to thank the Natural Sciences and Engineering Research Council of Canada for the financial support through the NSERC CREATE grant.

I wish to thank all my lovely friends – the list is big and you all know who I am referring to. Thanks for being there – both during my time of happiness and distress. You all have had a huge impact in my life.

This section would not be complete without acknowledging and thanking my parents, Shankar and Meera for all they had done. I would like to acknowledge all the sacrifices they had to do, for my sake. They have always shown unconditional love and have considered me their world. I also wish to acknowledge the love of my grandparents Mythili and Sambandham.

Chapter 1

Introduction

1.1 Background

Sustainable buildings have steadily become more common in recent years, owing to the savings in resources and energy. These buildings employ ways of achieving sustainable design, such as natural ventilation. These natural-ventilation systems replace mechanical-ventilation systems with ventilation systems that achieve pressure differentials through buoyancy and wind effects. Such systems, however, can only create small pressure differentials (under 10 Pa at the facade and possibly less than 1 Pa between rooms), leading to the requirement for large openings in internal partitions, to achieve sufficient airflow between rooms. These openings, while supporting airflow, also transmit sound from one space to another, leading to poor noise isolation and speech privacy. In order to overcome this, the openings can be lined with sound-absorbing materials, or the geometry of the opening modified, to turn them into silencers and attenuate the noise. This is an ongoing challenge for designers, since such modifications tend to reduce the airflow, leading to lower ventilation and air quality inside the building. The performance of these openings must be optimized in such a way that their noise isolation is improved, with minimal impact on the airflow performance. Associated work on the measurement and optimization of the acoustical

and airflow performance in naturally-ventilated buildings has been carried out at the University of British Columbia, by the Acoustics and Noise Research Group headed by Dr. Hodgson, for a few years now.

The UBC Liu Institute for Global Issues is a sustainable building on the campus of the University of British Columbia, which was designed with a natural-ventilation system, to reduce energy consumption. This building has large openings in internal partitions for low air-flow resistance; this resulted in poor speech privacy and noise isolation between workspaces. Hodgson and Khaleghi [3], along with Stantec Architecture Ltd., studied this problem and performed acoustical measurements on these large openings with and without acoustical treatment (absorber lining and baffles). The results of air-flow and air-quality tests before and after treatment suggested that acoustical treatment had little effect on ventilation and air quality (possibly because the acoustic treatment was inadequate in the untreated building), and provided acceptable sound isolation. It was concluded that further work was required to optimize the design of these openings.

Bibby, in his Masters thesis [4], continued the work by studying further interior ventilation openings in naturally-ventilated buildings, in order to provide engineers and architects with design techniques. Ventilation openings were classified into short openings and long openings. Short openings are openings that have a short thickness (eg. small aperture in the wall). Long openings are openings that have thickness greater than the width and breadth of the duct opening (eg. they are short ducts). Bibby studied and measured short openings in detail by predicting, measuring and comparing the acoustical and airflow performance of various silencers such as Straight, L-type, U-type, Z-type, etc. Bibby developed an optimization metric for maximizing the performance of an interior natural-ventilation openings that consider both acoustics and airflow. Best-practice guidelines for designing successful interior natural-ventilation openings were also proposed. Work by Bibby that is relevant to this study is discussed throughout this thesis wherever required.

(a)

(b)

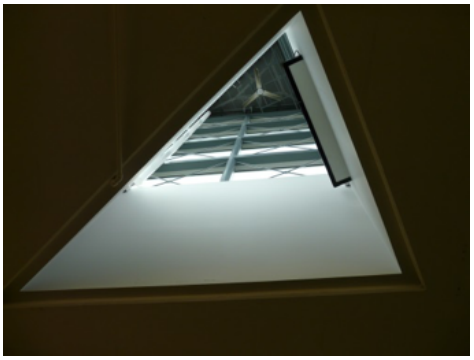

(c)

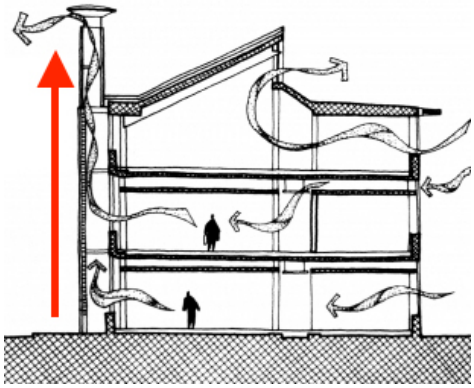

(d) Illustration sourced from [5]

Figure 1.1: Examples of long purpose-provided duct-like openings in naturally-ventilated buildings.

Under the supervision of Prof. Hodgson, this study continued the work done by Bibby. It focusses on studying and optimizing the acoustical and airflow performance of long openings (i.e. ducts). Ducts in naturally-ventilated buildings could connect workspaces on the same floor, to provide airflow or, more commonly, connect various floors in a building, to provide airflow through the stack effect. Stack effect is the flow of air into, outside or through the building, resulting from air buoyancy. Buoyancy occurs due to a difference in the indoor and outdoor air densities resulting from temperature differences. A few duct-like

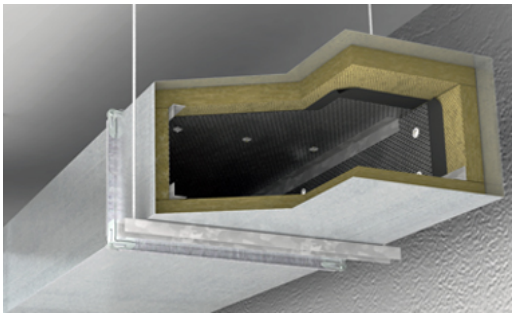

(a) Duct with absorber lining [6].

(b) Baffle silencer inserts for ducts [7].

Figure 1.2: Porous-absorber treatements for ducts, in the form of lining and baffles.

openings which could be short ducts created by thick partitions or long chimney-like structures are shown in Figure 1.1. The ducts by themselves offer no noise isolation. Porous absorbers are inserted into ducts to provide sound attenuation. Porous absorbers are inserted into ducts either in the form of a surface lining or in the form of baffles. Figure 1.2a shows an example of a duct with lining on all of the interior surfaces. Figure 1.2b shows an example of baffle silencer inserts for ducts.

The absorption of sound by porous absorbers is due to the viscosity in the air pockets contained inside the interconnecting pores. The absorber is generally regarded as ideally rigid and stationary, and the sound absorption is produced by the viscosity of the air, which undergoes alternate compressions and rarefactions as a sound wave passes through it, resulting in the dissipation of energy.

The effect of sound absorption in a duct is characterized by the sound attenuation. Sound attenuation is a measure of the energy loss during sound propagation in a medium, as a function of frequency. Many metrics are available to evaluate the acoustic performance of the medium. One metric that is used to evaluate the acoustical performance of ventilator openings is the Sound Transmission Loss (TL), which describes the ability of a material or system to block or attenuate the transmission of sound from one side to another. The higher the TL, the more the material attenuates the sound and provides noise isolation. Sound transmis-

sion loss is represented as a function of frequency and is reported in decibels (dB). The TL is measured between two reverberation chambers in an acoustical testing facility according to ASTM E-90. A reverberation chamber has a diffuse sound field, which means that the reverberant sound intensity throughout the room is highly uniform. The TL can be expressed as:

$$TL = SPL_s - SPL_r + 10 \log \left(\frac{S}{A} \right) \tag{1.1}$$

where SPL_s is the average sound-pressure level in the source room (i.e., the room with the sound source), SPL_r is the average sound-pressure level in the receiver room, S is the surface area of the partition and A is the absorption area in the receiver room. For a silencer (duct with absorber in this study), TL can also be expressed in terms of the transmission coefficient τ as $TL = 10 \log(1/\tau)$, where the transmission coefficient τ is the ratio of the transmitted energy to the incident energy.

Another metric used for measuring sound attenuation is the Insertion Loss (IL), which is the difference in sound-pressure levels with and without the silencing element, at the receiver location. This measure provides a direct indication of the improvement provided by the insertion of the silencing element:

$$IL = SPL_{ref} - SPL_x \tag{1.2}$$

where SPL_{ref} is the sound-pressure level at the location without the silencing element, and SPL_x is the sound-pressure level with the silencing element. A modified version of the IL was used in this study. The SPL was measured at microphone locations, near the inlet and outlet of the duct, with no sample in place. Then the SPL was recorded again with the absorbent sample inserted. For a duct with absorptive lining, the difference in the SPL near the inlet and the outlet of the duct, with and without the absorber, was used as the Insertion Loss.

Both TL and IL have their advantages. TL gives a close-to-reality picture of the sound-attenuating performance of the silencer (includes the effect of diffrac-

tion of sound near duct inlet and outlet). TL can be affected by flanking, and the transmission of sound through the partition. IL gives more consistent results across different testing conditions, but is only appropriate for measuring small silencing units. In this study, Insertion Loss was used as the descriptor of acoustic performance. Since IL is measured inside the duct, the effects of diffraction of sound near the inlet of the duct are negligible. This is useful when using a plane-wave approximation (Section 1.6.1), to model the duct theoretically. The assumption of negligible sound diffraction is a good approximation when the duct is long enough compared to the other dimensions.

When measuring the SPL, the unweighted sound levels do not account for the sensitivity of humans to sound; that is relative loudness that varies with frequency. A-weighting is employed to address this problem, as a simple correction to the levels of the sound at different frequencies according to the A-weighting curve.

When an opening is created in a partition that separates two large regions of still-air at different pressures, flow occurs. The airflow performance is usually characterized by the variation of the volume flow rate (Q) through the opening with the associated pressure drop (Δp) across the opening. The volume flow rate (Q) is related to the pressure drop (Δp) by the discharge coefficient C_d as:

$$Q = A_d C_d \sqrt{\frac{2\Delta p}{\rho}} \tag{1.3}$$

where A_d is the cross-sectional area of the opening/duct in the partition. The discharge coefficient depends on the Reynolds number (Re) of the flow. The opening Reynolds number (Re_o) is defined as:

$$Re_o = \frac{\rho u_d d_h}{\mu} \tag{1.4}$$

where ρ is the density of air, d_h is the hydraulic diameter of the opening, μ is the dynamic viscosity of air and u_d is the velocity at the inlet of the duct opening,

given by:

$$u_d = \frac{Q}{A_d} \tag{1.5}$$

For $Re_o < 2000$, the flow is laminar; for $Re_o > 4000$, the flow is turbulent. When flow is turbulent, $(\Delta p) \propto {u_d}^{0.5}$ and C_d is fairly constant for variations in Reynolds number. When flow is turbulent, $(\Delta p) \propto u_d$ and C_d depends on the Reynolds number. For a simple, short aperture, the discharge coefficient C_d is 0.61. For other geometries of opening, the discharge coefficient is determined from measurements.

Bibby addressed the need for an optimization metric that combines both acoustical and airflow performance for interior openings in naturally-ventilated buildings by introducing the open area ratio (OAR). This metric provided a single-number metric for optimization, by maximizing the ratio of the equivalent open areas for airflow (EOA_f) and sound (EOA_s). The equivalent open areas were used to characterize the performance of the ventilator at a specific operating condition:

$$OAR = \frac{EOA_f}{EOA_s} \tag{1.6}$$

EOA_f and EOA_s are calculated from measurements or predicted – which means the ducts have to be built and measured, or modelled and predicted, to evaluate performance.

The equivalent open area for sound EOA_s was defined as a single-number metric given by:

$$EOA_s = A_d \tau_{A,speech} = A_d \left(10^{\frac{-TL_{A,speech}}{10}} \right) \tag{1.7}$$

where $TL_{A,speech}$ is the normalized A-weighted speech level minus the transmission loss of the silencer. Subtracting the A-weighting represents the most audible sound in the transmitted-sound spectrum. The $TL_{A_{speech}}$ can be modified to be used with IL as, $IL_{A,speech}$.

The equivalent open area for airflow EOA_f was defined as:

$$EOA_f = \frac{C}{0.61}\sqrt{\frac{\rho}{2}}(\Delta p)^{r-0.5} \tag{1.8}$$

where C and r are obtained by curve-fitting measurement data in the form:

$$Q = C(\Delta p)^r \tag{1.9}$$

This curve fitting is in accordance with the standard ASTM E779-10 [8]. It can be seen that the EOA_f is normalized to the C_d of a simple orifice, which is 0.61.

1.2 Problem statement

The state of research progress by the UBC Acoustics and Noise Research Group was discussed in the previous section. This thesis continues this work to optimize the acoustic and airflow performance of duct-like natural-ventilation openings. The *OAR* defined by Bibby required predictions or measurements to compare performance. Bibby performed experiments in a full-scale test-facility. This constrained the dimensions of the silencers that could be tested and not highly diffuse fields in the source and receiver rooms due to their small size.

The following problems were expected to be addressed in this thesis:

1. To provide a provisional tool for designers to quickly calculate and compare performances of different duct-configurations without having to construct and measure, or perform FEM. The output parameters for the tool should be direct measures that can be understood and easily applied.

2. To investigate the use of scale-models to measure the performance of ducts with large dimensions.

3. To identify best practices and suggest guidelines for the best configurations of the absorbers in a given duct.

1.3 Research objectives

In order to develop best practices, it was necessary to acquire performance data for various duct configurations. This can be done through physical measurements or through numerical-simulation predictions. An optimization algorithm could be used to identify the best configurations based on the performance objectives.

In this study it was decided to address the two problems mentioned in Section 1.2 together by building surrogate models that describes the sound attenuation and ventilation airflow in the duct. These surrogate models were to be designed to be used in an optimization algorithm. The surrogate models were to be simple enough to be used by designers to predict the desired output, for the estimation and comparison of performance. The surrogate models must also be flexible enough to accommodate different types of configurations, as far as possible. The surrogate models would help reveal the impact of various parameters on the acoustical and airflow performance. It is difficult to propose guidelines to designers, as the performance depends on a case-by-case basis. Attempts have been made to address this issue as best as possible.

In order to fulfil the basic requirements of this study, the following workflow was adopted:

1. Select appropriate duct configurations for investigation in this study, along with appropriate input and output performance parameters defining them.

2. For the selected duct configurations, predict the output performance parameters of the duct using two-dimensional Finite-Element modelling.

3. Build a relatively simple 2D surrogate model based on the prediction results (the data set) from Finite-Element modelling.

4. Extend the surrogate model to apply to configurations in the 3D domain.

5. Measure the performance of selected duct configurations, using a scale-model of the duct and applying appropriate scaling laws.

6. Compare results from the surrogate model with measurements and Finite-Element predictions.

7. Suggest best practices based on results from the surrogate model and experiments.

The above objectives were addressed for acoustics and airflow independently. The optimal configuration of the duct can only be defined relative to what the designer wants to achieve. This study provides the necessary tools they can use to predict optimal configurations.

1.4 Scope and definition of audience

The study attempts to answer the question of how to design ducts with absorbent lining or baffles that can provide the required airflow, and acceptable noise attenuation. There are no internationally recognized standards for internal background-noise limits with the use of natural ventilation. This thesis attempts to provide a flexible model that can be used at the design stage in combination with a suitable standard, at the discretion of the designer. The study also attempts to develop surrogate models that can be used in the case of existing ducts for retrofit noise control.

The study described in this thesis was intended to provide guidelines to the design community. The surrogate models that were developed in this work were intended to be engineering approximations to help make design decisions. Due to constraints in time and resources, approximations were made when constructing the surrogate model. These are described later in the thesis.

The work in this study was restricted to optimizing the performance of straight ducts with rectangular cross-section. The study investigates the addition of absorbent linings on some or all surfaces of the duct, and the effect of the addition and positioning of baffles, along with all their associated acoustical and airflow properties and dimensions, on the performance.

1.5 Literature review

The sound attenuation in a duct can be increased by optimizing the duct dimensions and adding reactive elements such as silencers, or absorptive elements such as sound-absorbing baffles and linings. Usually porous absorbers are preferred, since they attenuate noise with minimal obstruction to flow in the case of ducts. An analytical approach to the attenuation of sound in lined ducts was first discussed by Sabine [9]. It assumes that the wavelength is greater than the largest cross-sectional dimension of the duct, and that the acoustic impedance of the duct lining is a pure resistance. Later, in 1969, Kurze [10] focused on the effect on sound propagation of sound-absorbing materials when the sound is normally incident on the baffles. For materials having anisotropic properties and layered structures, Kurze developed an expression for predicting sound attenuation.

Strategically positioning absorbent baffles, and choosing optimal dimensions for liners and baffles, along with the optimal cross-sectional dimensions of ducts, one can optimize the performance of the absorbers or, in other words, achieve optimal sound attenuation with minimal effect on airflow.

Different arrangements of sound absorbers need to be considered in maximizing the sound attenuation in ducts. Orlowski [11] in 1983 tested various configurations of sound-absorbing baffles in rooms with diffuse sound fields, using 1 : 16 scale models. The work includes the comparison of freely-suspended absorbers and those with a solid backing. It was concluded that a porous absorber is more efficient at mid-to-high frequencies if freely suspended than against a solid backing. The effect of different densities of suspended absorbers was also compared. A large sample of suspended absorber showed better efficiency at mid-to-high frequencies if subdivided into small samples. If the absorbers were placed in alternating horizontal and vertical positions in an array, they were found to obscure each other from the sound field if their density was increased above 1 absorber/2 m^2, since the absorbers were 1 m^2 in area. Beyond this density, the efficiency was found to decrease. Effect of a central divider in a suspended absorber was found to have no improvement on the absorption coefficient. The

absorption of cylindrical suspended absorbers was also tested and found to be significantly lower that that of plane absorbers made from the same area of material.

Optimization of parameters involves predicting the performance using numerical methods, which are cost-effective and time-efficient. Finite-Element Analysis is commonly used to predict the performance of sound-attenuating elements. Borelli and Schenone [12] analyzed the sound propagation in lined ducts by means of a Finite-Element Model. The insertion loss was predicted for a frequency range of 250 to 4000 Hz. The model was validated in comparison with experimental data obtained in accordance with *ISO 11691* and *ISO 7235* standards. The sound-absorbing material for the lining was mineral wool, with thickness that varied from 25 to 150 mm. The comparisons showed a good agreement between experimental and numerical results, suggesting that FEM can be an accurate and inexpensive way to predict sound attenuation in lined ducts.

FEA models determine the output parameters for given input parameters by solving the wave-equation for each cell in the mesh. However, an inversion model is required to determine the appropriate input parameters (eg. flow resistivity, porosity, dimensions of absorbers) if the input and the output parameters are known. Eck and Probst [13] in 2007 developed an analytical model to determine the sound absorption of baffle systems using an energy-based approach. Their model also helps understand the dependence of baffles spacing and thickness on the Insertion Loss. However, since the model is based on the energy approach, it may not be very accurate when modelling complex systems, due to the neglecting of phase effects.

Optimization can be alternatively achieved by using regression models [14] or more complex Genetic Algorithm models [15]. Though the genetic algorithm is considerably faster than other algorithms, it is still time consuming if there are many dependent-parameters to be optimized. Determining the solution from Finite-Element model for every seed from the Genetic algorithm is highly time consuming. For this reason, Chang et al. [16] established a simplified objec-

tive function by linking a boundary-element model (BEM) to a neural-network model. Selective solutions from the BEM were used to train the neural network and to determine the objective function. This objective function was optimized using genetic-algorithm procedures.

Prediction models need to be validated before they are put to real-world use. However, building full-scale models is quite expensive. For this purpose, scale models can be used as an alternative. However, building scale models comes with its own set of problems. Hodgson and Orlowski [17, 18] established principles and guidelines for the scale modelling of industrial rooms that can be applied to other enclosed environments. In order to model the sound field in an enclosure scaled by $\frac{1}{n}$, the model wavelength-to-dimension ratios must equal those at full scale. Thus, the frequencies of the test signals are scaled by n. One other important consideration is the choice of materials for the scale model. The impedances of the scaled materials at the test frequencies must match those of the full-scale model at their corresponding full-scale frequencies.

Delany and Bazley [19] developed an empirical relation that describes the impedance of fibrous/porous materials in terms of the ratio of frequency to flow-resistivity. Scaling the flow-resistivity of scaled models to that of full-scale results as shown in Equation 1.10, scales the acoustical properties appropriately for certain sound-absorbing materials:

$$\frac{f_{FS}}{R_{f_{FS}}} = \frac{f_M}{R_{f_M}} \tag{1.10}$$

where f is the frequency, R_f is the flow-resistivity of the material and FS and M represent full-scale and model-scale, respectively. A detailed description of the scaling laws is presented in Section 4.1.

However, the Delany and Bazley relationship does not hold for all materials. According to the work of Samimi [20], materials such as cotton fibers are in good accordance with the Delany-Bazley model, but fibreglass and wood-fibre materials are not. Attenborough [21] developed a more generally-applicable four-

parameter model involving flow-resistivity, porosity, tortuosity and pore-shape factor. This model conforms to the experimental results quite well for most materials. However finding a scaled material that has the right scaled values of all four of the parameters is highly improbable. Voronina [22] found that the four-parameter model holds good only when choosing fibrous (eg. wool) materials for both full-scale and scale models, or choosing porous (eg. foam) materials for both models. This difference is attributed to the difference in the reactance term for fibrous and porous materials.

The duct is assumed to radiate noise only from the opening. The walls are made thick enough that no sound flanking transmission occurs through the walls. The scale model needs to be built in close accordance with the full-scale model. Standards for building and testing of ducts include ISO 7235 and ANSI E477-06a. ANSI E477 suggests that an anechoic room be located on the source side containing a loudspeaker and that the receiver end terminate in an anechoic room. Details of recommended dimensions of the room and measurement procedures are described in the standard.

In addition to the acoustical performance, the airflow of ventilation openings also needs to be optimized. Oldham [23] suggested a single-number metric to evaluate the combined acoustical and airflow performance of the opening. Effective Open Area for sound and for airflow were proposed. Bibby [4] improved on the use of an effective open area to describe ventilation performance. He also accounted for a speech weighting in his metric of acoustical performance. Bibby extensively studied various configurations of silencers in detail. For long ducts, he suggests that greater silencer length results in greater air-flow. For openings in naturally-ventilated buildings, Bibby suggests that laminar flow possibly occurs due to low pressure drop across the openings, leading to a Reynolds-number-dependent discharge coefficient. Etheridge [24, 25], discusses the effect of Reynolds number on the airflow performance of purpose-provided and adventitious openings. Etheridge also suggests that the discharge coefficient is dependent on Reynolds number for adventitious openings. However he describes

the flow to be at-least-partly turbulent in purpose-provided openings. He also presented the Reynolds numbers encountered in practice for different kinds of openings, and at low and high pressure differences across the openings. More information on this is discussed in Section 1.6.5.

1.6 Concepts and theory

1.6.1 Governing equations for acoustics

Three-dimensional sound-wave propagation in a stationary medium is given by the *wave equation* as:

$$\left[\frac{\partial^2}{\partial t^2} - {c_o}^2\nabla^2\right]p = 0 \tag{1.11}$$

where c_o represents the speed of sound, p the acoustic pressure, and the Laplacian operator ∇^2, the second-order derivative of divergence operator ∇ in cartesian co-ordinates, is defined as:

$$\nabla^2 = \frac{\partial^2}{\partial x^2} + \frac{\partial^2}{\partial y^2} + \frac{\partial^2}{\partial z^2} \tag{1.12}$$

The general solution to the 3D wave-equation shown in Eq. (1.11) for a rectangular duct is given by Eq. (1.13) as:

$$p(x, y, z, t) = (C_1 e^{-jk_z z} + C_2 e^{-jk_z z})(e^{-jk_x x} + C_3 e^{-jk_x x})(e^{-jk_y y} + C_4 e^{-jk_y y})e^{j\omega t} \tag{1.13}$$

where x, y and z are coordinates along the directions of the width (w), breadth (b) and length (l) of the duct, respectively.

Plane-wave theory

For acoustic-wave propagation in a rigid-walled duct, when the cross-sectional dimensions of the duct are sufficiently small, the waves propagate as plane waves. The acoustic pressure p and particle velocity u are uniform over wavefronts nor-

mal to the direction of wave propagation. For a plane-wave approximation, the wave-equation from Eq. (1.11) can be simplified to a one-dimension equation as:

$$\left[\frac{\partial^2}{\partial t^2} - {c_o}^2 \frac{\partial^2}{\partial z^2}\right] p = 0 \tag{1.14}$$

The general solution to Eq. (1.14) is then:

$$p(z,t) = (C_1 e^{-jk_z z} + C_2 e^{-jk_z z}) e^{j\omega t} \tag{1.15}$$

A plane-wave approximation for a duct of cross-section $w \times b$ and $w > b$, when the wavelength is large or the frequency is small, is:

$$\lambda < \frac{2}{\sqrt{\left(\frac{m}{w}\right)^2 + \left(\frac{n}{b}\right)^2}} \tag{1.16}$$

$$f < \frac{c_o}{2w} \tag{1.17}$$

The frequency below which only plane-waves propagate is defined as the cut-off frequency:

$$f_{cutoff} = \frac{c_o}{2w} \tag{1.18}$$

1.6.2 Sound ratings

The acoustical performance of the ventilation silencers can be evaluated with resect to various sound-isolation metrics. Furthermore, depending on the type of space, the quality of the sound expected – i.e. the frequency content of the signal and the required sound attenuation – differs. Speech privacy is one of the major concerns in naturally-ventilated buildings. Different metrics and their actual correlation to subjective ratings of speech is a debatable topic. There is no standard or guidelines for acoustic-design methodology in naturally-ventilated buildings in particular. Therefore, different designers prefer different metrics of

sound. This thesis does not attempt to disambiguate the question of the best metric to use; rather, it tries to develop a model that is flexible enough to be used with various metrics. Some commonly used sound metrics are described briefly below.

Sound Transmission Class (STC) is a single-number metric used to rate partitions, for their effectiveness in blocking sound. The number assigned to a particular partition design as a result of STC testing represents a best fit of frequency-varying transmission losses to a set of curves which define that sound transmission class. STC is based on the performance between 125 to 4000 Hz, which are the frequencies relevant to speech communication.

Total, A-weighted sound level (dBA) is a simple measure that adds the A-weighting to the unweighted levels and sums the contributions of sounds at different frequencies to approximate the total loudness experienced by listeners. Total, A-weighted sound level has maximum sensitivity between 1-6 kHz.

Speech Intelligibility Index (SII) determines how well an individual understands speech, and is rated between 0-1. It adds spectral weightings as a modular function that includes reverberation, noise and distortion, according to their relative importance to the intelligibility of speech. The main peak in the spectrum corresponds to the fundamental frequency, which is around 125 Hz for male speakers and 250 Hz for females.

Most of the metrics depend on the use of Transmission Loss (refer Eq. (1.1)) for their calculation. Transmission Loss is independent on the absorption in the receiver room, as can be seen from the equation. In this study, since Insertion Loss was used, the term $10\log(S/\alpha)$ can be added to the Insertion Loss for use with the metrics. It should be noted however that using Insertion Loss in such a way should be done with caution, as it neglects the effects of diffraction of sound on the TL, which is only valid for ducts, but not openings of small thickness.

1.6.3 Governing equations for fluid flow

This section briefly describes the governing equations for flow. The Navier-Stokes equation and the Bernoulli equation together form the basis for the theory of fluid flow.

Navier-Stokes Equation

The Navier-Stokes equations govern the motion of fluids and can be seen as Newton's second law of motion for fluids. The Navier-Stokes equation in the case of an unsteady flow, with non-uniform density, is given as:

$$\rho\left(\frac{\partial u}{\partial t}+u\frac{\partial u}{\partial x}+v\frac{\partial u}{\partial y}+w\frac{\partial u}{\partial x}\right)=-\frac{\partial P}{\partial x}+\mu_0\left(\frac{\partial^2 u}{\partial x^2}+\frac{\partial^2 u}{\partial y^2}+\frac{\partial^2 u}{\partial z^2}\right) \tag{1.19}$$

$$\rho\left(\frac{\partial u}{\partial t}+u\frac{\partial u}{\partial x}+v\frac{\partial u}{\partial y}+w\frac{\partial u}{\partial x}\right)=-\frac{\partial P}{\partial y}+\mu_0\left(\frac{\partial^2 u}{\partial x^2}+\frac{\partial^2 u}{\partial y^2}+\frac{\partial^2 u}{\partial z^2}\right) \tag{1.20}$$

$$\rho\left(\frac{\partial u}{\partial t}+u\frac{\partial u}{\partial x}+v\frac{\partial u}{\partial y}+w\frac{\partial u}{\partial x}\right)=-\rho g-\frac{\partial P}{\partial z}+\mu_0\left(\frac{\partial^2 u}{\partial x^2}+\frac{\partial^2 u}{\partial y^2}+\frac{\partial^2 u}{\partial z^2}\right) \tag{1.21}$$

Bernoulli Equation

The Bernoulli equation describes the flow at high Reynolds numbers, at which the flow can be assumed to be inviscid along a streamline. The Bernoulli equation represents the conservation of energy for a flow with uniform density as:

$$\frac{p}{\rho g}+\frac{u^2}{2g}+z_1=constant \tag{1.22}$$

1.6.4 Vena-contracta

When fluid flows from a larger to a smaller cross-sectional area due to a sudden contraction, there is a reduction in the area of the jet. The point of minimum cross-sectional area of the jet, or in other words, the point of maximum velocity,

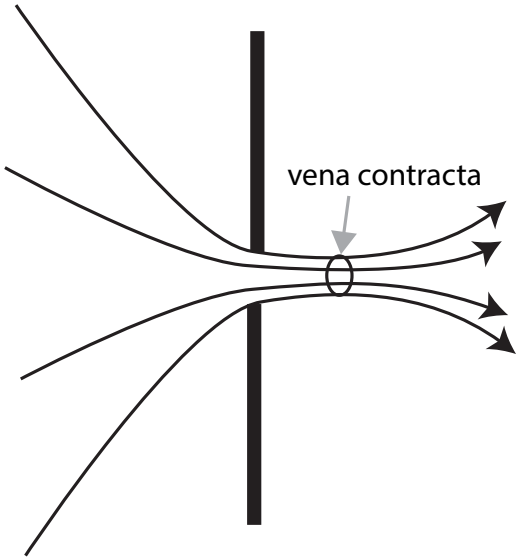

Figure 1.3: Formation of a vena-contracta due to sudden contraction.

is known as the vena-contracta (see Figure 1.3). This phenomenon is caused by the inertia of the fluid to direction change. The discharge coefficient C_d for flow through an opening is a result of the vena-contracta.

1.6.5 Classification of ventilation openings

This section is based on the work by Etheridge in his book on natural ventilation in buildings [24]. Ventilation openings can be broadly classified into two types – purpose-provided and adventitious. Purpose-provided openings include intentional openings designed for airflow, such as air-vents, ducts and windows. Adventitious openings are unintentional openings such as gaps and cracks in walls, doors and windows, that usually have high-aspect-ratio cross-sectional dimensions. The basic flow characteristics of most purpose-provided openings can be described qualitatively as for either a sharp-edged orifice or a long duct.

Sharp-edged orifices

Sharp-edged orifices tend to have a constant discharge coefficient equal to 0.61. As discussed before, the Bernoulli equation (Eq. (1.22)) provides a square-law relationship between velocity (u) and pressure (Δp). It is interesting to note that, in [24], the author states that the square-law relationship described as being due to turbulent flow is incorrect. This is due to the flow separation that occurs at the sharp edges, independent of the flow velocity. Turbulence occurs due to the formation of a vena-contracta close to the inlet of the edge. Thus, even for Re_o as low as just over 100, a constant discharge coefficient can be expected.

Long opening – adventitious

Long, adventitious openings have a large L/d_h ratio, where L and d_h are the length and hydraulic diameter of the duct, and have small values of d_h, leading to low Re_o – this in turn results in a C_d that depends on Re_o. A Reynolds-number-dependent flow can be expressed either as the power-law equation or a quadratic equation. If it is expressed as a power law equation, the coefficient r in Eq. (1.9) is between 0.5 and 1. Fully laminar flow is described with a coefficient of 1, and fully turbulent with a coefficient of 0.5. Another way of representation would be a quadratic equation, where the flow is described as a combination of linear and square terms as:

$$\Delta p = c_1 u + c_2 u^2 \tag{1.23}$$

Long opening – purpose-provided

For long, purpose-provided openings such as ducts and chimneys, the flow is expected to be at least partly, if not entirely, turbulent [24], due to the high Re_o for such ducts. The value of C_d, however, still depends on the length of the duct.

1.6.6 Is the flow in natural-ventilation ducts laminar or turbulent?

The ducts that are being investigated in this thesis are long, purpose-provided openings. Interestingly, in contrast to what was described in Section 1.6.5, Bibby [4], found that the flow could be laminar for ventilation openings operating in natural-ventilation conditions, for the types of ventilation silencers he tested. It is clear that the flow regime largely depends on the type of silencer being investigated. Before the airflow results can be predicted using FEA, it is necessary to know if the flow through the ducts of interest has a laminar or turbulent flow. Measurements for various configurations of ducts (refer to Section 4.6) were done in this study, as described in Chapter 4. Even for a duct of small cross-sectional dimensions – 0.15 m × 0.15 m – if the Re_o is calculated as:

$$Re_o = \frac{Q_{in}}{A_d}\frac{\rho d_h}{\mu} \tag{1.24}$$

it was determined to be as high as approximately 9800 at 1-Pa pressure drop, which should lie in the fully-turbulent range. It should also be noted that Re_o is calculated using the airflow divided by the cross-sectional area of the duct. The flaw in this method of calculation is that the estimated velocity at the inlet of the duct does not account for the reduction in flow area due to the presence of the vena-contracta. Higher velocities at the inlet of the duct result in higher Re_o. Given this result, it was concluded that it is safe to assume that long openings of interest in naturally-ventilated buildings have turbulent flow. However, it must be noted that, if the duct opening has a very large aspect ratio of the cross-sectional dimensions, which was not considered in this study, the flow could possibly be laminar, depending on the hydraulic diameter and the formation of the vena-contracta. The effect of the vena-contracta on the pressure drop in ducts is discussed in Chapter 3.

1.6.7 Surrogate modelling

For identifying optimal configurations of the duct, there is a requirement to predict numerous test cases of different configurations with various input parameters. While predictions from finite-element analysis can produce accurate results, evaluation can be relatively expensive for performing a search, especially with a large number of variables. A surrogate model can be constructed that mimics the behaviour of the simulation model as closely as possible while being computationally inexpensive. This model can be used to search for an optimal solution. The surrogate model evaluates an objective function with constraints as a function of input variables from a limited number of data points determined from finite-element simulations. The selection of data points plays a critical role in determining the accuracy of the surrogate model. The surrogate model is mainly used to capture the relationship between the inputs and outputs of the dataset and is not expected to provide insights into the exact underlying physics. Construction of the surrogate model involves machine-learning methods. Some common machine-learning methods employed include artificial neural networks (ann), and various forms of regression, such as linear, Kriging, symbolic regression, etc.

Artificial neural networks, inspired by biological neural networks, are generally presented as systems of interconnected primal units called *neurons*. Weightings are assigned to the various connections, based on learning from the dataset. Several learning algorithms exist that are used to train the neural network. With appropriate implementations, neural networks can be used to model complex models accurately, where simpler estimations of functions fail. However, the neural network is usually a black box, and tuning its parameters requires significant experimentation. Moreover, neural networks do not perform well if the inputs have very non-linear effects on the output. This is especially true in the case of frequency-dependent problems.

Symbolic regression

In addition to the objective of developing a surrogate model for optimization, it is desirable to develop a simple model that can be used to quickly estimate the model-outputs. For this work, neural networks were initially chosen. However, due to unsatisfactory results and the inability to tweak the output with known knowledge, symbolic regression was later chosen to model the outputs. Conventional regression models assume a pre-conceived template for the model, and then determine the parameters that best-fit the model form. Symbolic regression makes use of an evolutionary process like the genetic algorithm, on the other hand, to determine a set of the most plausible model forms (i.e. the parameters and the form of the equations are determined simultaneously). Symbolic-regression models are usually simple representations and easy to modify. A set of operators that are expected to be observed in the model are chosen in advance, based on the level of complexity required. The greatest benefit of this method is that it provides a degree of insight by providing intrinsic relationships in the data through simple model forms – this might not necessarily be physically accurate, but can be used to understand the sensitivity of and correlations among various variables. Eureqa [26, 27], a symbolic regression software, was used in this study.

Squashing functions

Squashing functions are used to model discrete step functions as continuous functions. Squashing functions, as the name suggests, are used to squash or normalize the output data into a limited range. This is particularly useful to model the phenomenon of abrupt change and negligible growth following the change. Some of the commonly-used squashing functions are shown in Figure 1.4. A *logistic* function is of the form:

$$\frac{1}{1 + e^{-a(x-x_0)}} \tag{1.25}$$

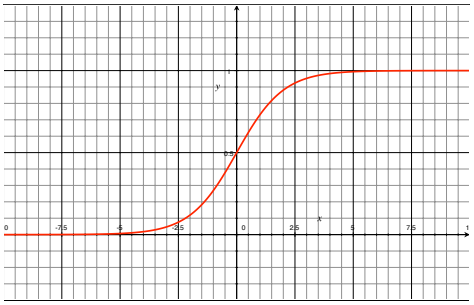

(a) Logistic function of form $\frac{1}{1+e^{-x}}$

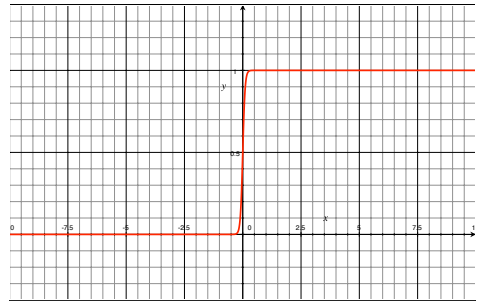

(b) Logistic function of form $\frac{1}{1+e^{-20x}}$

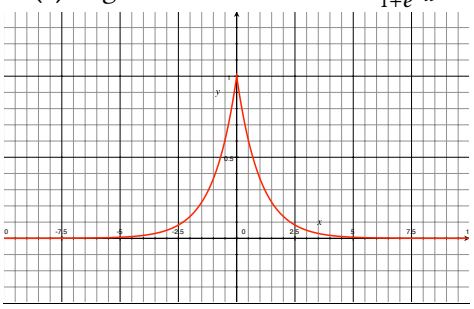

(c) Gaussian function of form $e^{|-x|}$

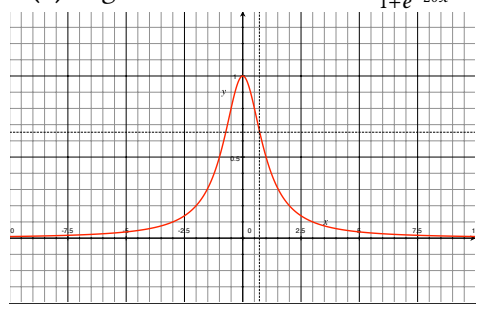

(d) Cauchy function of form $\frac{1}{1+x^2}$

Figure 1.4: Commonly-used squashing functions used in surrogate modelling.

As can be seen in Figures 1.4a and 1.4b, for high values of the coefficient a in Eq. (1.25), the equation behaves like a step function.

1.7 Thesis overview

The procedure adopted in this thesis is described by the flowchart in Figure 1.5. It can be seen that the process was quite non-linear; efforts have been made to represent the information in a linear fashion, to the best of the author's abilities. The reader might have to cross-reference different chapters to get a full picture of the work.

Chapter 2 discusses the Finite-Element Method that was adopted to generate the sample set for the surrogate models for acoustics and airflow, using 2D models. It also discusses the 3D models that were used to validate the results from

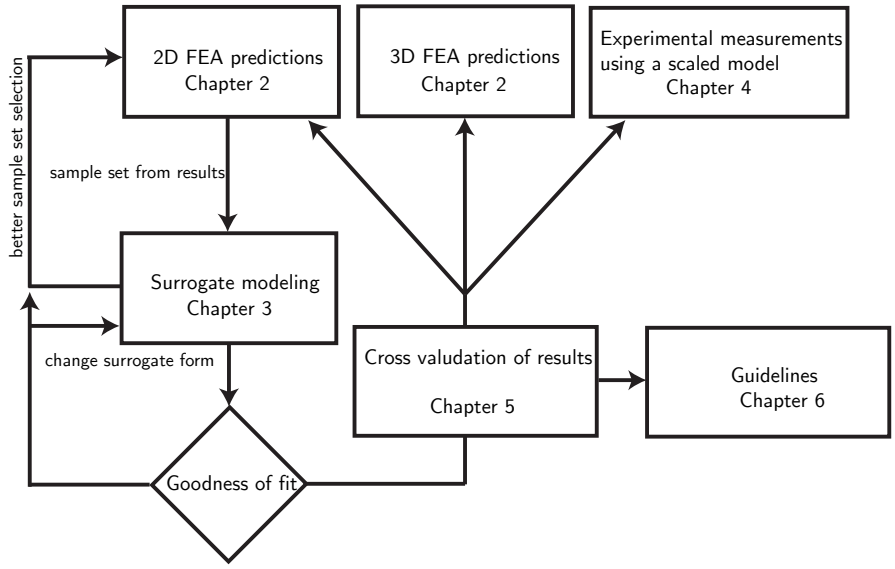

Figure 1.5: Overview of the workflow adopted in this thesis.

the surrogate model. Chapter 3 discusses the surrogate model that was built using the results from FEM, along with the choice of various parameters used in the model. Chapter 4 describes the construction and design of the experimental setup used to validate the surrogate model. This chapter also discusses details of the different configurations that were chosen for testing. Chapter 5 discusses the comparison of results from the surrogate model with measurements and FEM predictions, for selected configurations discussed in Chapter 4. This chapter also discusses the sensitivity of the performance to various parameters. Finally, Chapter 6 discusses inferences from the study and proposes guidelines/ recommendations for designers based on its results.

Chapter 2

Finite-Element Modeling

The previous chapter provided detailed background and objectives for this study and the overall workflow that was employed. In this study, in order to optimize the performance of ducts, surrogate models for acoustics and airflow were independently designed. To build the surrogate models, results from Finite-Element Method (FEM) predictions were used as the input data set. This chapter describes in detail the methodology that was adopted for modelling the acoustic and airflow domains in Finite-Element analysis. This is followed by the details of the generation of the desired data set for surrogate modelling. The assumptions that were made during Finite-Element predictions, along with the limitations of the modelling procedure, are also discussed in this chapter.The following chapter discusses the surrogate models that were constructed from the FEM data.

2.1 Finite-element method

The Finite-Element Method basically takes a complex problem, described by differential equations, whose solution may be difficult to obtain, and divides the domain into pieces. For each of the pieces, a simple approximation of the solution is constructed, and then the local, approximate solutions are combined together to obtain a global approximate solution. FEM is widely used to find approximate solutions for differential equations which are not solvable by analytical meth-

ods, or which have geometrically complex domains. Comsol Multiphysics [28], a commercial FEM package, was used in this study to predict the solutions for both acoustics and airflow in this study. Finite-Element prediction was done for two reasons:

- To use the results as the data set for constructing the surrogate model – this involves deriving required outputs from FEM for a range of various input parameters. The models used were simplified versions for faster computing.
- To serve as a cross-validation between the surrogate models and the experimental results using elaborate models that closely mimic the experimental setup, for selected configurations.

2.2 Finite-element method for acoustics

Untreated ducts are not capable of significant sound attenuation. For this reason, porous-absorber elements are generally added to the duct, either by means of lining or baffle inserts. Insertion of porous absorbers in ducts increases the attenuation of sound by dissipating sound energy. Ducts are lined by mounting porous absorbers along the inside surfaces of the duct, held in place with sound-transparent materials. The thickness, and the length of the porous-absorber linings affect the Insertion Loss of the duct. In order to increase the Insertion Loss of the duct further, baffles made of porous-absorber materials are inserted inside the duct. The prediction of sound attenuation when sound propagates through these lined ducts, was done by means of FEM. With absorbers and linings, several configurations of ducts can be created. Developing a single surrogate model that is flexible enough to model all such configurations is a challenge. The predictions from FEM are crucial in generating the data set for the surrogate model. An efficient FEM model was desired which would be quick to predict, and also be able to capture the necessary physics. The following sections look into the Finite-Element modelling for acoustics in detail.

2.2.1 Modelling specifications

In the Acoustics module of Comsol, the Pressure Acoustics interface has the equations, boundary conditions and sources required for modelling acoustics and solving for the sound-pressure field in the frequency domain – for problems concerning pressure waves in a fluid. In this study, air at room temperature was chosen as the acoustic medium.

To begin with, it was decided to use 2D modelling over 3D. Though a 3D model would be more accurate, simulation times are many times higher. Modelling large ducts at high frequencies resulted in excessive use of computer memory (RAM). For such a memory-intensive model, direct solvers cannot be used. Iterative solvers that efficiently manage RAM must be used; however they increase the runtime by many times. Also, Finite-Element Modelling was used to generate a data set for the surrogate model. This meant that numerous FE predictions were required, which was not practical with a 3-D model in the available time frame.

While 2D modelling was used, from Figure 2.1 it can be seen that a 2D model of a lined duct can only represent a lining on one side or two sides when it is extruded to the 3D domain. The sound absorption for lining on all four sides would be underestimated by the 2D acoustic model. Thus, it was desired that the surrogate model be built for a 3D duct with lining covering from one to four sides of the duct, from FEA predictions of the duct with lining on only one side and two sides, in 2D. A surrogate model for a simple configuration would be used to build complex configurations of 3D models; how this was done is described in the next chapter.

2.2.2 Domain

The acoustic domain defines the sound field that was considered in the model. An accurate way of modelling the acoustic domain that would be close to the real-life scenario would be to model a duct inserted across the partition between the source and receiver rooms. The source room is to be designed to contain a

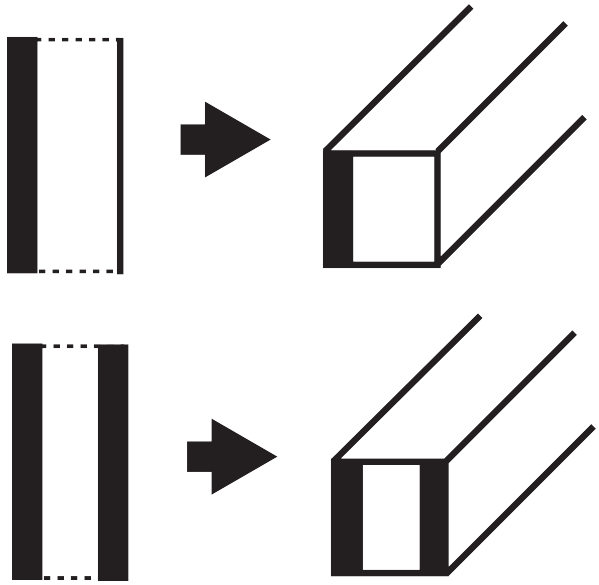

Figure 2.1: 2-D illustration of the duct (top) and its equivalent 3-D extrusion (bottom).

diffuse field and the receiver room is anechoic. More details on the reasons for choosing the source and receiver rooms to be diffuse and anechoic, respectively, are discussed in Chapter 4. Inclusion of source and receiver rooms as parts of the domain resulted in higher RAM usage, along with longer simulation times. Moreover, at lower to mid frequencies, this would also affect the Insertion Loss. This is because, at low frequencies, the sound field in the source room is not diffuse. The dominant modes that are a function of the dimensions of the room affect the Insertion Loss at low frequencies. At higher frequencies, the sound in the source room becomes diffuse. The acoustic domain that was modelled only included the duct, along with the porous absorber.

2.2.3 Boundary conditions

Instead of a source room with multiple point sources, a plane-wave radiation boundary condition was used at the duct-inlet. This simulates a source at infinity generating incoming plane waves. Plane waves assume the propagation of sound

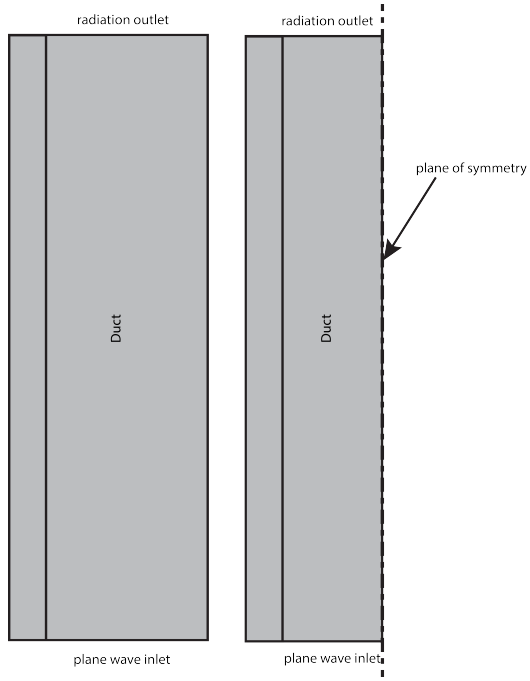

Figure 2.2: Acoustic-domain geometry of the duct with lining on one side (left) and lining on both sides (right).

to be normal to the opening of the duct. As long as the duct is long enough, this is a good estimation of the insertion loss below the cut-off frequency. The cut-off frequency for plane waves in rectangular ducts is equal to $\frac{c}{2d}$, where c is the speed of sound and d is the characteristic dimension of the duct cross-section. The use of plane waves eliminates the need to model the source room. Moreover, the physics of the model becomes much simpler.

A *sound hard* (reflective) boundary condition was used to model the duct walls. A *symmetry* boundary condition was used, with only half the duct being modelled, whenever possible – i.e. for modelling ducts with lining on both sides. Figure 2.2 shows the geometry of the acoustic domain, with boundary conditions.

Porous-absorber modeling

The presence of a porous-absorber material accounts for sound absorption and attenuation in the duct. In Comsol, porous absorbers can either be modelled as a surface impedance, with values of impedance based on measurements from impedance-tube measurements, for example, or as an equivalent-fluid, whereby the porous absorber is treated as a fluid with damping properties. The latter approach of modelling as an equivalent fluid was adopted in this study. Among the different fluid models, the Delany-Bazley model [19] was used. The Delany-Bazley model describes the impedance and wavenumber of the domain as follows:

$$Z_c = \rho_a c_a \left(1 + 0.057\left(\frac{\rho_a f}{R_f}\right)^{0.734} - j0.087\left(\frac{\rho_a f}{R_f}\right)^{-0.732}\right) \tag{2.1}$$

$$k_c = \frac{\omega}{c_a}\left(1 + 0.098\left(\frac{\rho_a f}{R_f}\right)^{-0.7} - j0.189\left(\frac{\rho_a f}{R_f}\right)^{-0.595}\right) \tag{2.2}$$

where R_f is the flow resistivity, f is the frequency, Z_c and k_c are the complex impedance and wavenumber, respectively, and the subscript a represents air. As can be seen, the model is described as a function of flow resistivity and frequency. Materials having a high value of flow resistivity are usually chosen to be the porous absorber. It should however be noted that the Delany-Bazley model was developed for fibrous absorbent materials. The model is only valid in the range of $0.01 < \frac{f}{R_f} < 1$, and for high-porosity materials (with porosity approaching 1) which have a rigid frame.

2.2.4 Mesh

A tetrahedral structured mesh was used for modelling the duct. The number of mesh elements per wavelength was selected to be 5. The choice of 5 elements per wavelength was based on the recommendations of previous authors [4, 29, 30]. Since prediction was done as a parametric sweep of the input variables, it was not possible to check mesh convergence for every geometry used.

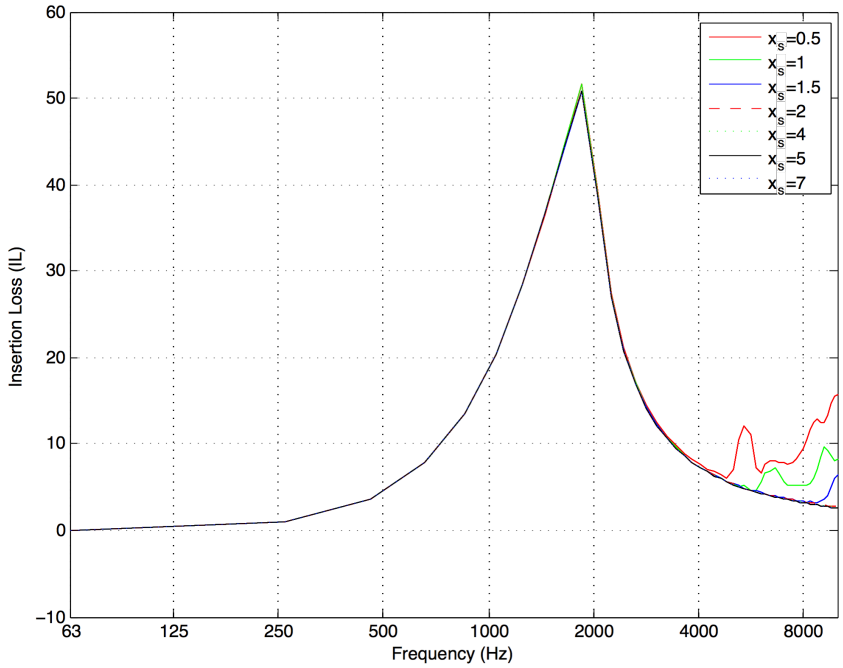

Figure 2.3: Mesh-convergence study, where x_s is the number of elements per wavelength, for width=0.2 m, thickness=0.025 mm, length=1 m and flow-resistivity=25000 Rayls/m for the lined duct.

For the purpose of demonstration, the mesh convergence is shown for a sample configuration of the duct (width (w)=0.2 m, thickness (t)=0.025 mm, length (l)=1 m and flow-resistivity (R_f)=25000 Rayls/m), in Figure 2.3. In Figure 2.3, the mesh convergence is shown for different values of x_s – the number of elements per wavelength. x_s was varied between 0.5 and 7. For x_s greater than 2, the variation in IL is less that 1% for frequencies up to 10,000 Hz, which is very good. The porous absorbers were modelled with 7 elements per wavelength, due to the higher impedance of the porous media, and therefore, the lower velocities (smaller wavelengths) of sound in the media, requiring a higher mesh density in the porous absorber.

2.2.5 Solver

In order to solve the system of linear equations by finite-element discretization, Finite-Element softwares usually employ two classes of solvers – *direct* and *iterative*. The different types of solvers available in Comsol, and their descriptions, are taken from the official Comsol documentation [31]. Direct solvers are based on LU decomposition. Comsol offers three direct solvers, namely MUMPS, PARADISO and SPOOLES. Convergence is usually achieved quickly and consistently for all three solvers, for well-conditioned problems. They can also be used to achieve convergence for certain ill-conditioned problems. Iterative solvers, on the other hand, reach the solution in several iterations, rather than in one large computational step. Iterative solvers are slower than direct solvers, but for large problems, can be memory efficient. However, the time taken to reach convergence depends on how well-conditioned the model is.

It was decided to use direct solvers in this study. From the available solvers in Comsol, the PARDISO solver was used. Among the available direct solvers, PARDISO tends to be the fastest and can offload the solutions to the hard-disk, which can help conserve RAM when running multiple simulations simultaneously, when performing a parametric sweep.

2.2.6 Insertion loss

Insertion Loss, a metric for evaluating the sound-attenuation performance of a silencer, was chosen as the parameter to be predicted. Insertion Loss is the difference in sound level measured at a given receiver location before and after a noise-control measure is installed. As already discussed in Chapter 1, a modified version of the Insertion Loss was used for the experiments, to dissociate the effect of diffraction and the source-room modes on the Insertion Loss, by subtracting the Sound Pressure Levels measured near the inlet and outlet of the lined duct, from the levels measured in an unlined duct. This measure provides a direct indication of the improvement provided by the insertion of a sound-attenuating device between the noise source and the listener. In the FE model, since only

the duct was modelled, subtraction of the Insertion Loss of the untreated duct is not necessary. Using this method, the result, in a way, can be interpreted as the Transmission Loss of the duct. However, to maintain a consistent reference to the metric, it is still referred to as the Insertion Loss of the duct in this thesis.

To evaluate the Insertion Loss of the duct, the Sound Power Levels at the inlet and the outlet were calculated from the sound pressures at the duct-boundaries as:

$$IL = L_{wi} - L_{wo} = 10\log_{10}\frac{{p^2}_i}{{p^2}_o} \tag{2.3}$$

where L_w is the sound-power level, p the sound pressure, with subscripts i and o denoting the inlet and outlet of the duct, respectively. The IL is predicted at one-third octave-band frequencies. In order to save memory, only three equally-spaced frequencies per energy band were predicted and logarithmically averaged, instead of predicting all the frequencies in the spectrum at a 1-Hz frequency interval.

2.2.7 Sample result and verification

The output of the surrogate model was the Insertion Loss (IL) of the duct with the porous absorbers, predicted from inputs of flow resistivity (R_f), thickness of the porous absorber (t), length of the duct (l), length of the porous absorber (l_b), width of the duct (w) and the frequency (f). Figure 2.4 shows the propagation of sound waves in a duct lined on two sides, from FEA predictions. The dissipation of energy by the absorbers can be seen in this figure. Figure 2.5 shows the calculated Insertion Loss of the duct shown in Figure 2.4. The absorbers attenuate sound at 500 Hz by approximately 20 dB.

2.2.8 Comparison of plane-wave and diffuse-field sources

As discussed in the previous sections, a plane-wave approximation was used to model the sound source. However, standard duct Insertion-Loss measurements involve a diffuse-field source room and an anechoic receiver room. This is dis-

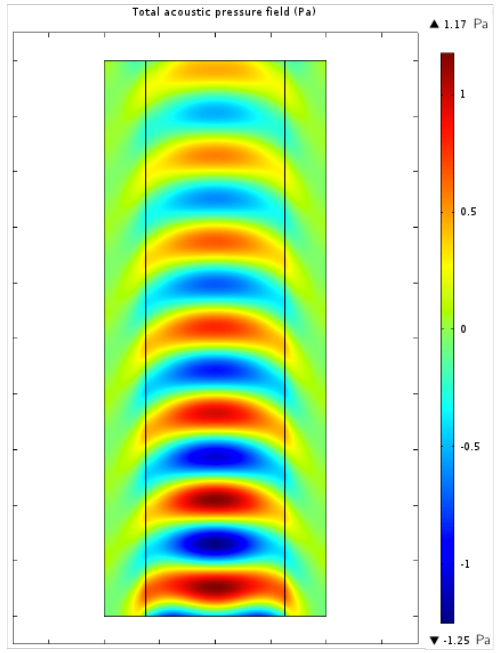

Figure 2.4: Acoustic-pressure waves in a duct from FEA predictions for a duct with lining on two sides (w=0.8 m, l_b=l=2 m, t=0.15 m, R_f=12500 Rayls/m).

cussed in detail in Chapter 4. The duct, along with the source and receiver room, were modelled in Comsol to compare the results with the plane-wave model. The model that was used is shown in Figure 2.6. Point sources were placed in a room with aspect ratio close to 1, at the farthest position from the duct inlet. The receiver room was made anechoic using Perfectly Matched Layers (PML). From the Comsol documentation, PML is a very good approximation of an anechoic termination. The measurement of Sound Power Level is done at a distance of 15% of the length from the inlet and the outlet of the duct, as shown.

Figure 2.7 shows the comparison of the Insertion Loss using a diffuse-field source and the plane-wave approximation for two duct configurtions. For small ducts, the assumption of a plane-wave source holds quite well. However, for larger ducts, which would result in lower values of Insertion Loss, the higher-

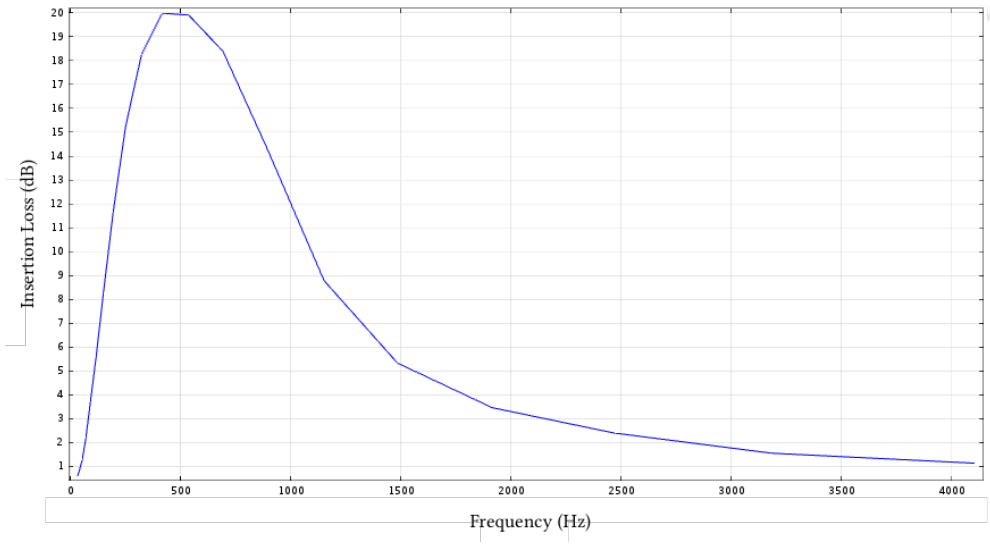

Figure 2.5: Insertion Loss calculated from FEA predictions for a duct with lining on two sides (w=0.8 m, l_b=l=2 m, t=0.15 m, R_f=12500 Rayls/m).

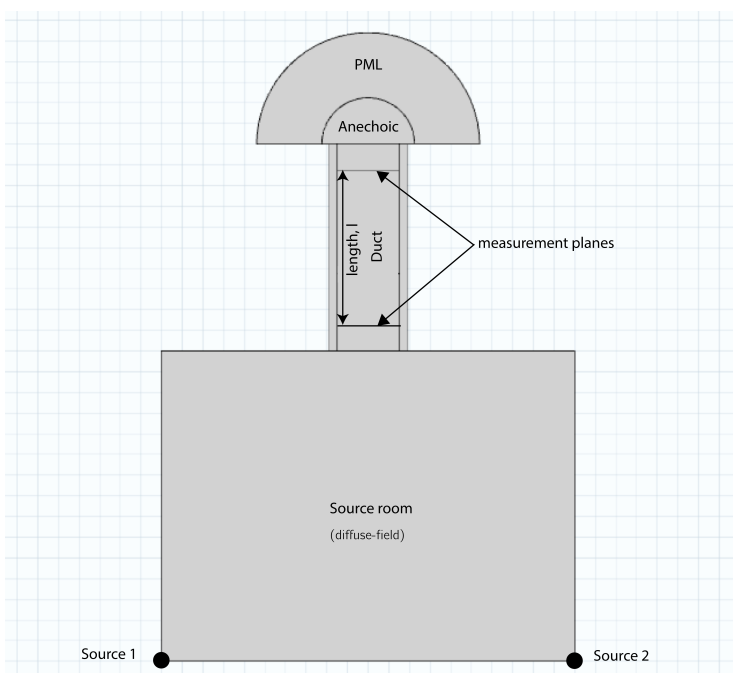

Figure 2.6: The geometry used to model the duct inserted between a diffuse-field source room and an anechoic receiver room

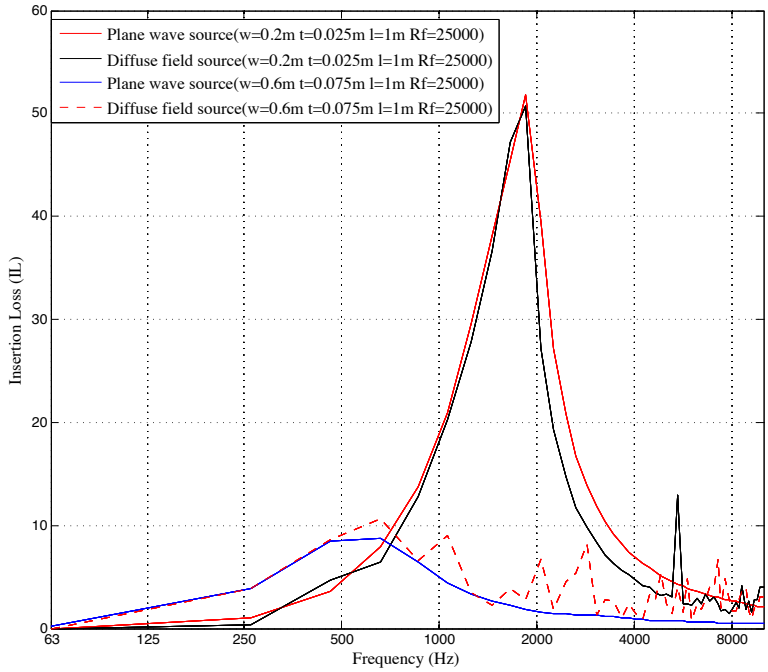

Figure 2.7: Comparison of IL from diffuse-field source and plane-wave source approximation, for two duct configurations.

order modes are seen to create differences of around 2-8 dB at certain frequencies. Less than 10 dB of difference is considered acceptable in this study. Moreover, the IL due to the existence of these higher-order modes varied with the size of the room. The design of the acoustic surrogate model is discussed in Chapter 3. Sharp changes in the contour of the Insertion Loss curve, when including the effects of the higher-order modes, make it difficult to develop a surrogate model that can capture these effects well. A plane-wave source approximation was used for the surrogate model.

2.2.9 Selection and generation of data set

A parametric sweep was used to vary the various duct parameters. Insertion Loss (IL) was selected as the output parameter, predicted for a parametric sweep of the input parameters – w, l_b, t, R_f and f as shown in Table 2.1. Comsol supports

Table 2.1: Ranges of input parameters for acoustic modelling.

Parameter	Range	No. of values
w	0.1 to 0.6 [m]	10
l_b	$(w \times 4)$ to $(w \times 16)$ [m]	4
t	$(w/4)$ to $(w/64)$ [m]	10
R_f	1000 to 30,000 [N.s/m^4]	10
f	63 to 8000 [Hz]	3 for every 1/3 octave = 72

nested functions, whereby parameters can be varied as a function of other parameters. This is particularly useful, for example, to sweep the length of the duct lining l_b between $(4 \times w)$ and $(16 \times w)$, as shown in Table 2.1. The dimensions of the duct were chosen as a compromise between the number of mesh elements and capturing the required physics. For example, Figure 2.8 shows the variations of Insertion Loss with frequency for w=0.15 m and w=0.6 m, keeping the other parameters constant. It can be seen that the absorber creates a peak at 2300 Hz for $w = 0.15$ m and at 800 Hz when w=0.6 m. A duct with a short w would result in only a portion of the IL curve be captured in the predicted frequency range, the rest of the curve lying outside the range. A duct with a very large w would create a narrow IL curve, with a peak at low frequencies, along with a low magnitude of IL – in addition to higher memory requirements.

The IL was found to be independent of the length of the duct (l) and only depended on the part of the duct that was lined. For this reason, the length of the duct was ignored in the simulation. From quick FE predictions, it was also clear that the TL was directly proportional to the length of the duct lining l_b. In other words, $\frac{IL}{l_b}$ remained a constant, provided the other parameters did not change. For the data set for the surrogate model, the insertion losses were predicted for ducts with lining on only one side. Chapter 3 describes how a duct with lining only on one side was used to model other configurations of the duct.

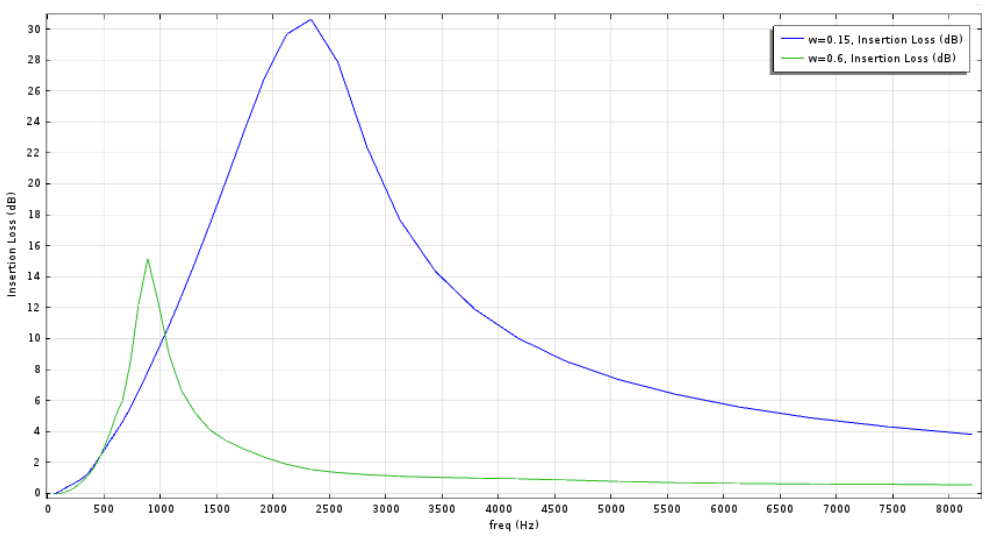

Figure 2.8: Comparison of Insertion Loss between ducts having w=0.15 m and w=0.6 m, calculated from FEA predictions for a duct with lining on two sides.

2.3 Finite-element method for airflow

The following discussion describes the Finite-Element Method that was adopted to model airflow through the ventilation duct. It is to be noted that the Finite-Element Modelling, some of the surrogate modelling and the experimental investigation were all done in parallel. This helped gain more insights and understanding to create the most optimal surrogate model. The process was iterative, but the work is presented in a linear fashion in this manuscript. It might be necessary to refer to other sections to better understand the overall picture of this study. Multiple surrogate models were developed for predicting the pressure drop due to an abrupt change in cross-section, and due to the propagation of flow in the duct. The development of these surrogate models from FEA are described in the next chapter.

When the flow through an opening is fully turbulent, the discharge coefficient C_d is expected to be a constant for variations in flow velocity. However, C_d perhaps would not be the same for two different configurations of the ducts.

For complicated geometries the relationship between C_d and Re_o are usually tabulated, provided they cover the relevant range of Re_o [24]. It was the objective of this study to predict C_d using the surrogate models. If implemented well, this would be an useful tool for designers to be able to directly predict the airflow at required pressures.

2.3.1 Modelling specifications

The CFD module in Comsol was used for Finite-Element predictions of fluid performance. The commercial software was used to solve the Navier-Stokes equation in the fluid domain at steady-state. The following sections describe the methodology that was used for flow-performance predictions in this study. The flow-domain geometry, the boundary conditions, the mesh used, solver specifications, data-set modelling and test results are presented.

2.3.2 Domain

The configuration considered in modelling the domain is a ventilator duct inserted in a partition between two volumes – namely the source and receiver rooms. A 2D geometry was used to model the flow domain. Using a 2D geometry means that the results from this work are only valid for high aspect ratios of the duct-opening cross-section. However, certain steps were taken when creating the surrogate model to extend it to other aspect ratios, as discussed in the following chapter. For the acoustics model, the Insertion Loss of the duct was predicted independent of the source and receiver rooms to simplify the problem. However, such a simplification was not made for airflow modelling. This can be justified by trying to understand the objectives of this study; the output parameter of interest is the flow rates observed for different silencers for a given pressure drop between the rooms. The pressure drop across the rooms is mainly attributed to the sudden change in cross-section at the entrance of the duct, and only a little due to friction, for flow through the duct. When baffles and linings of considerable thickness are added to the duct, a reduction in area occurs in the

regions where they were inserted. For this reason, the FEA modelling takes into consideration the source and receiver rooms. Moreover, as will be described in subsequent sections, the change in cross-section results in a vena-contracta near the inlet of the duct, that is dependent on the areas of the two rooms.

In subsequent chapters, results from the approximate 2D FEA, the surrogate model and the experimental results are compared to those from a 3D model that is modelled as closely as possible to the experimental setup, to compare the results. The simulation was restricted to incompressible flow, since the Mach number M in this case is typically less than 0.3. Due to the relatively large cross-sectional areas of the openings of ducts in naturally-ventilated buildings, a turbulence model was presumed to be appropriate to model the fluid domain.

As already discussed in Chapter 1, for ducts, unlike adventitious openings, the flow is atleast partially turbulent for the range of sizes of ducts that are of interest. This was investigated in experiments using the blower door that are discussed in Chapter 4. The flow in ducts in naturally-ventilated buildings is expected to be at least partly turbulent. If the duct aspect ratio is very high, they would be considered as an adventitious opening that has laminar flow at low velocities. A study of ventilation silencers in such a configuration was made by Bibby [4]. This thesis does not cover very high aspect-ratio openings, which are not typical of duct-like natural ventilation openings.

In a Finite-Element package, the flow model – turbulent or laminar – is chosen beforehand. That means that incorrectly choosing the flow domain would give poor results. For this study, even if the flow through the duct is not fully turbulent, due to the presence of at least partial turbulence, a turbulence model was used. A turbulence model – RANS method – was used for the flow regime, with a k-ω model. Close to the walls of the duct, the flow is different from that in the free stream due to the viscous sublayer. Using a turbulence model that describes this effect close to the wall would require a very high resolution of the mesh. Instead, models such as k-ϵ and k-ω use analytical expressions, known as wall functions, that closely approximate the flow near the walls. A $k-\omega$ model is

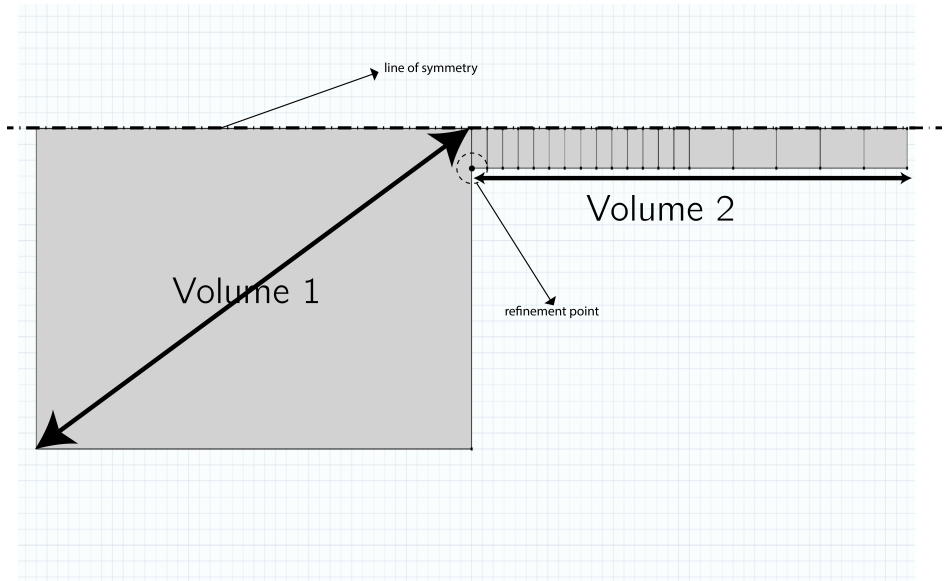

Figure 2.9: Fluid-domain geometry of the volumes modelled.

more accurate, compared to a k-ϵ model for internal flows, for strong curvatures in flow path such as in pipe bends and jets.

2.3.3 Boundary conditions

For implementing boundary conditions, a velocity-inlet, pressure-outlet, no-slip condition was used. The lining was modelled as a hard surface, and the pressure drops due to subsurface flow through porous media were assumed to be negligible. Moreover, in the available version of Comsol, there was no provision to include surface roughness. The property of symmetry was utilized wherever possible to reduce the number of mesh elements.

2.3.4 Mesh

A tetrahedral mesh structure was used to model the fluid domain. Mesh refinements were made near the walls and boundaries.

The wall functions in Comsol assume that the computational domain starts an

offset distance from the wall. This offset is given by the wall resolution function, y^+. The wall function is never smaller than half of the height of the boundary-mesh cell. Ideally the value of y^+ is 11.06. However, for a coarse mesh, this function can take a value greater than 11.06. In order to ensure mesh convergence near the boundaries, mesh refinements were done until the wall resolution (y^+) was 11.06 on most part of the boundaries.

In the following sections, the details of the dimensions chosen and of the parametric sweep are prescribed. From Table 2.2, it can be appreciated that, for so many configurations of the duct, it was not possible to check mesh convergence in every case. The mesh was auto-generated for each case in the parametric sweep. In order to maintain convergence across all samples, meshing was made adaptive to the size of the domain section – i.e. mesh density was kept constant for Volumes 1 and 2, for all dimensions (refer to Figure 2.9).

Mesh convergence was checked for selected configurations, by increasing the density of the mesh until Δp varied less than 10% for the selected samples. The author is aware that 10% is a relatively high error, and more error would be introduced when constructing the surrogate model. However, refining the mesh further to achieve less error resulted in unacceptable simulation times and, sometimes, failure to converge to a solution. Section 2.3.7 demonstrates the mesh convergence for one selected configuration. Mesh independence of the flow was done for selected cases from the sweep, which is discussed in Section 2.3.7.

2.3.5 Effect of change in cross-section

In order to build a good surrogate model, it was essential to capture the physics that is relevant to the study, in the FEA simulations. First, the effect of a change in cross-section was studied for varying sizes of the source room and the duct. It was observed that, at the point where the fluid enters the duct, there is a change in the area/diameter of the fluid jet due to the sharp change in cross-section called the vena-contracta. The formation of the vena-contracta is accompanied by a conversion of static pressure to velocity pressure, and from velocity pressure

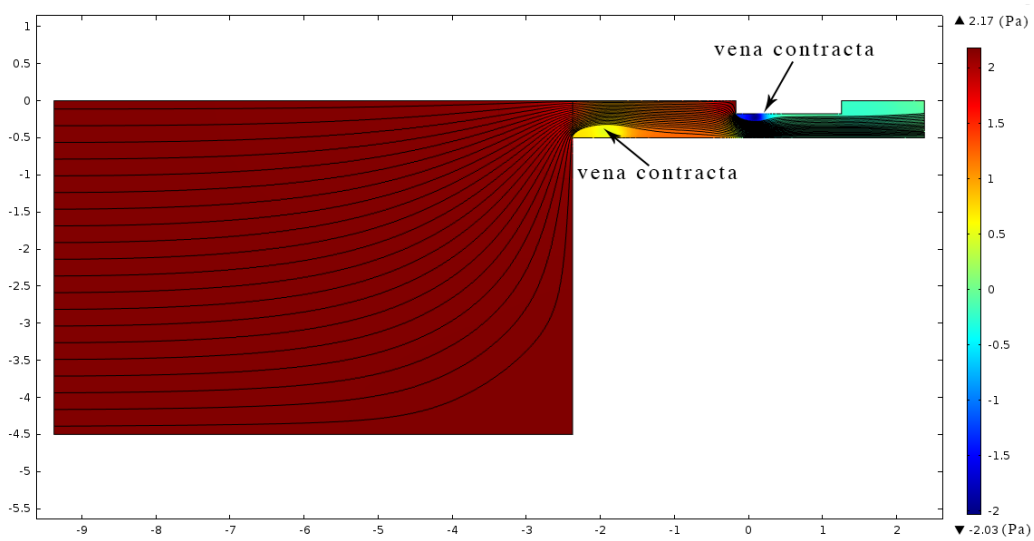

Figure 2.10: Illustration of the presence of a vena-contracta, along with the streamlines.

back to static pressure. The pressure drop associated with this sudden change recovers with distance along the length of the duct. A detailed discussion can be found in Chapter 3.

The vena-contracta depends on the length of the duct, its profile, and on the ratio of the cross-section area of the duct and of the room that encloses the duct inlet (source room). For long ducts, the effect of the vena-contracta on the pressure drop is negligible, as pressure recovery occurs along the length of the duct. However, for ducts with cross-sectional areas not much larger than that of the source room, and in the presence of bends or baffles in the duct, the pressure recovery is affected and results in higher pressure drops.

The velocity-vector profile at the vena-contracta is parabolic at lower flow rates and flattens out at higher flow rates [32]. Upon reviewing the literature, it was found that the estimation of the shape of the area change as a function of duct length has not been done before. It was necessary for the surrogate model to account for this phenomenon.

In order to accurately study the above effect, the length of the duct was di-

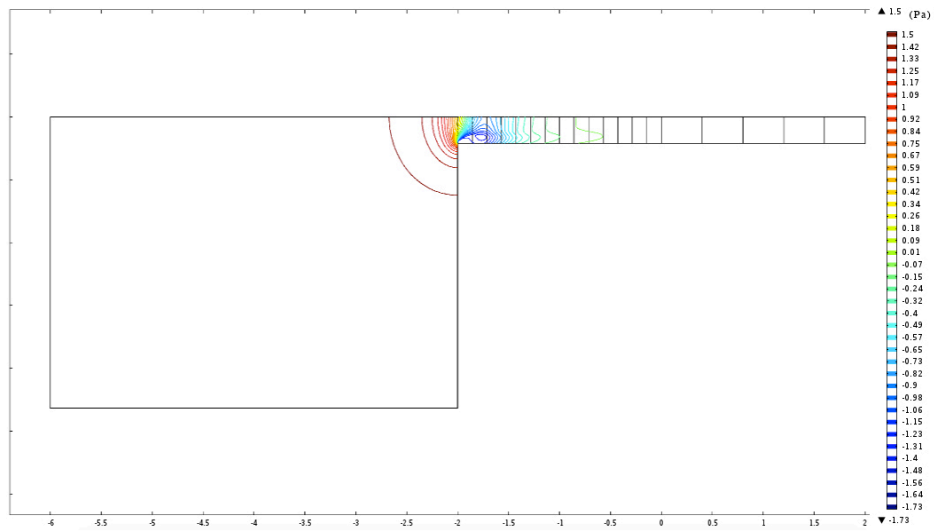

Figure 2.11: Illustration of the vena-contracta, along with the pressure contours, with the sub-divisions of the duct for d_w=0.42 m, s_h=4.6 m and Re_o=34, 649.

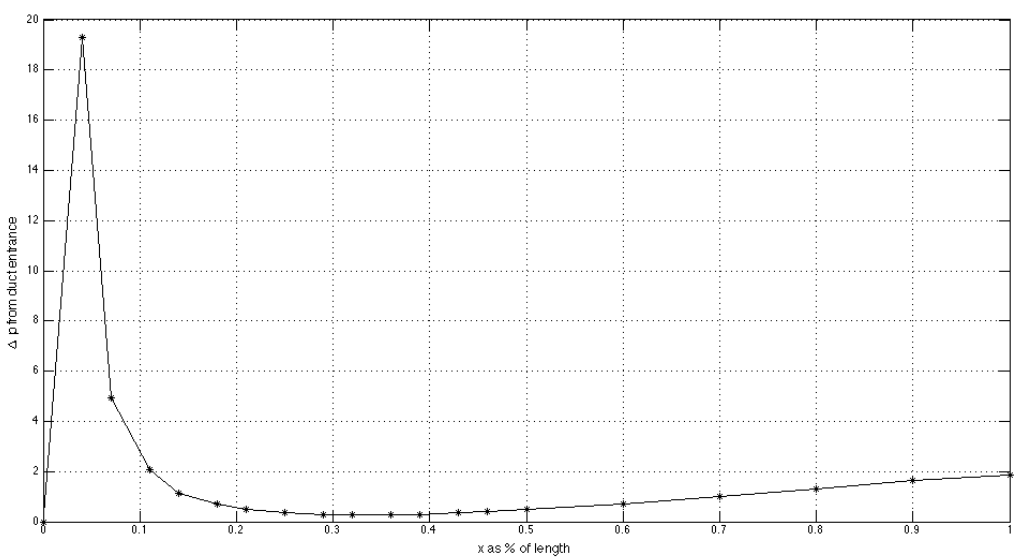

Figure 2.12: Pressure drop along the length of duct x, as a percentage of l, for d_w=0.173 m, s_h=5.7 m and Re=61, 150.

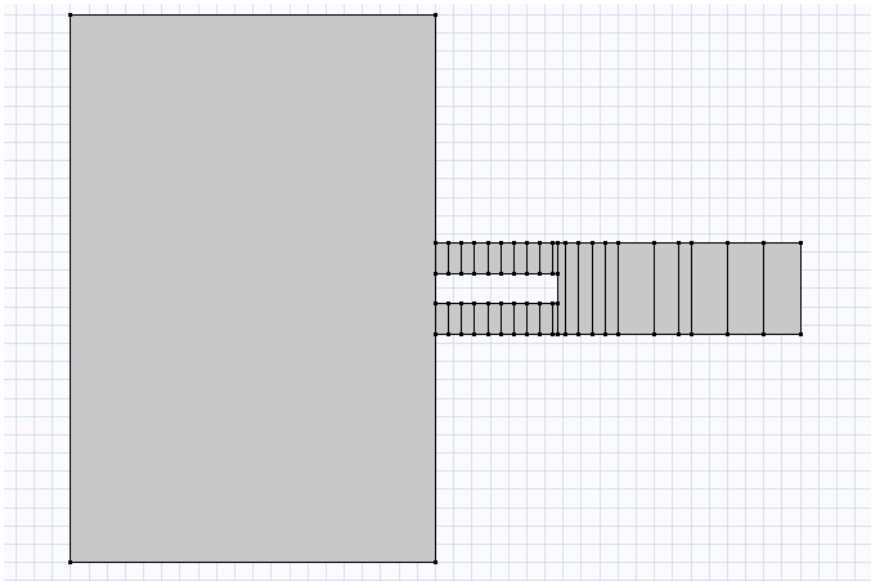

Figure 2.13: Geometry of the duct with a baffle, as built in Comsol.

vided into several sections. The dynamic pressure was averaged over each section, and the pressure drop relative to the inlet of the duct (Δp) was found as a function of the position x, along the length l of the duct. In Figure 2.11, the presence of the vena-contracta and the sub-division of the duct are shown.

The constriction in airflow associated with the vena-contracta occurs close to the inlet of the duct. For this reason, more sampling sections were required close to the inlet of the duct. The pitch of the sampling sections was gradually increased towards the outlet end of the duct. Figure 2.12 shows the pressure drop relative to the inlet of the duct, which was averaged over each duct section. The pressure drop is presented as a function of x, the distance of the section from the inlet, normalized to the length of the duct, l.

2.3.6 Effect of addition of baffles

The study of the change in Δp along the length of the duct when baffles are inserted was done as a separate set of simulations. All the boundary conditions from the previous sections apply, with the exception of the symmetry-property

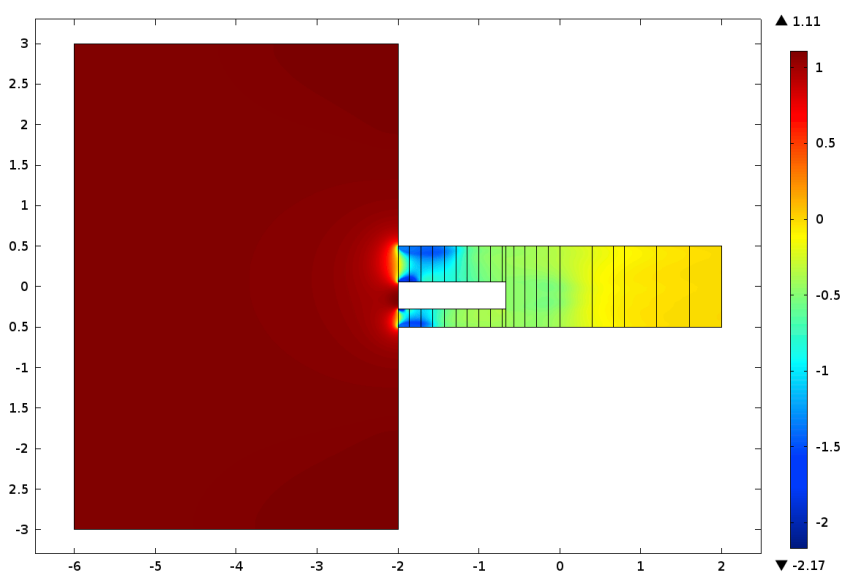

Figure 2.14: Pressure gradient from prediction in Comsol for baf_{wx}=−0.12 m, l=1 m, s_h=6 m.

which was not used, since the change in the position of the baffle across the width of the duct would lead to asymmetry. A screenshot of the geometry, built in Comsol, is shown in Figure 2.13.

The results of the Comsol predictions for one such configuration are shown in Figure 2.14. The sections included to capture the vena-contracta were adapted to move along with the baffle when the baffle was swept along the length of the duct.

2.3.7 Mesh sensitivity analysis

From the previous sections, it is clear that the FEM was used to predict the pressure drop due to a change in cross-section, the vena-contracta that occurs after the change in cross-section, and the pressure drop due to flow propagation in the duct.

Mesh convergence was tested for two different scenarios. The first is the error that occurred when predicting the pressure drop between the inlet of Volume 1

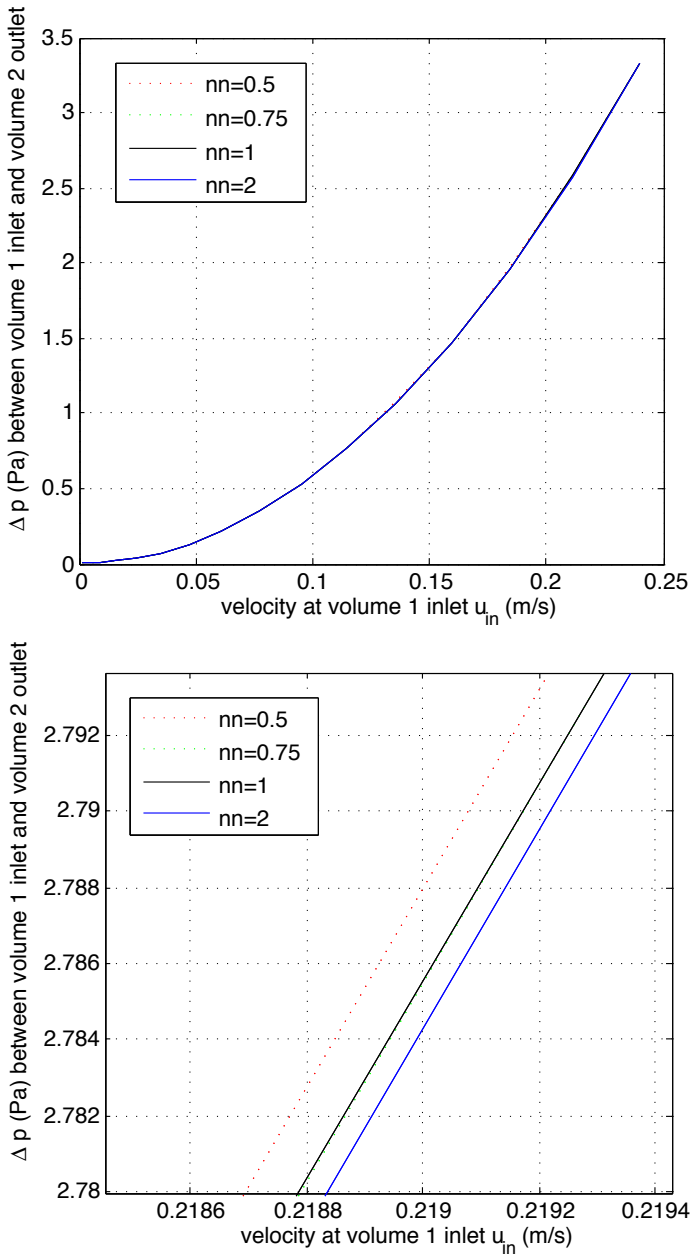

Figure 2.15: Mesh-convergence study for the airflow model: variation of pressure drop with velocity for different mesh densities *nn* (top). Zoomed view of the top plot (bottom). *nn*=1 is the mesh density used; *nn*=0.5 is half the mesh density and *nn*=2, double the mesh density.

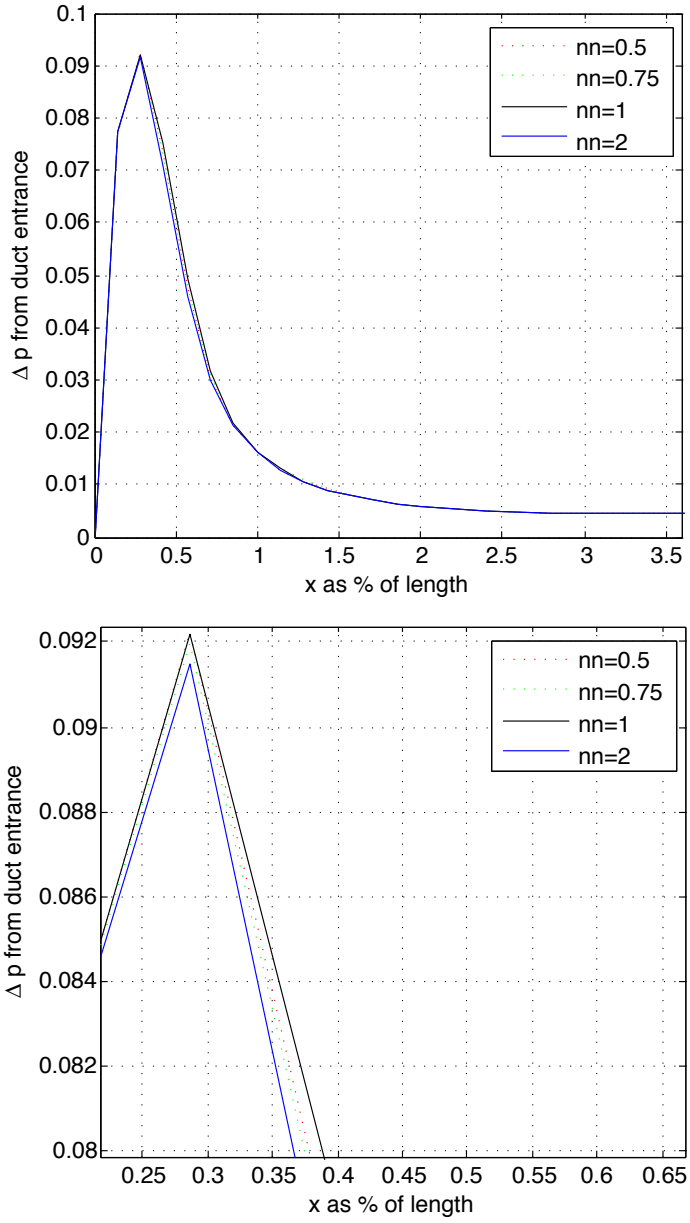

Figure 2.16: Mesh-convergence study for the airflow model: variation of pressure drop with position in duct for different mesh densities *nn* (top). Zoomed view of the top plot (bottom). *nn*=1 is the mesh density used; *nn*=0.5 is half the mesh density and *nn*=2, double the mesh density.

Table 2.2: Range of input parameters for airflow modelling.

Parameter	Range	No. of values
s_h	0.09 to 6.25 [m]	10
d_w	6.25 to 0.09 [m]	10
Re	300 to 65,000	16
l	1 to 4 [m]	4
x (normalized to l)	0 to 1	20

and the inlet of Volume 2. The second is the drop in pressure along the length of Volume 2 with respect to the inlet of Volume 2. Figure 2.15 show the error in pressure drop as a function of velocity between the inlet of Volume 1 and the inlet of Volume 2. This is also the measured pressure drop from experiments. The error in the prediction of pressure drop in such a situation is very small (0.1%). Figure 2.16 shows the error in prediction of pressure drop along the length of Volume 2. The maximum error found in this case is 10%, which is quite large. However, for a simple surrogate model, this error is considered to be acceptable in this study. Also the contribution of the pressure drop due to flow through a duct is rather small in comparison to the total pressure drop between the inlet of Volume 1 to outlet of Volume 2. The error is thus greatly minimized when measuring the pressure drop between Volume 1 and Volume 2. In both sets of plots the mesh density nn was referenced at 1 for the mesh density that was used in the final model; $nn = 0.5$ means, halving the mesh density and $nn = 2$, doubling the mesh density.

2.3.8 Selection and generation of sample set

In order to use FEA results for the surrogate model, a parametric sweep similar to that used with the acoustics model was done. The ranges of input parameters shown in Table 2.2 were swept to study the change in cross-section of the duct.

It should be noted that the ranges of values were not divided equally – more sampling points were used in the regions of interest, as was demonstrated before

for the sample set for x. The inlet boundary condition was set to a velocity inlet; this was written as a function of the opening Reynolds number for the duct inlet, for the different ranges of Reynolds number.

Predicting so many configurations is time consuming. For this reason, the option to use the previous solution as the initial solution for the next solution was used for the Reynolds-number parameter, Re. This helped achieve faster convergence of solutions.

The cases of the study of the effect of changing the dimensions and position of the baffles, and the changing the dimensions of the duct, would have resulted in far too many data points to be computed for the surrogate model. Therefore, only selected configurations from experiments were modelled and compared with the surrogate model – this is discussed in Chapter 5.

2.3.9 Finite-element modelling assumptions

When validating results from the surrogate model using FEA, as discussed in Chapter 5, a FEA model for the airflow domain was modelled in close agreement with the experimental configuration. However, certain assumptions were made when using FEM. The experimental duct protrudes into the source and receiver rooms in the experimental setup, while the FEM-modelled duct entrance was flush with the walls to reduce the mesh density near the duct walls. This is expected to affect the vena-contracta. Another approximation was the assumption of at least partially turbulent flow in the duct. The use of turbulence models for flows with low Reynolds number could introduce substantial errors. Finally, surface roughness was ignored, when modelling the absorbers inside the duct, as it was not an available option in the version of Comsol that was used in this study.

Chapter 3

Surrogate Modelling

In the previous chapter, the modelling of sound attenuation and airflow in ducts using the Finite-Element Method was discussed. This chapter discusses the construction of surrogate models from the FEM prediction results. This is followed by a discussion of methods that were used to expand the scopes of the models. Finally, a sample calculation of how to apply the surrogate models to different duct configurations is described. The surrogate models were validated using measurements from experiments. The next chapter will discuss the scale-model experiments that were conducted to validate the surrogate model.

To construct a surrogate model using symbolic regression, Eureqa Desktop [27] was used. More discussion about surrogate modelling can be found in Chapter 1. The surrogate model was intended to be used by designers as a quick tool to estimate acoustic and airflow performance. For this, it was taken into consideration while developing the surrogate model, that the model should be simple, not computationally intensive, and highly accurate. The following sections discuss in detail how the surrogate models were built for each case. Also, existing theoretical models related to the modelling of acoustic and airflow performance in ducts are discussed in the following sections.

3.1 Acoustic modelling

This section discusses the surrogate model that was constructed for predicting the acoustic performance of the duct. The surrogate model for acoustics was constructed from FEM. The FEM modelling was based on the assumption that the sound source is a plane-wave. This section begins with a discussion of the Transfer-Matrix Method, a well-known theoretical model that can predict the acoustic field in a lined duct, for a plane-wave source. This is followed by a discussion about the development of the surrogate model.

3.1.1 Transfer-matrix method for sound attenuation in ducts

The wave equation most accurately describes the acoustic field in a lined duct. However, it is not always possible to determine a closed-form solution of the wave equation, for all geometries. Even if determining a closed solution were possible, it usually turns out to be complicated.

Munjal [33] and others have successfully used the Transfer-matrix method (TMM) for predicting the acoustics of ducts and mufflers. By the TMM, any duct system is represented as a combination of discrete elements. A 2×2 matrix is used to relate the acoustic pressure and velocity at one point (n) in the duct to the acoustic pressure and velocity at another point (n-1) as:

$$\begin{bmatrix} p_{n-1} \\ u_{n-1} \end{bmatrix} = \begin{bmatrix} T_{11} & T_{12} \\ T_{21} & T_{22} \end{bmatrix} \begin{bmatrix} p_n \\ u_n \end{bmatrix} \tag{3.1}$$

The derivation of the transfer matrix for a rectangular duct is discussed below. Most of the derivations found in this section are based on [33]. A lot of literature is available on the method of formulating the transfer matrix for complex geometries. Only a simple case of the application of the TMM is presented here.

For a rectangular duct of cross section $w \times b$, wave propagation along the length of the duct (z axis) is described by defining the pressures and velocities at

the start and end of the duct. In cartesian co-ordinates, the acoustic pressure-field in the acoustically-lined duct is given by:

$$p(z) = Ae^{-jk_z^+ z} + Be^{+jk_z^- z} \tag{3.2}$$

For rectangular ducts, the wave numbers along the x and y directions, k_x and k_y, can be represented as an effective wave-number k_z, shown in Eq. (3.2). k_z can be written as:

$$k_z = \left[k_o^2 - \left\{(k_x)^2 + \left(k_y\right)^2\right\}\right]^{1/2} \tag{3.3}$$

$$\frac{Z_{w,x}}{\rho_o c_o}\frac{k_x}{k_o} = j\cot\left(\frac{k_x b}{2}\right) \tag{3.4}$$

$$\frac{Z_{w,y}}{\rho_o c_o}\frac{k_y}{k_o} = j\cot\left(\frac{k_y h}{2}\right) \tag{3.5}$$

The expression for axial particle velocity is given by:

$$u_z(z) = \frac{k_z}{k_o}\left(\frac{Ae^{-jk_z z} - Be^{+jk_z z}}{\rho_o c_o}\right) \tag{3.6}$$

$$p(0) = A + B \tag{3.7}$$

$$u_z(0) = k_o\frac{A - B}{\rho c_o} \tag{3.8}$$

Combining Equations (3.1) and (3.6) to (3.8) gives:

$$p(0) = p(z)\cos(k_z z) + ju_z(z)\frac{\rho k_o}{c_o k_w}\sin(k_z z) \tag{3.9}$$

and

$$u_z(0) = u_z(z)\cos(k_z z) + j\left(\frac{p(z)k_z}{\rho k_o c_o}\right)\sin(k_z z) \tag{3.10}$$

Equations (3.9) and (3.10) can be written in transfer-matrix form as:

$$\begin{bmatrix} p(0) \\ u_z(0) \end{bmatrix} = \begin{bmatrix} \cos(k_z z) & \frac{jk_o}{\rho k_o c_o} \sin(k_z z) \\ \frac{jk_z}{\rho k_o c_o} \sin(k_z z) & \cos(k_z z) \end{bmatrix} \begin{bmatrix} p(z) \\ v(z) \end{bmatrix} \tag{3.11}$$

The Insertion Loss for the transfer matrix in the generalized form shown in Eq. (3.1), can be found as:

$$IL = 20 \log \left[\left(\frac{Y_1}{Y_n} \right) \left| \frac{T_{11} + T_{12}/Y_1 + T_{21} Y_n + (Y_n/Y_1)\, T_{22}}{2} \right| \right] \tag{3.12}$$

and the characteristic impedances are given as $Z_n = \rho_o c_o k_o / k_n$ and $Z_1 = \rho_o c_o k_o / k_1$.

3.1.2 Surrogate-modelling considerations

The acoustic surrogate model was constructed based on a limited number of carefully chosen data points that were generated from the FEA simulations for parameters w, l_b, t, R_f and f, as shown in Table 2.1. A total of 288,000 simulation cases for a parametric sweep of all parameters were used. All the parameters were normalized to their respective standard deviations before inputting into Eureqa. The software allows the control of which functions must appear in the surrogate model. The documentation found in [34] can be referred with respect to what functions are supported by Eureqa as building blocks for the model. For this simulation, only simple operations – namely *addition*, *subtraction*, *multiplication*, *division* and *power functions* – were used.

It was important to capture the physics (i.e. shape of the data) across various magnitudes of the output. Among the fitness functions available in Eureqa, *R-squared* was used – this is a measure of goodness of fit or, in other words, how well the curve fits the data points. The main benefit of *R-squared* is that the explained variance is normalized to the output value scale.

While constructing the surrogate model for sound, the following points were taken into consideration:

1. To construct a base surrogate-model that can be used to model different duct configurations.

2. To ensure that the surrogate model agrees well with acoustic scaling laws (refer to Section 4.1.1 for more information on acoustic scaling laws).

3. To maintain simplicity of the surrogate model without compromising on the goodness of fit.

3.1.3 Insertion loss

As was mentioned in Chapter 1, the output of the 2D surrogate model was intended to be the Insertion Loss (IL) of the duct containing porous absorbers, given the inputs of flow resistivity (R_f), thickness of the porous absorber (t), length of the duct (l), length of the porous absorber (l_b), width of the duct (w), and frequency (f). A duct can be configured in many different ways using porous absorbers. It was intended to model these configurations from one simple basic configuration. The simplest case of a duct containing porous absorbers would be a duct with lining on one side. As can be seen from the previous chapter, FEM was used to predict the IL for ducts with lining on only one side.

The target expression for the surrogate model was defined in Eureqa as:

$$IL_{\text{single}} = F\left(R_f, f, w, t, l_b\right) \tag{3.13}$$

where IL_{single} is the Insertion Loss for a duct with lining on one side:

$$IL_{\text{single}} = \frac{8.08e-6R_f f^2 t^2 l_b}{1+0.0074R_f t+6.53e-15R_f w^4 f^5 t^2} \tag{3.14}$$

From the various equations generated by Eureqa, Eq. (3.14) was the simplified surrogate model chosen to predict the Insertion Loss of a duct with lining on one side. Though Eureqa is very efficient at predicting good models, manual adjustments and simplifications to the model were necessary to achieve an opti-

Table 3.1: Statistics for the surrogate model for sound (Eq. (3.14)).

Statistic Measure	Value
R^2 Goodness of Fit	0.95
Correlation Coefficient	0.97
Mean Squared Error	8.93 dB

mal model. The lowest power of the frequency parameter that gave good fitness was chosen, to avoid overfitting. The function is of the form:

$$IL = \frac{c_1 f^2}{c_2 + c_3 f^5} \tag{3.15}$$

Another way to model the surrogate would be to use a squashing function such as a *logistic* function. A logistic function gave better R^2 values for the model. However, the model did not agree well with acoustic scaling laws. Table 3.1 shows the various statistical measures for the selected model.

From Eq. (3.14), it can be seen that IL is directly related to the length of the baffle l_b. The IL predicted by the surrogate model was found to be in good agreement with FEA results (refer to Chapter 5 for comparison of results from surrogate model with FEM and experimental measurements). A sample calculation that shows how to use the surrogate model can be found in Section 3.1.6.

3.1.4 Analysis of model

In this section, the surrogate model is analyzed in further detail. Lining the duct attenuates the modes due to standing waves that form inside the duct. The frequency of occurrence of the first mode in a duct can be found from:

$$f = \frac{c}{2w} \tag{3.16}$$

The occurrence of a peak in the Insertion Loss curve identifies the frequency at which the maximum IL occurs. Therefore, comparing the frequency at which

the maximum IL occurs with Eq. (3.16) can help validate the surrogate model. In order to do this, the maximum value of IL needs to be determined and the associated frequency needs to be found. The maximum value of any function can be found by differentiating the function and equating it to zero. In this case, setting $IL' = 0$ and solving for frequency f should find the frequency at which the peak occurs in the Insertion Loss curve for the surrogate model.

Differentiating Eq. (3.14) and solving for frequency f gives:

$$f = 237.5\left(\frac{R_f t + 135.13}{R_f t^2 w^4}\right)^{1/5} \tag{3.17}$$

It can be seen from Eq. (3.17) that the peak frequency depends on R_f, t and w. It is to be noted that this is for a duct with lining on only one side. The theoretical value of the frequency at which a peak occurs, for a duct with lining on both sides, is given by Eq. (3.16). A duct of width w with lining on two opposite sides can be represented as a duct of width $w/2$ lined on only one side with the other side having a reflective boundary, as shown in Figure 3.1. In other words, the theoretical value of the frequency at which the peak IL occurs, for a duct with lining on only one side, is:

$$f = \frac{c}{w} \tag{3.18}$$

Comparing Equations (3.17) and (3.18), it is not apparent that simplifying Eq. (3.17) leads to the Eq. (3.18). However, substituting R_f, t and w in Eq. (3.17), with values from ducts of practical consideration, the frequencies of maximum IL are fairly close for these two equations. For example, for a duct with $R_f = 25000$ N.s/m^4, $t = 0.025$ m and $w = 0.15$ m, the frequencies of maximum IL from the surrogate model and the theoretical models are 2356 Hz and 2287 Hz, respectively.

In Eq. (3.18), the width of the duct w does not include the thickness of the lining. For small thicknesses of the lining, this expression can be used. However, it becomes unclear what the width of the duct is when a lining of significant thickness is added. Thus, for very large values of thicknesses of the lining, there

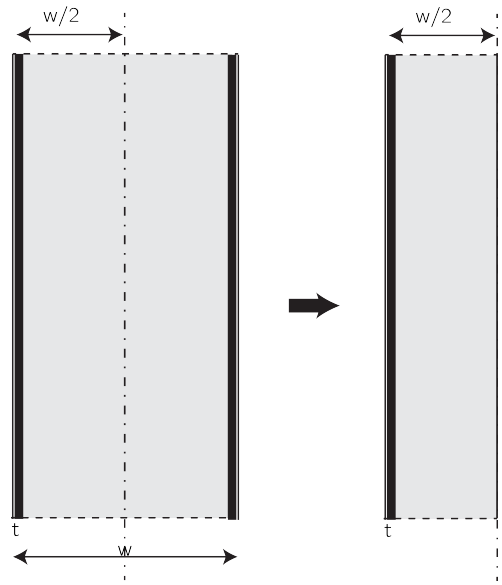

Figure 3.1: Model showing the equivalence of a duct with lining on one side and two sides.

is divergence from the theoretical expression – as can be similarly expected from acoustic FEA simulations in comparison with the theoretical expression.

Surrogate models are approximations of the original phenomena. As such, surrogate models tend to progressively diverge from reality outside the domain of the data set that was used to build the surrogate model. This usually is addressed by choosing a data set that is appropriate for the range of interest. A particular problem exists in using surrogate models to describe a case of acoustic scaling. The selected model agrees well with acoustic scaling and there is minimal divergence of error outside the domain of input data points used to build the surrogate model. Scaling all of the variables by a scaling factor n according to applicable scaling laws gives $R_f = R_f * n$, $f = f * n$, $t = t/n$, $w = w/n$, $l_b = l_b/n$. Substituting these scaled variables in Eq. (3.14) gives:

$$IL_2 = \frac{8.08e-6\left(R_f n\right)\left(f^2 n^2\right)\left(\frac{t^2}{n^2}\right)\left(\frac{l_b}{n}\right)}{1+0.0074\left(R_f n\right)\left(\frac{t}{n}\right)+6.53e-15\left(R_f n\right)\left(\frac{w^4}{n^4}\right)\left(f^5 n^5\right)\left(\frac{t^2}{n^2}\right)} \tag{3.19}$$

Comparing Equations (3.14) and (3.19), it can be seen that $IL_2 = IL_{single}$. This property of scaling is discussed in detail in Chapter 4. In brief, the Insertion Loss (IL) is the same if the parameters of the duct are scaled appropriately. With a surrogate model that diverges outside the range of the input data set, such a property would be a challenge to reproduce. The surrogate model was constructed in such a way that the scaling property was maintained. This property is critical to allow the model to be extended beyond the range of the data set.

3.1.5 Extension of the surrogate model

In the previous section, Eq. (3.14) describes the Insertion Loss of a duct with lining on only one side. Only one surrogate model was developed, due to limitations in time and resources necessary to generate an extensive data set from FEM for all different configurations (Section 4.6 discusses the different configurations of the duct with absorber inserts that were considered in this study). With the available data, however, it was of interest to modify the surrogate model in such a way that it could be applied to other configurations. Eq. (3.14) can only be used to predict the Insertion Loss of a 2D duct with lining on one or two sides. Complex configurations (eg. a 3D duct with lining on two sides and a baffle insert) were modelled as a combination of the simple configurations. Following is the methodology that was used to model such complex configurations:

1. IL for a duct with lining on two sides was already modelled in the previous section by scaling the width w to one half in Eq. (3.14) to give,

$$IL_{double} = \frac{8.08e-6R_f f^2 t^2 l_b}{1+0.0074R_f t+4.08e-16R_f w^4 f^5 t^2} \tag{3.20}$$

2. Similarly, IL for a duct with a baffle in the middle, with thickness double the lining thickness, can be modelled as a duct with lining on two sides whose width is halved. Then the Insertion Loss of the duct is, $IL = IL_{double}(w = w/2)$.

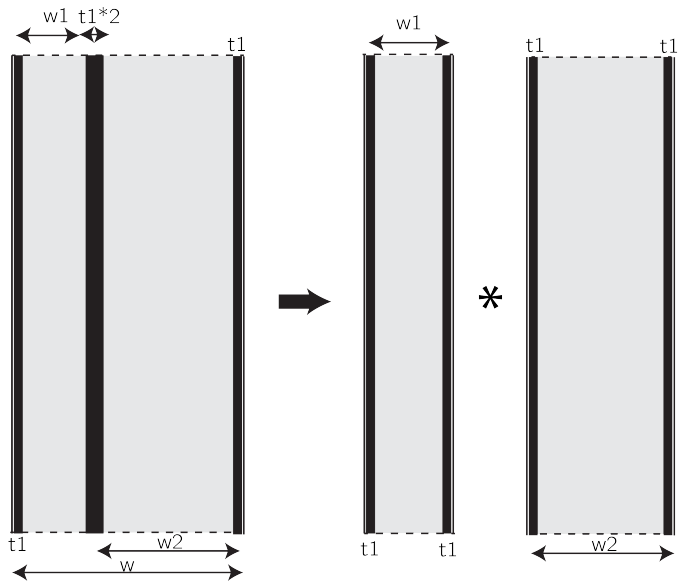

Figure 3.2: Model showing the equivalent model for a duct with baffle of twice the lining thickness, where $(*)$ is the logarithmic addition operator.

3. What if the baffle does not lie in the middle of the duct? Then the *IL* is found from the logarithmic addition (i.e. the addition of energy in acoustics) of the *IL*s of the two-part ducts on either side of the baffle, with their respective widths and lining thichness on both sides. This is shown in Figure 3.2, where the operator $(*)$ is the logarithmic addition of the *IL*s of the two ducts.

4. For baffle thicknesses other than double the lining thickness, logarithmic addition of the *IL* of the ducts shown in Figure 3.3, gives the *IL* of the system.

   In generalized form, the *IL* for a lined duct with a baffle of any thickness

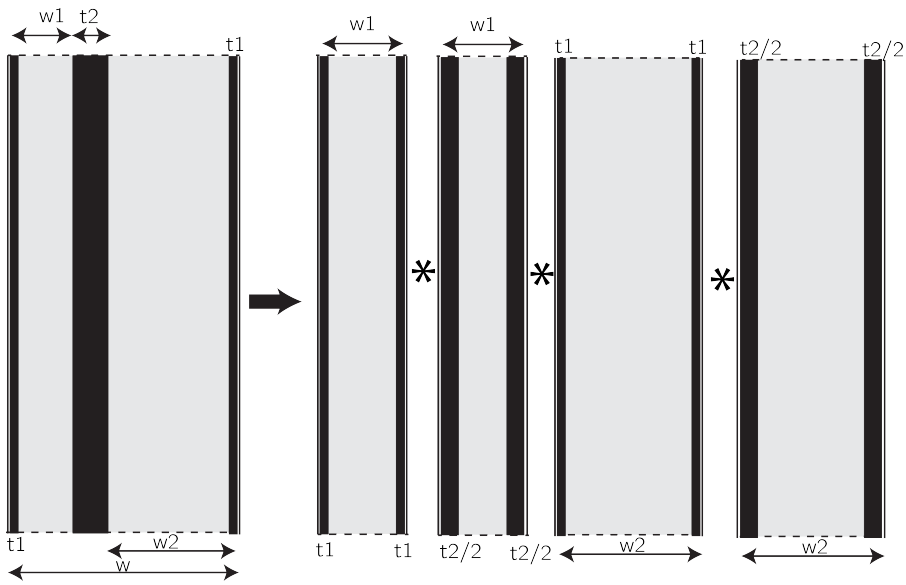

Figure 3.3: Model showing the equivalent model for a duct with baffle of any thickness, where (∗) is the logarithmic addition operator.

and any position is:

$$IL_{eff}(w, t1, t2) = -\frac{10}{n_d}\log_{10}\Big\{10^{\left(-\frac{IL(w1,t1)}{10}\right)} + 10^{\left(-\frac{IL(w1,t2/2)}{10}\right)} + 10^{\left(-\frac{IL(w2,t1)}{10}\right)} + 10^{\left(-\frac{IL(w2,t2/2)}{10}\right)}\Big\} \quad (3.21)$$

where IL_{eff} is the IL of the system, $t1$ is the thickness of the duct lining, $t2$ is the thickness of the baffle, $w1$ and $w2$ are the widths of the duct on either side of the baffle, w is the width of the baffle, and n_d is the number of elements being operated on, which is 4 in this case. This can similarly be extended to more complex systems having more than one baffle across the width.

5. From Chapter 2, it can be seen that, when building a FE model, 2D modelling was chosen to generate a sample set instead of 3D. In Figure Figure 2.1, the analogous 3D models are shown. In order to expand the model

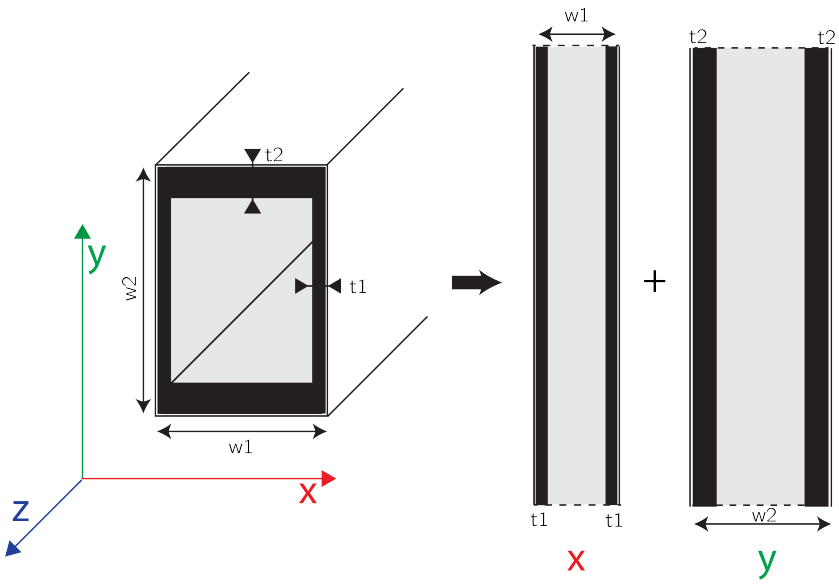

Figure 3.4: Model showing the equivalent model for a duct with lining on all sides, where $(*)$ is the logarithmic addition operator.

to the 3D domain, the Insertion Losses of the duct in the two axes (x-axis along width and y-axis along breadth), as shown in Figure 3.4, are added directly as:

$$IL_{xy} = IL_x + IL_y \tag{3.22}$$

6. Finally different elements along the length of the duct (z-direction) can be directly added.

Combining all the above methods, the calculation and comparison of the Insertion Loss of a sample configuration are shown in the next section.

3.1.6 Model calculation

In this section, a sample calculation is shown for one selected configuration.

Figure 3.5 shows the model of a duct of cross-section $w \times b$ with linings on all sides, of thickness t_x across the width and t_y across the breadth of the duct.

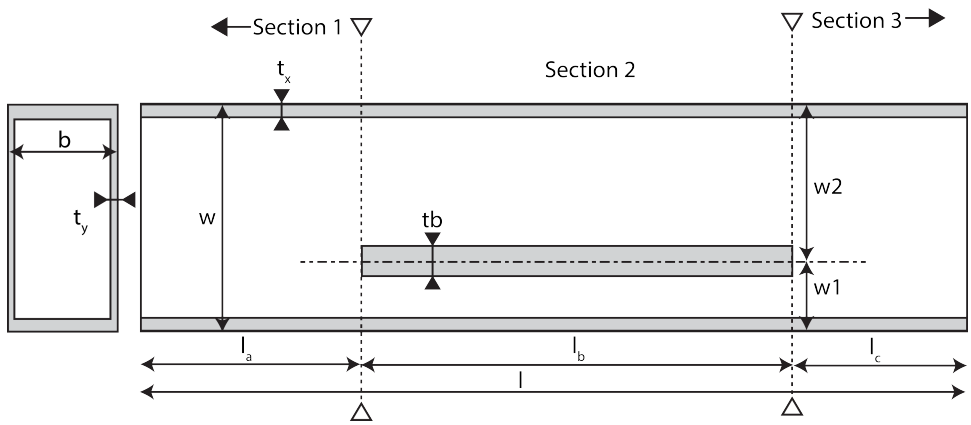

Figure 3.5: Model configuration with sections named for a sample calculation.

A baffle of thickness t_b and length l_b is inserted at a distance of l_a from the duct inlet, ending at a distance l_c from the outlet. The baffle is offset from the centre of the duct across the width such that the baffle median splits the duct into widths $w1$ and $w2$. The model is divided into three sections – Sections 1, 2 and 3 based on its topology, for ease of calculation. The insertion loss for each section is described individually.

<u>**Section 1**</u>:

For Section 1, the Insertion Loss can be represented as a combination of the following:

1. Insertion Loss of a 2D duct of width $(w - t_x)$ and lining thickness t_x on both sides. This is done by halving the width in the model for the IL of a 2D duct with lining on one side, as discussed in the previous section. The Insertion Loss is then:

$$IL_{1a} = \frac{8.08e - 6R_f(t_x)f^2{t_x}^2 l_a}{1 + 0.0074R_f(t_x)t_x + 6.53e - 15R_f(t_x)\left(\frac{w-2t_x}{2}\right)^4 f^5{t_x}^2} \tag{3.23}$$

2. Insertion Loss of a 2D duct of width $(b - t_y)$ and lining thickness of t_y. Similar to IL_{1a}, the Insertion Loss is:

$$IL_{1b} = \frac{8.08e - 6R_f(t_y)f^2{t_y}^2 l_a}{1 + 0.0074R_f(t_y)t_y + 6.53e - 15R_f(t_y)\left(\frac{b-2t_y}{2}\right)^4 f^5{t_y}^2} \tag{3.24}$$

Combining the Insertion Losses for $(1a)$ and $(1b)$, the Insertion Loss for Section 1 can be described as:

$$IL_1 = IL_{1a} + IL_{1b} \tag{3.25}$$

<u>**Section 2**</u>:

In Section 2 the baffle divides the width of the duct; the Insertion Loss can be represented as a combination of the following:

1. Insertion Loss of a 2D duct of width $w2 - t_x - \frac{t_b}{2}$ and lining thickness t_x on both sides, due to the baffle inside:

$$IL_{2a} = \frac{8.08e - 6R_f(t_x)f^2{t_x}^2 l_b}{1 + 0.0074R_f(t_x)t_x + 6.53e - 15R_f(t_x)\left(\frac{w2-t_x-\left(\frac{t_b}{2}\right)}{2}\right)^4 f^5{t_x}^2} \tag{3.26}$$

2. Insertion Loss of a 2D duct of width $w2 - t_x - \frac{t_b}{2}$ and lining thickness $\frac{t_b}{2}$ on both sides, due to baffle inside:

$$IL_{2b} = \frac{8.08e - 6R_f(t_b)f^2\left(\frac{t_b}{2}\right)^2 l_b}{1 + 0.0074R_f(t_b)\left(\frac{t_b}{2}\right) + 6.53e - 15R_f(t_b)\left(\frac{w2-t_x-\left(\frac{t_b}{2}\right)}{2}\right)^4 f^5\left(\frac{t_b}{2}\right)^2} \tag{3.27}$$

3. Insertion Loss of a 2D duct of width $(b - t_y)$ and lining thickness t_y. Similar

to IL_{1b}, the Insertion Loss is:

$$IL_{2b} = \frac{8.08e-6R_f(t_y)f^2{t_y}^2 l_b}{1+0.0074R_f(t_y)t_y+6.53e-15R_f(t_y)\left(\frac{b-2t_y}{2}\right)^4 f^5{t_y}^2} \tag{3.28}$$

Combining the Insertion Losses for $(2a)$, $(2b)$ and $(2c)$, the Insertion Loss for Section 2 can be described as:

$$IL_2 = -\frac{10}{2}\log_{10}\left(10^{\left(-\frac{IL_{2a}}{10}\right)} + 10^{\left(-\frac{IL_{2b}}{10}\right)}\right) + IL_{2c} \tag{3.29}$$

<u>**Section 3**</u>:
Section 3 is similar to Section 1, with the exception of a different length l_c, so this is not detailed here. The IL for this section is IL_3.

The Insertion Loss of the whole system is the sum of the Insertion Losses of the individual elements:

$$IL_{eff} = IL_1 + IL_2 + IL_3 \tag{3.30}$$

3.1.7 Estimation of flow resistivity from absorption

The surrogate model for Insertion Loss was developed keeping in mind the requirements of designers. However, the Insertion Loss expression involves the parameter flow-resistivity (R_f), which is not a commonly-used metric in industry, to describe the absorption of a material. A more widely-used metric is the absorption coefficient (α). The absorption coefficient, or the normal-incidence absorption coefficient to be more precise, is the percentage of incident sound energy that has been absorbed. An absorption coefficient of 1 corresponds to a perfectly absorbing material and 0 corresponds to a perfectly reflective material. It was of interest to estimate R_f from α.

Delany-Bazley model:

Delany and Bazley developed empirical expressions to predict the acoustical properties of porous sound-absorbing materials from their airflow resistivities [19]. The experiments were based on impedance-tube measurements of glass wool and rock wool, measured in the frequency range 250 to 4000 Hz. The acoustical properties of a porous sound-absorbing material – namely the characteristic impedance Z_c and the propagation constant k – were given as complex expressions, as follows:

$$Z_c = \rho_o c_o \left(1 + 0.0495\left(\frac{f}{\sigma}\right)^{-0.754} - j0.0754\left(\frac{f}{\sigma}\right)^{-0.732}\right) \tag{3.31}$$

$$k = \frac{\omega}{c_o}\left(1 + 0.0848\left(\frac{f}{\sigma}\right)^{-0.7} - j0.164\left(\frac{f}{\sigma}\right)^{-0.595}\right) \tag{3.32}$$

where ω is the angular frequency ($2\pi f$), ρ_0 is the density of air (1.213 kg/m^3) and c_o= speed of sound in air (342.2 m/s). Mirowska and Czysewski [35] provide a way of calculating the sound absorption from the Impedance Test Method for a porous material as:

$$\alpha = 1 - \left|\frac{Z_c - 1}{Z_c + 1}\right|^2 \tag{3.33}$$

From the above equations it can be seen that the absorption coefficient can be estimated from the flow resistivity. However, it is difficult to invert Eq. (3.33) such that the flow resistivity can be derived from absorption coefficient. In order to estimate the flow resistivity from a given value of absorption, a surrogate model was developed.

For this model, the sample set was generated by inputting flow resisitivities into the Delaney-Bazley equation (Eq. (3.31)) and determining the absorption coefficient from Eq. (3.33). For a given material of measured flow resistivity R_f and thickness t, the absorption coefficient α at frequency f, was determined by

Table 3.2: Statistics for surrogate model for flow-resistivity estimation.

Statistic Measure	Value
R^2 Goodness of Fit	0.9948
Correlation Coefficient	0.9975
Mean Squared Error	0.129

linear-regression as:

$$\alpha = \frac{9tf^2 + t^2f^3}{181f + 9tf^2 + t^2f^3 + R_f\,(2 + 0.00624t^2f^2)} \tag{3.34}$$

From the above relationship it can be seen that there is a unique relationship between R_f and α. So there can be only one solution for R_f for every α, while keeping other parameters constants. This allows us to determine the value of R_f by rearranging Eq. (3.34) as,

$$R_f = \frac{\left(\frac{9tf^2+t^2f^3}{\alpha}\right) - \left(181f + 9tf^2 + t^2f^3\right)}{(2 + 0.00624t^2f^2)} \tag{3.35}$$

R_f can be substituted back into the Delaney-Bazley equation to determine the impedance of the given material. Table 3.2 shows the various statistical measures for the model.

It is worth noting that the relationship in Eq. (3.35) holds only for fibrous absorbers and normal-incidence absorption. This equation serves as a rough estimate to determine flow resistivity, if an experimental setup for measuring flow-resistivity is unavailable. For this study, however, flow resistivity was determined directly from the Flow Resistivity Apparatus (FRA). More information about the measurement of flow resistivity using the Flow Resistivity Apparatus is discussed in Chapter 4.

3.2 Airflow modeling

The following section discusses the surrogate model that was constructed for predicting ventilation airflow. The section begins with a discussion of theoretical relationships for airflow in ducts, and continues with the development of the surrogate model.

3.2.1 Theoretical relationships for airflow in ducts

Effect of vena-contracta for a simple aperture

As already discussed, a vena-contracta is the reduction in the flow area of a fluid jet as it emerges from an aperture, caused by the sudden change in cross-sectional area. The flow equations are discussed for the sudden contraction of area. Two cases are presented below [36]; the first case describes flow equations for a simple model in which the vena-contracta is ignored – then the flow equations are modified to accommodate its effect.

A source volume that opens to an aperture of smaller cross-section, as shown in Figure 3.6, is considered. As shown in the figure, in the absence of the vena-contracta, the flow emerging from of the aperture undergoes no distortion. The continuity equation is written as:

$$A_1 u_1 = A_2 u_2 \tag{3.36}$$

Here the energy losses due to viscosity are ignored. The Bernoulli law for the conservation of energy is written as:

$$P_1 + \frac{1}{2}\rho {u_1}^2 = P_2 + \frac{1}{2}\rho {u_2}^2 \tag{3.37}$$

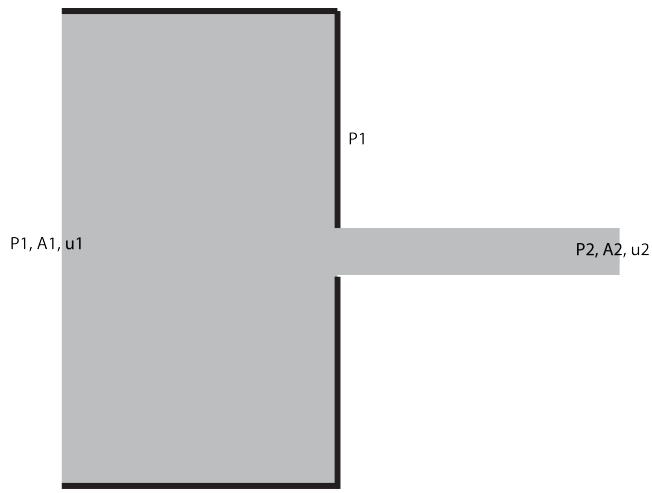

Figure 3.6: Flow through aperture ignoring vena-contracta.

Solving Equations (3.36) and (3.37), the velocity at the outlet can be written as:

$$u_2{}^2 = \frac{2\left(P_1 - P_2\right)}{\rho\left(1 - \left(\frac{A_2}{A_1}\right)^2\right)} \tag{3.38}$$

Next, the momentum and force equations are solved for the system. The momentum flux of the fluid passing through an area A is $(\rho u A)\,.\,(u)$. The summation of external forces for fluid entering through A_1 and exiting through A_2 can be written as:

$$\frac{dp}{dt} = \rho\left(u_2{}^2 A_2 - u_1{}^2 A_1\right) \tag{3.39}$$

The pressure on the wall of $(A_1 - A_2)$ is the same as P_1. So, the net force on the system is,

$$F = P_1 A_1 - \left[P_1\left(A_1 - A_2\right) + P_2 A_2\right] = \left(P_1 - P_2\right) A_2 \tag{3.40}$$

The change in momentum is equal to the force on the system. Equating both, and substituting from the continuity equation, we can solve for the velocity u_2 as:

$$\left(u_2{}^2 - u_1{}^2 \frac{A_1}{A_2}\right) = \frac{\left(P_1 - P_2\right)}{\rho} \tag{3.41}$$

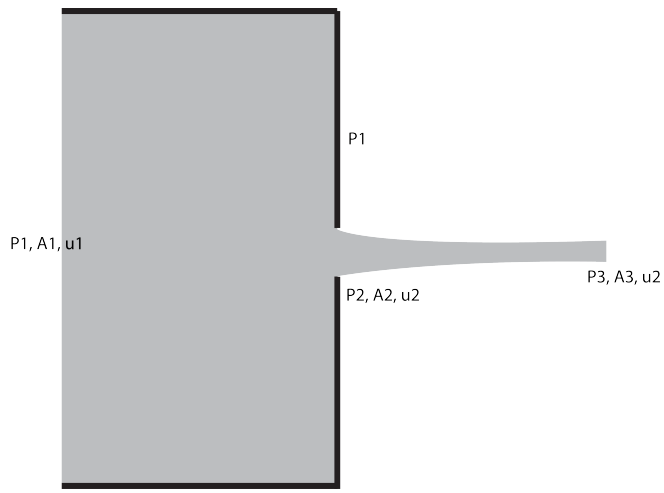

Figure 3.7: Flow through aperture including vena-contracta.

$$u_2{}^2 = \frac{(P_1 - P_2)}{\rho\left(1 - \frac{A_2}{A_1}\right)} \tag{3.42}$$

Comparing Equations (3.38) and (3.42), we can infer that the velocity found from the conservation of force does not agree with that found from the conservation of energy. The difference is due to the vena-contracta – the contraction of fluid as it passes though the aperture, as shown in Figure 3.7.

To account for the vena-contracta, Eq. (3.39) is modified as:

$$\frac{dp}{dt} = \rho\left(u_3{}^2 A_3 - u_1{}^2 A_1\right) \tag{3.43}$$

When the potential energy before the flow enters the duct is entirely converted to kinetic energy downstream, then:

$$\rho u_3{}^2 A_3 = 2P_1 A_3 \tag{3.44}$$

Also assuming that $u_3 \gg u_1$:

$$\frac{dp}{dt} = 2P_1 A_3 \tag{3.45}$$

Assuming $P_3 \ll P_1$, the Bernoulli equation can be written as:

$$F = P_1 A_1 - \left[P_1 \left(A_1 - A_2\right) + P_3 A_3\right] = P_1 A_2 - P_3 A_3 \approx P_1 A_2 \tag{3.46}$$

This gives the relationship between A_3 and A_2 as $A_3 = A_2/2$. From experiments, the ratio A_3/A_2 has been found to be around 0.61. Substituting this in to the continuity equation:

$$u_2 = 0.61 u_3 \tag{3.47}$$

The velocity is usually expressed in its corrected form (i.e. including the area ratio) as:

$$u_2 = C_d \sqrt{\frac{2\left(P_1 - P_3\right)}{\rho\left[1 - \left(\frac{A_2}{A_1}\right)^2\right]}} \tag{3.48}$$

where C_d is the called the discharge coefficient, which has a value of 0.61 for a small orifice.

Effect of vena-contracta due to change in duct cross-section

This section describes the flow equation in ducts due to a change in cross-section, namely sudden expansion and sudden contraction [37].

Sudden expansion:

For flow through a duct, the Bernoulli equation can be written as:

$$\frac{{u_1}^2}{2g} + \frac{P_1}{\rho} = \frac{{u_2}^2}{2g} + \frac{P_2}{\rho} + H \tag{3.49}$$

where H is the head-loss due to an abrupt expansion:

$$H = \frac{{u_1}^2 - {u_2}^2}{2g} + \frac{P_1 - P_2}{\rho} \tag{3.50}$$

Now, assuming that after the sudden expansion the fluid does not change in cross-section up to a distance l_{ch}, as shown in Figure 3.8, the impulse in the fluid

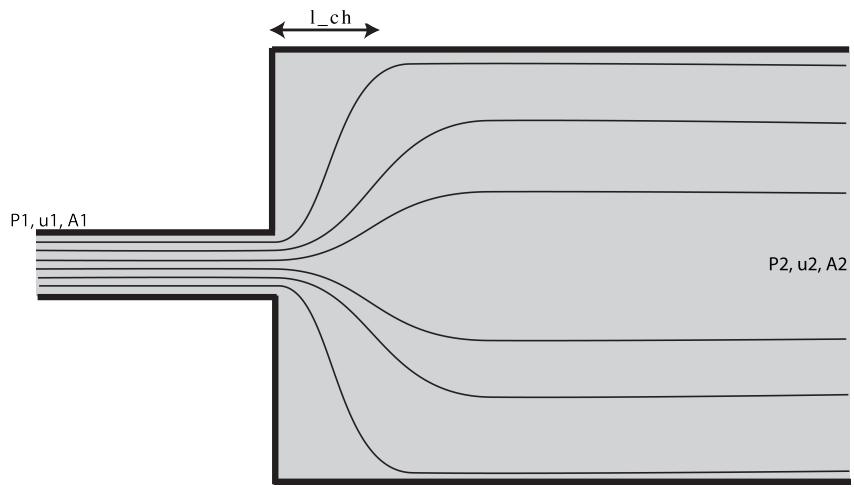

Figure 3.8: Flow through a sudden expansion.

is equated to the change in momentum as:

$$P_1 A_1 + P_1 (A_2 - A_1) - P_2 A_2 = \frac{\rho}{g} u_2 A_2 (u_2 - u_1) \tag{3.51}$$

Simplifying:

$$\frac{(P_1 - P_2)}{\rho} = -\frac{u_2 (u_1 - u_2)}{g} \tag{3.52}$$

Combining Equations (3.50) and (3.52):

$$H = \frac{(u_1 - u_2)^2}{2g} \tag{3.53}$$

Applying the continuity equation:

$$H = \frac{{u_1}^2}{2g} \left(1 - \frac{A_1}{A_2}\right)^2 \tag{3.54}$$

Eq. (3.54) is known as the Borda-Carnot relation.

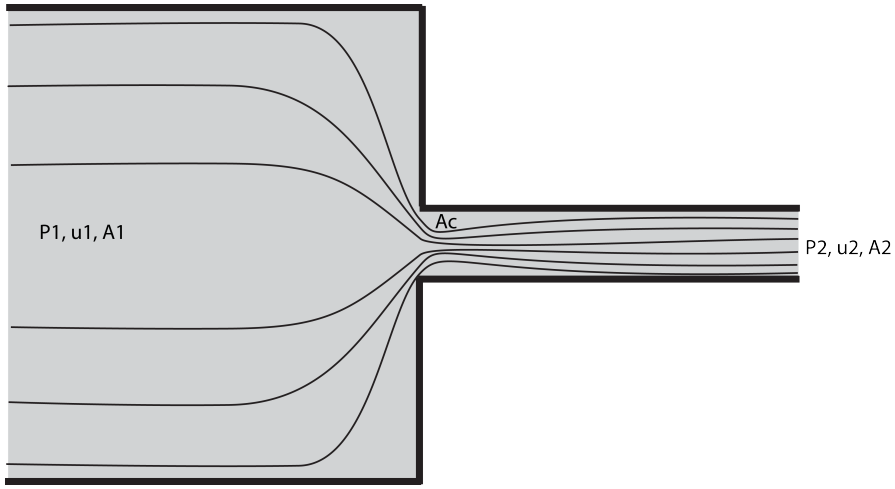

Figure 3.9: Flow through a sudden contraction.

Sudden contraction:

When the fluid undergoes a sudden contraction, the stream is contracted for some distance beyond the entrance to the smaller section, and a vena-contracta is formed. Following this, the stream expands, due to pressure recovery. The total pressure loss in a contracting section results from the expansion that follows the contraction:

$$H = \frac{(u_c - u_2)^2}{2g} = \left(\frac{A_2}{A_c} - 1\right)^2 \frac{{u_2}^2}{2g} \tag{3.55}$$

The ratio A_c/A_2 is known as the contraction coefficient. Sometimes the factor $(A_2/A_c - 1)^2$ is taken to be resistance coefficient K, which is associated with the energy loss. The value of K or A_c is determined experimentally and is given by an empirical graph. As cited in [37], the values of K differ as much as 50% between various authors, as shown in Figure 3.9. Moreover, most of the empirical data is valid for circular cross-section pipes.

McElroy [37] gives the following equation for the ratio A_c/A_2:

$$\frac{A_c}{A_2} = \sqrt{\frac{1}{z - z\left(\frac{A_2}{A_1}\right)^2 + \left(\frac{A_2}{A_1}\right)^2}} \tag{3.56}$$

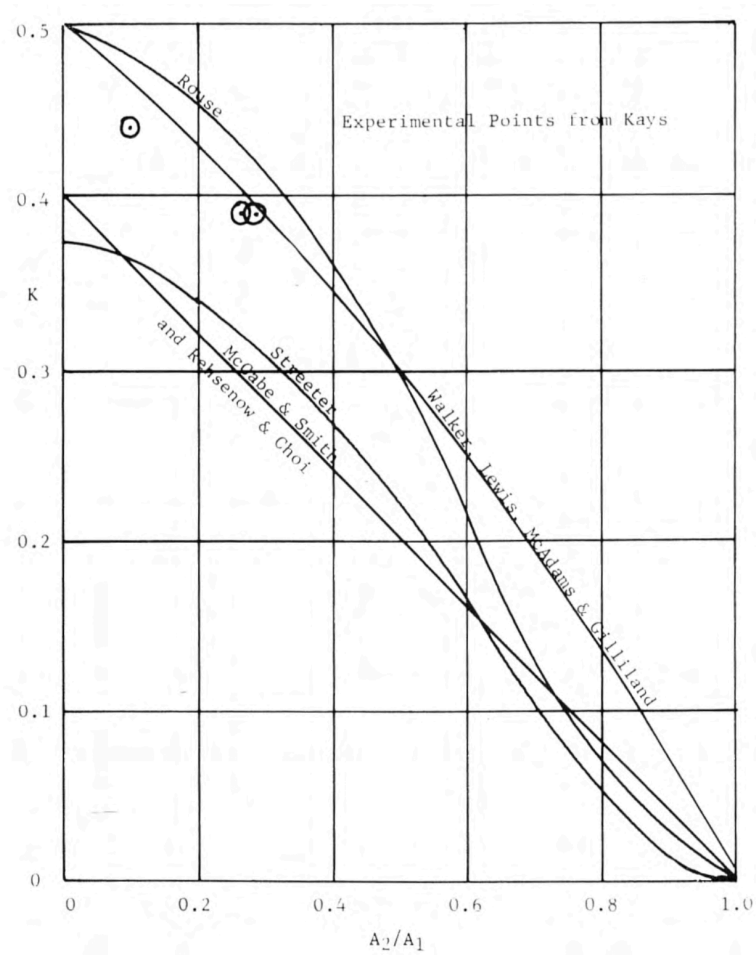

Figure 3.10: Value for K for various area ratios A_2/A_1 as suggested by various authors [1].

where z is an empirical factor called the contraction factor. The value of z was found to be 2.5 for an abrupt contraction. Then:

$$\frac{A_c}{A_2} = \sqrt{\frac{1}{2.5 - 2.5\left(\frac{A_2}{A_1}\right)^2}} \tag{3.57}$$

and

$$H = \left(\sqrt{2.5 - 2.5\left(\frac{A_2}{A_1}\right)^2} - 1 \right)^2 \frac{{u_2}^2}{2g} \tag{3.58}$$

Flow propagation through duct:

The resistance-loss for flow through pipes, due to friction, along a given length of pipe, can be described by the Darcy-Weisbach equation as:

$$H_f = f_D \frac{L}{d_h} \frac{u^2}{2g} \tag{3.59}$$

where H_f is the head loss due to friction, L is the length of the pipe, d_h is the hydraulic diameter and f_D is called the Darcy friction factor, which is dependent on the surface roughness and Reynolds number Re of the duct. The Darcy friction factor is non-dimensional and can be determined for laminar flow from:

$$f_D = \frac{64}{\mathrm{Re}} \tag{3.60}$$

and for turbulent flow from:

$$\frac{1}{f_D^{1/2}} = -2 \log \left[\frac{2.51}{\left(\mathrm{Re}\, f_D^{1/2}\right)} + \frac{(\epsilon/d_h)}{3.72} \right] \tag{3.61}$$

where ϵ is the roughness height (in m) for the duct. The Darcy friction factor can be more easily determined from the Moody diagram [38].

For all the scenarios described above, pressure drop Δp can be determined from the head loss H as:

$$\Delta p = \rho g H \tag{3.62}$$

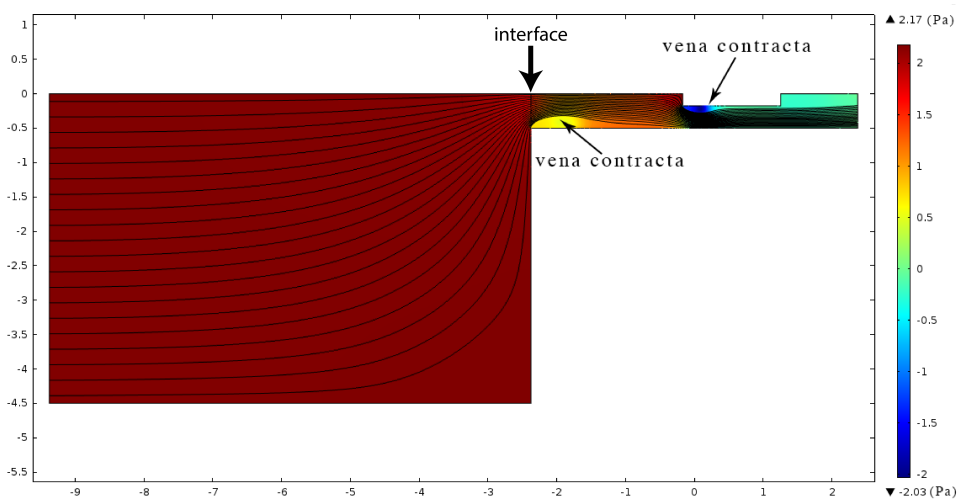

Figure 3.11: Different regions of flow propagation of interest inside a duct.

3.2.2 Surrogate modelling considerations

In order to build a surrogate model for airflow, the following phenomena had to be captured:

1. Pressure drop due to sudden change in cross section,
2. Pressure drop due to flow propagation in duct.

Surrogate models were constructed based on the assumption that most of the flow profiles in ducts can be represented as a combination of the above phenomena. How well this assumption works is discussed in the following sections.

As for the acoustics model, Eureqa Desktop was used to build the surrogate model, using symbolic regression. From the FEA simulations, a total of 128,000 data points based on the permutations of parameters s_h, d_w, Re, l and x, as shown in Table 2.2, were used. Wherever possible, the number of parameters was reduced by normalizing them with respective reference parameters, for faster and more efficient model construction. For example, the ratio s_h/d_w, where s_h and d_w are the projected lengths of cross-sectional areas A_1 and A_2, respectively, and the ratio of the position in the duct to the length of the duct x/l were used. All

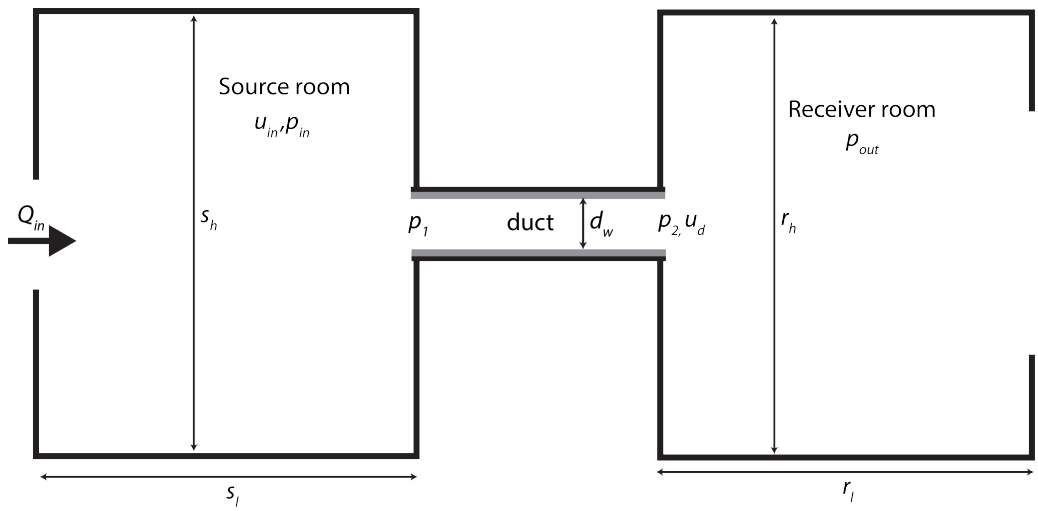

Figure 3.12: Conventional symbols used in the surrogate model for a lined duct installed between two rooms.

parameters were normalized to their respective standard deviation before input into Eureqa.

3.2.3 Surrogate model

When a fluid undergoes a change in its course – for example due to a sudden change in the duct geometry – a loss of energy occurs that results in pressure drop; this was discussed in previous sections. It also creates turbulence in the duct near the inlet, which extends a considerable distance downstream. The surrogate models for predicting the pressure drop for a sudden change in cross-section at an interface, due to sudden expansion and contraction, and the pressure drop due to flow through the duct, as shown in Figure 3.11, are discussed in this section.

Theoretical expressions for the head loss due to an abrupt change in duct cross-section were described in the previous section. For a sudden contraction, the fluid first contracts and then expands in the duct. The cross-sectional area A_c is determined through empirical models.

From the Finite-Element analysis for airflow that was done in this study (refer to Chapter 2), it was clear that the length of the vena-contracta inside the pipe depends on the cross-sectional areas of the source room and the duct. Furthermore, upon observing various prediction results, it was clear that the pattern, the position and the extent of the vena-contracta did not change with variations in the duct length l, when the cross-sectional areas of the source room A_s and of the duct A_d were kept constant. This means that, for very short lengths of the duct, the flow does not stabilize from the vena-contracta before the termination of the duct. This leads to a lower discharge coefficient (close to 0.64) for a short aperture, and a quickly rising discharge coefficient (up to around 0.8) until pressure recovery fully occurs. After pressure the recovery occurs, there is gradual increase in pressure drop with length, resulting in slight drop in discharge coefficient.

The exact position along the length of the duct, of maximum A_c, which can be observed from the FEM results (see Figure 3.11), could not be determined without manual interpretation. So the design of the surrogate models for pressure drop was done based on the geometry of the duct system, in three parts as follows,

- *Part 1:* The pressure drop across the interface between two cross-sections before and after the cross-sectional change, for sudden contraction (near the inlet of the duct).

- *Part 2:* The pressure drop along the length of the duct that would include the effect of the vena-contracta, and energy loss due to resistance of the flow though the duct.

- *Part 3:* The pressure drop across the interface between two cross-sections before and after the cross-sectional change, for sudden expansion (near the outlet of the duct).

For ease of calculation, since the air-exchange rate in the source room is usually known, the pressure drops described in the equations below are described

Table 3.3: Statistics for airflow surrogate model for sudden contraction.

Statistic Measure	Value
R^2 Goodness of Fit	0.999
Correlation Coefficient	0.999
Mean Squared Error	0.002 Pa

as a function of the airflow rate across the ventilation partition, Q_{in}. Figure 3.12 shows the naming convention for the parameters used in the surrogate models. $(p_{in} - p_1)$ is taken as Δp_{in} for the pressure drop described in *Part 1*, $(p_1 - p_2)$ as Δp_{duct} for the pressure drop described in *Part 2* and $(p_2 - p_{out})$ as Δp_{out} for the pressure drop described in *Part 3*.

Part 1: Pressure drop for sudden expansion

This section discusses the surrogate model that was developed for the pressure drop due to sudden contraction. In Eureqa, *addition*, *subtraction*, *multiplication* and *division*, were chosen as the operators/building blocks for the model, along with the *R-squared* fitness function as the measure of error. The form of the target expression for the pressure drop was defined as follows:

$$\Delta p_{in} = F\left(\frac{s_h}{d_w}, s_l, d_w, u_{in}\right) \tag{3.63}$$

After processing and simplifying the expression from Eureqa, the following expression was obtained:

$$\Delta p_{in} = \left(-0.985 + 0.896\left(\frac{s_h}{d_w}\right)^2\right)\left(\frac{Q_{in}}{s_h}\right)^2 \tag{3.64}$$

where s_h is the height of the source room, d_w is the height of the duct and Q_{in} is the airflow rate. Eq. (3.64) predicts the pressure drop right up to before the formation of the vena-contracta. Table 3.3 shows the model statistics for Eq. (3.64).

Table 3.4: Statistics for airflow surrogate model for flow through duct.

Statistic Measure	Value
R^2 Goodness of Fit	0.991
Correlation Coefficient	0.996
Mean Squared Error	0.003 Pa

Part 2: Pressure drop across the duct

The following section describes the surrogate model that was developed for predicting the pressure drop that occurs due to flow propagation inside the duct, when it is preceded by a sudden contraction near the inlet of the duct.

As mentioned in the previous sections, the existence of the vena-contracta resulting from the change in cross-section results in a spike in pressure drop close to the inlet of the duct. The effect of the vena-contracta could decrease very early in the duct, or it could extend the whole length of the duct, depending on the cross-section s_h and on d_w. The position and the extent of the vena-contracta did not change with variations in the duct length l when the areas of cross section of the source room s_h and the duct d_w were kept constant. From trying to build a surrogate model, it quickly became apparent that simple functions could not predict the abrupt increase in pressure. For this reason, it was decided to try to use squashing functions to model the spike in pressure. In Eureqa, *addition*, *subtraction*, *multiplication*, *division*, *logistic*, *gauss* and *cauchy* were chosen as the operators/building blocks for the model, along with the *R-squared* fitness function as the measure of error. The form of the target expression was defined as follows:

$$\Delta p_{duct} = F\left(s_h, d_w, x, d_w, u_{in}\right) \tag{3.65}$$

Among the squashing functions that were used for the surrogate model, a *logistic* function gave a model with reasonable accuracy. A *logistic* function, as discussed in Chapter 1, can be used to model natural phenomena that approximately behave like a step function – i.e. that undergo an abrupt change and

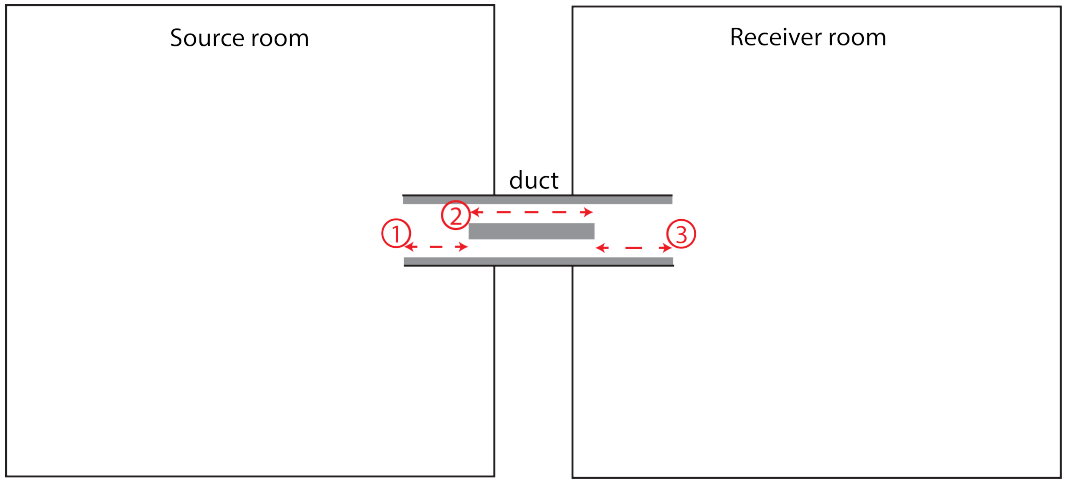

Figure 3.13: Illustration showing the different regions of interest for flow propagation through a duct.

remain constant after that.

Since the position and the shape of the vena-contacta did not change with a change in the duct length, the position x was substituted for the length l in the surrogate model. Eq. (3.66) is the surrogate model that was developed:

$$\Delta p_{duct} = \left(0.013l + 0.676\,\text{logistic}\left(\frac{2.092d_w}{l - 0.086} + \frac{0.227s_h l^2}{(0.086 - l)\,d_w}\right)\right)\left(\frac{Q_{in}}{d_w}\right)^2 \tag{3.66}$$

In Eq. (3.66), the term with the *logistic* function represents the abrupt change in pressure drop due to the vena-contracta. The term $0.013l\left(\frac{Q_{in}}{d_w}\right)^2$ represents the gradual buildup of pressure when fluid flows through the duct, possibly due to friction. Table 3.4 shows the model statistics for Eq. (3.64).

From Figure 3.13, which shows regions of interest numbered as 1, 2 and 3, and from the understanding obtained from the theoretical model, it is possible to locate baffles such that the pressure drop across the duct is minimal. The baffles could theoretically be positioned along the duct such that they are after the pressure recovery that occurs in the duct, and when there is enough length of duct after the baffle for pressure recovery to occur following the change in

Table 3.5: Statistics for the airflow surrogate model for a sudden expansion.

Statistic Measure	Value
R^2 Goodness of Fit	0.994
Correlation Coefficient	0.997
Mean Squared Error	0.002 Pa

cross-section at the end of the baffle.

Part 3: Pressure drop for sudden expansion

This section discusses the surrogate model that was developed for a pressure drop from sudden contraction. In Eureqa, *addition*, *subtraction*, *multiplication* and *division* were chosen as the operators/building blocks for the model, along with the *R-squared fitness function*, as the measure of error, as before. The form of the target expression for the pressure drop was defined as follows:

$$\Delta p_{out} = F\left(d_w, r_w, r_l, d_w, u_d\right) \tag{3.67}$$

The following expression was obtained:

$$\Delta p_{out} = (0.006 + 0.052l - 0.012l^2)\left(\frac{Q_{in}}{d_w}\right)^2 \tag{3.68}$$

It is interesting to note that the equation is independent of the cross-sectional dimensions of the receiver room and only depends on the length of the room from the outlet of the duct to the exhaust ($p = 0$ Pa). The model statistics for Eq. (3.68) are shown in Table 3.5.

The total pressure drop for the system can be written as:

$$\Delta p = \Delta p_{in} + \Delta p_{duct} + \Delta p_{out} \tag{3.69}$$

In Figure 3.14, numbers 1, 2, 3 and 4 refer to scenarios of change in cross-section. In scenarios 2 and 3, the presence of baffles result in the change in

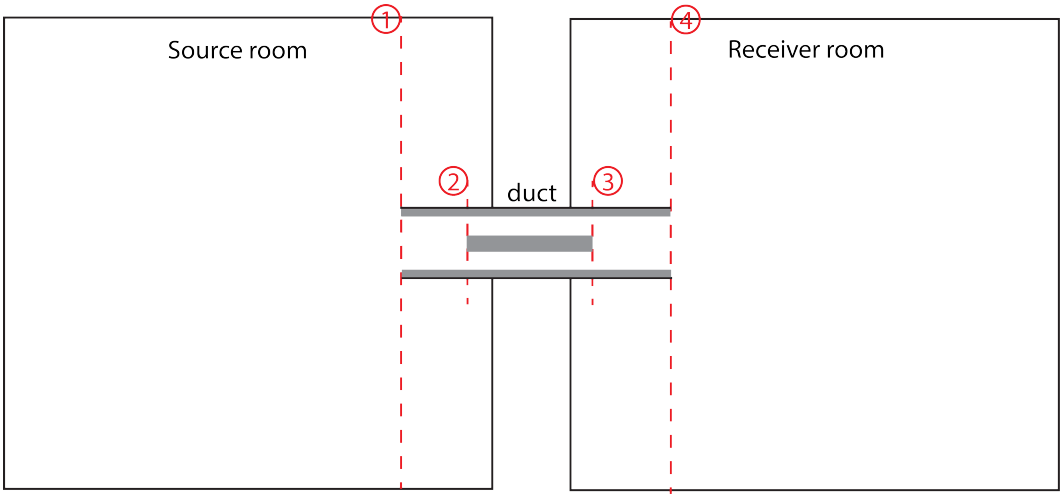

Figure 3.14: Different regions of interest for a lined duct installed between two rooms.

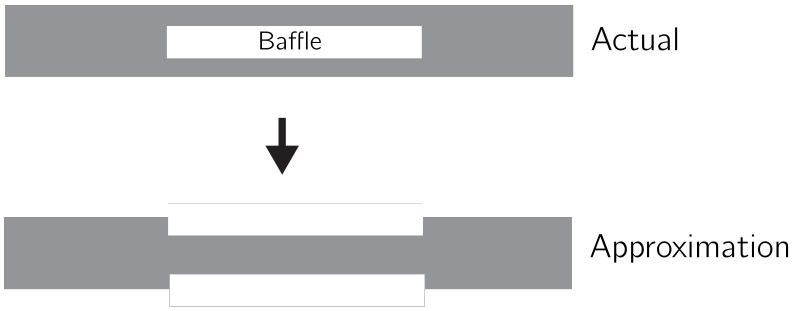

Figure 3.15: Approximation of change in cross-section due to presence of a baffle.

cross-section. The flow splits into two streams, in addition to experiencing the sudden contraction in flow area. However, due to time limitations and the necessity to have a simple model, this was modelled as a sudden change in cross-section, approximated by Equations (3.64) and (3.68) (refer to Figure 3.15). From the limited number of FEA simulations with baffles that was done, as described in Section 2.3.8, the change in position of the baffles resulted in up to 15% error in the corresponding measurement of pressure drop.

3.2.4 Extension of the surrogate model

As for the acoustics model, the FEM model for airflow was only created in 2D. In order to extend it to the third dimension, the characteristic length of the source room and duct were replaced by their respective cross-sectional areas. Thus, Equations (3.64) and (3.68) can be rewritten as:

$$\Delta p_{in} = \left(-0.985 + 0.896\left(\frac{A_s}{A_d}\right)^2\right)\left(\frac{Q_{in}}{A_s}\right)^2 \tag{3.70}$$

$$\Delta p_{out} = (0.006 + 0.052l - 0.012l^2)\left(\frac{Q_{in}}{A_d}\right)^2 \tag{3.71}$$

However the similar procedure applied to Eq. (3.66) did not agree well with results from 3D FEA. This is due to the *logistic* function, that does not agree well when scaling the range of the inputs. This was addressed by using the hydraulic diameters instead of the cross-sectional areas for the source room and the duct. Eq. (3.66) can be rewritten as:

$$\Delta p_{duct} = \left(0.013l + 0.676\,\text{logistic}\left(\frac{2.092d_{hyd}}{l - 0.086} + \frac{0.227s_{hyd}l^2}{(0.086 - l)\,d_{hyd}}\right)\right)\left(\frac{Q_{in}}{A_d}\right)^2 \tag{3.72}$$

where d_{hyd} and s_{hyd} are the hydraulic diameters of the duct and source room cross-sections, respectively.

The surrogate models can also be represented in their non-dimensional form

3.2.5 Analysis of model

Determination of resistance coefficient K for the surrogate model

The pressure drop Δp can be written in terms of the resistance coefficient K as:

$$\Delta p = K\frac{\rho {u_d}^2}{2} = 0.59K{u_d}^2 \tag{3.73}$$

For Equations (3.70) to (3.72), K can be determined as:

$$K_{in} = \left(-1.669\left(\frac{A_d}{A_s}\right)^2 + 1.519\right) \tag{3.74}$$

$$K_{duct} = \left(0.013l + 0.676\,\text{logistic}\left(\frac{2.092d_{hyd}}{l - 0.086} + \frac{0.227s_{hyd}l^2}{(0.086 - l)\,d_{hyd}}\right)\right) \tag{3.75}$$

$$K_{out} = (0.01 + 0.088l - 0.02l^2) \tag{3.76}$$

Combining all the three equations, we obtain:

$$\begin{aligned} K = &- 1.669\left(\frac{A_d}{A_s}\right)^2 + 1.529 + 0.101l - 0.02l^2 \\ &+ 0.676\,\text{logistic}\left(\frac{2.092d_{hyd}}{l - 0.086} + \frac{0.227s_{hyd}l^2}{(0.086 - l)\,d_{hyd}}\right) \end{aligned} \tag{3.77}$$

Surrogate models are usually presented in non-dimensional form in order to maximize their utility. However, this was difficult to achieve in this work, with the current form of the surrogate model. However, an approximate non-dimensional form of the loss coefficient K for the surrogate model would be:

$$\begin{aligned} K = &\left(-1.669\beta^4 + 1.528\right) + (0.176\gamma - 0.081\gamma^2) \\ &+ \left(0.088x + 0.146\,\text{logistic}\left(\frac{0.523\beta}{\xi - 0.022} + \frac{0.057\xi^2}{(0.022 - \xi)\,\beta}\right)\right) \end{aligned} \tag{3.78}$$

where $\beta = d_w/s_h$, $\gamma = y/r_l$, $\xi = x/l$ and y is the distance of the outlet for airflow in the receiver room from the duct outlet. The discharge coefficient or the loss coefficient is usually presented as a function of the Reynolds number and the area ratio. The surrogate model, however, suggests a Reynolds-number-independent loss coefficient. In Chapter 5, the results from the surrogate model are compared with the theoretical model.

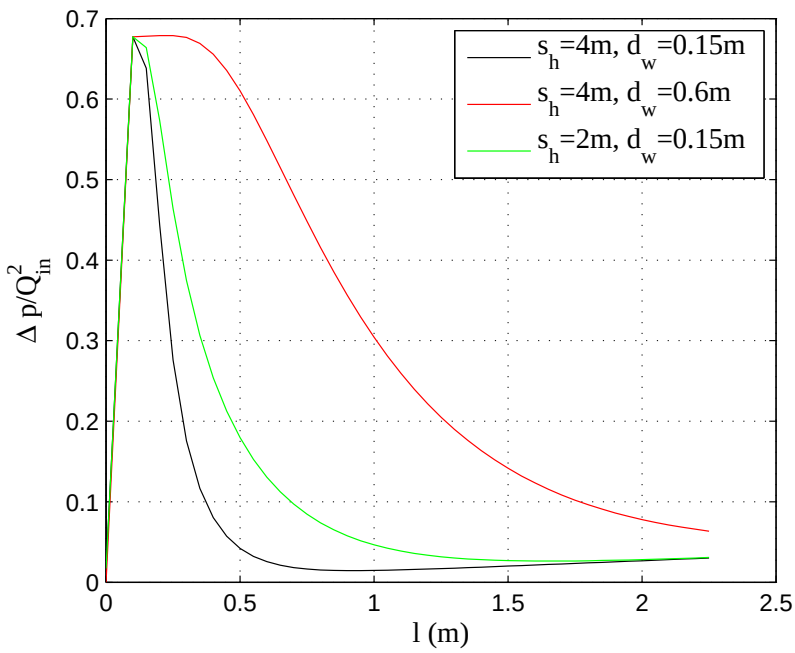

Figure 3.16: Variation of effect of vena contracta with source-room height s_h and duct width d_w.

Effect of vena-contracta with length

The effect of the vena-contracta on the pressure drop across the duct Δp_{duct} from Eq. (3.71), is shown in Figure 3.16 as a function of duct length l, for different heights of the source room s_h and duct widths d_w. The pressure drop in the plot is normalized with respect to the airflow rate Q_{in}. It can be observed from the plot that, for small ducts, the pressure drop due to the vena-contracta recovers early in the duct. For larger ducts, pressure recovery is more gradual. The information that this equation provides is critical in determining the length of a duct, the positioning of the bend in a duct, or the placement of baffles, in order to minimize the effect of the vena-contracta.

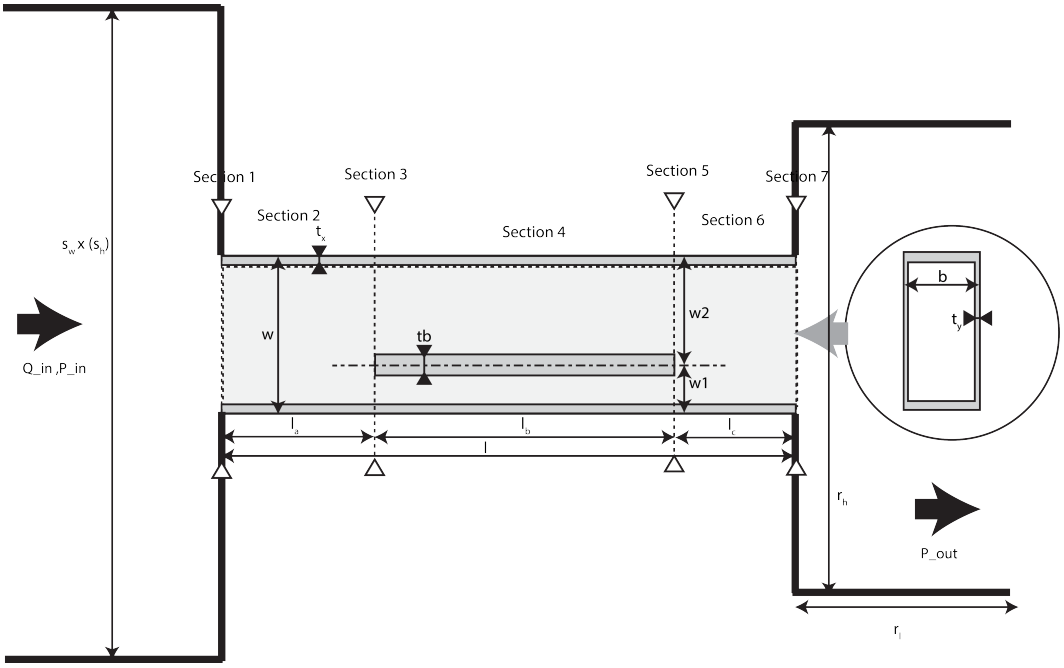

Figure 3.17: Model configuration with sections named for a sample calculation.

3.2.6 Model calculation

In this section, a sample calculation is shown for the same configuration for which sample calculations were shown for acoustics, illustrated in Figure 3.5. However, since the airflow models are dependent on the volumes on either side of the duct, let the cross-sectional area of the source room normal to the duct be $s_h \times s_w$, and the cross-sectional area of the receiver room be $r_h \times r_w$. The illustration of the model configuration is shown in Figure 3.17.

Let the inlet air flow-rate in the source room be Q_{in} and the pressure be P_{in}. The pressure drop across each section is described below, referring to Figure 3.17.

Section 1

The pressure drop across Section 1 is due to the sudden contraction in cross-

section from the source room to the duct. The velocity in the source room is taken as u_{in}, which is equal to Q_{in}/A_s. Then the pressure drop at section 1 can be written as:

$$\Delta p_1 = \left(-0.985 + 0.896 \frac{(s_h s_w)^2}{\left((w - 2t_x)(b - 2t_y)\right)^2}\right)\left(\frac{Q_{in}}{s_h s_w}\right)^2 \tag{3.79}$$

<u>**Section 2**</u>

The pressure drop across Section 2 is due to the change in the velocity profile due to the sudden contraction and due to the pressure drop associated with the propagation in the duct:

$$\Delta p_2 = \left(0.013l + 0.676 \,\text{logistic}\left(\frac{2.092 d_{hyd}}{l - 0.086} + \frac{0.227 s_{hyd} l^2}{(0.086 - l) d_{hyd}}\right)\right) \left(\frac{Q_{in}}{(w - 2t_x)(b - 2t_y)}\right)^2 \tag{3.80}$$

where $s_{hyd} = \dfrac{4 s_h s_w}{2(s_h + s_w)}$ and $d_{hyd} = \dfrac{4(w - 2t_x)(b - 2t_y)}{2(w + b - 2(t_x + t_y))}$

<u>**Section 3**</u>

The pressure drop in Section 3 is due to the presence of the baffle in the duct. As was discussed in the previous section, the existence of the baffle is assumed to be equivalent to a change in cross-section of the duct. In that case, the pressure drop would be due to sudden expansion:

$$\Delta p_3 = (0.006 + 0.052 l_b - 0.012 {l_b}^2)\left(\frac{Q_{in}}{(w - t_b - 2t_x)(b - 2t_y)}\right)^2 \tag{3.81}$$

<u>**Section 4**</u>

The pressure drop due to sudden expansion after the baffle is:

$$\Delta p_5 = \left(-0.985 + 0.896\frac{(w - t_b - 2t_x)^2}{((w - 2t_x))^2}\right)\left(\frac{Q_{in}}{\Big((w - 2t_x - t_b)(b - 2t_y)\Big)}\right)^2 \quad (3.82)$$

Section 5

The pressure drop due to expansion into the receiver room is:

$$\Delta p_7 = (0.006 + 0.052r_l - 0.012{r_l}^2)\left(\frac{Q_{in}}{(w - 2t_x)(b - 2t_y)}\right)^2 \quad (3.83)$$

The combined pressure drops can be used to determine P_{out}:

$$P_{out} = P_{in} - (p_1 + p_2 + p_3 + p_4 + p_5) \quad (3.84)$$

Chapter 4

Experimental Investigation

The previous chapter discussed the methodology that was used to build the surrogate models, based on prediction results from FEM. These surrogate models were intended to help optimize the acoustic and airflow performance of the ducts. This raises the question of how well these theoretical-model predictions relate to real-world measurements. Conducting measurements in full-scale ducts is not always possible, due to constraints in space and resources. This study makes use of scale-models of the duct, along with scaled source and receiver rooms. Experiments using scale-models were used to validate the surrogate models.

This chapter discusses the methodology used for scaling the acoustic and airflow models. This is followed by a detailed description of the experimental transmission facility and its construction. Finally, different configurations that were built are illustrated. The next chapter will compare the results obtained from the surrogate model, Finite Element predictions and the experiments, for the test configurations discussed in this chapter.

4.1 Scaling

As can be understood from previous chapters, certain assumptions were made in predicting and developing the surrogate models in order to simplify the problem. Having understood the need for experimental validation of the surrogate mod-

els, it was beyond the scope of this project to measure performance of real-world ducts in their natural environments. It was decided to build and measure the performance of duct configurations in a laboratory test facility. However, full-scale models of ducts would be very difficult to construct and measure. The major advantages offered by scale-model techniques are those of space, economics and time-saving. For this reason, scale-models of the duct configurations were used for the experiments. Using scale-models for experiments helps validate the results from the surrogate model and FEM; it is also of considerable interest to validate the use of scale-models as alternatives to full-scale models, by cross-validating each other. For the design and use of scale-models, certain principles were followed, as discussed below.

4.1.1 Acoustic scaling

Acoustic-scaling principles were first suggested by Spandock [39]. Several authors have since then used these principles to study the acoustics of environments using scaled-prototypes. This section discusses in brief the theory behind the acoustic-scale modelling that was used in this study [17, 18]. The scaling laws require that all physical laws that govern the acoustic behaviour of the full-scale model also govern the scale-model. The variables involved are scaled to the desired ratio of 1:n between the model-scale and full-scale models. Modelling the sound-field in a model room of 1:n scale is primarily based on the criterion that the wavelength-to-dimension ratio must be kept constant. This ensures similar wave-propagation effects in the full-scale and scaled models. For this to be done, while all the dimensions are scaled by a factor of $\frac{1}{n}$, the frequencies of the generated and measured signals are scaled up by a factor of n. The impedances of the surfaces must be scaled to match those of the full-scale model. The duct walls were assumed to have negligible effect on the IL – they were assumed to be hard surfaces of infinite impedance. From the Delany-Bazley equation for impedance (refer to Eq. (2.1)), it can be see that, in order to maintain the acoustical properties for the full-scale and scale-models of the absorber material, the flow resistivity

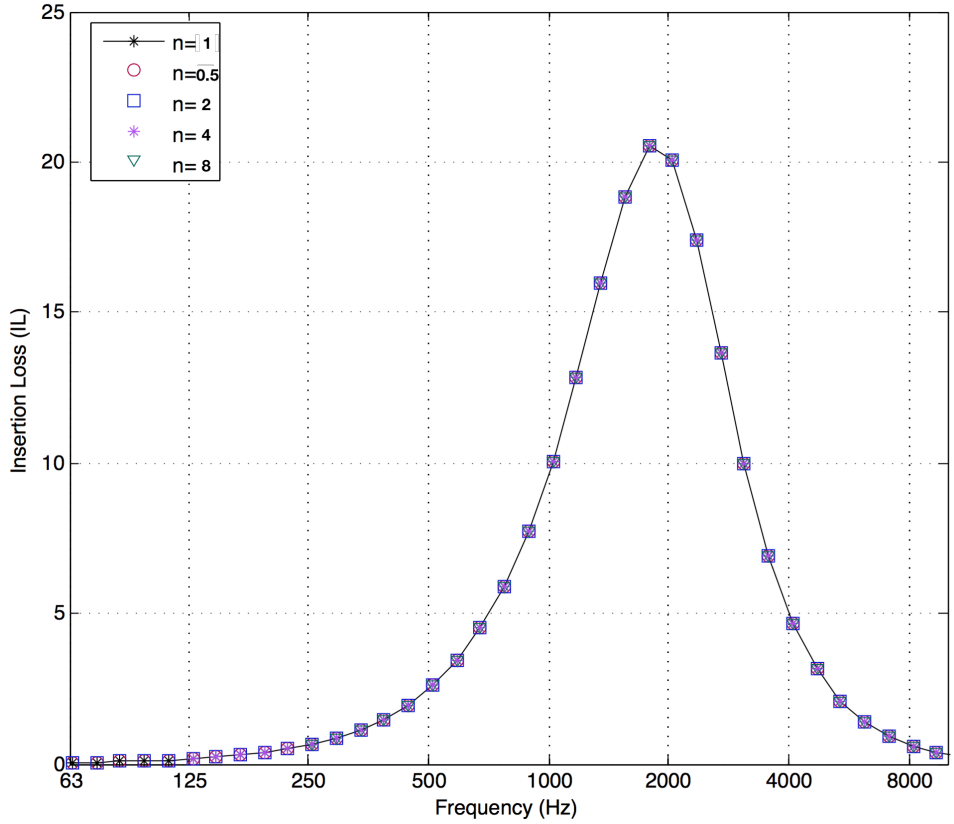

Figure 4.1: Comparison of variation of predicted Insertion Loss with frequency at scale factors $n = 0.5, 1, 2, 4$ and 8 for a full-scale duct of dimensions $0.3\,\mathrm{m} \times 0.3\,\mathrm{m} \times 1\,\mathrm{m}$ and lining of thickness 0.00625 m, R_f=58, 176 Rayls/m.

R_f must be scaled by a factor of n, when the frequency is scaled by a factor of n. Also the air absorption must be scaled by a factor n – however the effects are small if the scaling factor is not too high. The scaling of air absorption and of the impedance of the unlined duct walls were ignored in this study.

These scaling laws have found a range of applications for scaling the sound-fields in reverberant enclosures, and for outdoor noise propagation. However, to our knowledge, they have not been used for modelling the Insertion Loss of silencers in transmission suites before. In theory, scaling down the dimensions of

the duct by a factor of n, and scaling up the flow-resistivity of the absorbent materials by n should result in similar Insertion Losses for the full-scale and scaled models. Briefly, the acoustic scaling of the duct in this study, for $IL_M \simeq IL_{FS}$ is:

$$\frac{w_M}{w_{FS}} = \frac{1}{n} \qquad \frac{b_M}{b_{FS}} = \frac{1}{n} \qquad \frac{l_M}{l_{FS}} = \frac{1}{n}$$
$$\frac{t_M}{t_{FS}} = \frac{1}{n} \qquad \frac{R_{f_M}}{R_{f_{FS}}} = n \qquad \frac{f_M}{f_{FS}} = n$$

where subscripts M and FS denote model-scale and full-scale, respectively. This was verified using Finite Element Analysis predictions – with the plane-wave assumption that was also used to develop the surrogate model. There was an excellent match between the full-scale and scale-model. The results from Finite Element predictions when scaling the model by scale factors $n = 0.5, 1, 2, 4$ and 8 are shown in Figure 4.1.

4.1.2 Flow scaling

The scaling methodology used for airflow modelling is discussed in this section. When scaling, it was intended to have similitude between the full-scale and scale-model. A scale-model is said to have similitude with the full-scale model if they share geometric, kinematic and dynamic similarity. In order to achieve similitude between these models, a dimensionless quantity was chosen to be kept constant. In this case, a dimensionless quantity, the opening Reynolds number Re_o of the duct, was assumed to be the same for the full-scale and the scale-model. The flow regime of the air entering the duct is largely dependent on Re_o as:

$$Re_o = \left(\frac{\rho u d_w}{\mu}\right) \tag{4.1}$$

$$u_s = \left(\frac{\rho}{\rho_s}\right) \times u \times \left(\frac{d_w}{d_{ws}}\right) \times \left(\frac{\mu_s}{\mu}\right) \tag{4.2}$$

Now, assuming the density ρ and the dynamic viscosity μ to be constant, and

keeping Re_o the same, the velocity has to increase by the scaling factor n. For the same duct geometry, it was expected that the flow regimes inside the duct would be similar. Another way to achieve similitude would be to keep the dimensionless quantity, discharge coefficient C_d, constant. However, this would be more difficult to handle when using the blower door, with which the airflow rate can be more easily controlled to achieve desired inlet velocities.

4.1.3 Selection of scaling factor

An appropriate scaling factor needs to be chosen for the scale-model test facility and duct. For this study a $1 : 4$ scale factor was chosen to model the duct configurations. This section discusses the reasons behind choosing this scale.

As discussed in the previous sections, when the dimensions are scaled by a factor of $\frac{1}{n}$, the flow resistivity R_f must be scaled by a factor of n. This means that porous absorbers of thickness $\frac{t}{n}$ should have flow resistivity, $n \times R_f$. Finding materials with desirable flow resistivities is quite challenging. Felt, a material that has found use in scale-models due to its high flow resistivity, was used as a porous absorber in this study. The flow resistivity of felt generally varies from $50,000$ to $85,000$ Rayls/m [40]. The flow resistivity of felt of thickness = 3 mm was measured using the method described in Section 4.4.4, and found to be around $58,000$ Rayls/m. At full scale, the felt can be used as a surrogate for a material that has a flow resistivity close to $15,000$ Rayls/m. The felt measured 3 mm in thickness. Commercial sound-absorber panels are available in 12.5, 25, 50 and 75 mm thicknesses. In order to match the 12.5 mm thickness, two-layered felt was used as the absorber material. In addition to felt, another material, Sonoflex, was used in the scale-model. Sonoflex is a commercially available fibreglass sound-absorber, available as panels. The Sonoflex that was used measured 12.5 mm in thickness and had a flow resistivity of around 7000 Rayls/m [20].

Commercial duct-liner materials are available in different ranges of flow-resistivity. A material that has a flow-resistivity close to that of fibreglass (4000 Rayls/m measured) at 1:4 scale is ROXUL. ROXUL would have been a good choice as the

lining for the scale-model duct, but it is 75 mm thick and it was not possible to cut ROXUL into thin sheets. However, it was used to line the walls of the anechoic receiver room due to its good absorption properties at high frequencies.

As described in the following sections, a blower door was used to measure the airflow performance of the model duct. The blower door is designed to be used at high pressure drops between the source and receiver rooms. Naturally-ventilated rooms have low pressure drops (<1 Pa) across them. This poses a problem to measure flow with acceptable accuracy, at low Reynolds number with a blower door, if the duct hydraulic diameter is large. The flow profile that is expected in large ducts with low pressure drops across them can be studied in scale-model ducts with higher pressure drops, if Re_o is kept constant.

4.2 Test chamber requirements

While designing the test facility for measuring acoustic and airflow performance, considerations had to be made to work at model scale; this section discusses these considerations in detail.

Ideally, to test the performance of full-scale duct-silencers in a test facility, the acoustic and airflow measurements are done in accordance to the guidelines provided by the *ASTM E477* standard [41]. The test method uses a source chamber, a test duct (that includes a test specimen), and a reverberation chamber (i.e with an approximately diffuse sound field) as the receiver room. The source chamber contains one or more loudspeakers that generate pink noise. The noise that propagates from the loudspeaker, through the test duct, is measured in the reverberation chamber. The acoustic performance is measured using the metric, Insertion Loss, as:

$$IL = SPL_{empty\ duct} - SPL'_{silencer} \tag{4.3}$$

where $SPL_{empty\ duct}$ is the time and space averaged SPL measured in the reverberation room for an empty (no lining or baffles) duct configuration, and $SPL'_{silencer}$ is the time and averaged SPL measured in the reverberation room with a test

specimen placed in the duct, corrected for background noise.

While using a scale-model, as discussed in the previous section, scaling the model down by a factor of n requires scaling up the frequencies by a factor of n. So the third-octave-band frequencies of interest are translated from 63-10, 000 Hz to 250-40, *ooo* Hz. At high frequencies, in a reverberant room, the sound field would be diffuse. Though this is beneficial in making it possible to measure a uniform reverberant *SPL* in the room, as required by the standard, the average *SPL* in the reverberation room would be lower than that at the outlet of the duct. This is because the frequency range of measurement is in the ultrasonic range – the attenuation of sound in air increases with frequency and sound attenuation is higher than at the corresponding full-scale frequency, for the same distance of propagation. It was therefore decided to make the *SPL* measurements inside the duct rather than in the receiver room. But then, if the receiver room is made reverberant, as recommended by the standard, the reflected sound from a reverberant room increases the *SPL* that is measured close to the duct termination. Therefore, in order to prevent reflected waves from propagating back in to the duct, the receiver room was made anechoic. The source room was made to promote a diffuse-field and the sound-pressure level was measured at the inlet of the duct on the source side.

For airflow performance, *ASTM E477* recommends the measurement of the pressure drop of the test specimen as a function of airflow. A fan chamber is required with ductwork that provides airflow to the duct-silencer. Transition and substitution ductwork are attached to either sides of the duct-silencer to eliminate the effect of the vena-contracta. Instead, this study makes use of a blower door, to study the effect of the pressure drop due to the silencer, along with the effect of the vena-contracta.

4.3 Chamber construction and equipment setup

For the test transmission facility, a room in the School of Public and Population Health (SPPH) was chosen. The room measured 5 m × 2.8 m × 2.8 m along

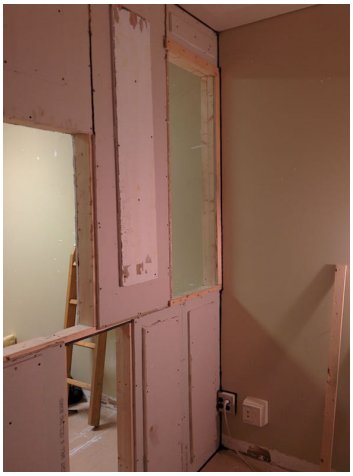

(a)

(b)

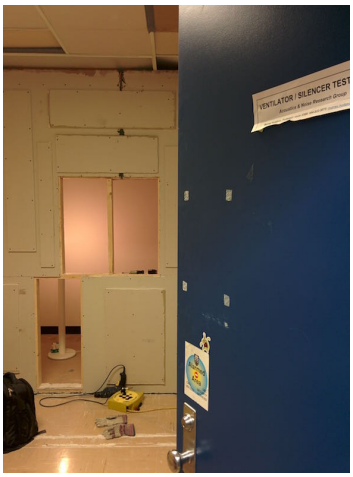

(c)

(d)

(e)

(f)

Figure 4.2: Photographs of the test facility during the construction phase.

the length, width and height, respectively. The walls in the room were made of gypsum-board. The room had a suspended ceiling made of acoustic ceiling tiles (ACT) and a supporting grid system. The plenum above the ceiling connected to other neighbouring spaces. The room was divided into source and receiver rooms by constructing a partition in the middle. The source and receiver rooms were isolated from each other both acoustically and for air-flow. The partition was made of 4 in studs with gypsum boards on either side and fibreglass insulation between them, as shown in Figure 4.2. The fibreglass insulation helps reduce flanking sound transmission through the partition. The gaps in the drywall were sealed with an acoustic sealant and covered with duct-tape to prevent air leakage. It is to be noted that the partition was only built up to the suspended ceiling and could not be extended above it. This resulted in flanking transmission of sound from the source to the receiver room. The receiver-room surfaces were covered with a commercial stone-wool acoustic insulation – ROXUL SAFE 'N' SOUND [42]. The acoustic-insulation panels were held in place by wire-mesh stapled to the walls and ceiling. Porous absorbers like ROXUL have low absorption characteristics at low frequencies. This makes the room not quite anechoic at low frequencies, but increasingly anechoic at higher frequencies with respect to the consideration of the receiver room to be a scale-model, the room can be said to be anechoic.

When performing air-flow measurements, in order to relieve the pressure in the receiver room, a trap door opened to the plenum above the suspended ceiling. This trap door was closed and covered with acoustic insulation when performing acoustic measurement. Certain ROXUL panels were made detachable, to be able to open the trap door for airflow measurement. All test ducts were made from gypsum board. The ducts were made in square and rectangular cross-section configurations. More details about the dimensions and the configurations of the duct are provided in Section 4.6. Absorber materials for duct linings and baffle inserts for the scale-model were chosen to be felt and Sonoflex. The duct located between the source and receiver room is shown in Figure 4.3 for one configu-

(a) (b)

Figure 4.3: Photographs of the duct located between the reverberant source room *(left)* and the anechoic receiver room *(right)*.

ration. As for deciding the lengths of the duct to protrude into the source and receiver rooms, this was done such that the outlet was not close to the walls in the anechoic room, to prevent back-pressure. Figure 4.4 shows top and front illustrations of the completed test facility.

4.4 Measurement methodology

The measurement setups and the procedures used to measure the acoustics and airflow performance are individually discussed in this section.

4.4.1 Equipment setup for acoustics

Ultrasonic tweeters are loudspeakers that generate sound in the high-frequency range, beyond 20, 000 Hz, in the ultrasound range as the name implies. For generating noise in the source room, REALISTIC 40-1377 type tweeters were used.

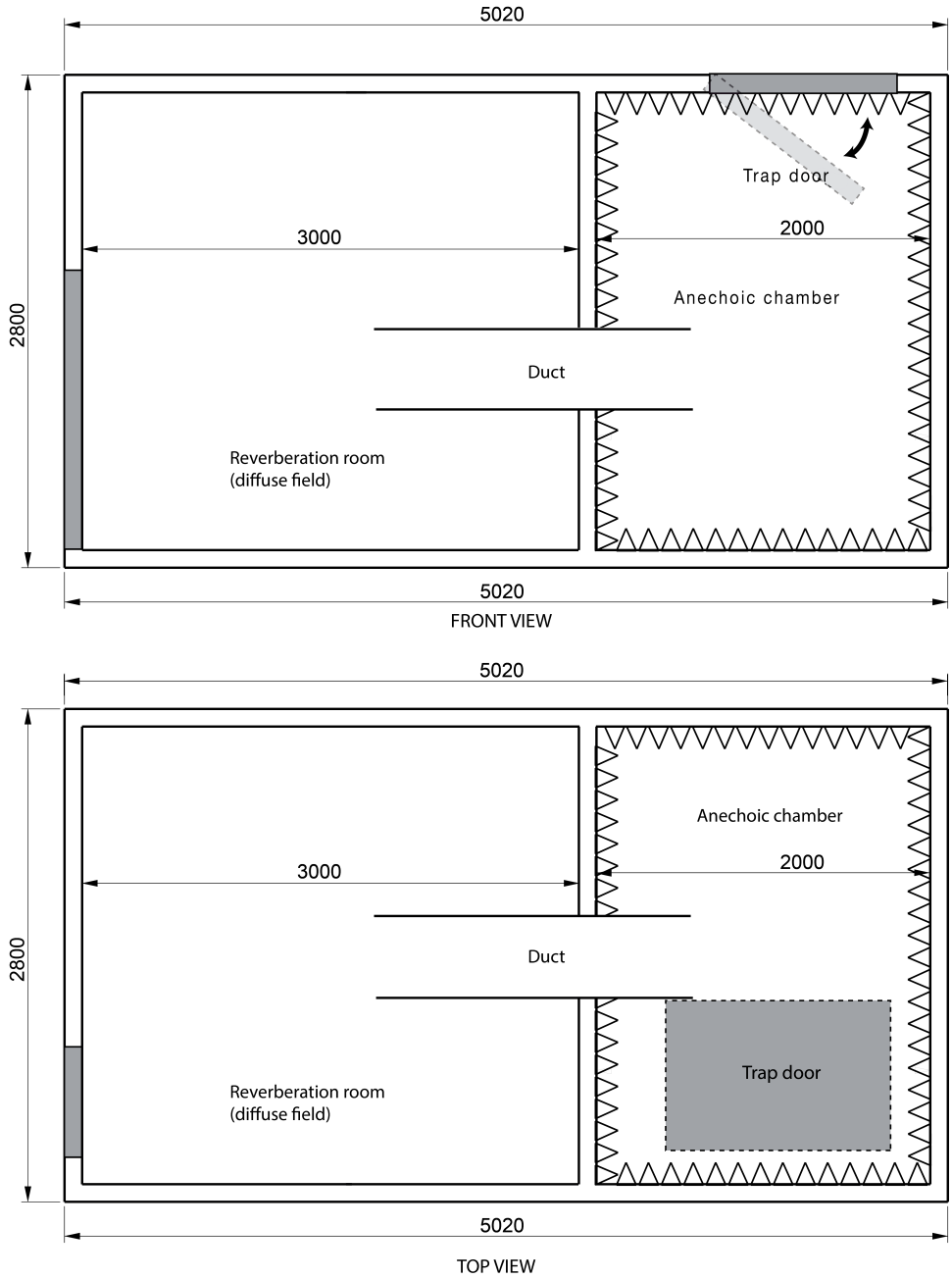

Figure 4.4: Side and Top view illustrations of the test rooms (all dimensions in mm).

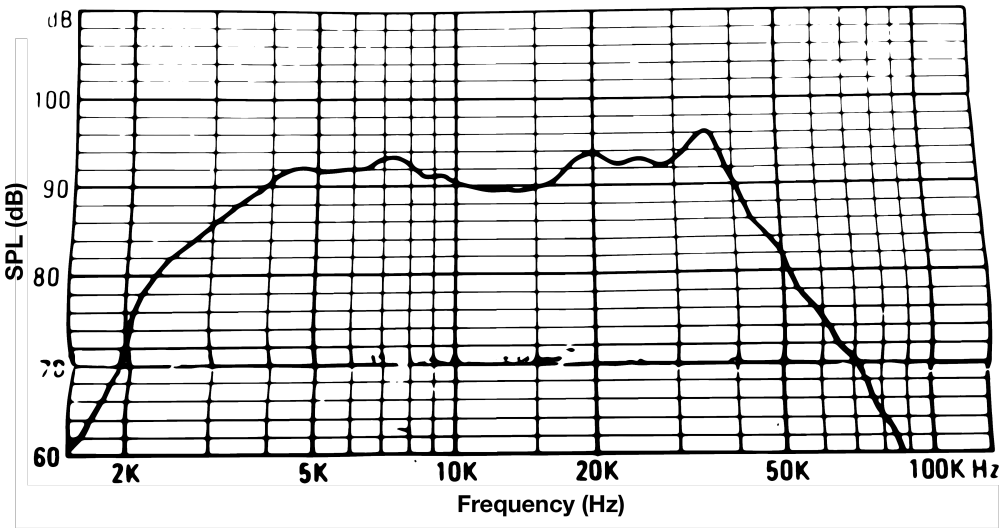

Figure 4.5: Frequency response curve for the REALISTIC 40-1377 tweeter.

The frequency response of this module is shown in Figure 4.5. The frequency response is fairly flat until around 35 kHz and starts to fall-off after that. The tweeter had an input impedance of 8 Ω ± 15% at 6000 Hz. An amplifier that can drive power up to 40 kHz was used. The power of the amplifier was rated at 185 W at 4 Ω. Note that the power output is not uniform at frequencies above 20, 000 Hz. Fluctuations in power output would blow up the tweeter if the output is beyond the maximum load that the tweeter can take. Therefore, fuses were used with the tweeters to prevent damage. The tweeters would also blow up if excited at low frequencies – therefore, a high-pass filter that filters sound signals below 6000 Hz was used. A FFT Network Analyzer SR770 by Stanford Research Systems was used to generate the white-noise signal. The SR770 can generate white noise from 100 Hz up to 100,000 Hz.

An array of eight tweeters was used to generate white noise in the source room. The tweeters were connected as four in parallel, in series with another four in parallel, to obtain an effective impedance of 4 Ω to conform to the amplifier's output impedance requirements for 185 W power output. Figure 4.6

Figure 4.6: Arrangement of tweeters in the source room.

shows the arrangement of the tweeters on the floor of the source room. Tweeters were used to generate noise only from 6000 Hz and above. For generating sound at lower frequencies, an omni-directional dodecahedron loudspeaker array was used, with a low-pass filter that cuts off at 6000 Hz.

A pair of Brüel & Kjaer Type 4135 1/4" free-field microphones was used to measure the Sound Pressure Levels on the source and receiver sides of the test duct. A free-field microphone is essentially designed to measure the sound pressure as it existed before the microphone was introduced into the sound field, compensating for capsule diffraction. The Type 4135 microphone has a relatively flat response up to around 80 kHz [2] as seen in Figure 4.7.

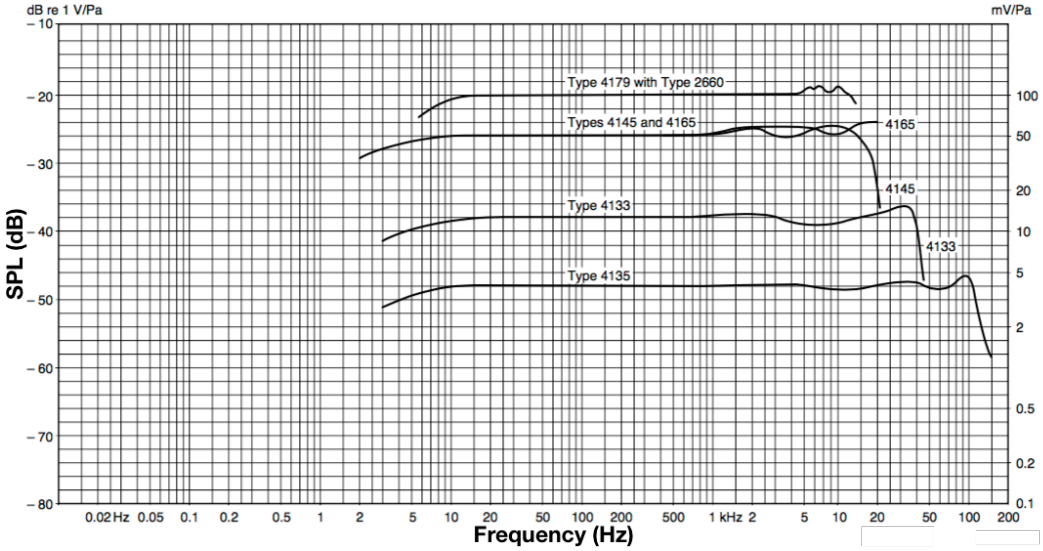

Figure 4.7: Free-field responses of different Brüel & Kjaer microphones [2].

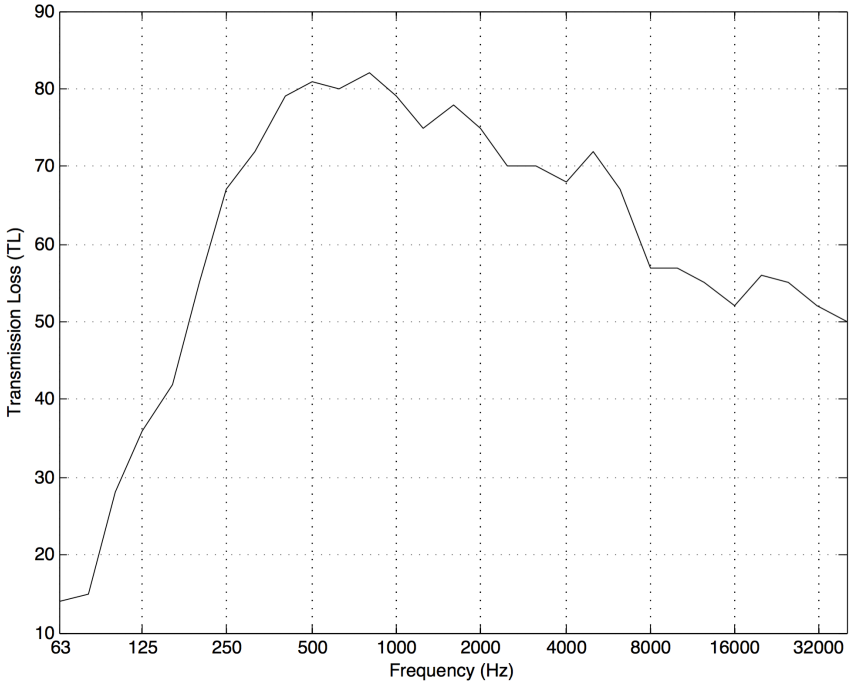

Figure 4.8: Measured flanking transmission loss between source and receiver rooms when the ventilator was blocked.

4.4.2 Sound-transmission measurement and flanking test

Initially, before the duct was inserted in the partition between the source and receiver rooms, the partition wall was completely blocked off. The flanking transmission loss between the rooms (through the partition and the ceiling) was measured in accordance with ASTM E90-09 to make sure that measured Insertion Losses of duct silencers do not included significant errors from flanking transmission. In theory, the flanking transmission should not affect the measurement of IL, since IL is independent of the background noise – however this is not true in reality, since the measurements with and without the silencing element (absorber liners and baffles) were taken at different times, involving slight differences in the arrangement. Figure 4.8 shows the measured variation of flanking transmission loss with frequency for the test facility partition when the ventilator was blocked. The transmission loss of the partition is sufficiently high – 68-82 dB from 250-6000 Hz. For measurements in a scale-model, frequencies lower than 250 Hz (31.5 Hz model-scale), are not of interest. For frequencies from 6000-40, 000 Hz, the minimum transmission loss is 50 dB. This is the upper limit on the silencer performance that could be measured. In practice, Insertion Losses above 40 dB are not generally observed for duct-silencers.

4.4.3 Duct insertion loss measurement

To measure the insertion loss of the duct, two 1/4" microphones were inserted inside the duct at an offset of 10% of duct-length, from the two ends of the duct. The microphones were inserted at an offset to minimize the effect of diffraction on the IL near the duct ends. The microphones were interfaced using preamplifiers, and connected to a SINUS Soundbook [43], a sound-measurement system for realtime data processing. For every set of measurements, the SPL was measured as a 16 sec average in one-third-octave bands from $125 - 40,000$ Hz (the maximum frequency that can be measured by the Soundbook), at three different locations along the breadth of the duct. Figure 4.9 shows the setup used for the

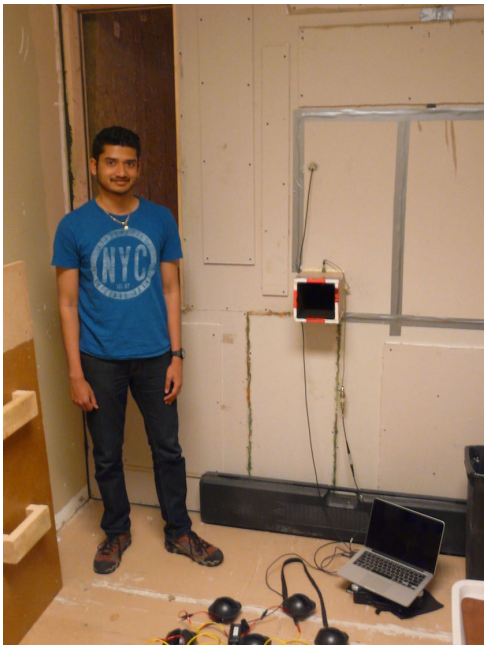

(a)

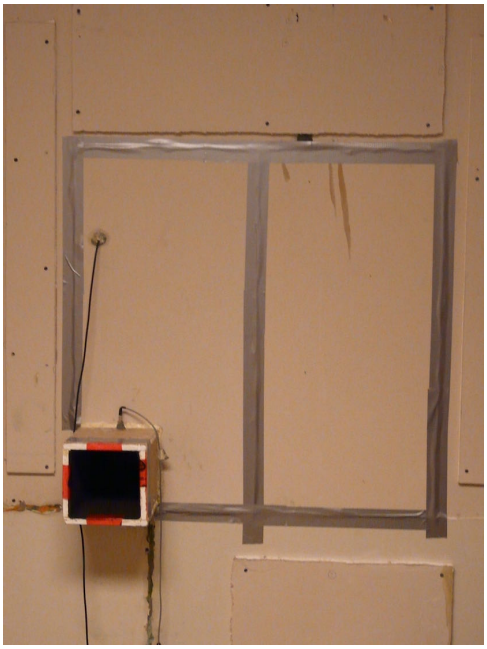

(b)

(c)

Figure 4.9: Acoustic measurement setup.

Table 4.1: Measured flow resistivities of different porous materials.

Material	Flow resistivity (Rayls/m)
Fibreglass	3, 398
Roxul	11, 696
Felt	58, 176
Sonoflex	7, 216

acoustic measurement. The insertion loss is defined in this study as:

$$IL = (SPL_{src,lined} - SPL_{rec,lined}) - (SPL_{src,unlined} - SPL_{rec,unlined}) \tag{4.4}$$

where $SPL_{src,lined}$ is the SPL measured inside the duct on the source side with absorbers installed, $SPL_{rec,lined}$ is the SPL measured inside the duct on the receiver side with absorbers installed, $SPL_{src,unlined}$ is the SPL measured inside the duct on the source side for an unlined duct, and $SPL_{rec,unlined}$ is the SPL measured inside the duct on the receiver side for an unlined duct. All measurements involved subtracting the background noise from the SPL at all microphone positions.

4.4.4 Flow-resistivity measurement

This section discusses the methodology that was used to measure the flow resistivity of absorber materials.

As was discussed in Chapter 2, the FEA simulation for acoustics in Comsol uses the Delany-Bazley model [19] to describe the impedance of a finite-thickness material. The Delany-Bazley model can be used to predict the normal-incidence absorption coefficient using flow resistivities derived from measurement. Flow-resistivities were measured using a flow-resistivity apparatus (FRA). Measured flow-resistivities were also used to determine the appropriate absorber material for scale-modelling. The FRA is based on the guidelines prescribed in Standard *C522-03* [44]. The flow-resistivity apparatus is used to characterize the relationships between the differential pressure in Pa and the airflow rate through the

sample of the absorber. By multiplying $\frac{\Delta p}{Q}$ by the surface area of the sample A_s, the specific airflow resistivity is given in Rayls (analogous to Pa.s/m). To determine the airflow resistivity in Rayls/m, the specific airflow resistivity is divided by the thickness of the test sample. The flow resistivity is defined as:

$$R_f = \frac{A_s \Delta p}{Qt} \tag{4.5}$$

where R_f is the flow resistivity, Δp is the pressure drop across the sample, Q is the airflow rate, A_s is the surface area of the sample and t is the thickness of the sample. The flow resistivities of the measured porous-absorber materials are listed in Table 4.1.

4.5 Flow-rate measurement setup

A blower door was used to characterize the flow in ducts. The pressure drop across the duct was measured as a function of airflow rate. A blower door is used to measure the air-leakage and the airflow across zones in buildings. Guidelines from Standard *E779* [45], which describes the test methods for determining airtightness of buildings using a blower door, were followed while performing the measurements. A blower door is used to pressurize or depressurize a building zone by blowing air in to or out of the building, using a calibrated, speed-controlled fan that can generate a range of airflows. The blower door induces pressure differences across the different building zones. The differences in pressure, along with the fan airflow rates, are used to determine the airflow performance and leakage across the building envelope. The fan flow rates are determined from the pressure differentials across the fan.

Air-tightness of the room is essential when performing the blower-door test for evaluating the airflow performance of the ventilator. Pressurizing the room would cause leakage from the ventilator, in addition to that from the other sources of leaks, such as cracks and holes. The amount of air leakage from such sources must be measured, and compensated for, in the flow-rate measurements. In order

to do this, blower-door tests are done with the ventilator blocked. The leakage airflow rates are measured for different pressure drops and subtracted from the ventilator airflow rates, at corresponding pressure drops.

Another method of measuring air leakage is the tracer-gas method. By this method, an inert gas is used to determine the air-exchange rate by measuring the change in concentration of the gas over time. This method works for low flow-rates, is non-intrusive and can be used in building environments in their natural state. The pressure drop is not generally measured by this method.

4.5.1 Airflow measurement method

A Retrotec Series 2000 [46] blower door was used to characterize airflow performance in this study. The blower fan is fitted into an aluminium frame that was mounted in the entrance door to the test-facility. A nylon cloth wrapped around the frame seals the entrance. Pressure taps were inserted on either side of the ventilator in the source and receiver rooms. The trap door in the receiver room was opened to the outside plenum, to equalize the pressure. The pressure taps from the room, as well as from the fan, were connected to a DM32 digital gauge that can measure pressure differences up to 0.1 Pa resolution. The maximum flows generated by blower-door fans depend on which range configuration (controlled through flow baffles) the fan has installed. Obtaining different flow ranges involves progressively constraining the opening on the fan from fully open to a small opening. The different ranges for the blower door are detailed in the user manual. The blower-door setup that was used is shown in Figure 4.10.

Pressurization testing was chosen over depressurization in this study. For different ranges of fan pressure, the room pressure (pressure difference between the source room and receiver room) was measured. The range configuration was chosen such that the fan pressure was greater than the room pressure. Moreover, for overlapping ranges, it was ensured that the fan power was greater than 10% of maximum load and less than 90% of maximum load. The fan speed was varied manually so that the flow rate was measured for pressure drops ranging from 1 to

Figure 4.10: Blower-door setup for airflow measurement.

50 Pa. The ventilator was sealed off initially to characterize the leakage. Then the measurements were repeated with the ventilator open. The leakage, measured in terms of airflow rate (m^3/s), was subtracted from the measured flow rate with the ventilator open, over the whole pressure-drop range. Re_o was also calculated, as an indication of the type of flow at the inlet of the duct.

It is important to note that, since a scale-model of the duct was tested, the performance would not be similar to the full-scale model for the same pressure drop or flow-velocity. The opening Reynolds number Re_o was kept constant, to scale the flow between the full-scale and scale-models. This was based on the assumption that, for the same Reynolds number, similar flow regimes would exist between the reduced-scale and full-scale models.

4.6 Duct test configurations

Different duct configurations, that are discussed in this section, were studied. The construction type and values of different parameters are discussed. In the following chapter, the results for different test configurations are discussed. The configuration names prescribed in this section are used to refer to them in future chapters.

When performing acoustic measurements, the microphones were inserted inside the duct at an offset of 10% of duct-length, at the two ends of the duct. Therefore, the length that was considered in the calculation of acoustic performance was reduced accordingly and scaled to match the duct-length used in airflow-performance calculations.

4.6.1 Configuration 1

For Configuration 1, a duct of scaled dimensions 0.15 m × 0.15 m cross-section and 0.8 m length was studied. This corresponds to full-scale dimensions of 0.6 m × 0.6 m cross-section and 3.2 m length.

Type *a* refers to the unlined duct. For Types *b*, *c*, *d* and *e*, a double layer of felt (6 mm thick) was used as the absorbent lining on all four surfaces. Type *b* has lining but no baffles. For Types *c*, *d*, *e* and *f*, felt was used as baffle inserts. However, the felt by itself was not sturdy, so it was faced with an acoustically-transparent wire mesh to increase stiffness. The thickness of the baffles was also kept at 6 mm. The position of the baffle was varied as follows: near the inlet of the duct (Type *c*), near the center (Type *d*), and near the outlet of the duct – with one baffle (Type *e*) and two baffles (Type *f*). Figures 4.11 to 4.16 illustrate the duct configurations for Configuration 1. A few of the configurations as built are shown in Figure 4.17.

While trying to insert more than one baffle into the duct, it was difficult to position the baffles precisely, due to the small size of the duct. For this reason only one configuration, with the baffle close to the inlet, was tested. The distortion of the baffle after inserting it in the centre of the duct is shown in Figure 4.18.

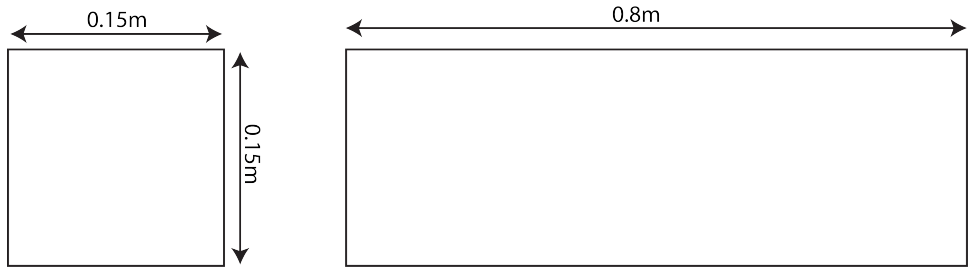

Figure 4.11: Configuration 1a of a square duct with no porous absorbers (front and top views).

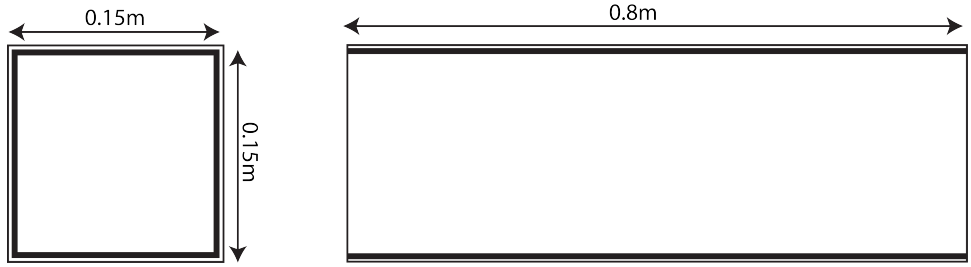

Figure 4.12: Configuration 1b of a square duct with felt lining (front and top views).

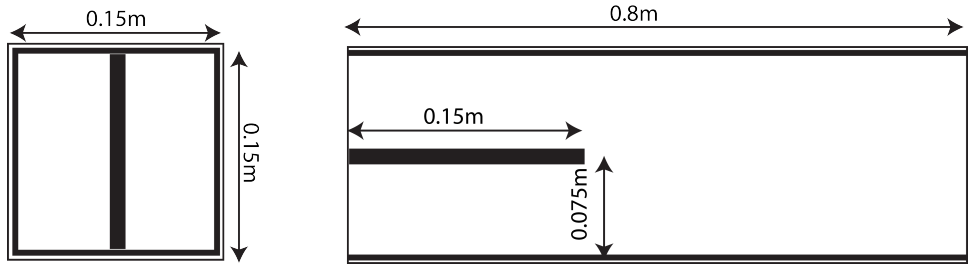

Figure 4.13: Configuration 1c of a square duct with felt lining and felt baffle near duct inlet (front and top views).

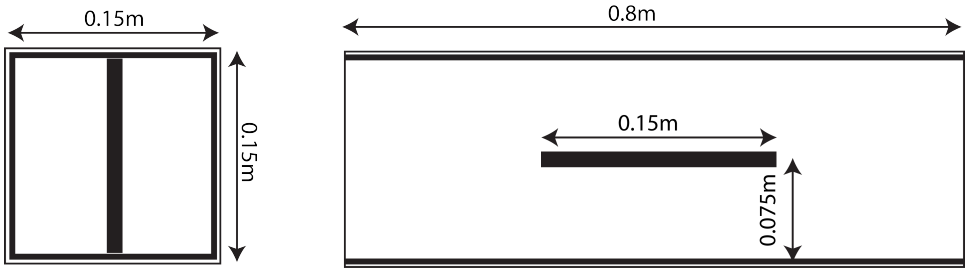

Figure 4.14: Configuration 1d of a square duct with felt lining and felt baffle near duct centre (front and top views).

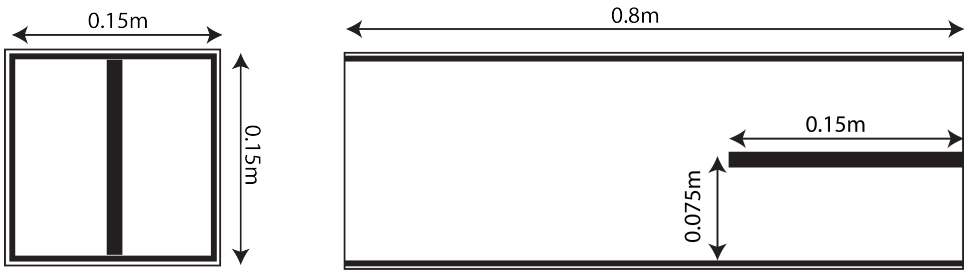

Figure 4.15: Configuration 1e of a square duct with felt lining and felt baffle near duct outlet (front and top views).

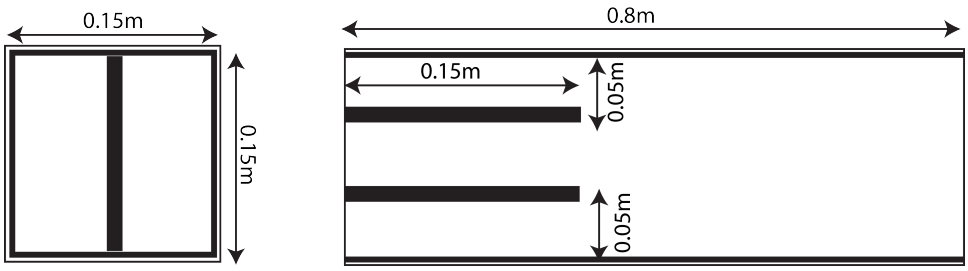

Figure 4.16: Configuration 1f of a square duct with felt lining and two felt baffles near duct inlet (front and top views).

(a) Configuration 1a showing an unlined duct.

(b) Configuration 1b showing a duct with felt lining.

(c) Configuration 1c showing a duct with felt lining and felt baffle near duct inlet.

(d) Configuration 1d showing a duct with felt lining and felt baffle near duct center.

Figure 4.17: Images of 1:4 scale-model ducts built in Configuration 1.

Figure 4.18: Distortion of the baffles when inserted in the duct.

4.6.2 Configuration 2

For Configuration 2, a rectangular duct of scaled dimensions 0.15 m × 0.075 m cross-section and 0.8 m length (full-scale dimensions 0.6 m × 0.3 m cross-section and 3.2 m length) was tested. Using the existing duct from Configuration 1, a styrofoam panel was inserted into the duct to reduce the width to half (0.075 m). The breadth was maintained at 0.15 m. The styrofoam-panel partition created a non-essential opening on one side which was filled with fibreglass and sealed with gypsum board and duct-tape to prevent acoustic flanking and airflow leakage through it. A styrofoam panel was preferred over gypsum board in this case, as the styrofoam panel could be snugly fit, to minimize leakage during airflow measurements.

Configuration 2 was interesting to test for acoustical performance, since the duct was lined on three sides (the fourth side being styrofoam). From the perspective of airflow, this configuration was designed to test airflow for a duct with cross-section of non square aspect ratio. Figures 4.19 and 4.20 illustrate the duct configurations for Configuration 2. The duct, as modified with the styrofoam partition, is shown in Figure 4.21.

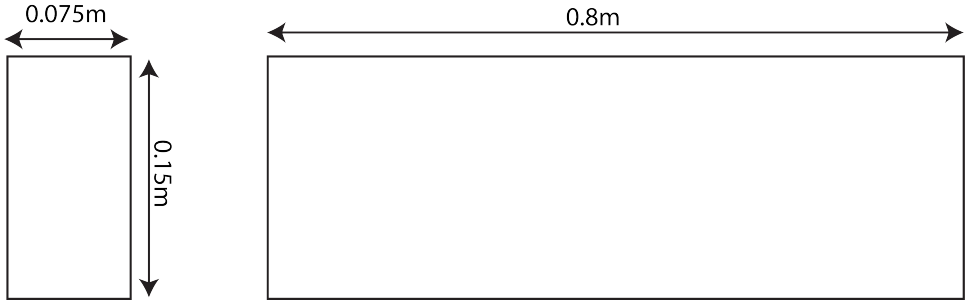

Figure 4.19: Configuration 2a of a rectangular duct with no porous absorbers (front and top views).

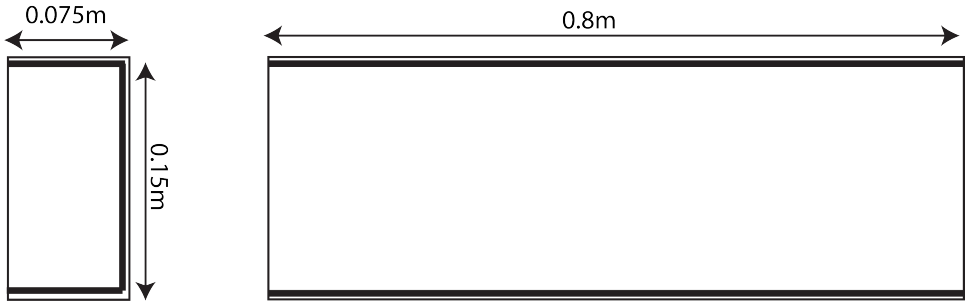

Figure 4.20: Configuration 2b of a rectangular duct with felt lining (front and top views).

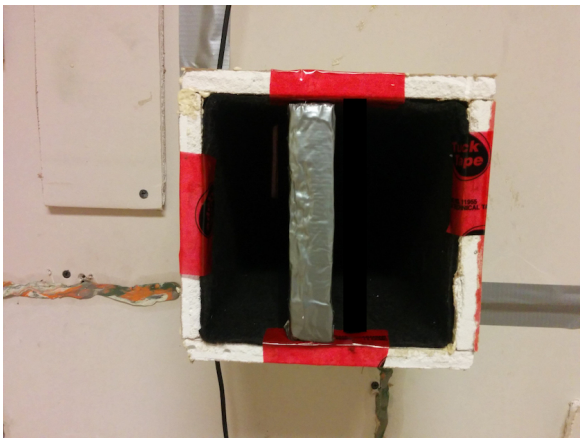

Figure 4.21: Configuration 2b – modified duct with styrofoam partition used for airflow prediction of a rectangular duct.

4.6.3 Configuration 3

For configuration 3, a duct of scaled dimensions 0.6 m × 0.6 m cross-section and 1.8 m length (full-scale dimension 2.4 m × 2.4 m cross-section and 7.2 m length) was studied. This configuration was intended to be a larger duct than Configuration 1. The length was restricted to 1.8 m due to the limitation in the size of the test rooms, For types *b*, *c*, *d* and *e*, panels of Sonoflex 12.5 mm thick were used as the absorbent lining on all four surfaces, and for baffle inserts. The Sonoflex typically came with a facing which was removed. As for Configuration 1, the position of the baffle was varied: near the inlet of the duct (Type *c*), near the centre of the duct (Type *d*), and near the outlet of the duct – with one baffle (Type *e*) and two baffles (Type *f*). Figures 4.22 to 4.27 illustrate the duct configurations for Configuration 3. A few of the configurations as built are shown in Figures 4.28 and 4.29.

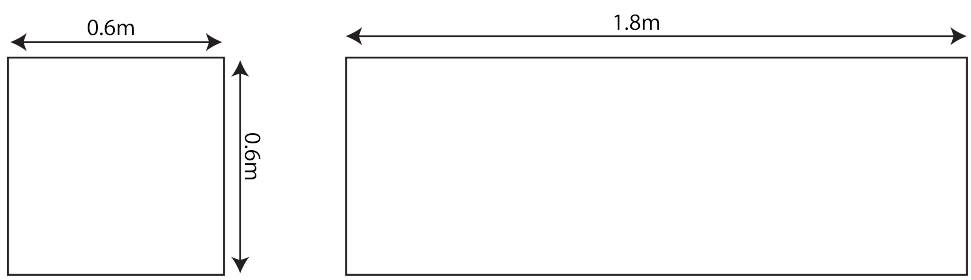

Figure 4.22: Configuration 3a of a square duct with no porous absorbers (front and top views).

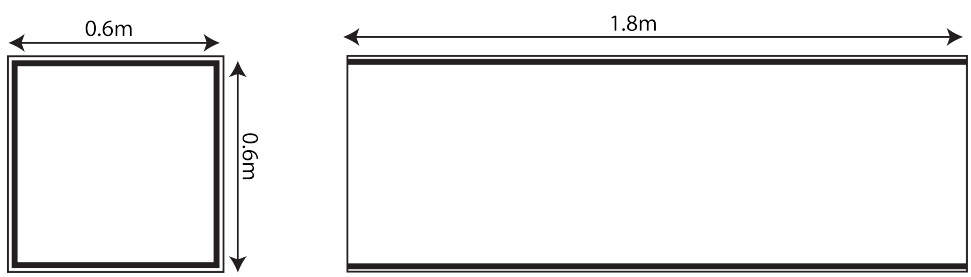

Figure 4.23: Configuration 3b of a square duct with Sonoflex lining (front and top views)

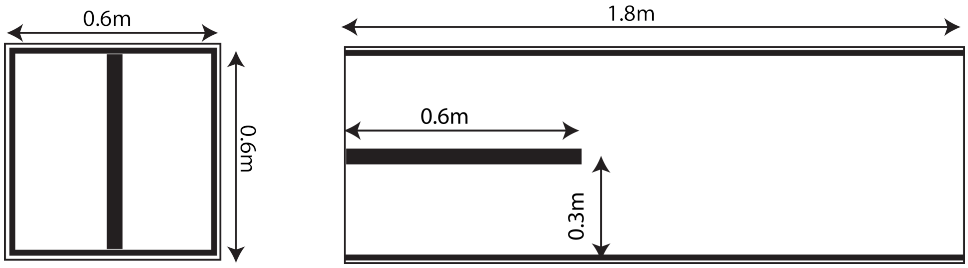

Figure 4.24: Configuration 3c of a square duct with Sonoflex lining and Sonoflex baffle near duct inlet (front and top views).

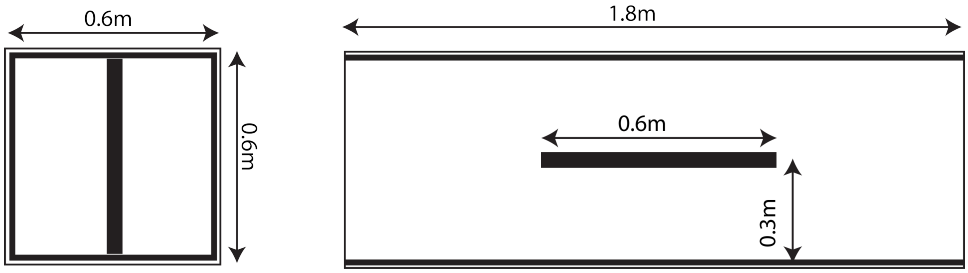

Figure 4.25: Configuration 3d of a square duct with Sonoflex lining and Sonoflex baffle near duct centre (front and top views).

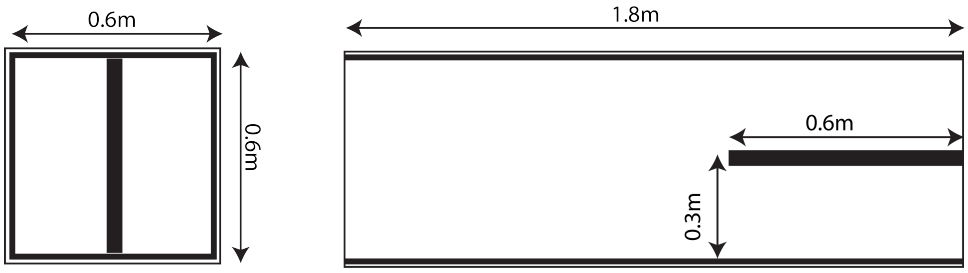

Figure 4.26: Configuration 3e of a square duct with Sonoflex lining and Sonoflex baffle near duct outlet (front and top views).

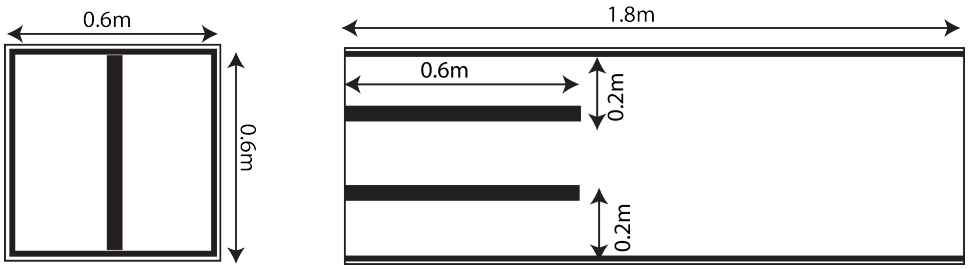

Figure 4.27: Configuration 3f of a square duct with Sonoflex lining and two Sonoflex baffles near duct inlet (front and top views).

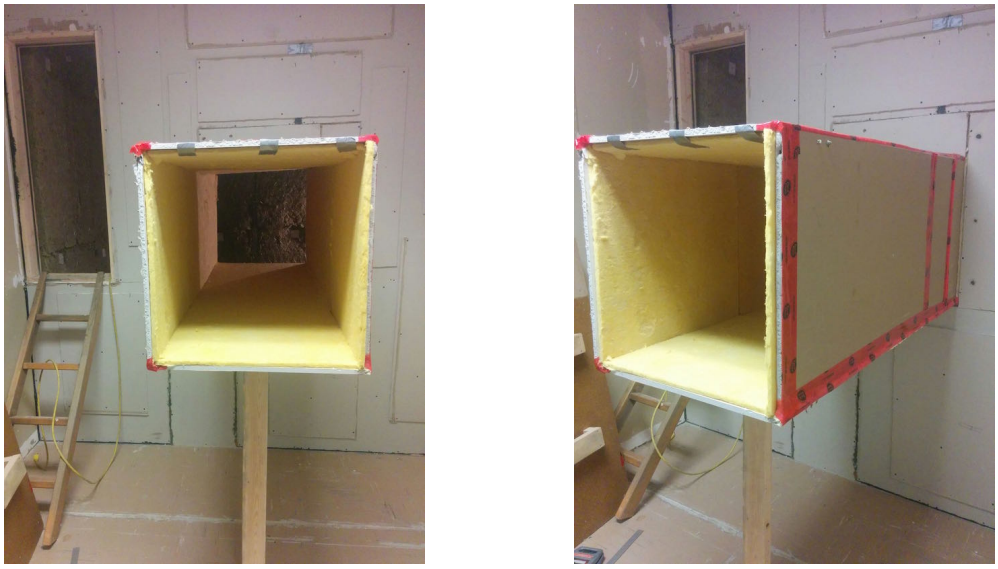

(a) **(b)**

Figure 4.28: Images of ducts built in Configuration 3 with Sonoflex lining.

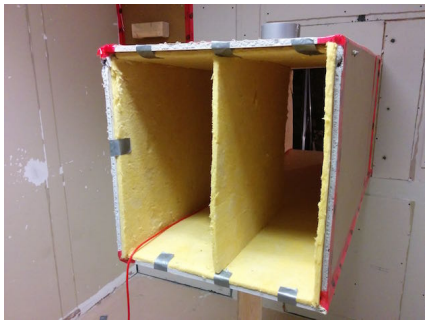

(a) Configuration 3c showing duct with Sonoflex lining and Sonoflex baffle insert near the inlet.

(b) Configuration 3b showing duct with Sonoflex lining and the acoustic measurement setup.

Figure 4.29: Images of ducts built in Configuration 3.

4.6.4 Configuration 4

For Configuration 4, a rectangular duct of scaled dimensions 0.6 m × 0.3 m cross section and 1.8 m length (full-scale dimensions- 2.4 m × 1.2 m cross section and 7.2 m length) was tested. For this configuration, the top gypsum panel was lowered and fixed. Similar to Configuration 3, Sonoflex was used to line the duct walls. For the baffles, however, six Sonoflex panels were used together (see Figure 4.35). The different types of Configuration 4 are shown in Figures 4.30 to 4.34. Figures 4.34 and 4.35 show Configuration 4 as built.

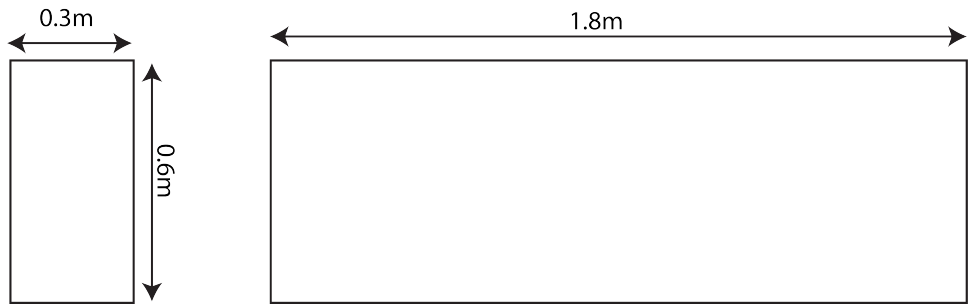

Figure 4.30: Configuration 4a of a rectangular duct with no porous absorbers (front and top views).

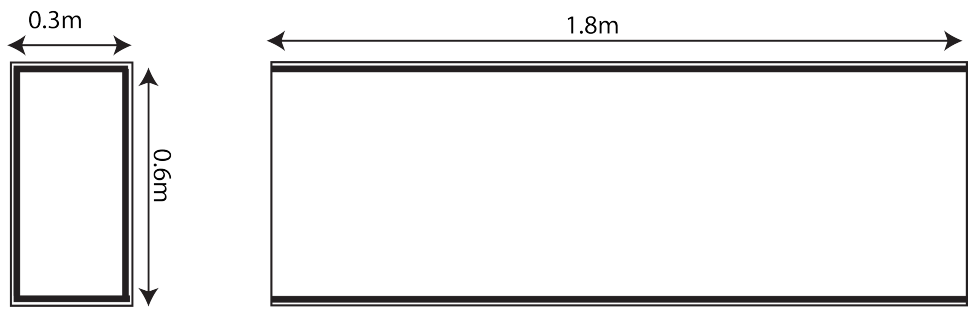

Figure 4.31: Configuration 4b of a rectangular duct with Sonoflex lining (front and top views)

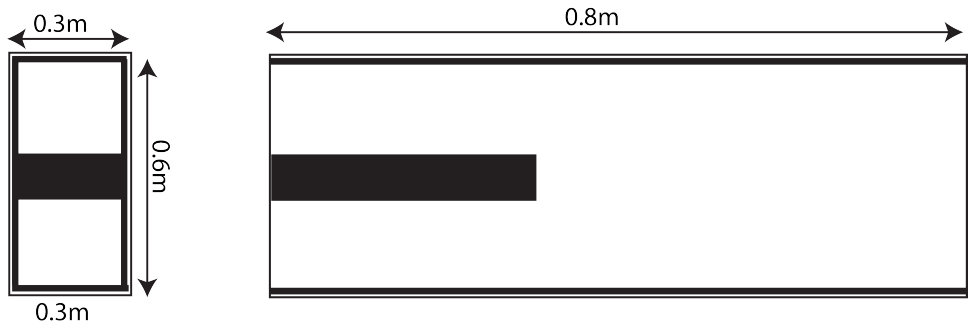

Figure 4.32: Configuration 4c of a rectangular duct with Sonoflex lining and Sonoflex baffle near duct inlet (front and top views).

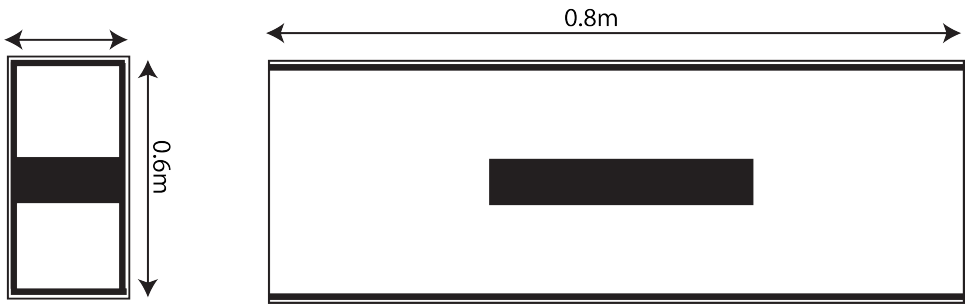

Figure 4.33: Configuration 4d of a rectangular duct with Sonoflex lining and Sonoflex baffle near duct centre (front and top views).

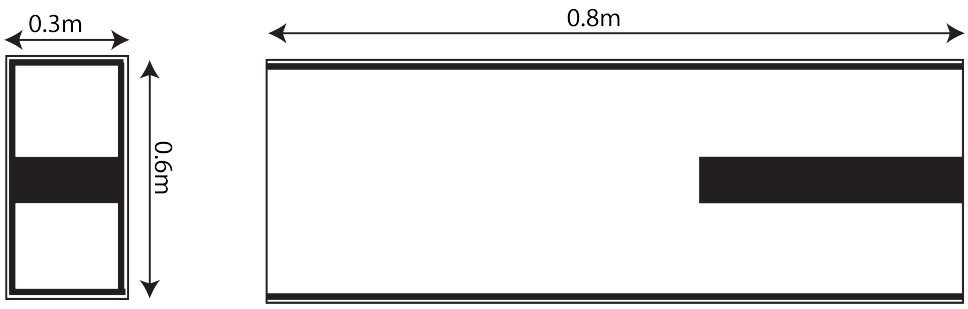

Figure 4.34: Configuration 4e of a rectangular duct with Sonoflex lining and Sonoflex baffle near duct outlet (front and top views).

(a) Configuration 4b showing rectangular duct with Sonoflex lining.

(b) Configuration 4c showing rectangular duct with Sonoflex lining and baffle made of 6 × Sonoflex panels.

Figure 4.35: Images of ducts built in Configuration 4.

4.6.5 Configuration 5

Configuration 5 was constructed to evaluate the effect of duct bends on the acoustic and airflow performance. To do this, the duct was constructed to terminate in a bend that exited in the receiver room. In this configuration, Sonoflex was used again as the lining material. For Configuration 5, a duct of scaled dimensions 0.6 m × 0.3 m cross-section with 1.8 m length before the bend and 0.6 m after the bend (full-scale dimensions 2.4 m × 1.2 m cross section with 7.2 m length before bend and 2.4 m after the bend) was tested. The configurations that were tested are shown in Figures 4.36 and 4.37. Images of the duct with bend, as built, are shown in Figure 4.38.

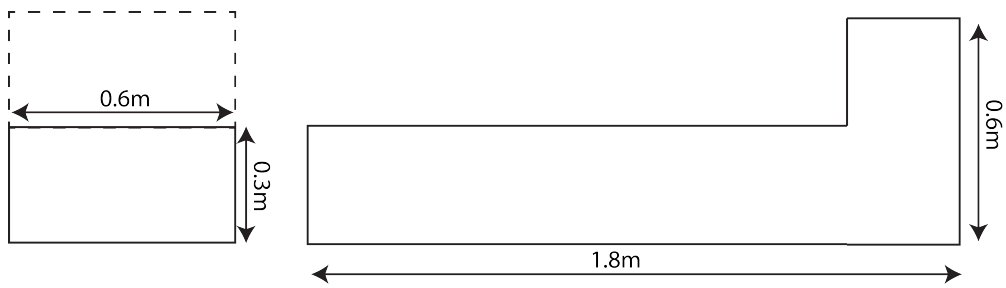

Figure 4.36: Configuration 5a of a rectangular duct with bend at termination with no porous absorbers (front and top view).

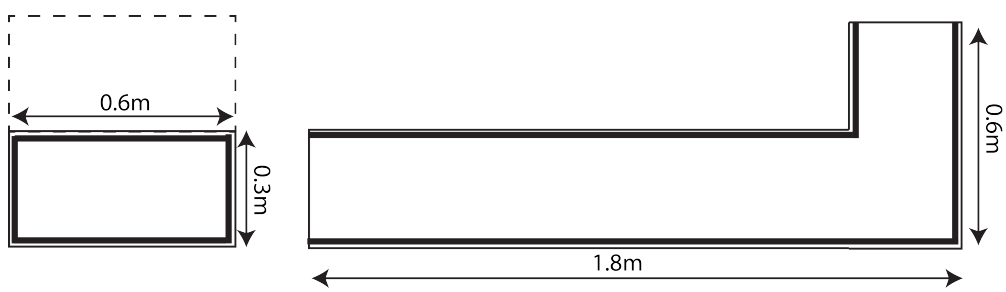

Figure 4.37: Configuration 5b of a rectangular duct with bend at termination with Sonoflex lining (front and top view).

(a)

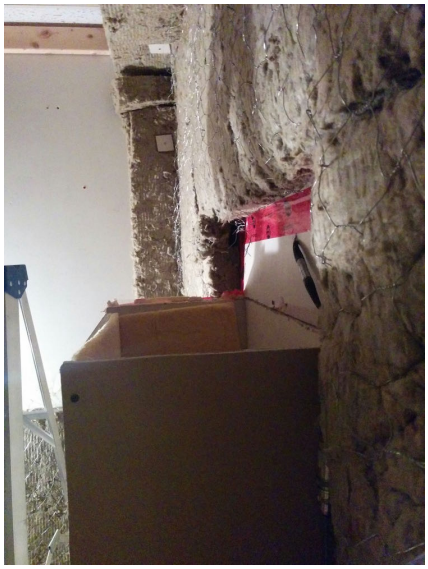

(b)

Figure 4.38: Images of ducts built in Configuration 5 showing bend at termination in the receiver room.

Chapter 5

Results and Discussion

This chapter discusses the results from surrogate-model predictions and compares them with predictions by theoretical relationships, FEA and results from experiments. Simple FE models were used for building the surrogate models. In this chapter, however, FE models that closely mimic the experimental setup were used, to cross-validate their predictions with results from scale-model experiments and the surrogate model. The next chapter discusses the conclusions drawn from the results and presents guidelines for optimal duct design.

5.1 Validation of surrogate models

The comparison of the surrogate models for sound and airflow with existing theoretical models is discussed in this section.

5.1.1 Validation of acoustic surrogate model using TMM

The Transfer Matrix Method [TMM] can be used to predict the Insertion Loss of a lined duct, for a plane-wave source approximation. The Insertion Loss predicted by the surrogate model was validating TMM for lined ducts in two configurations, as follows:

1. Duct dimensions $0.15\,\mathrm{m} \times 0.15\,\mathrm{m} \times 1\ \mathrm{m}$, lining thickness $0.00625\,\mathrm{m}$ and

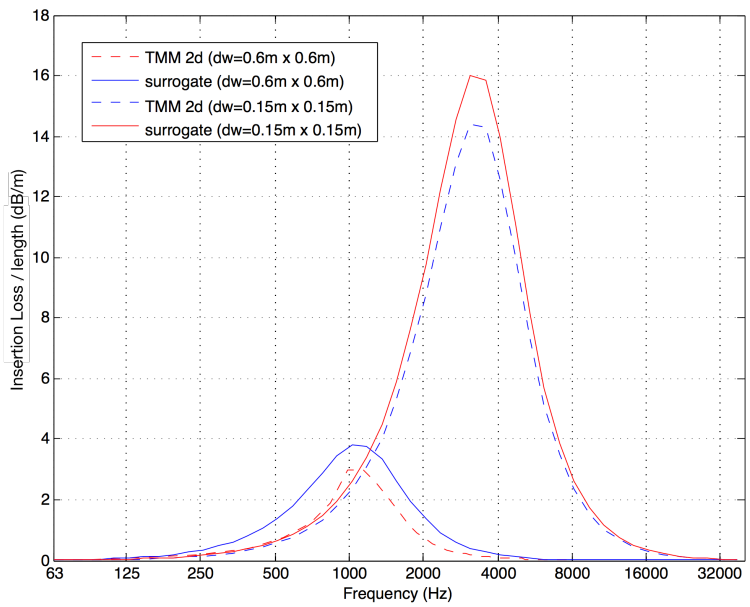

Figure 5.1: Comparison of Insertion Loss per unit length versus frequency predicted by the 2D surrogate model and the Transfer Matrix Method for two duct configurations.

R_f=58176 Rayls/m.

2. Duct dimensions 0.6 m × 0.6 m × 1 m, lining thickness 0.0125 m and R_f=7216 Rayls/m.

Results in Figure 5.1 show that the surrogate model is in good agreement with the TMM (within 2 dB). Although TMM is a 1D approximation of the wave equation, and is relatively quick to solve, the surrogate model in comparison takes only a fraction of the time to build and compute.

5.1.2 Comparison of airflow surrogate model with theoretical model

The theoretical relationships available for a sudden change in cross-section were discussed in Section 3.2.1. As shown in Section 3.2.1, there has been a long tra-

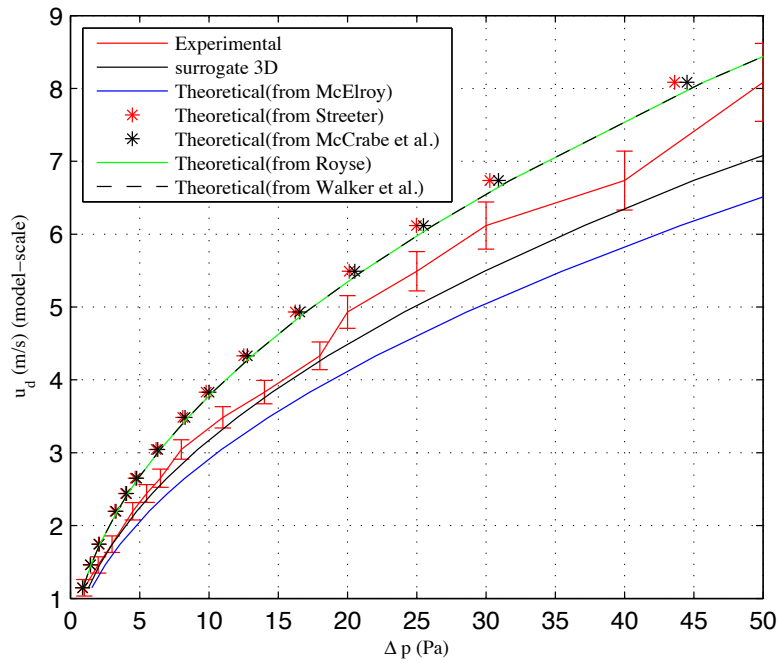

Figure 5.2: Comparison of predicted velocity at duct inlet vs. pressure drop, between 3D surrogate model, experiments and theoretical relationships with resistance coefficient K from various authors for duct dimensions $0.15\,\mathrm{m} \times 0.15\,\mathrm{m} \times 0.8\,\mathrm{m}$.

dition of modelling the pressure drop in ducts using a loss coefficient. This approach is often not accurate for short ducts. The pressure drop for the duct inserted between the source room and receiver room can be represented as the sum of the pressure drops due to a sudden contraction, the frictional loss due to flow through pipe, and the pressure drop due to sudden contraction. The theoretical relationships shown in Section 3.2.1, however, do not describe the pressure drop as a function of duct length. The surrogate model, in comparison, was able to predict a discharge coefficient close to 0.6 for a short duct, increasing with an increase in the length of the duct, up to 0.77 for long ducts.

The comparison of results from the experiment, the surrogate model and relationships from theoretical results shown in Figure 5.2. The theoretical relation-

ships shown in the plot make use of an empirical value of the resistance coefficient K for a sudden contraction, as suggested by various authors, due to the non-existence of simple relationships for determining the area of contraction A_c. As can be seen, most of the semi-empirical theoretical models, except for the relationship suggested by McElroy, overestimate the airflow as compared to results from experiments. The surrogate model, however, underestimates the airflow. There is better agreement between the surrogate model and experimental results at low pressure drops, but they quickly start to deviate for higher pressure drops, where the theoretical models seem to agree better.

5.2 Comparison between surrogate, experimental and FEA models

The predictions by the surrogate model are compared with results from experiments and FEA predictions for the various configurations listed in Section 4.6 in model-scale and full-scale dimensions, in the below section. In order to compare the performance of the configurations, performance metrics from [4] are used. The metrics include Specific equivalent open area for sound ($SEOA_s$), and Specific equivalent open area for airflow ($SEOA_f$) and $OAR \left(= \frac{SEOA_f}{SEOA_s}\right)$ as the single metric that combines airflow and acoustical performance. A brief description of the metrics can be found in Chapter 1.

5.2.1 Configuration 1

Configuration 1 – Type a:

Configuration 1a represents an unlined duct of cross-section 0.15 m × 0.15 m and length 0.8 m (refer to Figure 4.11). Since the duct was unlined, under the assumption of the duct walls being reflective, the Insertion Loss is very low. The sound pressure levels for the unlined duct were taken as the reference levels for the measurement of IL for all other duct configurations with silencing elements.

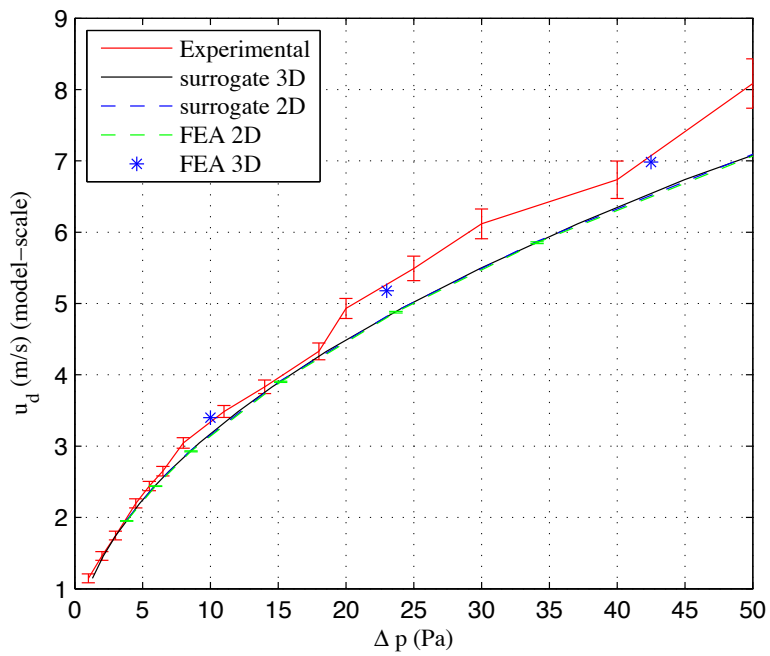

Figure 5.3: Comparison of predicted velocity at duct inlet vs. pressure drop, between 2D and 3D surrogate model, 2D and 3D FEA and experiments for Configuration 1a of the scale-model duct. For the full-scale model, u_d is scaled by a factor of 1.25.

Acoustics: N/A

Airflow: For *Configuration 1a* , results from the surrogate model were compared with results from scale-model experiments and FEA. Figure 5.3 compares the results from the 2D surrogate model, 3D surrogate model, 2D FEA, 3D FEA and experiments for the scale-model configuration. The surrogate models are based on results from 2D FEA for change in cross-section, as discussed in previous chapters. However, the results from 2D and 3D FEA models shown in Figure 5.3 are for domains that were modelled to closely mimic the experimental setup. It can be seen that the results from the surrogate model and FEA are in good agreement. The hydraulic diameter was used as the width of the duct for the 2D predictions from FEA and surrogate models. From the experimental results,

Table 5.1: Performance metrics for Configuration 1a.

(a) Specific equivalent open area for acoustics for Configuration 1a.

Method	$SEOA_s$
Experimental (3D)	1
Surrogate (3D)	1
FEA (3D)	1

(b) Flow metrics for Configuration 1a.

Method	C_d	$SEOA_f$	C	r
Experimental (3D)	0.82	1.34	0.02	0.51
Surrogate (3D)	0.77	1.26	–	–
FEA (2D)	0.77	1.26	–	–
Surrogate (2D)	0.77	1.27	–	–

(c) Open area ratio for Configuration 1a.

Method	OAR
Experimental (3D)	1.34
Surrogate (3D)	1.26

it quickly becomes apparent that there is good agreement with the surrogate models only at low pressure drops, with deviations at higher pressures. It was confirmed with predicted results from FEM that the predicted airflow from 2D and 3D FEA models differed by about 15%. In this study, 3D FEA was done only for a few configurations due to time constraints.

From Table 5.1b, the average C_d is seen to be higher for results from experiments, meaning the duct performed better in reality than as predicted by the surrogate model. The flow coefficient C and the exponent r (refer to Eq. (1.9)) are included in the table. For a fully turbulent flow, r can be taken to be 0.5. The r from experiments was found to be 0.51. The $SEOA_f$ is greater than 1 for the surrogate model – since the metric is normalized to the discharge coefficient for

Table 5.2: Performance metrics for Configuration 1b.

(a) Specific equivalent open area for acoustics for Configuration 1b.

Method	$SEOA_s$
Experimental (3D)	0.51
Surrogate (3D)	0.47
FEA (3D)	0.73

(b) Flow metrics for Configuration 1b.

Method	C_d	$SEOA_f$	C	r
Experimental (3D)	0.82	1.13	0.02	0.53
Surrogate (3D)	0.77	1.17	–	–
FEA (2D)	0.77	1.16	–	–
Surrogate (2D)	0.78	1.16	–	–

(c) Open area ratio for Configuration 1b.

Method	OAR
Experimental (3D)	2.22
Surrogate (3D)	2.49

a short aperture ($C_d = 0.61$), the duct has better flow performance than a short aperture.

Open Area Ratio: The OAR for this configuration is shown in Table 5.1c. The OAR is low for an unlined duct, due to the poor acoustical performance.

Configuration 1 – Type b:

Configuration 1b elucidates the effect of the addition of duct lining on the performance of the duct. As shown in Figure 4.12, felt of thickness 0.00625 m was used to line the duct.

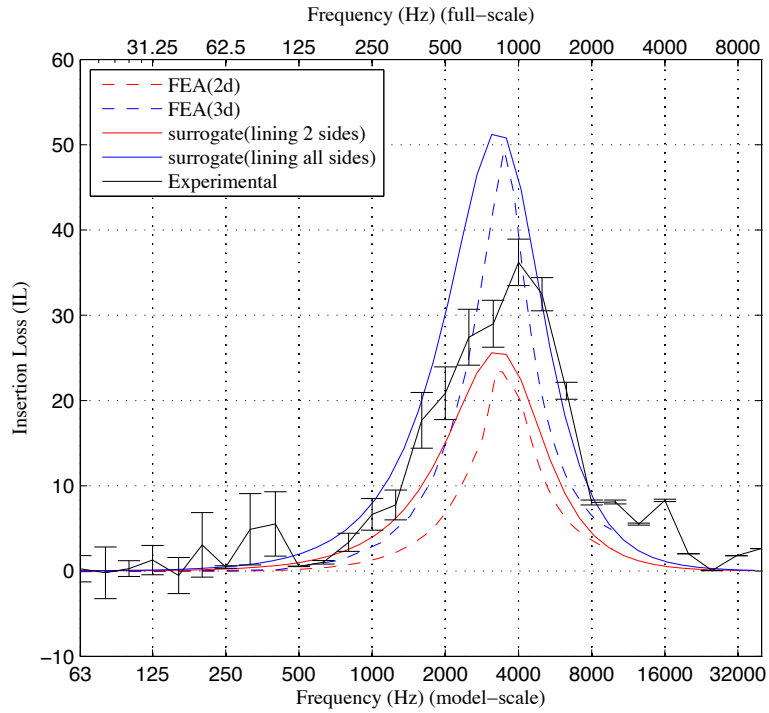

Figure 5.4: Comparison of Insertion Loss vs. frequency between surrogate and FEA predictions, and experiments for Configuration 1b.

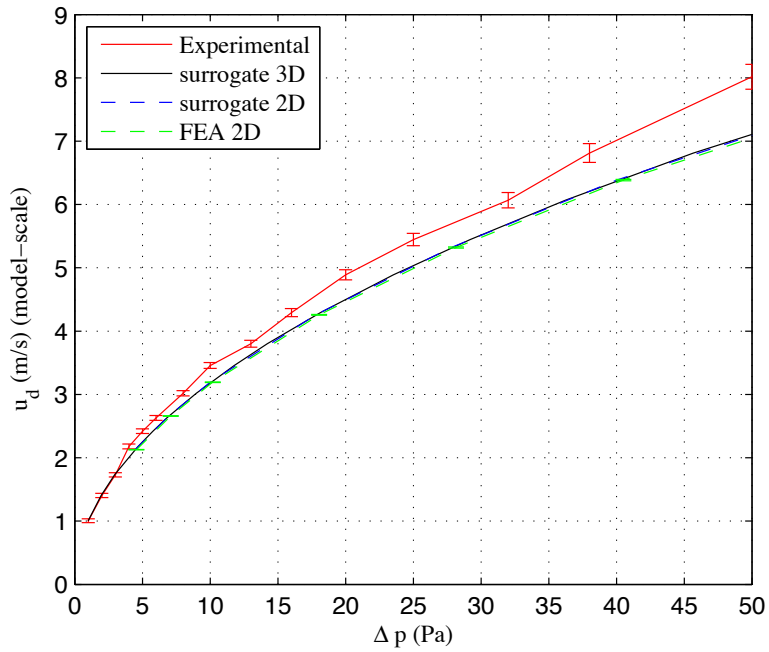

Figure 5.5: Comparison of predicted velocity at duct inlet vs. pressure drop, between 2D and 3D surrogate model, 2D FEA and experiments for Configuration 1b of the scale-model duct. For the full-scale model, u_d is scaled by a factor of 1.27.

Acoustics: The comparison of the Insertion Losses predicted by 2D and 3D FEA models, the surrogate model with lining on two and four sides, and from experiments, are shown in Figure 5.4.

The 3D FEA model closely mimics the duct configuration that was used in the experiments. The IL for the surrogate model of the duct with lining on two opposite sides is found to have a 0.5-times scaled-down values of the IL from 3D FEM for a duct with lining on all sides – this is in agreement with the hypothesis (refer to Chapter 1) of using 2D models to build 3D surrogate models. In other words, the 2D FEA model for a duct with lining on all sides, predicts the IL to be 50% lower than the model from 3D FEA.

The magnitude of the peak in the IL curve, and the frequency band in which it occurs, match closely between the FEA and surrogate models – although the decrease of the IL curve above the peak frequency is more gradual for the surrogate. Comparison with the experimental results show good agreement for the location of the peak in the frequency spectrum. Insertion Losses are typically less than 40 dB in reality, for silencers. It is therefore acceptable that the peak IL is off by around 10 dB. It is, however, surprising that the higher-order modes have mush less effect on the IL, despite being outside the plane-wave cutoff window. It is unclear why the IL is very low between 8000 Hz and 32000 Hz model scale, since absorbers generally tend to attenuate high frequencies quite well. For evaluating the IL of the full-scale model, the frequency can be scaled down by the scale-factor (4 times), as shown in Figure 5.4.

Table 5.2a compares the $SEOA_s$ between the surrogate model, FEA and experiments. The lower is the value of $SEOA_s$, the better is the acoustical performance. Although the $SEOA_s$ from experiments and the surrogate model match well, and that for FEA is quite different in comparison, it would be wrong to assume that the surrogate model correlates better with experimental results than results from the FEA model.

Airflow: Except for the addition of a lining that reduces the cross-sectional area of the duct, *Configuration 1b* is similar to *Configuration 1a*. Figure 5.5 compares the airflow performance of the surrogate and FEA models with experimental results for *Configuration 1b*. Similar to *Configuration 1a*, experimental results show higher values of airflow rate than the FEA and the surrogate model predictions at higher pressure drops. Again, there is good agreement between FEA and the surrogate model. When compared to *Configuration 1a*, the airflow rate is lower than expected, due to the reduction in the duct inlet area.

Open Area Ratio: The *OAR*s from the acoustics and airflow performance are shown in Table 5.2c, and can be seen to be higher than *Configuration 1a*.

Configuration 1 – Type c:

Configuration 1c elucidates the effect of the inclusion of a baffle of thickness 0.00625 m to *Configuration 1b*. The baffle was inserted near the inlet of the duct, as shown in Figure 4.13. *Configurations 1c, 1d* and *1e* represent the positions of baffle near the inlet, middle and outlet of the duct, respectively. For these three configurations, the Insertion Losses are similar. For this reason, Figure 5.6 can be taken to be representative of all the three configurations.

Acoustics: From Figure 5.6, it can be seen that the addition of baffle increases the Insertion Loss in the 8000 Hz band model scale. The second peak is quite prominent in the FEA predictions but appears only as a slight bulge in the surrogate model peak predictions. The predicted results from the surrogate and FEA models for *Configuration 1b* are also included in the figure to show the effect of the baffle clearly. Modular building of the surrogate model is able to correctly predict the position of the peak, though the drop-off of the *IL* curve above the peak frequency is more gradual for the surrogates. The experimental result does not have a prominent second peak, but there is a slight increase in the *IL* near 6000 Hz model scale. The sound metrics are shown in Table 5.3a.

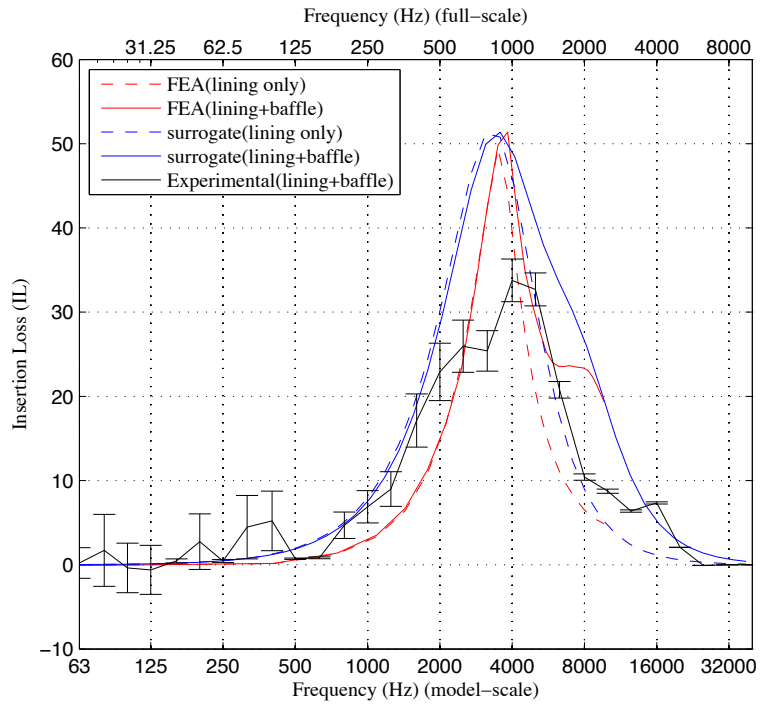

Figure 5.6: Comparison of Insertion Loss vs. frequency between surrogate and FEA predictions, and experiments for Configuration 1c, 1d and 1e.

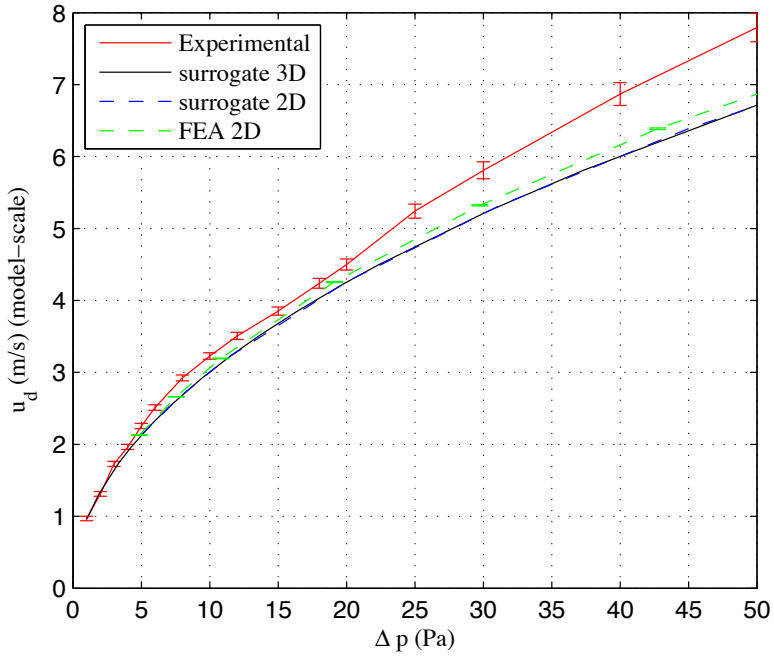

Figure 5.7: Comparison of predicted velocity at duct inlet vs. pressure drop, between 2D and 3D surrogate model, 2D FEA and experiments for Configuration 1c of the scale-model duct. For the full-scale model, u_d is scaled by a factor of 1.24.

Table 5.3: Performance metrics for Configuration 1c.

(a) Specific equivalent open area for acoustics for Configuration 1c.

Method	$SEOA_s$
Experimental (3D)	0.5
Surrogate (3D)	0.49
FEA (3D)	0.72

(b) Flow metrics for Configuration 1c.

Method	C_d	$SEOA_f$	C	r
Experimental (3D)	0.78	1.08	0.02	0.53
Surrogate (3D)	0.73	1.01	–	–
FEA (2D)	0.75	1.12	–	–
Surrogate (2D)	0.73	1.10	–	–

(c) Open area ratio for Configuration 1c.

Method	OAR
Experimental (3D)	2.16
Surrogate (3D)	2.06

Airflow: For *Configuration 1c*, the addition of the baffles was approximated as a change in cross-section of the duct. For this reason, it can be seen from Figure 5.7 that the results from the surrogate model deviate slightly from the FEA 2D model. The difference between the predicted and measured airflow rates is higher than for *Configurations 1a* and *1b*. Even the 2D FEA model has a higher disagreement with the measured airflow rate. The reason for this difference is the use of a hydraulic diameter to describe both the duct and the baffles – the flow characteristics are altered by doing this. In this situation, the assumption made for the surrogate model, to describe the insertion of a baffle as a change in cross-section, is not necessarily a less accurate model than the 2D FEA predictions. It is difficult to evaluate the maximum error associated with such an

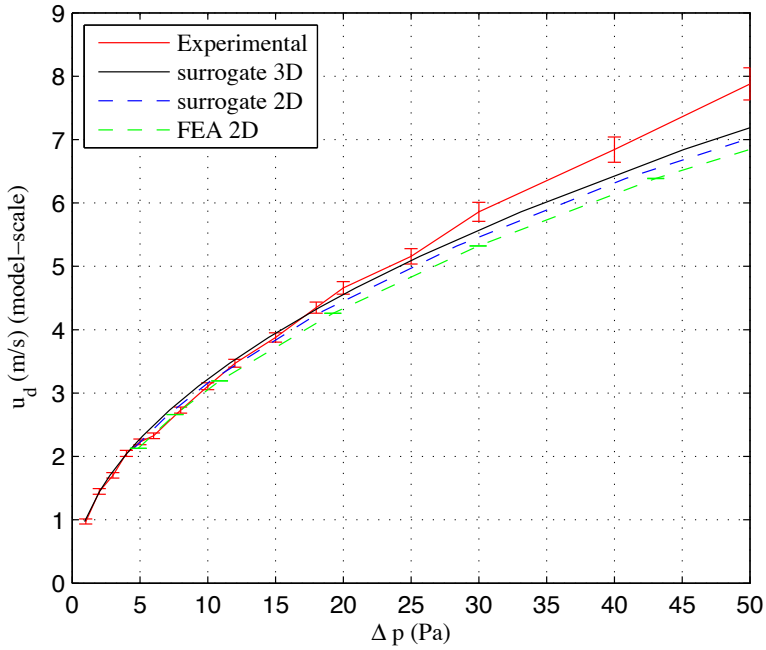

Figure 5.8: Comparison of predicted velocity at duct inlet vs. pressure drop, between 2D and 3D surrogate model, 2D FEA and experiments for Configuration 1d of the scale-model duct. For the full-scale model, u_d is scaled by a factor of 0.98.

assumption, without comparing the results between the actual and approximate models for the entire dataset. The flow metrics for this configuration are shown in Table 5.3b.

Open Area Ratio: From Table 5.3c it can be seen that the *OAR* is lower in comparison to a duct with lining only.

Configuration 1 – Type d:

Configuration 1d considers the performance of the duct with lining and baffle inserted in the centre of the duct (refer to Figure 4.14).

Acoustics: Refer to Section 5.2.1.

Table 5.4: Performance metrics for Configuration 1d.

(a) Specific equivalent open area for acoustics for Configuration 1d.

Method	$SEOA_s$
Experimental (3D)	0.5
Surrogate (3D)	0.49
FEA (3D)	0.72

(b) Flow metrics for Configuration 1d.

Method	C_d	$SEOA_f$	C	r
Experimental (3D)	0.78	1.08	0.02	0.53
Surrogate (3D)	0.78	1.08	–	–
FEA (2D)	0.74	1.12	–	–
Surrogate (2D)	0.77	1.15	–	–

(c) Open area ratio for Configuration 1d.

Method	OAR
Experimental (3D)	2.16
Surrogate (3D)	2.20

Airflow: For *Configuration 1d*, Figure 5.8 compares the airflow performance from the surrogate and FEA models with experimental results. On comparison to *Configuration 1c*, there is no evidence of a change in airflow performance between the two configurations, from the experimental results. However the surrogate model suggests a marginal improvement in airflow performance for *Configuration 1d*. The 3D surrogate model appears to be in better agreement with the results from experiments than 2D FEA. The $SEOA_f$ is also comparatively better than *Configuration 1c* from experiments.

Open Area Ratio: Comparing the *OAR* with that of *Configuration 1c*, the *OAR* from experiments appear to be the same for both configurations. However the

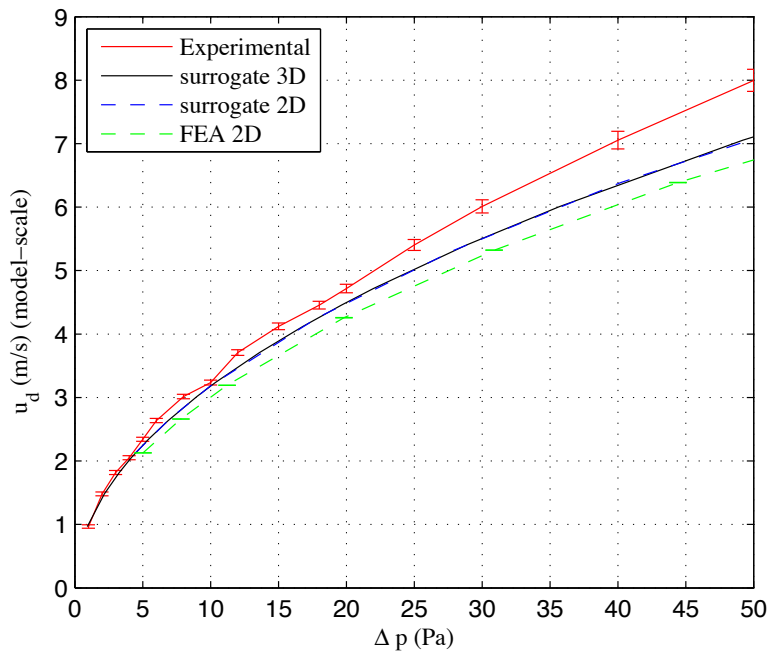

Figure 5.9: Comparison of predicted velocity at duct inlet vs. pressure drop, between 2D and 3D surrogate model, 2D FEA and experiments for Configuration 1e of the scale-model duct. For the full-scale model, u_d is scaled by a factor of 1.3212.

surrogate model suggests better performance for *Configuration 1d*.

Configuration 1 – Type e:

Configuration 1e considers the performance of the duct with lining and baffle inserted near the outlet of the duct (refer to Figure 4.15).

Acoustics: Refer to Section 5.2.1

Airflow: In *Configuration 1e*, the baffle is inserted near the outlet of the duct. From Figure 5.9, it can be seen that the 3D surrogate model matches the results from experiments quite well at low pressure drops. In comparison to *Configurations 1c* and *1d*, there is marginal improvement in the airflow performance. This

Table 5.5: Performance metrics for Configuration 1e.

(a) Specific equivalent open area for acoustics for Configuration 1e.

Method	$SEOA_s$
Experimental (3D)	0.5
Surrogate (3D)	0.49
FEA (3D)	0.72

(b) Flow metrics for Configuration 1e.

Method	C_d	$SEOA_f$	C	r
Experimental (3D)	0.81	1.12	0.02	0.53
Surrogate (3D)	0.77	1.06	–	–
FEA (2D)	0.73	1.10	–	–
Surrogate (2D)	0.77	1.16	–	–

(c) Open area ratio for Configuration 1e.

Method	OAR
Experimental (3D)	2.24
Surrogate (3D)	2.16

could be attributed to the placement of the baffles away from the formation of the vena-contracta near the duct inlet.

Open Area Ratio: In comparison to *Configurations 1c* and *1e*, there is a modest improvement in the OAR – when compared to the results from experiments and the surrogate model.

Configuration 1 – Type f:

Configuration 1f represented a duct with lining and two equi-spaced baffles parallel to the opening of the duct, close to the inlet (refer to Figure 4.16).

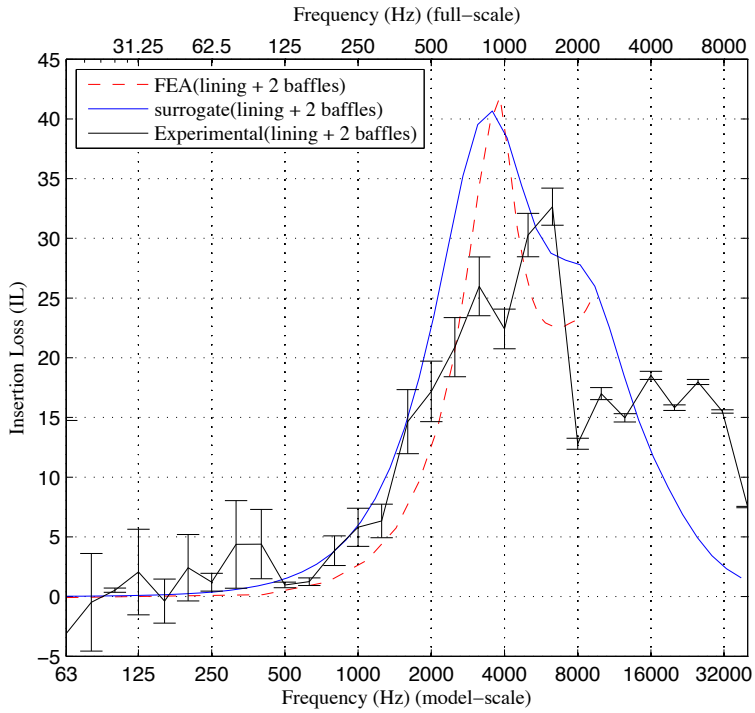

Figure 5.10: Comparison of Insertion Loss vs. frequency between surrogate and FEA predictions, and experiments for Configuration 1f.

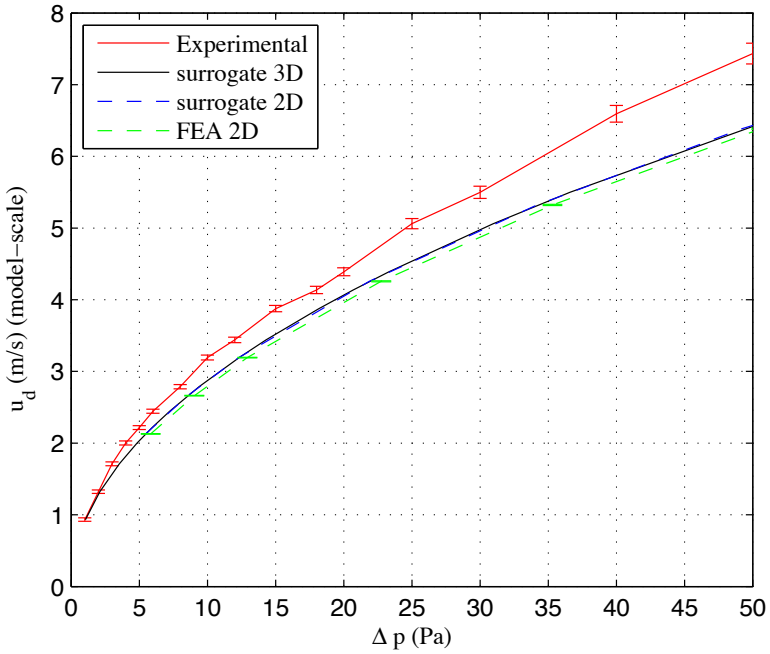

Figure 5.11: Comparison of predicted velocity at duct inlet vs. pressure drop, between 2D and 3D surrogate model, 2D FEA and experiments for Configuration 1f of the scale-model duct. For the full-scale model, u_d is scaled by a factor of 1.21.

Table 5.6: Performance metrics for Configuration 1f.

(a) Specific equivalent open area for acoustics for Configuration 1f.

Method	$SEOA_s$
Experimental (3D)	0.5
Surrogate (3D)	0.54
FEA (3D)	0.74

(b) Flow metrics for Configuration 1f.

Method	C_d	$SEOA_f$	C	r
Experimental (3D)	0.76	1.05	0.02	0.52
Surrogate (3D)	0.70	0.96	–	–
FEA (2D)	0.68	1.03	–	–
Surrogate (2D)	0.70	1.05	–	–

(c) Open area ratio for Configuration 1f.

Method	OAR
Experimental (3D)	2.10
Surrogate (3D)	1.77

Acoustics: Figure 5.10 shows the comparison of IL between the surrogate models, FEA models and experiments for *Configuration 1f*. The addition of two baffles improves the IL of the duct at around $8000 - 12000$ Hz model scale for the surrogate model. For the range of frequency that was predicted for 3D FEA, the peak appears to occur at a higher frequency than that predicted by the surrogate model. The experiments produce a slightly different pattern of the peaks and, interestingly, create multiple peaks at 12000 Hz, 16000 Hz and 24000 Hz model scale that are not predicted by the surrogate and FEA models.

Airflow: The airflow predictions for a duct with two baffles follow a similar trend as to what was described for *Configuration 1c* (refer Figure 5.11). There is a drop

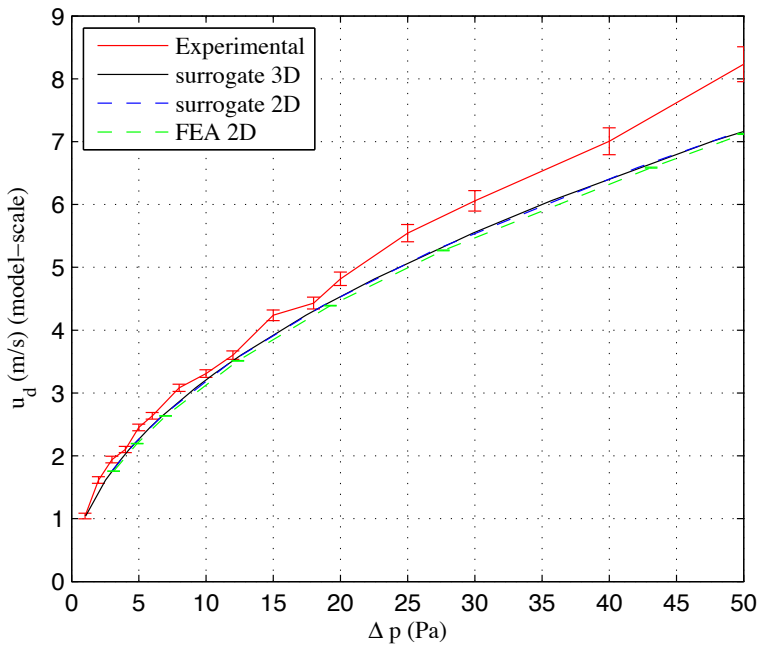

Figure 5.12: Comparison of predicted velocity at duct inlet vs. pressure drop, between 2D and 3D surrogate model, 2D FEA and experiments for Configuration 2a of the scale-model duct. For the full-scale model, u_d is scaled by a factor of 1.32.

in airflow performance by adding an addition baffle near the duct inlet.

Open Area Ratio: The *OAR* for this configuration is shown in Table 5.6c. As can be seen, the *OAR* is lower for *Configuration 1f* than for *Configuration 1e*.

5.2.2 Configuration 2

Configuration 2 was created to study the effect of making the cross-section of the duct rectangular on the acoustical and airflow performance of the duct. *Configuration 2* represents a duct of cross-sectional dimensions 0.15 m × 0.075 m and length 0.8 m.

Configuration 2 – Type a:

Configuration 2a represents an unlined, rectangular duct (refer to Figure 4.19). As for *Configuration 1*, the sound-pressure levels from *Configuration 2a* were used as the reference levels for the rest of the configurations of *Configuration 2*.

Acoustics: N/A

Airflow: The airflow performance for *Configuration 2a* is shown in Figure 5.12. From the figure, it can be seen that the velocity at the duct inlet is almost the same as for *Configuration 1a*. This means that the airflow would be 50% of what can be observed in *Configuration 1a*. The surrogate models are in close agreement with the 2D and 3D FEA models. The average discharge coefficient C_d shown in Table 5.7b is close to that for *Configuration 1a*, for the 3D surrogate model and results from experiments. However, the 2D FEA and surrogate models show a different discharge coefficient, due to the use of the hydraulic diameter. This was not an issue for *Configuration 1a* since the hydraulic diameter was equal to the width of the duct.

Open Area Ratio: The *OAR*, shown in Table 5.7c, is marginally higher than that for *Configuration 1a*.

Configuration 2 – Type b:

Configuration 2b represents a duct of cross-section 0.15 m × 0.075 m with lining on three sides. This was done by adding a styrofoam insert in the middle of the duct lined with felt (*Configuration 2a*) (refer to Figure 4.20).

Acoustics: The FEA and surrogate models predict a single peak at around 3000 Hz (model scale). The measured Insertion Loss has a peak at around 2500 Hz (model scale) and a second peak at around 12000 Hz (model scale). Considering the 3D surrogate model as a combination of two 2D models, one of width w having lin-

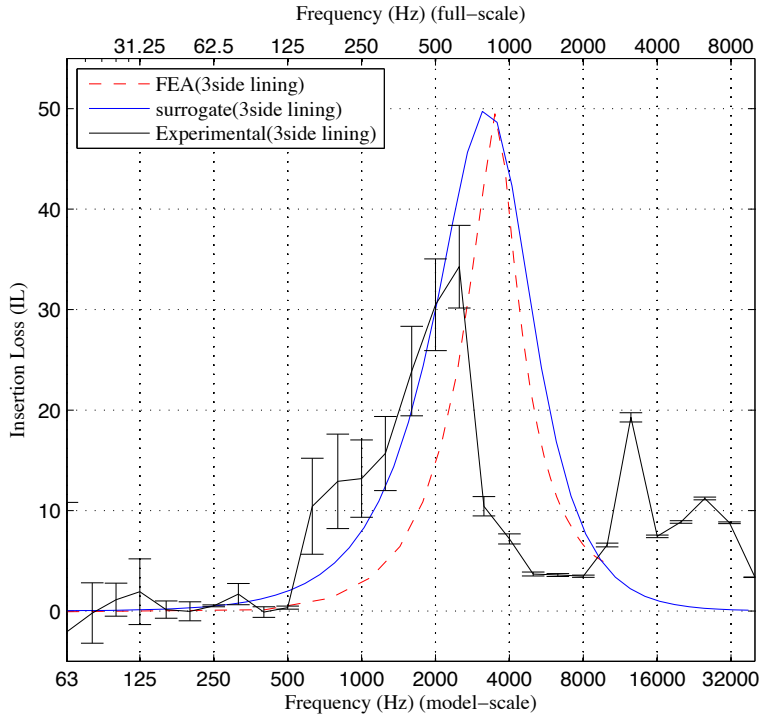

Figure 5.13: Comparison of Insertion Loss vs. frequency between surrogate and FEA predictions, and experiments for Configuration 2b.

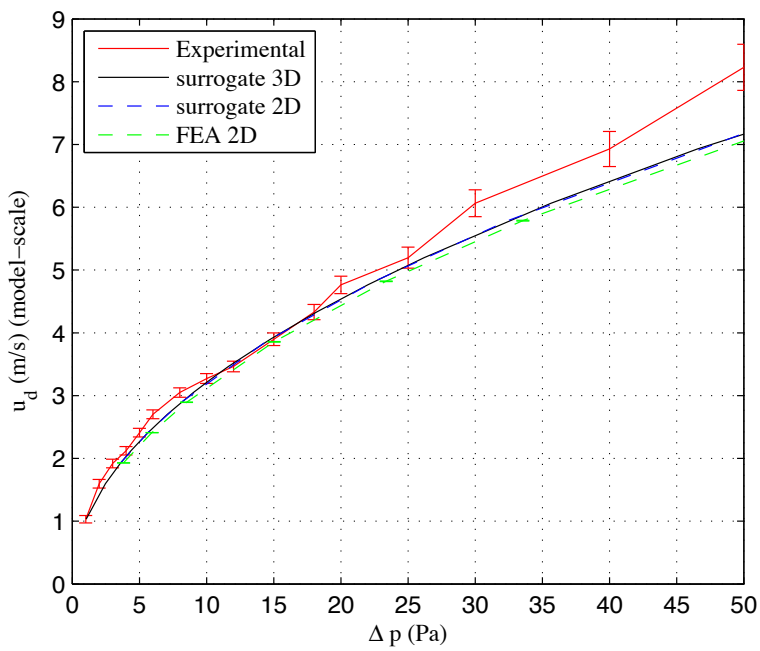

Figure 5.14: Comparison of predicted velocity at duct inlet vs. pressure drop, between 2D and 3D surrogate model, 2D FEA and experiments for Configuration 2b of the scale-model duct. For the full-scale model, u_d is scaled by a factor of 1.32.

Table 5.7: Performance metrics for Configuration 2a.

(a) Specific equivalent open area for acoustics for Configuration 2a.

Method	$SEOA_s$
Experimental (3D)	1
Surrogate (3D)	1
FEA (3D)	1

(b) Flow metrics for Configuration 2a.

Method	C_d	$SEOA_f$	C	r
Experimental (3D)	0.84	1.37	0.01	0.51
Surrogate (3D)	0.78	1.28	–	–
FEA (2D)	0.68	1.26	–	–
Surrogate (2D)	0.69	1.28	–	–

(c) Open area ratio for Configuration 2a.

Method	OAR
Experimental (3D)	1.37
Surrogate (3D)	1.28

ing on both sides and another of width $w/2$ having lining on only one side, was supposed to have rendered a single peak at around 3500 Hz (model scale). The absence of such behaviour in the experimental results and the improvement in sound absorption close to 12000 Hz (model scale) could be due to the styrofoam insert not being perfectly reflective and being partly absorptive or acoustically transparent at higher frequencies. The acoustical performance of this configuration is shown in Table 5.8a.

Airflow: The airflow performance for Configuration 2b exhibits a similar trend to *Configuration 2a.* The velocity at the duct inlet, shown in Figure 5.14, is similar to *Configuration 2a* – this means that there is a reduction in airflow performance

Table 5.8: Performance metrics for Configuration 2b.

(a) Specific equivalent open area for acoustics for Configuration 2b.

Method	$SEOA_s$
Experimental (3D)	0.45
Surrogate (3D)	0.48
FEA (3D)	0.73

(b) Flow metrics for Configuration 2b.

Method	C_d	$SEOA_f$	C	r
Experimental (3D)	0.82	1.08	0.01	0.50
Surrogate (3D)	0.78	1.02	–	–
FEA (2D)	0.65	1.09	–	–
Surrogate (2D)	0.66	1.11	–	–

(c) Open area ratio for Configuration 2b.

Method	OAR
Experimental (3D)	2.4
Surrogate (3D)	2.13

due to lining by a factor of the reduction of the area of the duct. The flow metrics for this configuration are shown in Table 5.8b.

Open Area Ratio: The OAR for *Configuration 2b*, as shown in Table 5.8c, is roughly twice that of *Configuration 2a* due to the improvement in the acoustical performance.

5.2.3 Configuration 3

Configuration 3 represents a duct of cross-sectional dimensions 0.6 m × 0.6 m and length 1.8 m.

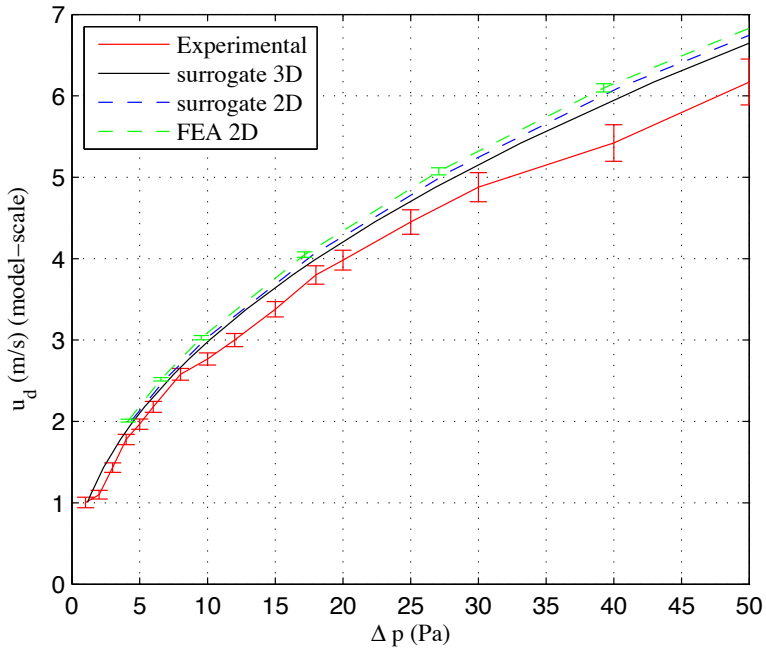

Figure 5.15: Comparison of predicted velocity at duct inlet vs. pressure drop, between 2D and 3D surrogate model, 2D FEA and experiments for Configuration 3a of the scale-model duct. For the full-scale model, u_d is scaled by a factor of 1.25.

Configuration 3 – Type a:

Configuration 3a represents an unlined duct (refer to Figure 4.22). The acoustical performance is assumed negligible in this case too.

Acoustics: N/A

Airflow: In contrast to *Configurations 1* and *2*, *Configuration 3* has reduced airflow rate (and inlet duct velocity) for the same pressure drop. This is because the pressure drop developed due to the vena-contracta is not completely recovered. For a change in cross-section from area A_1 to area A_2, if $A_1 \gg A_2$, the pressure recovery from the vena-contracta happens early along the length of the duct.

Table 5.9: Performance metrics for Configuration 3a.

(a) Specific equivalent open area for acoustics for Configuration 3a.

Method	$SEOA_s$
Experimental (3D)	1
Surrogate (3D)	1
FEA (3D)	1

(b) Flow metrics for Configuration 3a.

Method	C_d	$SEOA_f$	C	r
Experimental (3D)	0.68	1.11	0.32	0.50
Surrogate (3D)	0.72	1.19	–	–
FEA (2D)	0.72	1.23	–	–
Surrogate (2D)	0.71	1.21	–	–

(c) Open area ratio for Configuration 3a.

Method	OAR
Experimental (3D)	1.11
Surrogate (3D)	1.19

For A_1 not much greater than A_2, as in this case, the pressure recovery is more gradual – this means there is an additional pressure drop for this configuration as compared to *Configurations 1* and *2*. From Figure 5.15, it can be seen that the 3D surrogate model and the results from experiments are off by about 8%. However, in contrast to the underestimation of airflow by the surrogate model in the case of *Configurations 1* and *2*, for *Configuration 3a* the surrogate model over-estimates the airflow. Though not accurate, the surrogate model is able to capture the general behaviour of the flow quite well.

The $SEOA_f$ from experiments, shown in Table 5.9b, is lower than for *Configurations 1* and *2*, leading to a lower discharge coefficient. It should be recalled here that the $SEOA_f$ is normalized to the area of the inlet, so a higher $SEOA_f$ does

not necessarily mean it has better airflow, rather better airflow performance.

Open Area Ratio: The *OAR* is quite low owing, to poor acoustical performance, and is lower than *Configuration 1a* due to the relative poorer airflow performance.

Configuration 3 – Type b:

Configuration 3b represents a duct of cross-section 0.6 m × 0.6 m and length 1.8 m with 0.0125 m Sonoflex lining on all surfaces (refer to Figure 4.23)

Acoustics: From Figure 5.16, it can be seen that with larger ducts, the comparison between the surrogate model (derived from 2D FEA) and the 3D FEA show a slight variation in the position of the peak. Upon further investigation, it was found that 2D FEA, similarly, predicts the peak at around 1000 Hz (model-scale) which formed the basis for the surrogate model. From experimental results, it can be seen that at high frequencies above 2000 Hz (model scale), there is strong domination of higher-order modes. The surrogate model under-predicts the IL at higher frequencies, but this is a known issue caused by the assumption of plane-wave propagation in the duct. When compared to *Configuration 1* and *2*, the *IL* peaks at only 14 dB, in contrast to close to 30 dB, but is more spread out across the spectrum.

Airflow: As can be expected, the airflow exhibits a similar trend to *Configuration 3a* with proportional reduction in airflow due to reduction in cross-sectional area, and is not discussed further.

Open Area Ratio: The *OAR* is much higher than for *Configuration 3a* due to improved acoustical performance. The existence of higher-order modes improves the acoustical performance, as seen from Table 5.10a. The surrogate model that ignores this effect underpredicts the acoustical performance. This is reflected in the *OAR*, with experiments showing better performance than predictions.

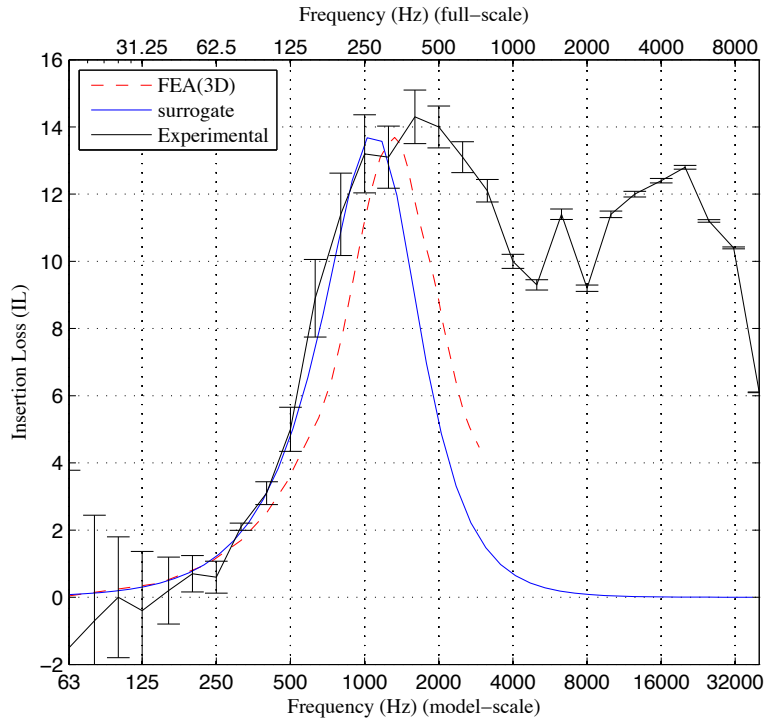

Figure 5.16: Comparison of Insertion Loss vs. frequency between surrogate and FEA predictions, and experiments for Configuration 3b.

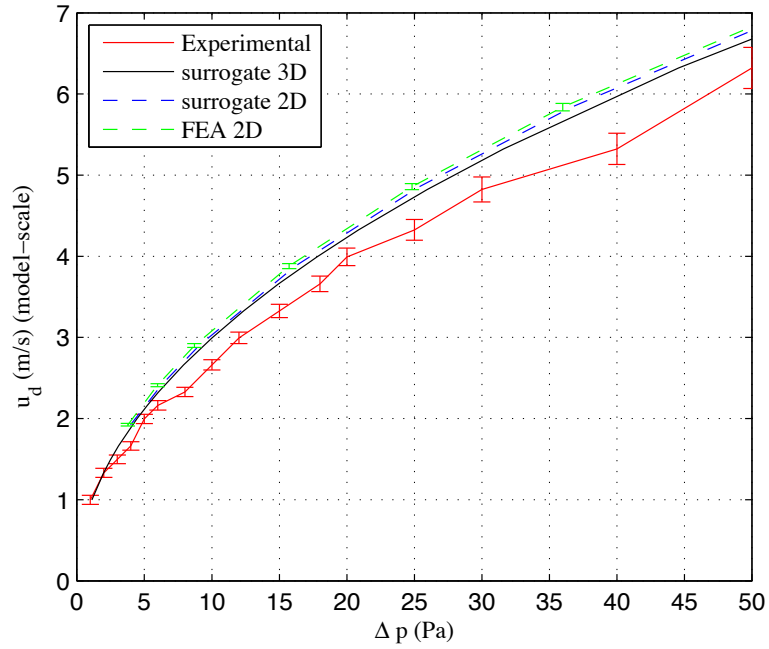

Figure 5.17: Comparison of predicted velocity at duct inlet vs. pressure drop, between 2D and 3D surrogate model, 2D FEA and experiments for Configuration 3b of the scale-model duct. For the full-scale model, u_d is scaled by a factor of 1.31.

Table 5.10: Performance metrics for Configuration 3b.

(a) Specific equivalent open area for acoustics for Configuration 3b.

Method	$SEOA_s$
Experimental (3D)	0.27
Surrogate (3D)	0.31
FEA (3D)	0.45

(b) Flow metrics for Configuration 3b.

Method	C_d	$SEOA_f$	C	r
Experimental (3D)	0.68	1.02	0.30	0.49
Surrogate (3D)	0.73	1.10	–	–
FEA (2D)	0.75	1.18	–	–
Surrogate (2D)	0.74	1.16	–	–

(c) Open area ratio for Configuration 3b.

Method	OAR
Experimental (3D)	3.78
Surrogate (3D)	3.55

Configuration 3 – Type c:

Configuration 3c represents a lined duct of cross-section 0.6 m × 0.6 m and length 1.8 m with a baffle made of Sonoflex inserted near the inlet of the duct (refer to Figure 4.24).

Acoustics: From Figure 5.18, insertion of a baffle near the inlet of the duct is shown to slightly increase the *IL* close to 2000 Hz (model scale) for the surrogate model. With the strong dominance of higher-order modes, it is difficult to observe the same in the experimental results. As for *Configuration 1a*, the position of the peak in the frequency spectrum that is predicted by the surrogate model is slightly off, when compared to the 3D FEA model.

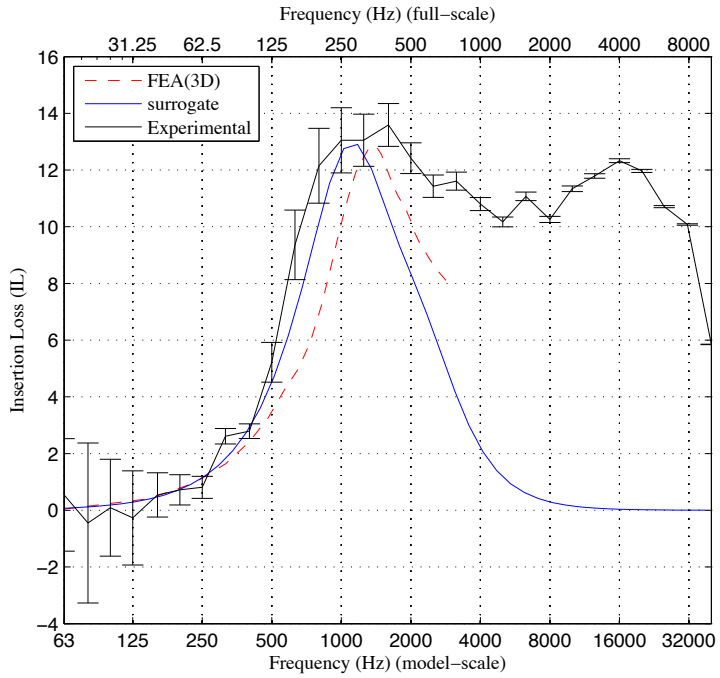

Figure 5.18: Comparison of Insertion Loss vs. frequency between surrogate and FEA predictions, and experiments for Configuration 3c.

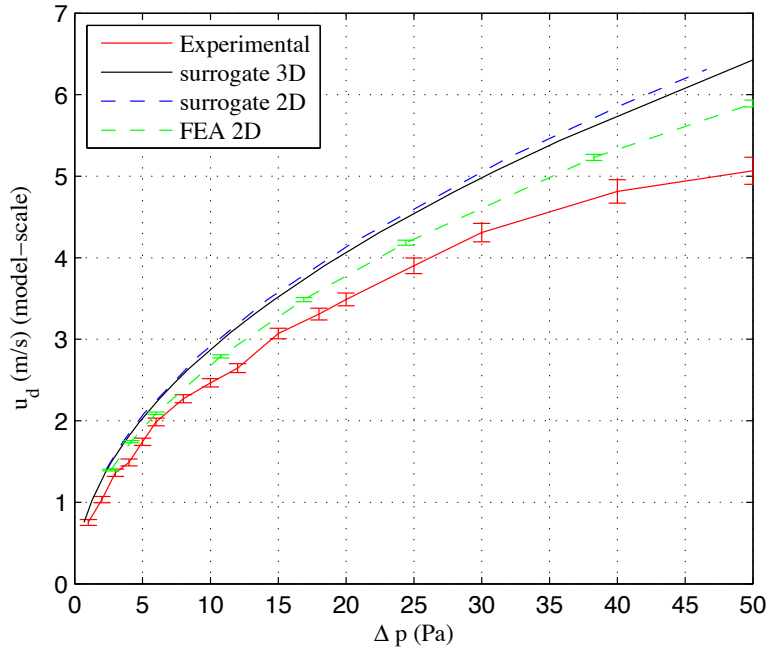

Figure 5.19: Comparison of predicted velocity at duct inlet vs. pressure drop, between 2D and 3D surrogate model, 2D FEA and experiments for Configuration 3c of the scale-model duct. For the full-scale model, u_d is scaled by a factor of 1.04.

Table 5.11: Performance metrics for Configuration 3c.

(a) Specific equivalent open area for acoustics for Configuration 3c.

Method	$SEOA_s$
Experimental (3D)	0.26
Surrogate (3D)	0.31
FEA (3D)	0.37

(b) Flow metrics for Configuration 3c.

Method	C_d	$SEOA_f$	C	r
Experimental (3D)	0.59	0.89	0.26	0.50
Surrogate (3D)	0.70	1.05	–	–
FEA (2D)	0.65	1.02	–	–
Surrogate (2D)	0.71	1.12	–	–

(c) Open area ratio for Configuration 3c.

Method	OAR
Experimental (3D)	3.42
Surrogate (3D)	3.38

Airflow: Addition of the baffle near the inlet reduces the airflow performance, as shown in Figure 5.19. The FEA model is in better agreement with the results from the experiments than the surrogate model. This difference is due to the approximation of the baffles as a change in cross-section of the duct, as was done for *Configurations 1c, 1d* and *1e*. As for other configurations of *Configuration 3*, the flow exponent is 0.5, signifying fully-turbulent flow.

Open Area Ratio: The *OAR* is slightly lower compared to *Configuration 3b*. The slight improvement in acoustical performance (Table 5.11a) is masked by the higher-order modes, showing no visible improvement in performance.

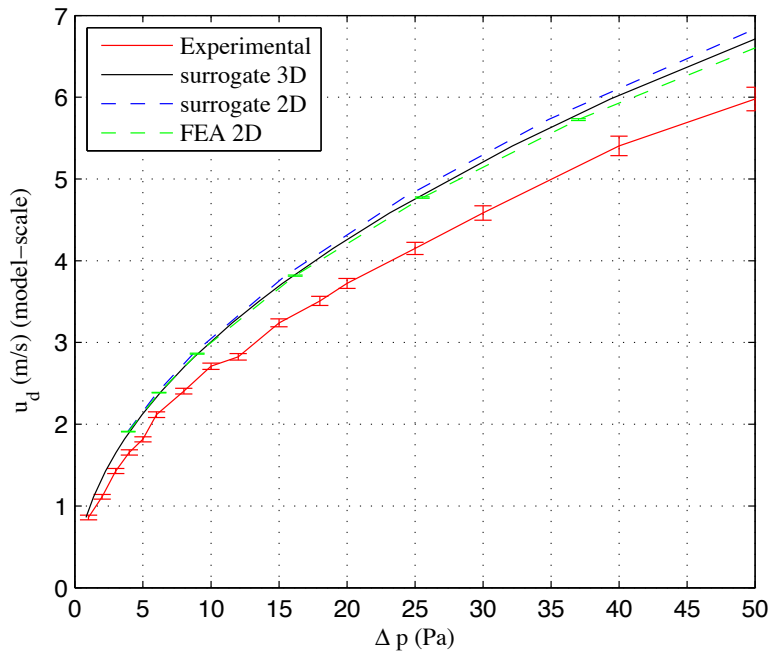

Figure 5.20: Comparison of predicted velocity at duct inlet vs. pressure drop, between 2D and 3D surrogate model, 2D FEA and experiments for Configuration 3d of the scale-model duct. For the full-scale model, u_d is scaled by a factor of 1.05.

Configuration 3 – Type d:

Configuration 3d represents a lined duct of cross-section 0.6 m × 0.6 m and length of 1.8 m with a baffle made of Sonoflex in the middle of the duct (refer to Figure 4.25).

Acoustics: Refer to Section 5.2.3

Airflow: From Figure 5.20, there is evidence of improvement in airflow performance by placing the baffles away from the inlet of the duct. When compared to *Configuration 3c*, there is an improvement in airflow, as seen from results from experiments. The surrogate model also shows a similar trend, but the improve-

Table 5.12: Performance metrics for Configuration 3d.

(a) Specific equivalent open area for acoustics for Configuration 3d.

Method	$SEOA_s$
Experimental (3D)	0.26
Surrogate (3D)	0.31
FEA (3D)	0.37

(b) Flow metrics for Configuration 3d.

Method	C_d	$SEOA_f$	C	r
Experimental (3D)	0.64	0.97	0.27	0.51
Surrogate (3D)	0.73	1.10	–	–
FEA (2D)	0.73	1.15	–	–
Surrogate (2D)	0.75	1.17	–	–

(c) Open area ratio for Configuration 3d.

Method	OAR
Experimental (3D)	3.73
Surrogate (3D)	3.55

ment in the predicted performance is much lower compared to the experimental results. As seen in Table 5.12b, the discharge coefficient is higher for *Configuration 3d* compared to *Configuration 3c*, both from experiments and the surrogate model.

Open Area Ratio: From Table 5.12c it can be seen that OAR is higher for *Configuration 3d* compared to *Configuration 3c*, both from experiments and the surrogate model, due to better airflow performance.

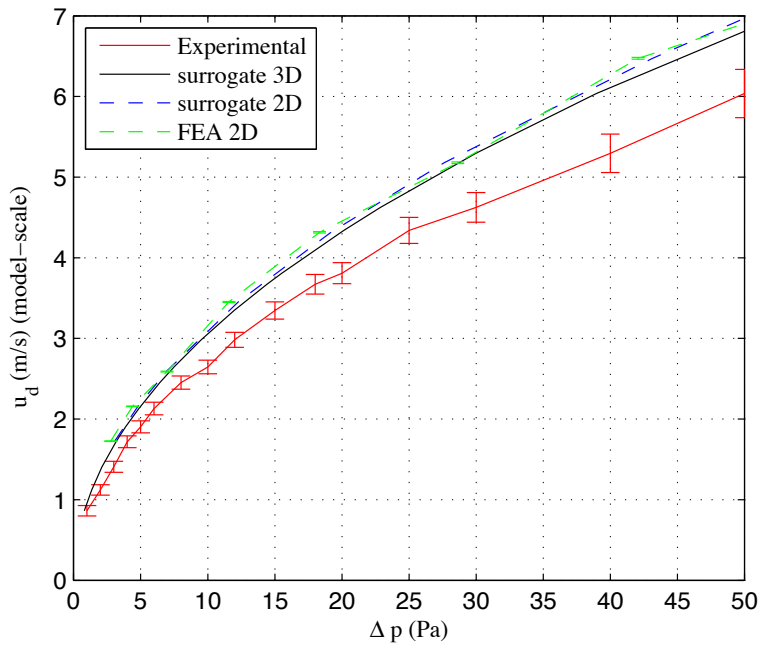

Figure 5.21: Comparison of predicted velocity at duct inlet vs. pressure drop, between 2D and 3D surrogate model, 2D FEA and experiments for Configuration 3e of the scale-model duct. For the full-scale model, u_d is scaled by a factor of 1.06.

Configuration 3 – Type e:

Configuration 3e represents a lined duct of cross-section 0.6 m × 0.6 m and length 1.8 m with a baffle made of Sonoflex near the outlet of the duct (refer to Figure 4.26). Acoustic results from *Configuration 3c* are applicable here.

Acoustics: Refer to Section 5.2.3

Airflow: From Figure 5.21, it can be seen that for *Configuration 3e*, placing the baffle further inside the duct, near the outlet, does not necessarily improve the airflow performance. There is only marginal improvement in airflow performance, for any position of the baffle after the point of recovery of the vena-

Table 5.13: Performance metrics for Configuration 3e.

(a) Specific equivalent open area for acoustics for Configuration 3e.

Method	$SEOA_s$
Experimental (3D)	0.26
Surrogate (3D)	0.31
FEA (3D)	0.37

(b) Flow metrics for Configuration 3e.

Method	C_d	$SEOA_f$	C	r
Experimental (3D)	0.67	1.00	0.27	0.53
Surrogate (3D)	0.74	1.12	–	–
FEA (2D)	0.77	1.21	–	–
Surrogate (2D)	0.76	1.19	–	–

(c) Open area ratio for Configuration 3e.

Method	OAR
Experimental (3D)	3.85
Surrogate (3D)	3.61

contracta. However, the average discharge coefficient seems to be higher for *Configuration 3e*, as seen in Table 5.13b. The flow exponent is also increased to 0.51, though it is not clear why.

Open Area Ratio: The *OAR* shown in Table 5.14c is seen to be an increase over *Configurations 3c* and *3d*.

Configuration 3 – Type f:

Configuration 3f represents a lined duct of cross-section 0.6 m × 0.6 m and length 1.8 m with two baffles made of Sonoflex near the inlet of the duct (refer to Figure 4.27). The acoustical and airflow performance of this configuration is dis-

cussed in this section.

Acoustics: Figure 5.22 shows the comparison of Insertion Losses for *Configuration 3f*. Insertion of two baffles creates a second peak at around 3000 Hz (model scale) for the surrogate model. There is still a difference in the position of the peak in the frequency spectrum between the surrogate and FEA models. It was not possible to model above 3000 Hz (model scale) for 3D FEA for such a large duct. Hence the exact positioning of the second peak is unclear, though the tendency to form a peak is observed near 3000 Hz (model scale). The addition of baffles appears to reduce the energy in the peak and distribute it across a wider frequency range. The peak of the surrogate model now occurs at 13 dB, which is less than before. The *IL* for the experimental results seems to have increased when compared to *Configurations 3c, 3d* and *3e*, and the first peak shows higher Insertion Loss than before.

Airflow: Figure 5.23 compares the airflow performance for *Configuration 3f*. As for *Configuration 3c*, the surrogate model predicts only a slight reduction in airflow performance due to the addition of a second baffle. Experimental results show a much greater reduction in airflow performance. However, it is clear that the introduction of baffles near the inlet of the duct, before the point of pressure recovery from vena-contracta occurs, results in poor airflow performance. The discharge coefficient is lower than for other configurations, as can be seen from Table 5.14b.

Open Area Ratio: The *OAR* for this configuration is shown in Table 5.14c. The *OAR* from experimental measurements is much higher than the predicted *OAR*. This is due to the much better acoustical performance in the experimental results. Addition of two baffles appears to have created multiple peaks and better performance in general. For *Configuration 3f*, adding baffles must have improved performance at frequencies that are not of interest (above 6000 Hz for the model-

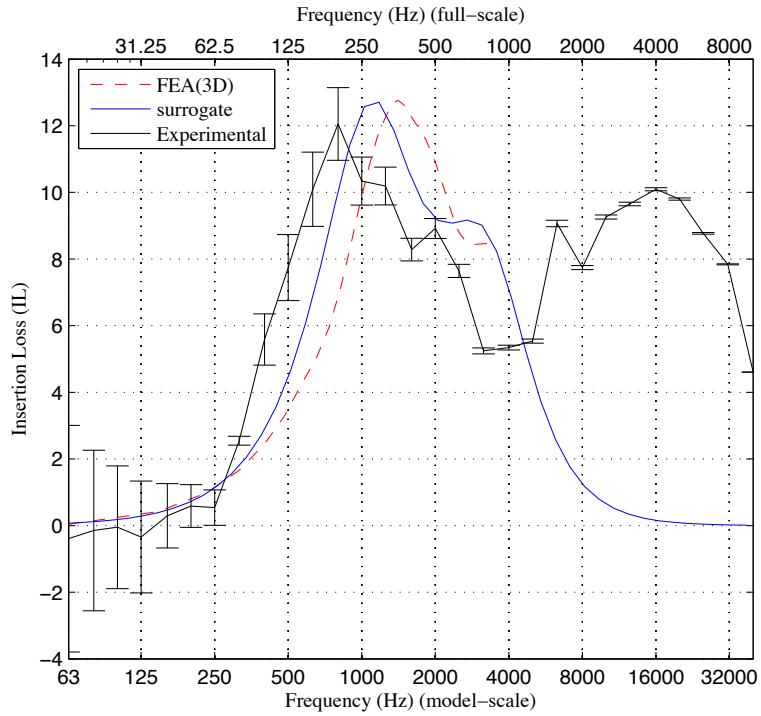

Figure 5.22: Comparison of Insertion Loss vs. frequency between surrogate and FEA predictions, and experiments for Configuration 3f.

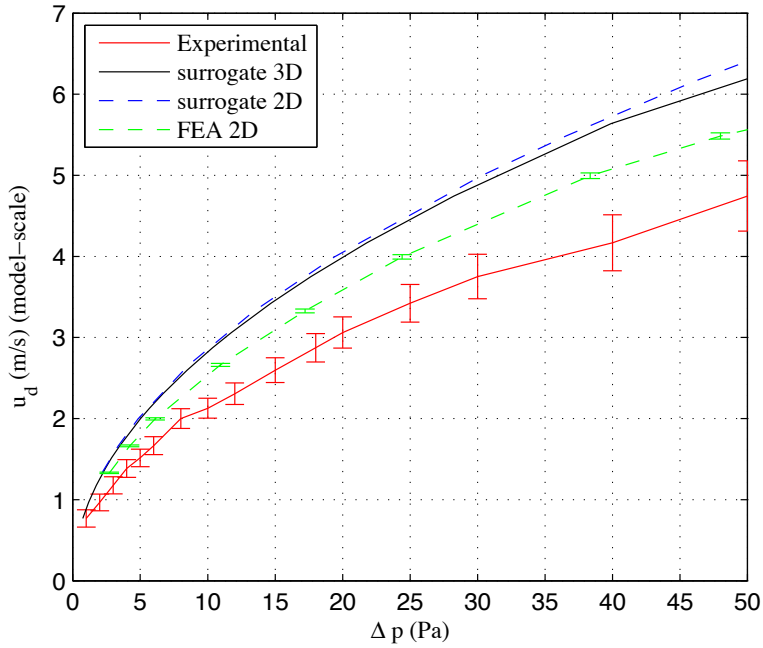

Figure 5.23: Comparison of predicted velocity at duct inlet vs. pressure drop, between 2D and 3D surrogate model, 2D FEA and experiments for Configuration 3f of the scale-model duct. For the full-scale model, u_d is scaled by a factor of 1.04.

Table 5.14: Performance metrics for Configuration 3f.

(a) Specific equivalent open area for acoustics for Configuration 3f.

Method	$SEOA_s$
Experimental (3D)	0.14
Surrogate (3D)	0.30
FEA (3D)	0.36

(b) Flow metrics for Configuration 3f.

Method	C_d	$SEOA_f$	C	r
Experimental (3D)	0.54	0.81	0.22	0.52
Surrogate (3D)	0.69	1.03	–	–
FEA (2D)	0.61	0.96	–	–
Surrogate (2D)	0.70	1.09	–	–

(c) Open area ratio for Configuration 3f.

Method	OAR
Experimental (3D)	5.79
Surrogate (3D)	3.43

scale). The improvement of acoustical performance with the addition of baffles is conditional on the size of the duct.

5.2.4 Configuration 4

Configuration 4 represents a rectangular duct of cross-sectional dimensions 0.6 m × 0.3 m and length 1.8 m. For types *d, e* and *f*, the baffles that were used are much thicker than the ones used in *Configuration 1* and *Configuration 3*, in order to clearly understand the effect on acoustical and airflow performance.

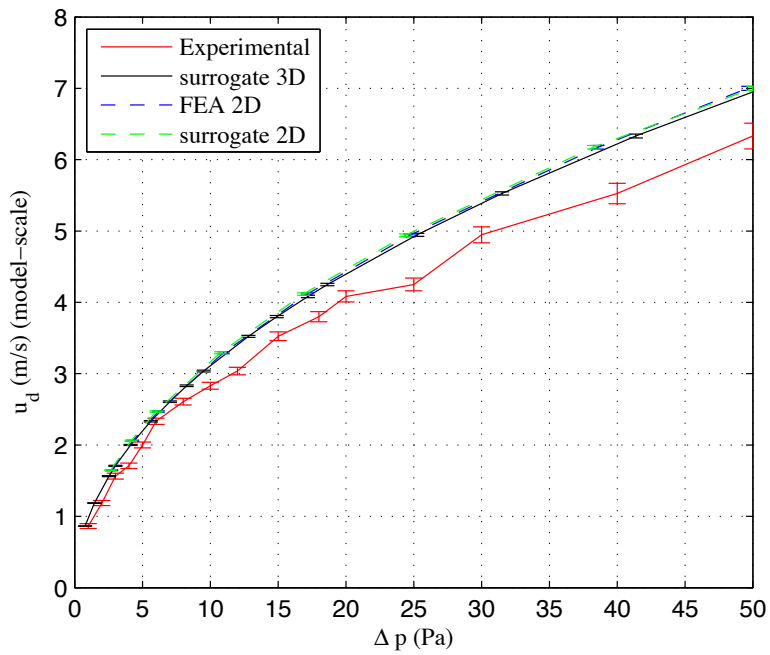

Figure 5.24: Comparison of predicted velocity at duct inlet vs. pressure drop, between 2D and 3D surrogate model, 2D FEA and experiments for Configuration 4a of the scale-model duct. For the full-scale model, u_d is scaled by a factor of 1.18.

Configuration 4 – Type a:

Configuration 4a represents the performance of an unlined rectangular duct (refer to Figure 4.30). The acoustical performance for this configuration is assumed negligible.

Acoustics: N/A

Airflow: The comparison of airflow performance for this configuration is shown in Figure 5.24. Following the trend of previous configurations, there is good agreement between the surrogate and FEA models. The airflow performance from experimental results is over-predicted by the surrogate model, as for *Con-*

Table 5.15: Performance metrics for Configuration 4a.

(a) Specific equivalent open area for acoustics for Configuration 4a.

Method	$SEOA_s$
Experimental (3D)	1
Surrogate (3D)	1
FEA (3D)	1

(b) Flow metrics for Configuration 4a.

Method	C_d	$SEOA_f$	C	r
Experimental (3D)	0.68	1.12	0.16	0.51
Surrogate (3D)	0.76	1.24	–	–
FEA (2D)	0.64	1.26	–	–
Surrogate (2D)	0.64	1.25	–	–

(c) Open area ratio for Configuration 4a.

Method	OAR
Experimental (3D)	1.12
Surrogate (3D)	1.24

figuration 3.

Open Area Ratio: The OAR is very close to that predicted for *Configuration 3a*, as seen in Table 5.15c.

Configuration 4 – Type b:

Configuration 4b represents a rectangular duct of cross-sectional dimensions 0.6 m × 0.3 m and length 1.8 m with Sonoflex lining of 0.0125 m thickness (refer to Figure 4.31).

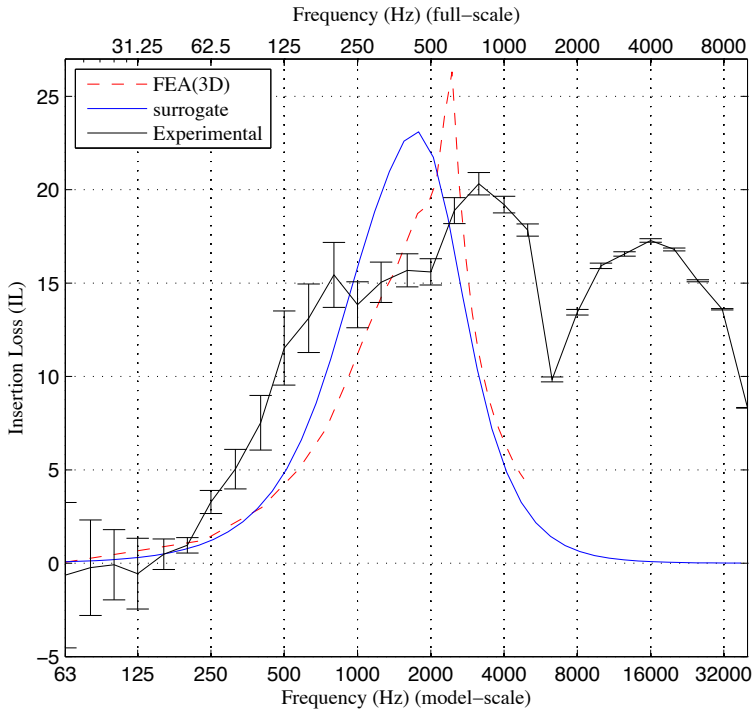

Figure 5.25: Comparison of Insertion Loss vs. frequency between surrogate and FEA predictions, and experiments for Configuration 4b.

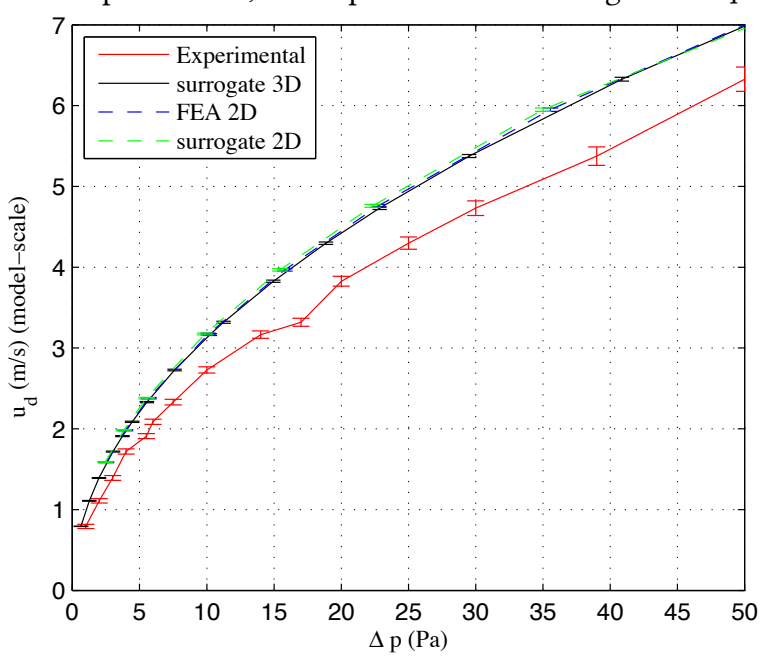

Figure 5.26: Comparison of predicted velocity at duct inlet vs. pressure drop, between 2D and 3D surrogate model, 2D FEA and experiments for Configuration 4b of the scale-model duct. For the full-scale model, u_d is scaled by a factor of 1.21.

Table 5.16: Performance metrics for Configuration 4b.

(a) Specific equivalent open area for acoustics for Configuration 4b.

Method	$SEOA_s$
Experimental (3D)	0.12
Surrogate (3D)	0.27
FEA (3D)	0.31

(b) Flow metrics for Configuration 4b.

Method	C_d	$SEOA_f$	C	r
Experimental (3D)	0.65	0.93	0.12	0.53
Surrogate (3D)	0.76	1.09	–	–
FEA (2D)	0.68	1.18	–	–
Surrogate (2D)	0.68	1.17	–	–

(c) Open area ratio for Configuration 4b.

Method	OAR
Experimental (3D)	7.66
Surrogate (3D)	4.03

Acoustics: From Figure 5.25 it can be seen that the difference between the surrogate model and the 3D FEA is more prominent here. The influence of the higher-order modes is relatively less than for *Configuration 3*, and a prominent peak can be seen at 3000 Hz (model scale).

Airflow: The airflow behaviour is similar to the trend described in *Configuration 4a* and is not discussed further here.

Open Area Ratio: The *OAR* for *Configuration 4b* is very high in comparison to that predicted for *Configuration 4a*, as seen in Table 5.16c, due to very good acoustical performance.

Table 5.17: Performance metrics for Configuration 4c.

(a) Specific equivalent open area for acoustics for Configuration 4c.

Method	$SEOA_s$
Experimental (3D)	0.11
Surrogate (3D)	0.21
FEA (3D)	0.22

(b) Flow metrics for Configuration 4c.

Method	C_d	$SEOA_f$	C	r
Experimental (3D)	0.47	0.67	0.09	0.53
Surrogate (3D)	0.55	0.80	–	–
FEA (2D)	0.49	0.84	–	–
Surrogate (2D)	0.44	0.76	–	–

(c) Open area ratio for Configuration 4c.

Method	OAR
Experimental (3D)	6.09
Surrogate (3D)	3.80

Configuration 4 – Type c:

Configuration 4c represents a rectangular duct of cross-sectional dimensions 0.6 m × 0.3 m and length 1.8 m with Sonoflex lining of 0.0125 m thickness. For this configuration six baffles of thickness 0.0125 m were inserted as a lumped element near the inlet of the lined duct (refer to Figure 4.32).

Acoustics: For *Configuration 4c*, as seen from Figure 5.27, when compared to the *Configuration 4b*, the *IL* is greatly increased to around 33 dB from 23 dB for the surrogate model and to 27 dB from 20 dB for measurements from experiments due to the addition of the stacked baffles.

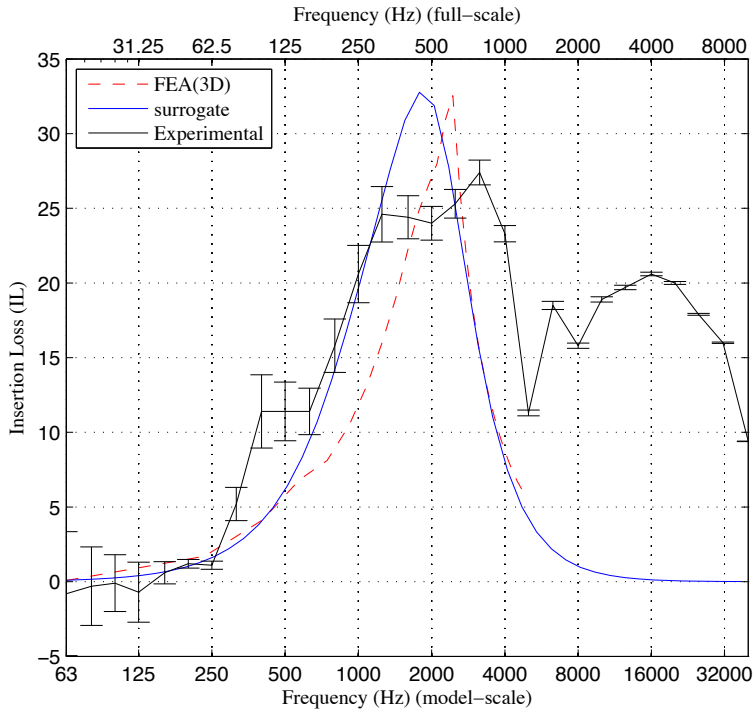

Figure 5.27: Comparison of Insertion Loss vs. frequency between surrogate and FEA predictions, and experiments for Configuration 4c.

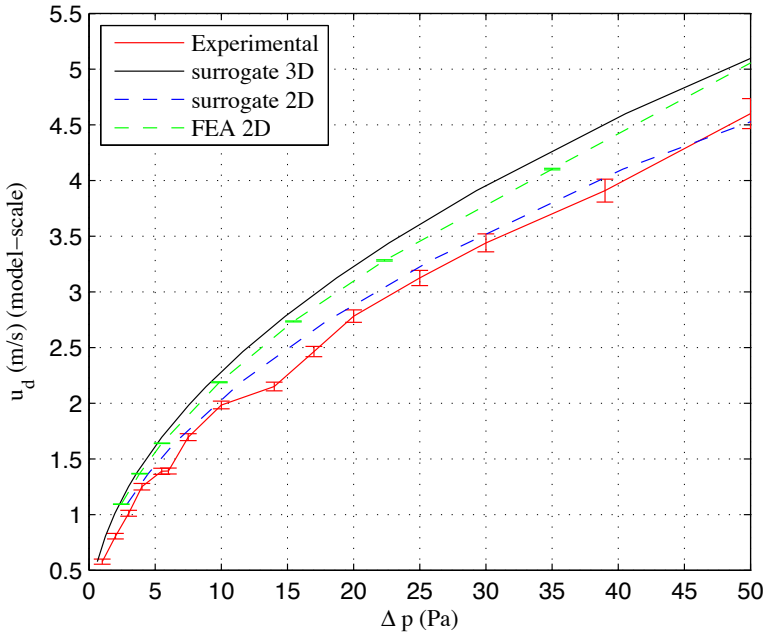

Figure 5.28: Comparison of predicted velocity at duct inlet vs. pressure drop, between 2D and 3D surrogate model, 2D FEA and experiments for Configuration 4c of the scale-model duct. For the full-scale model, u_d is scaled by a factor of 1.17.

Airflow: Figure 5.28 compares the airflow performances of the different models for *Configuration 4c*. For a duct with a rectangular cross-section, when a baffle is inserted, the hydraulic diameter of the baffle was used, along with the hydraulic diameter of the duct, to model in 2D. The hydraulic diameter is not the best choice in this case. For this reason there is non-agreement between the 2D and 3D surrogate models. The airflow performance is greatly reduced for this configuration compared to *Configuration 4b*. The average discharge coefficient is greatly reduced, as seen in Table 5.17b.

Open Area Ratio: Though there is an improvement in acoustical performance due to the addition of baffles, the reduction in airflow is much greater, thus leading to a lower *OAR* than for *Configuration 4b*.

Configuration 4 – Type d:

Configuration 4d represents a rectangular duct of cross-sectional dimensions 0.6 m $\times$ 0.3 m and length 1.8 m with Sonoflex lining of 0.0125 m thickness. For this configuration six baffles of thickness 0.0125 m were inserted as a lumped element near the middle of the lined duct (refer to Figure 4.33).

Acoustics: Refer to Section 5.2.4.

Airflow: From Figure 5.29, it can be seen that there is an improvement in airflow performance compared to *Configuration 4c* by placing the baffles in the middle of the duct. The surrogate models are in much better agreement than for *Configurations 3c, 3d* and *3e*. This might suggest that the deviation of the surrogate model results from the experimental results is due to the inability of the 2D FEA model to capture the effect of the vena-contracta as well as the 3D model does. When the pressure drop is dominated by the effect of the change in cross-section, and the magnitude of the effect of the vena-contracta is negligible in comparison, there is better agreement between the surrogate model and results from experi-

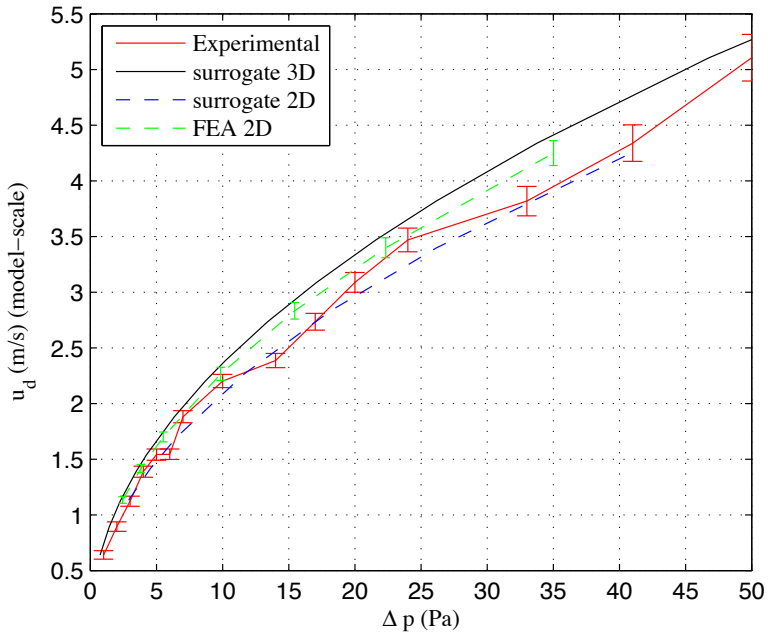

Figure 5.29: Comparison of predicted velocity at duct inlet vs. pressure drop, between 2D and 3D surrogate model, 2D FEA and experiments for Configuration 4d of the scale-model duct. For the full-scale model, u_d is scaled by a factor of 1.10.

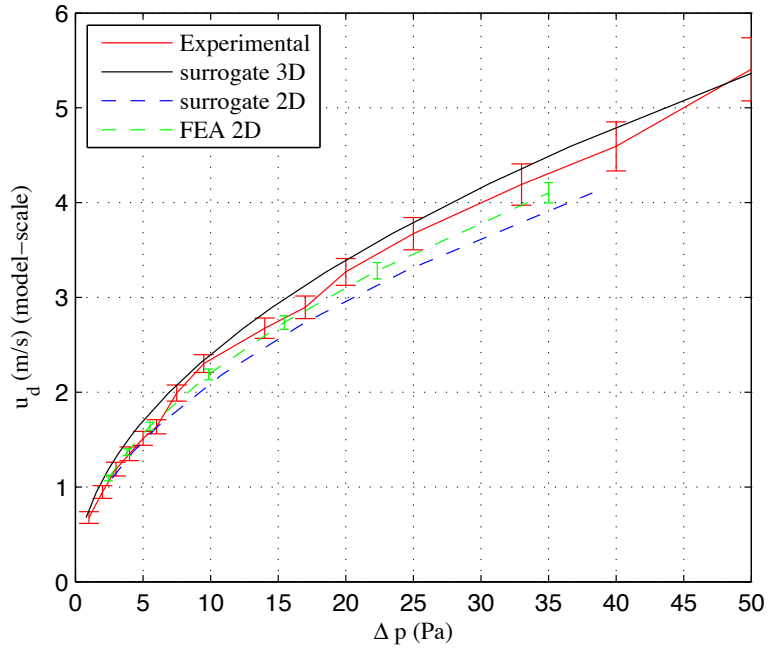

Figure 5.30: Comparison of predicted velocity at duct inlet vs. pressure drop, between 2D and 3D surrogate model, 2D FEA and experiments for Configuration 4e of the scale-model duct. For the full-scale model, u_d is scaled by a factor of 1.12.

Table 5.18: Performance metrics for Configuration 4d.

(a) Specific equivalent open area for acoustics for Configuration 4d.

Method	$SEOA_s$
Experimental (3D)	0.11
Surrogate (3D)	0.21
FEA (3D)	0.22

(b) Flow metrics for Configuration 4d.

Method	C_d	$SEOA_f$	C	r
Experimental (3D)	0.53	0.76	0.1	0.53
Surrogate (3D)	0.57	0.83	–	–
FEA (2D)	0.49	0.85	–	–
Surrogate (2D)	0.45	0.78	–	–

(c) Open area ratio for Configuration 4d.

Method	OAR
Experimental (3D)	6.9
Surrogate (3D)	3.95

ment. The flow metrics for this configuration are shown in Table 5.18b.

Open Area Ratio: The *OAR* for *Configuration 4d* is marginally higher than for *Configuration 4c* as expected, due to better airflow performance (see Table 5.18c).

Configuration 4 – Type e:

Configuration 4e represents a rectangular duct of cross-sectional dimensions 0.6 m × 0.3 m and length 1.8 m with Sonoflex lining of 0.0125 m thickness. For this configuration six baffles of thickness 0.0125 m were inserted as a lumped element near the outlet of the lined duct (refer to Figure 4.34).

Table 5.19: Performance metrics for Configuration 4e.

(a) Specific equivalent open area for acoustics for Configuration 4e.

Method	$SEOA_s$
Experimental (3D)	0.11
Surrogate (3D)	0.21
FEA (3D)	0.22

(b) Flow metrics for Configuration 4e.

Method	C_d	$SEOA_f$	C	r
Experimental (3D)	0.56	0.81	0.10	0.55
Surrogate (3D)	0.58	0.84	–	–
FEA (2D)	0.47	0.82	–	–
Surrogate (2D)	0.78	1.27	–	–

(c) Open area ratio for Configuration 4e.

Method	OAR
Experimental (3D)	7.36
Surrogate (3D)	4.00

Acoustics: N/A

Airflow: The comparison of the airflow performances of different models in Figure 5.30 shows that there is an improvement in airflow performance, compared to *Configurations 4c* and *4d*, by inserting the baffles near the outlet of the baffle. The surrogate model is in good agreement with the experimental results in this case.

Open Area Ratio: The *OAR* from Table 5.19c for *Configuration 4e* is seen to be an increase over *Configuration 4e*.

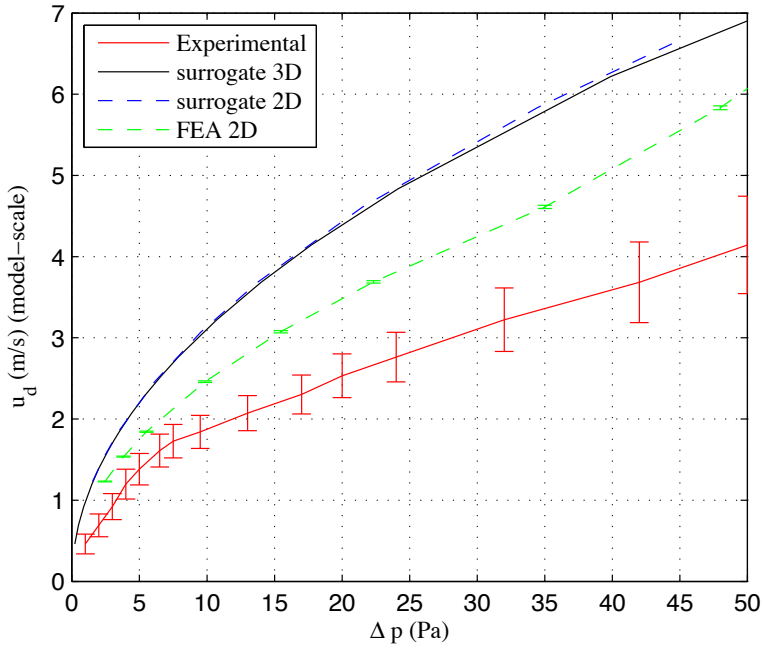

Figure 5.31: Comparison of predicted velocity at duct inlet vs. pressure drop, between 2D and 3D surrogate model, 2D FEA and experiments for Configuration 5a of the scale-model duct. For the full-scale model, u_d is scaled by a factor of 1.18.

5.2.5 Configuration 5

In order to investigate the effect of duct bends on the acoustics and airflow, one such configuration was built and tested. It was, however, not studied in detail due to constraints in time and is a suggestion for future work. The surrogate models were not built for use with ducts with bends.

Configuration 5 – Type a:

Configuration 5a represents an unlined rectangular duct of cross-sectional dimensions 0.6 m × 0.3 m and length 2.1 m, with a 90° bend at 1.8 m from the inlet (refer to Figure 4.36).

Table 5.20: Performance metrics for Configuration 5a.

(a) Specific equivalent open area for acoustics for Configuration 5a.

Method	$SEOA_s$
Experimental (3D)	1
Surrogate (3D)	1
FEA (3D)	1

(b) Flow metrics for Configuration 5a.

Method	C_d	$SEOA_f$	C	r
Experimental (3D)	0.52	0.83	0.08	0.64
Surrogate (3D)	0.76	1.24	–	–
FEA (2D)	0.51	1.01	–	–
Surrogate (2D)	0.64	1.25	–	–

(c) Open area ratio for Configuration5a.

Method	OAR
Experimental (3D)	0.83
Surrogate (3D)	1.24

Acoustics: N/A

Airflow: The airflow from the surrogate model for a straight duct is compared to the experimental measurements in Figure 5.31. The reduction in airflow compared to a straight duct, due to the bend in the posterior end of the duct, is around 1.5 times. The average discharge coefficient, as shown in Table 5.20b is around 0.52 for this configuration. Interestingly the flow exponent is increased to 0.64.

Open Area Ratio: The *OAR* for this configuration is shown in Table 5.22 and is found to be lower than the *OAR* for *Configuration 4a*.

Table 5.21: Performance metrics for Configuration 5b.

(a) Specific equivalent open area for acoustics for Configuration 5b.

Method	$SEOA_s$
Experimental (3D)	0.12
Surrogate (3D)	0.48
FEA (3D)	0.09

(b) Flow metrics for Configuration 5b.

Method	C_d	$SEOA_f$	C	r
Experimental (3D)	0.46	0.65	0.08	0.58
Surrogate (3D)	0.76	1.10	–	–
FEA (2D)	0.54	0.94	–	–
Surrogate (2D)	0.68	1.18	–	–

(c) Open area ratio for Configuration 5b.

Method	OAR
Experimental (3D)	5.42
Surrogate (3D)	2.3

Configuration 5 – Type b:

Configuration 5b represents an unlined rectangular duct of cross-sectional dimensions 0.6 m × 0.3 m and length 2.1 m with Sonoflex lining of thickness 0.0125 m and a 90° bend at 1.8 m from the inlet of the duct (refer to Figure 4.37).

Acoustics: Figure 5.32 shows the effect of a duct bend on the *IL* and compares it to the surrogate model for a straight duct. It can be seen that the duct bend creates several peaks, with an overall improvement in acoustical performance. Table 5.21a shows the sound performance metric $SEOA_s$ for this configuration.

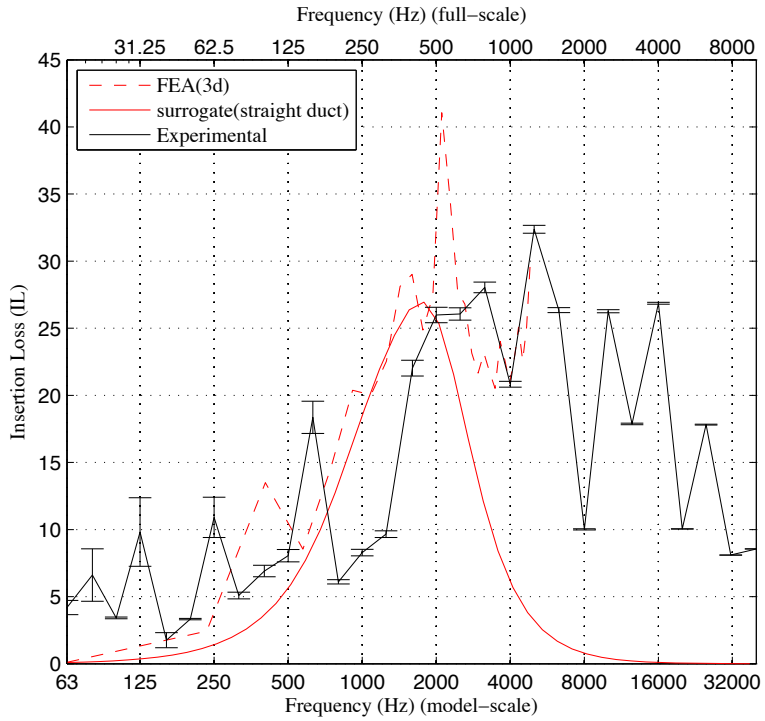

Figure 5.32: Comparison of Insertion Loss for 3D model from experiments , FEA and surrogate model for Configuration 5b.

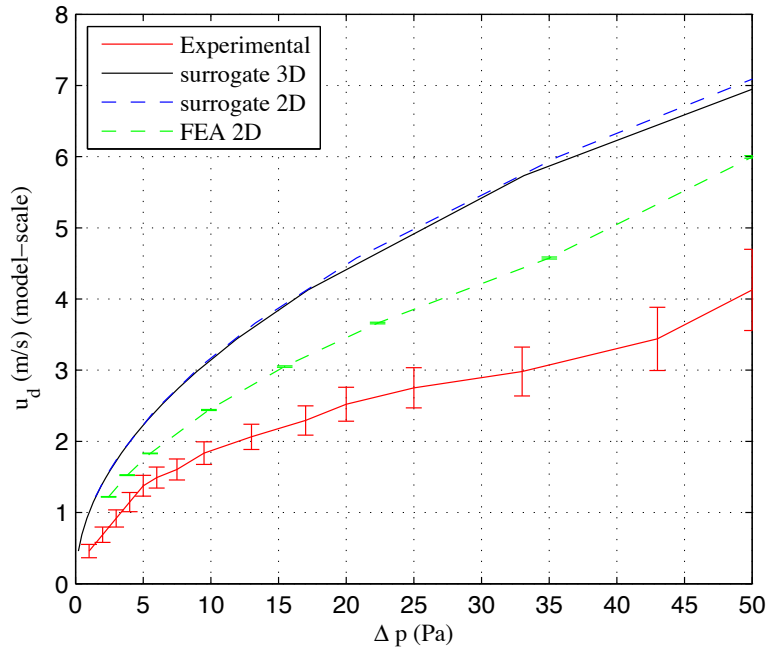

Figure 5.33: Comparison of predicted velocity at duct inlet vs. pressure drop, between 2D and 3D surrogate model, 2D FEA and experiments for Configuration 5b of the scale-model duct. For the full-scale model, u_d is scaled by a factor ofscaled by a factor 1.26.

Airflow: The airflow performance for the surrogate model for a straight duct is compared to the measurements for *Configuration 5b* in Figure 5.33. As for *Configuration 5a*, the airflow is reduced by approximately 1.5 times compared to a straight duct. The flow metrics for this configuration are shown in Table 5.21b.

Open Area Ratio: The *OAR* for *Configuration 5b* is shown in Table 5.21c. The *OAR* is higher than for *Configuration 5a* due to better airflow performance, but is lower in comparison to *Configuration 4b*. This means that although there is a considerable improvement in acoustical performance when introducing a bend, the overall performance is poor due to poorer airflow performance.

5.2.6 Compilation of acoustic results

For comparison, the *IL* curves for all of the duct configurations, from surrogate model predicts and experiments, are plotted in Figures 5.34 and 5.35, respectively. Based on the results from the surrogate model for the investigated duct configurations, the following can be summarized:

- For a lined duct of dimensions, 0.15 m × 0.15 m × 1 m (*Configuration 1b*), an *IL* of 50 dB can be observed at 3500 Hz.
- Addition of a baffle (*Configurations 1c, 1d, 1e*) resulted in an increase in *IL* at 8000 Hz from 9 dB to 26 dB.
- Addition of two baffles (*Configurations 1f*) resulted in an increase in *IL* at 8000 Hz from 9 dB to 35 dB.
- Halving the breadth of the duct, with lining on only three sides (*Configuration 2b*), resulted in an *IL* similar to *Configuration 1b*.
- For a lined duct of dimensions, 0.6 m × 0.6 m × 1.8 m (*Configuration 3b*) an *IL* of 12 dB can be observed at 1000 Hz.

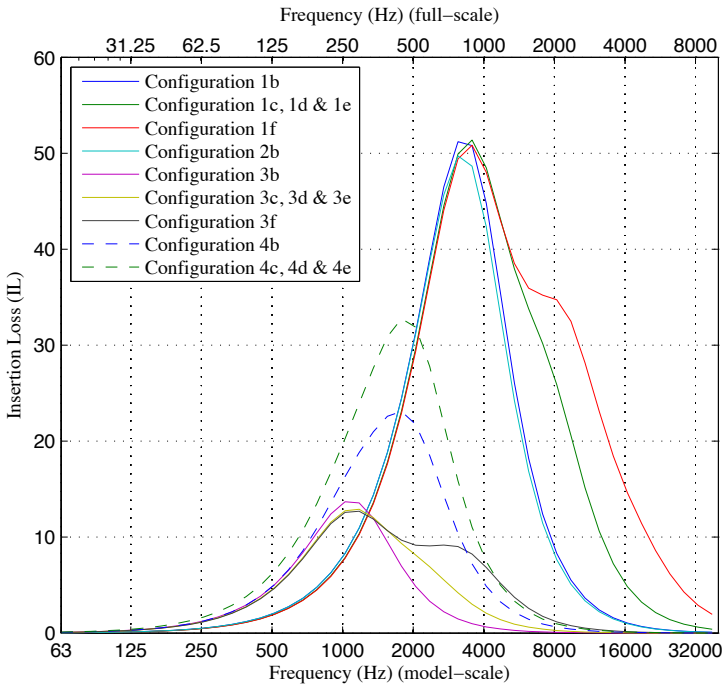

Figure 5.34: Compilation of *IL* curves from the surrogate model for all duct-configurations.

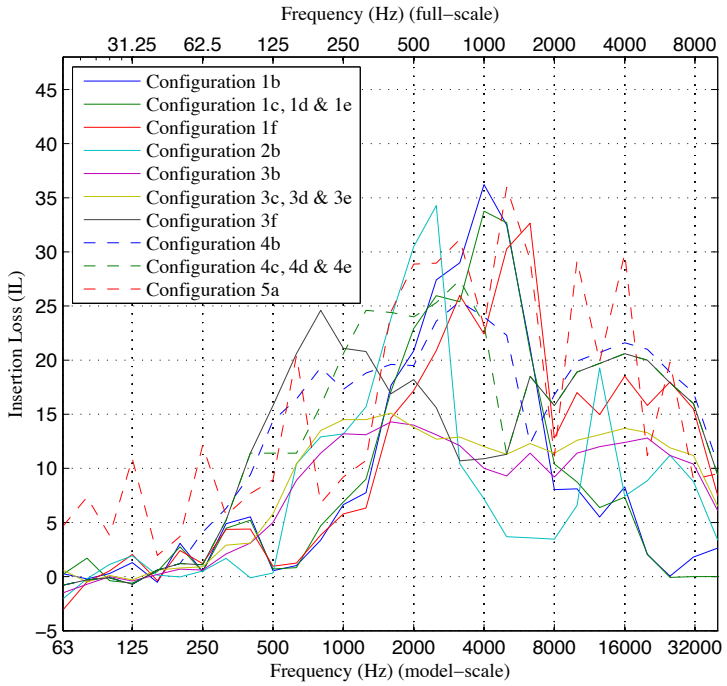

Figure 5.35: Compilation of *IL* curves from experiments for all duct-configurations.

- Addition of a baffle (*Configurations 3c, 3d, 3e*) resulted in an increase in IL at 3000 Hz from 2 dB to 5 dB.
- Addition of two baffles (*Configurations 3f*) resulted in an increase in IL at 3000 Hz from 2 dB to 9 dB.
- Halving the breadth of the duct, with lining on all sides (*Configuration 4b*), resulted in a shift in the peak to 1800 Hz, with an IL of 22 dB.
- Addition of a baffle (*Configurations 4c, 4d, 4e*) resulted in an increase of the IL at 8000 Hz from 26 dB to 35 dB.

5.2.7 Compilation of performance metrics

A summary of the performance metrics for all of the investigated duct configurations is shown in Table 5.22. Figures 5.36 to 5.38 compare the $SEOA_s$, $SEOA_f$ and OAR from experiments and the surrogate models. A good agreement in trend between the surrogate model and experiments is observed for all of the duct configurations. However, the surrogate models seem to greatly under-predict the OAR performance for *Configurations 3f, 4b, 4c, 4d* and *4e*.

Table 5.22: Summary of the performance metrics from the surrogate model and experiments for the investigated duct configruations.

Type	Illustration	$SEOA_s$ (expt.) (surr.)	$SEOA_f$ (expt.) (surr.)	OAR (expt.) (surr.)
1a	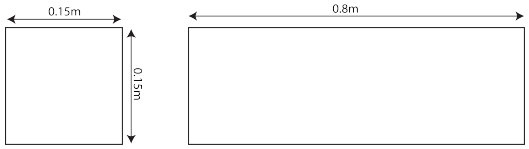	1.00 1.00	0.82 0.77	1.34 1.26
1b	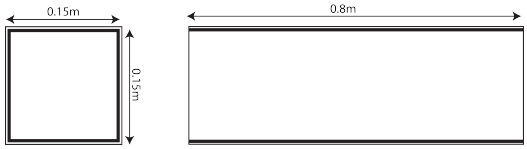	0.51 0.47	1.13 1.17	2.22 2.49

Table 5.22: Summary of the performance metrics from the surrogate model and experiments for the investigated duct configuruations.

Type	Illustration	$SEOA_s$ (expt.) (surr.)	$SEOA_f$ (expt.) (surr.)	OAR (expt.) (surr.)
1c	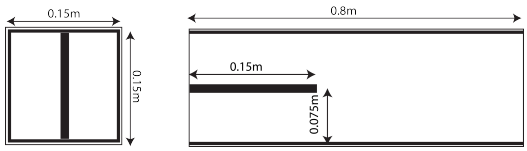	0.50 0.49	1.08 1.01	2.16 2.06
1d	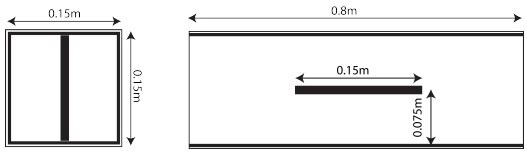	0.50 0.49	1.08 1.08	2.16 2.20
1e	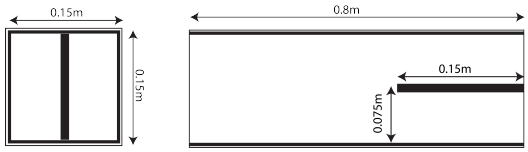	0.50 0.49	1.12 1.06	2.24 2.16
1f	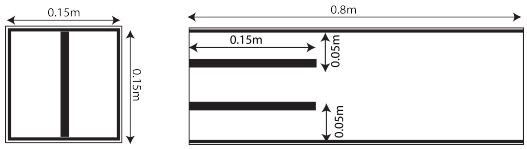	0.50 0.54	1.05 0.96	2.10 1.77
2a	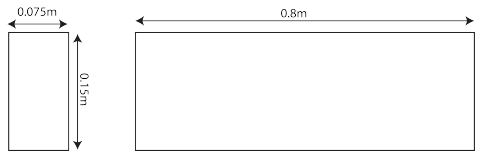	1.00 1.00	1.37 1.28	1.37 1.28
2b	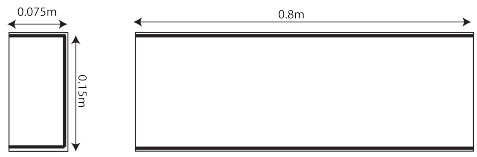	0.45 0.48	1.08 1.02	2.40 2.13
3a	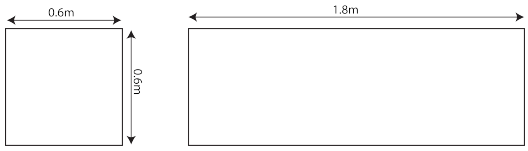	1.00 1.00	1.11 1.19	1.11 1.19

Table 5.22: Summary of the performance metrics from the surrogate model and experiments for the investigated duct configuations.

Type	Illustration	$SEOA_s$ (expt.) (surr.)	$SEOA_f$ (expt.) (surr.)	OAR (expt.) (surr.)
3b	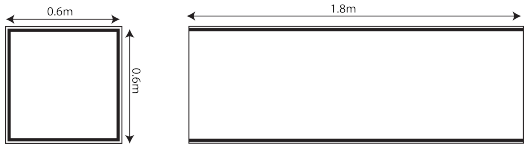	0.27 0.31	1.02 1.10	3.78 3.55
3c	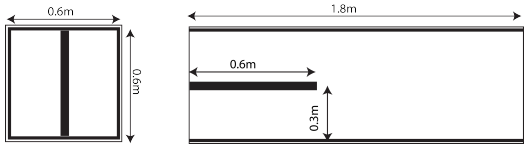	0.26 0.31	0.89 1.05	3.42 3.38
3d	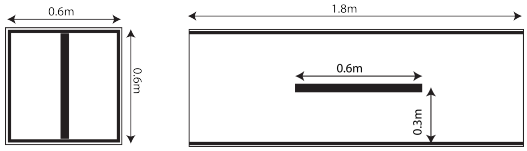	0.26 0.31	0.97 1.10	3.73 3.55
3e	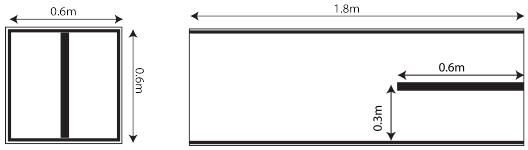	0.26 0.31	1.00 1.12	3.85 3.61
3f	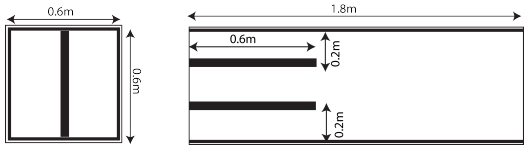	0.14 0.30	0.81 1.03	5.79 3.43
4a	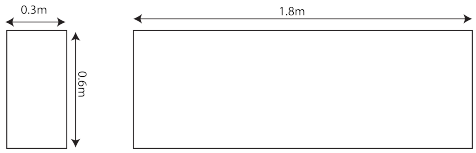	1.00 1.00	1.12 1.24	1.12 1.24
4b	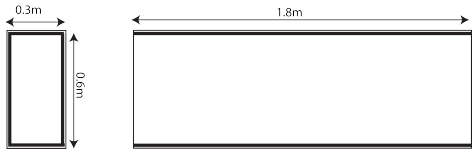	0.12 0.27	0.93 1.09	7.66 4.03

Table 5.22: Summary of the performance metrics from the surrogate model and experiments for the investigated duct configuations.

Type	Illustration	$SEOA_s$ (expt.) (surr.)	$SEOA_f$ (expt.) (surr.)	OAR (expt.) (surr.)
4c	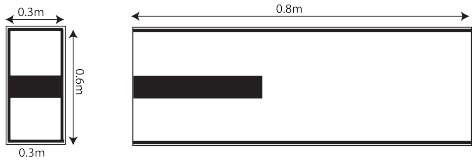	0.11 0.21	0.67 0.80	6.09 3.80
4d	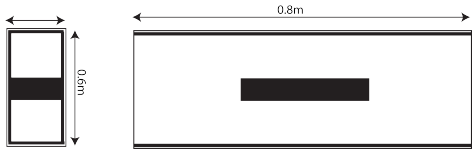	0.11 0.21	0.76 0.83	6.90 3.95
4e	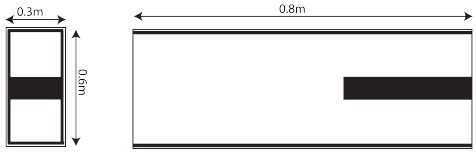	0.11 0.21	0.81 0.84	7.36 4.00
5a	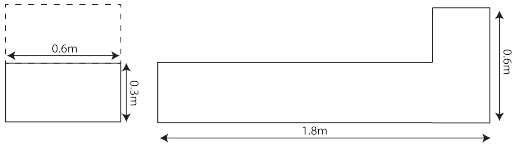	1.00 1.00	0.83 1.24	0.83 1.24
5b		0.12 0.48	0.65 1.10	5.42 2.30

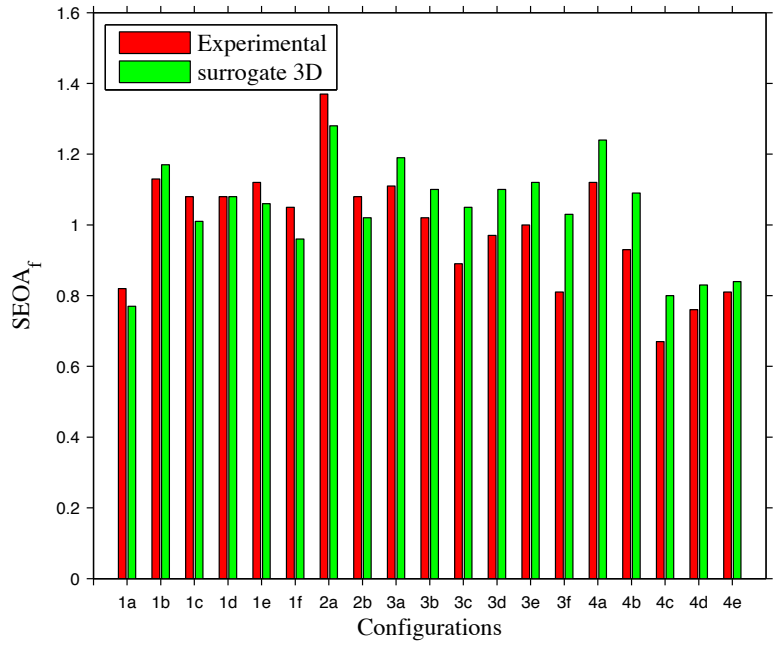

Figure 5.36: Compilation of $SEOA_f$ from the surrogate model and experiments for selected duct-configruations.

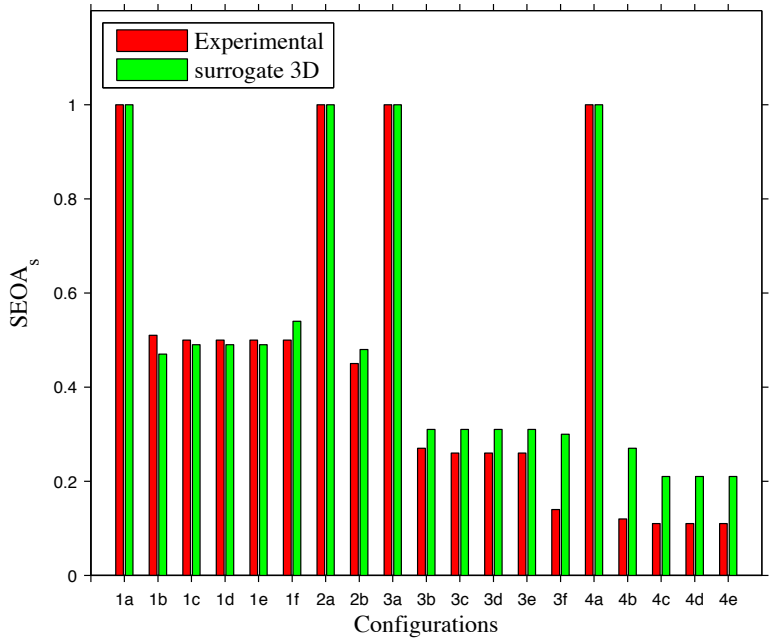

Figure 5.37: Compilation of $SEOA_s$ from the surrogate model and experiments for selected duct-configruations.

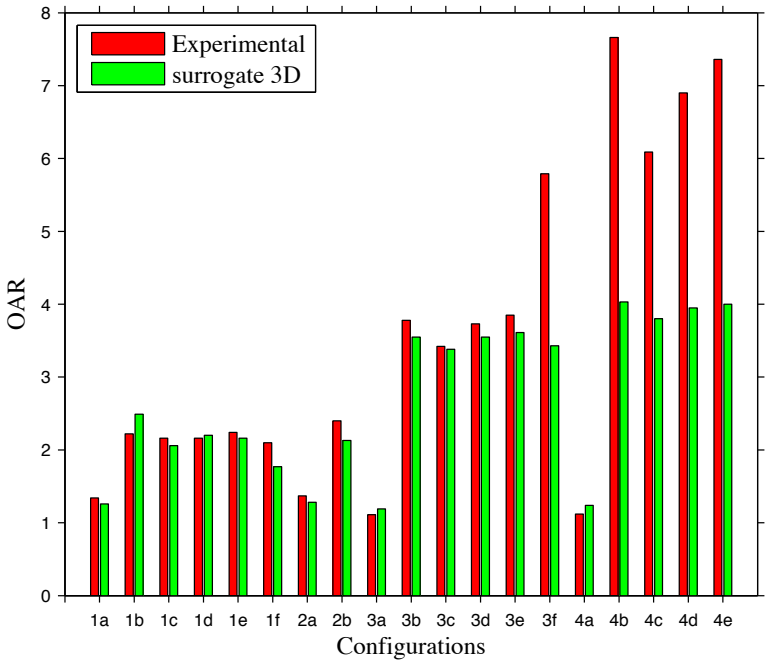

Figure 5.38: Compilation of *OAR* from the surrogate model and experiments for selected duct-configruations.

Chapter 6

Conclusion

This chapters draws conclusions from the results discussed in the previous chapter. The conclusions are presented as guidelines for designers, for the design of ducts in naturally-ventilated buildings. Recommendations for future work are also suggested.

6.1 Guidelines for designers

Based on results from Chapter 5, guidelines for designers for optimizing the combined airflow and acoustical performance are discussed below.

1. Unlined ducts perform poorly acoustically and, therefore, in terms of overall performance. It is almost always recommended to include absorptive liners when designing ducts.

2. Duct linings improve sound attenuation with minimal impact on airflow performance. The sound attenuation is independent of the length of the duct, and only depends on the length of the duct lining, for a partially lined duct.

3. The recommendations for the best configurations of duct for improving acoustical performance largely depend on the frequencies of interest to be

attenuated. The frequencies of interest depend on the sound metric and the applicable acceptability criteria chosen by the designer. For retrofit noise control, the sound metric and the acceptability criteria are chosen by the designer based on the characteristics of the sound transmitted through the openings, taking into account the human perception of sound (A-weighted sound levels) (eg. high-frequency ringing noise, low-frequency rumbling and poor speech-privacy).

4. For ducts of small cross-sectional area, lining the inside surfaces of the duct is enough to achieve good acoustical performance, with sound attenuation as high as 35 dB in the peak frequency band that is targeted, and about 10 dB of attenuation at frequencies greater than the target frequency. For improved performance, the thickness of the linings can be increased or an absorbent material with a higher flow-resistivity can be used. The surrogate model developed in this research can be used to convert the sound-absorption coefficient of a lining into flow-resistivity.

5. If the ducts have a large cross-sectional area, lining the ducts can improve acoustical performance at low frequencies. The sound attenuation is generally lower when compared to ducts of smaller cross-sectional area, with attenuation performance of around 10 dB, but covers a wider range of frequency bands. If the peak of the IL curve, as predicted by the surrogate model, lies lower than the frequencies of interest, baffles can be inserted to introduce a second peak in the IL curve at a higher frequency. The position of the baffles can be modified to achieve either high attenuation as a narrow peak in one frequency band, by placing the baffles in the middle of the duct, or a wider IL curve that covers multiple frequency bands but lower magnitude of attenuation, by offsetting the baffle towards one of the sides of the duct. The surrogate models can be used to calculate the ILs for such configurations quickly. The length of the baffles controls the level of attenuation of the second peak.

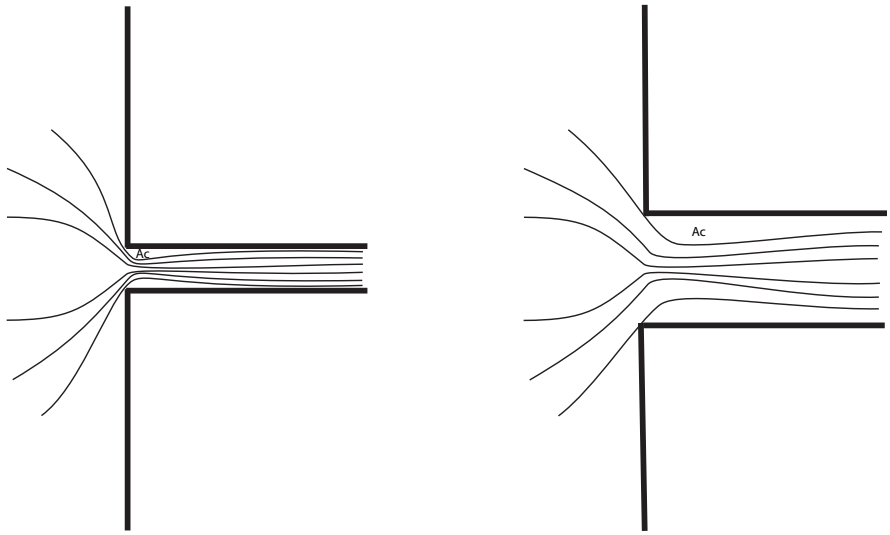

(a) Vena contracta for $A_s \gg A_d$ **(b)** Vena contracta for $A_s > A_d$

Figure 6.1: Dependance of cross-sectional areas of the source room and the duct, on the vena-contracta

6. The addition of baffles seems to affect the airflow performance considerably. If baffles are inserted, they should be positioned as far away from the inlet of the duct as possible, preferably close to the outlet. If that is not possible, they should at least be placed after the point of which pressure recovery from the vena-contracta occurs. The length of the duct after which the pressure drop from the vena-contracta is recovered can be calculated using the surrogate model for flow through the duct.

7. Instead of thick (along width), short (along length) baffles that constrict the opening of the duct, it is better to use long, thin baffles, that have minimal effect on flow performance.

8. The pressure drop in a duct with no baffles, with or without absorptive lining, can be minimized by making the duct longer.

9. The pressure drop in a duct with no baffles, with or without absorptive lining, can also be minimized by making the ratio of the cross-sectional areas

of the source room and duct as large as possible. High area ratios result in a stronger effect of the vena-contracta near the duct inlet, but pressure recovery happens early along the length of the duct (refer to Figure 6.1a). For low area ratios, the vena-contracta does not have as strong an effect on the pressure drop near the inlet of the duct, and pressure recovery happens much later along the length of the duct (refer to Figure 6.1b).

10. To reduce the effect of the vena-contracta, bell-mouths can be introduced near the inlet of the duct, if the design permits.

11. Duct bends appear to improve sound attenuation in both low and high frequency bands, but considerably reduce airflow performance. Duct bends were not studied in detail in this thesis.

6.2 Summary of work

This section summarizes the work presented in this thesis, by revisiting the research objectives.

1. Select appropriate duct configurations for investigation in this study, along with appropriate input and output (performance) parameters defining them.

Factors affecting performance were individually identified for acoustics and airflow. The parameters that affect acoustical performance were identified to be the width of the duct (w), breadth of the duct (b), length of the lined portion of the duct (l_b), thickness of the lining (t), flow-resistivity of the absorber (R_f) and the frequency (f). The parameters affecting airflow performance were identified to be the cross-sectional areas before and after a sudden change in cross-section (A_1, A_2), the cross-sectional area of the duct (A_d), the length of the duct (l) and the airflow (Q_{in}). The output parameters for acoustics and airflow were chosen to be Insertion Loss (IL) and the pressure drop across the duct (Δp), respectively. The configurations that were selected for investigation were based on varying the dimensions of straight ducts with lining and baffle inserts.

2. For the selected duct configurations, predict the output (performance) parameters of the duct using two-dimensional Finite-Element modelling.

2D FEM predictions were performed for a range the input parameters. Simple geometries were used as domains for the predictions. For the acoustical FEA model, the predictions were performed for a duct with lining on only one side, as discussed in Section 2.2. For the airflow model, the predictions were done for an abrupt change in cross section and flow through the duct, as discussed in Section 2.3. The surrogate model for the flow through a duct captures the effect of the vena-contracta as a function of duct length – this has not been done before and is useful in understanding the influence of the vena-contracta. The results from FEM – the output parameters, along with associated input parameters – were compiled into a data set.

3. Build a relatively simple 2D surrogate model based on the prediction results (the data set) from Finite-Element modelling.

Surrogate models involving simple arithmetic operations were modelled using the data set from 2D FEM for acoustics. The surrogate model was modified to apply to ducts with lining on one or two sides of the 2D duct. The surrogate models for sound were discussed in Section 3.1. The surrogate model for airflow comprises 2D models for sudden expansion, sudden contraction and for flow through the duct. The surrogate model for flow through the duct contains a *logistic* term to capture the effect of the vena-contracta, which is not a simple arithmetic operation, but is not difficult to compute. The surrogate models for airflow were discussed in Section 3.2.

4. Extend the surrogate model to apply to configurations in the 3D domain.

The surrogate models for sound were modularly combined to extend them to the 3D domain and to model various duct configurations involving baffles. The surrogate models for airflow were modified to apply to the 3D domain. Baffles in the duct were modelled approximately as a change in cross-section of the

duct. The extension of the surrogate models for sound and airflow, so that they apply to complex configurations, was discussed in Section 3.1.5 and Section 3.2.4, respectively.

5. Measure the performance of selected duct configurations, using a scale-model of the duct, applying appropriate scaling laws.

The use of scale-models for evaluating the airflow and acoustical performance of ducts was investigated in this study. A suitable scaling factor ($n = 4$) was chosen for both airflow and sound measurements. For sound measurements, the duct dimensions were scaled by a factor of n according to acoustical scaling laws. For airflow measurements, the Reynolds number was kept constant for the full-scale and reduced-scale models. This helped measure airflow performance at low Reynolds numbers which would be higher for the same pressure drops in larger ducts. It was, however, found that laminar flow could not be achieved, even for the scale model. The turbulence is caused by the sudden contraction near the inlet of the duct. The details of the experimental setup were discussed in Chapter 4. A set of configurations was chosen for measurement and was built. The configurations were built to study the effect of duct dimensions, the effect of the ratio of the cross-sectional areas of the source room and the duct, the effect of the addition of lining, and the effect of the addition and position of baffles, on the acoustical and airflow performance. The configurations selected for this study were discussed in Section 4.6.

6. Compare results from the surrogate model with measurements and Finite-Element predictions.

The results from the surrogate model were compared with predictions by theoretical relationships, results from experiments and predictions by the FEA models. The surrogate models that were modelled from 2D FEA models showed only limited agreement with experimental results – limited by the limitations of the 2D FEA model and the approximations made to simplify the surrogate models. However, these surrogate models perform better than existing tools available for

evaluating sound and airflow performance. The surrogate models for sound are able to capture the positions of peaks quite accurately. They are also in good agreement with 3D FEA models, if the sound source is approximated by a plane wave. The higher-order modes that are observed in the results of measurements are not captured by the surrogate model. However the model is quite acceptable as a tool that can be used to target frequencies of attenuation for noise-control in ducts.

The 3D surrogate model for sound, as mentioned before, is a modified 2D surrogate model, extended to apply to the 3D domain. The 3D surrogate model was found to be in very good agreement with results from 3D FEA. 3D FEA could not be performed at higher frequencies for large ducts, since the process is very time consuming and requires huge computational resources. The surrogate model is able to predict the results from 3D FEA, and at frequencies much beyond what can be done using FEA models, in only a fraction of the time. Such a way of modifying surrogate models to apply to complex configurations is novel and unique to this work.

When compared to results from experiments, the surrogate models are able to predict the airflow performance of ducts without baffles with up to 80-90% accuracy, and up to 70% accuracy for ducts with baffles. The surrogate model is able to capture the effect of the vena-contracta along the length of the duct quite well, and is helpful in optimizing the placement of baffles inside the duct. The comparison of the surrogate model with other models was discussed in Chapter 5.

7. **Suggest best practices based on results from the surrogate model and experiments**.

Best practices based on the comparison of results from Chapter 5 were discussed in this chapter, in Section 6.1.

6.3 Future work

The work done in this study opens doors to many areas of improvement and future work. Due to limitations in time and resources, the surrogate model was limited to modelling the acoustical and airflow performance of straight ducts. A surrogate model for the effect of duct bends as a function of the duct cross-sectional dimensions and position along the length of the duct would be interesting and useful. The surrogate model for airflow approximates the addition of baffles as a change in cross-section of the duct. Further study is required to fully understand the effects of vena-contracta, when a baffle is inserted. As an alternative to using results from FEA to build the surrogate model, results from scale-model experiments could be used to build or modify the surrogate model. The surrogate model for sound can be modified to include the effect of higher-order modes, by generating a data set for high-frequency insertion loss using a ray-tracing model. A ray-tracing model is able to predict the sound field accurately at high frequencies; at low frequencies this method is not very accurate. A surrogate model developed using the data-set generated by the ray-tracing method can be used modularly, in combination with the existing surrogate models for sound, to predict low- and high-frequency attenuation equally well.

Bibliography

[1] J. J. Martin, "Expansion and contraction losses in fluid flow," *University of Michigan. Chemical Engineering Education*, 1947. → pages xiii, 75

[2] "Product data sheet: Condenser microphone - bruel & kjaer.." www.bksv.com/doc/Bp0100.pdf. Accessed: 2015-09-30. → pages xiv, 103, 104

[3] M. Hodgson and A. Khaleghi, "Design and evaluation of noise-isolation measures for the natural-ventilation openings in a green building," *Noise Control Engineering Journal*, vol. 57, no. 5, pp. 493–506, 2009. → pages 2

[4] C. Bibby, "Investigation of the acoustical and airflow performance of interior natural ventilation openings," Master's thesis, University of British Columbia, 2011. → pages 2, 14, 21, 31, 41, 128

[5] "Illustration showing ducts used for airflow by stack effect.." https://ad7eb.wordpress.com/2013/11/15/stack-venturi-and-bernoullis-effects-in-cooling-a-building/. Accessed: 2015-09-30. → pages 3

[6] "Duct with absorber lining." http://www.rockwoolasia.com. Accessed: 2015-09-30. → pages 4

[7] "Commercial baffle insert for ducts." http://www.kineticsnoise.com. Accessed: 2015-09-30. → pages 4

[8] D. Reynolds and J. Bledsoe, "Sound attenuation of unlined and acoustically lined rectangular ducts," *ASHRAE Transactions*, vol. 95, no. 1, 1989. → pages 8

[9] H. J. Sabine, "The absorption of noise in ventilating ducts," *The Journal of the Acoustical Society of America*, vol. 12, no. 1, pp. 53–57, 1940. → pages 11

[10] U. Kurze and I. Ver, "Sound attenuation in ducts lined with nonisotropic material," *The Journal of the Acoustical Society of America*, vol. 52, no. 1A, pp. 148–149, 1972. → pages 11

[11] R. Orlowski, "The arrangement of sound absorbers for noise reduction–results of model experiments at 1: 16 scale," *Noise Control Engineering Journal*, 1984. → pages 11

[12] D. Borelli, C. Schenone, and I. Pittaluga, "Theoretical and numerical modeling of a parallel-baffle rectangular duct," *The Journal of the Acoustical Society of America*, vol. 130, no. 4, pp. 2564–2564, 2011. → pages 12

[13] H. Eck and W. Probst, "Experimental investigation of the sound absorption of baffle systems as a function of the angle of incidence," in *INTER-NOISE and NOISE-CON Congress and Conference Proceedings*, vol. 4, pp. 551–554, Institute of Noise Control Engineering, 1985. → pages 12

[14] J. P. Kleijnen, "Sensitivity analysis and optimization of system dynamics models: regression," *System Dynamics Review*, vol. 11, no. 4, pp. 275–288, 1995. → pages 12

[15] J. D. Schaffer, "Multiple objective optimization with vector evaluated genetic algorithms.," in *Proceedings of the 1st International Conference on Genetic Algorithms, Pittsburgh, PA, USA, July 1985*, pp. 93–100, 1985. → pages 12

[16] Y.-C. Chang, M.-C. Chiu, and C.-C. Hsieh, "Optimum design of mufflers hybridized with one-connected curved tube using the boundary element method, neural networks, and the genetic algorithm," *Journal of Marine Science and Technology*, vol. 20, no. 4, pp. 376–383, 2012. → pages 12

[17] M. Hodgson and R. Orlowski, "Acoustic scale modelling of factories, part i: principles, instrumentation and techniques," *Journal of sound and vibration*, vol. 113, no. 1, pp. 29–46, 1987. → pages 13, 92

[18] M. Hodgson and R. Orlowski, "Acoustic scale modelling of factories, part ii: 1-50 cale model investigations of factory sound fields," *Journal of sound and vibration*, vol. 113, no. 2, pp. 257–271, 1987. → pages 13, 92

[19] M. Delany and E. Bazley, "Acoustical properties of fibrous absorbent materials," *Applied acoustics*, vol. 3, no. 2, pp. 105–116, 1970. → pages 13, 31, 67, 107

[20] M. Samimi, "Sound absorbing porous materials: Modelling of normal absorption coefficient.," tech. rep., University of British Columbia, Vancouver., 2013. → pages 13, 95

[21] K. Horoshenkov, D. Hothersall, and K. Attenborough, "Porous materials for scale model experiments in outdoor sound propagation," *Journal of sound and vibration*, vol. 194, no. 5, pp. 685–708, 1996. → pages 13

[22] N. Voronina, "Acoustic properties of fibrous materials," *Applied Acoustics*, vol. 42, no. 2, pp. 165–174, 1994. → pages 14

[23] M. De Salis, D. Oldham, and S. Sharples, "Noise control strategies for naturally ventilated buildings," *Building and Environment*, vol. 37, no. 5, pp. 471–484, 2002. → pages 14

[24] D. Etheridge, *Natural ventilation of buildings: theory, measurement and design.* John Wiley & Sons, 2011. → pages 14, 19, 20, 40

[25] D. Etheridge and M. Sandberg, *Building ventilation: theory and measurement*, vol. 50. John Wiley & Sons Chichester, UK, 1996. → pages 14

[26] M. Schmidt and H. Lipson, "Distilling free-form natural laws from experimental data," *science*, vol. 324, no. 5923, pp. 81–85, 2009. → pages 23

[27] M. Schmidt and H. Lipson, "Eureqa (version 0.98 beta)[software]," 2013. → pages 23, 52

[28] C. Multiphysics, "Comsol multiphysics user guide (version 4.3 a)," *COMSOL, AB*, 2012. → pages 27

[29] J. Betts, *Finite element study of plane wave acoustic phenomena in ducts.* diplom. de, 2000. → pages 31

[30] M. J. Crocker, *Handbook of acoustics.* John Wiley & Sons, 1998. → pages 31

[31] "Solutions to linear systems of equations: Direct and iterative solvers.." https://www.comsol.com/blogs/solutions-linear-systems-equations-direct-iterative-solvers/. Accessed: 2015-09-30. → pages 33

[32] C. G. DeGroff, R. Shandas, and L. Valdes-Cruz, "Analysis of the effect of flow rate on the doppler continuity equation for stenotic orifice area calculations a numerical study," *Circulation*, vol. 97, no. 16, pp. 1597–1605, 1998. → pages 44

[33] M. L. Munjal, *Acoustics of ducts and mufflers with application to exhaust and ventilation system design.* John Wiley & Sons, 1987. → pages 53

[34] "Model building blocks in eureq.." http://formulize.nutonian.com/documentation/eureqa/general-reference/building-blocks/. Accessed: 2015-09-30. → pages 55

[35] R. Bukowski, "35th winter school on vibroacoustical hazards suppressions-wisła, poland, february 26-march 02, 2007," *Archives of Acoustics*, vol. 32, no. 1, pp. 189–195, 2007. → pages 67

[36] K. T. McDonald, "Vena contracta," 2011. → pages 69

[37] A. P. Kratz and J. R. Fellows, "Pressure losses resulting from changes in cross-sectional area in air ducts," *University of Illinois. Engineering Experiment Station. Bulletin; no. 300*, 1938. → pages 72, 74

[38] L. F. Moody, "Friction factors for pipe flow," *Trans. Asme*, vol. 66, no. 8, pp. 671–684, 1944. → pages 76

[39] F. Spandöck, "Akustische modellversuche," *Annalen der Physik*, vol. 412, no. 4, pp. 345–360, 1934. → pages 92

[40] T. Busch, M. Hodgson, and C. Wakefield, "Scale-model study of the effectiveness of highway noise barriers," *The Journal of the Acoustical Society of America*, vol. 114, no. 4, pp. 1947–1954, 2003. → pages 95

[41] A. Standard, "E477-84,"," *Standard Method of Testing Duct Liner Materials and Prefabricated Silencers for Acoustical and Airflow Performance," American Society of Testing Materials*, 1984. → pages 96

[42] "Roxul safe 'n' sound.." www.roxul.com/products/residential/products/roxul+safe'n'sound. Accessed: 2015-09-30. → pages 99

[43] "Product data sheet: Sinus soundbook.." www.soundbook.de/e/produkte/soundbook.htm. Accessed: 2015-09-30. → pages 105

[44] A. Standard, "C522-03)," *Standard Test Method for Airflow Resistance of Acoustical Materials, ASTM International*, 2009. → pages 107

[45] A. Standard, "E779-10," *Standard Test Method for Determining Air Leakage Rate by Fan Pressurization, ASTM International*, 1996. → pages 108

[46] "Product data sheet: Retrotec 2000.." retrotec.com/support-categories/1000-2000-3000-series. Accessed: 2015-09-30. → pages 109

Appendix A

Estimation of Measurement Uncertainty

This appendix discusses the estimation of uncertainty due to precision errors in measurements, for derived quantities.

A.1 Uncertainty in acoustic measurement

A modified form of the Insertion Loss was used in this study. The Insertion Loss is given by:

$$IL = (SPL_{src,lined} - SPL_{rec,lined}) - (SPL_{src,unlined} - SPL_{rec,unlined})$$

The standard deviation in measurement of IL due to precision errors is given as:

$$S_{IL} = \sqrt{S^2_{SPL,src,lined} + S^2_{SPL,rec,lined} + S^2_{SPL,src,unlined} + S^2_{SPL,rec,unlined}}$$

A 95% student t-distribution was used to define the confidence intervals for IL.

A.2 Uncertainty in airflow measurement

ASTM E779–10 [refer] discusses the estimation of uncertainty in the measurement of airflow. Relevant material from the standard is listed here to estimate the confidence interval for the airflow rate for the relationship between airflow rate and pressure drop given by:

$$Q = C(\Delta p)^n$$

A log linear regression can be applied to the above equation as:

$$y = \ln(C) + n\overline{x}$$

where,

$$\overline{x} = \frac{1}{N}\sum_{i=1}^{N} y_i$$

Then the variance and covariance of x and y can be written as:

$$S_x^2 = \frac{1}{N-1}\sum_{i=1}^{N}(x_i - \overline{x})$$

$$S_y^2 = \frac{1}{N-1}\sum_{i=1}^{N}(y_i - \overline{y})$$

$$S_{xy} = \frac{1}{N-1}\sum_{i=1}^{N}(x_i - \overline{x})(y_i - \overline{y})$$

The flow exponent can be found from:

$$n = \frac{S_{xy}}{S_x^2}$$

$$\ln(C) = \overline{y} - n \cdot \overline{x}$$

The flow coefficient is then:

$$C = \exp^{[\overline{y} - n \cdot \overline{x}]}$$

The standard deviation for n and $\ln(C)$ are:

$$S_n = \frac{1}{S_x}\left(\frac{S_y^2 - n \cdot S_{xy}}{N - 2}\right)^{0.5}$$

$$S_{\ln(C)} = S_n\left(\frac{\sum_{i=1}^{N} x_i^2}{N}\right)^{0.5}$$

The standard deviation for airflow rate can be found as:

$$S_y\left(x\right) = S_n\left(\frac{N-1}{N}S_x^2 + \left(x - \overline{x}\right)^2\right)^{0.5}$$

A 95% student t-distribution was used to define the confidence intervals for the curve fit.

Appendix B

MATLAB Code

Snippets of matlab codes used for acoustics and airflow are shown here.

B.1 Sample MATLAB code for surrogate model for acoustics

```
function absbafmain()
for lin=1  %Lining 1(yes) 2(no)
    for baf=2  %Number baffles 0(no)
        if or(lin>0, baf>0)
            %%%%%% lining
            if lin==1
                pos1=-w/2+t/2;
                pos2=w/2-t/2;
                pos3=-b/2+t/2;
                pos4=b/2-t/2;

                [IL1, freq]=absfs(abs(pos2-pos1)/2,t,l-bl,b,...
                    Rf);
                [IL2, freq]=absfs(abs(pos2-pos1)/2,t,l-bl,b,...
                    Rf);
```

```
            [IL3, freq]=absfs(abs(pos4-pos3)/2,t,l,b,Rf)...;
            [IL4, freq]=absfs(abs(pos4-pos3)/2,t,l,b,Rf)...;

            IL_lin_w=-10*log10((10.^(-IL1/10)+10.^(-IL2.../10))/2);
            IL_lin_b=-10*log10((10.^(-IL3/10)+10.^(-IL4.../10))/2);
            IL_lin=IL_lin_b+IL_lin_w;

        end
        %%%%%%%%%%%%% 2 sided lining %%%%%%%%%%
        if lin==0.5
            pos1=-w/2+t/2;
            pos2=w/2-t/2;

            [IL1, freq]=absfs(abs(pos2-pos1)/2,t,l,w,Rf)...;
            [IL2, freq]=absfs(abs(pos2-pos1)/2,t,l,w,Rf)...;

            IL_lin_w=-10*log10((10.^(-IL1/10)+10.^(-IL2.../10))/2);
            IL_lin=IL_lin_w;

        end
        %%%%%%%%%%%%%%

        %% baffles

        if baf>0

            if lin==0

                if baf==1

```

```
                pos=0   %Enter pos of baffle
                [IL1, freq]=absfs(w/2-pos-tb/2,tb/4,...
                    bl,b,Rf);
                [IL2, freq]=absfs(w/2+pos-tb/2,tb/4,...
                    bl,b,Rf);
                % ILeff=((w/2-pos)/w).*IL1+((w/2+pos...
                    )/w).*IL2;
                IL_baff=-10*log10((10.^(-IL1/10)+10....
                    ^(-IL2/10))/2);
            end

            if baf==2

                pos1=input('enter baffle 1 position ...
                    from centre')
                pos2=input('enter baffle 2 position ...
                    from centre')
                [IL1, freq]=absfs(w/2+pos1,tb/2,bl,b...
                    ,Rf);
                [IL2, freq]=absfs(abs(pos2-pos1)/2,...
                    tb/2,bl,b,Rf);
                [IL3, freq]=absfs(w/2-pos2,t/2,bl,b,...
                    Rf);

                IL_baff=-10*log10((10.^(-IL1/10)+10....
                    ^(-IL2/10)...
                +10.^(-IL3/10))/3);
            end

        else if (lin==1 || lin==0.5)

                if baf==1

                    pos=0
                    [IL1, freq]=absfs((w/2-pos-tb/2-...
                        t)/2,t,bl,b,Rf);
```

```
        [IL2, freq]=absfs((w/2+pos-tb/2-...
            t)/2,t,bl,b,Rf);
        [IL3, freq]=absfs((w/2-pos-tb/2-...
            t)/2,tb/2,bl,b,Rf);
        [IL4, freq]=absfs((w/2+pos-tb/2-...
            t)/2,tb/2,bl,b,Rf);
        % ILeff=((w/2-pos)/w).*IL1+((w...
            /2+pos)/w).*IL2;
        IL_baff=-10*log10((10.^(-IL1/10)...
            +10.^(-IL2/10)+...
        10.^(-IL3/10)+10.^(-IL4/10))/4);
    end

    if baf==2

        pos1=w/6
        pos2=-w/6
        [IL1, freq]=absfs((w/2-pos1-tb1...
            /2-t)/2,t,bl,b,Rf);
        [IL2, freq]=absfs((w/2-pos1-tb1...
            /2-t)/2,tb1/2,bl,b,Rf);
        [IL3, freq]=absfs((w/2+pos2-tb2...
            /2-t)/2,t,bl,b,Rf);
        [IL4, freq]=absfs((w/2+pos2-tb2...
            /2-t)/2,tb2/2,bl,b,Rf);
        [IL5, freq]=absfs(abs(pos2-pos1-...
            tb1/2-tb2/2)/2,tb/2,bl,b,Rf);
        IL_baff=-10*log10((10.^(-IL1/10)...
            +10.^(-IL2/10)+...
        10.^(-IL3/10)+10.^(-IL4/10)+10....
            ^(-IL5/10))/5);
        IL_baff2=-10*log10((10.^(-IL1...
            /10)+10.^(-IL2/10)+...
        10.^(-IL3/10)+10.^(-IL4/10)+10....
            ^(-IL5/10)+...
        10.^(-IL5/10))/6);
    end
```

```
                    end
                end
            end

            if (lin==1 || lin==0.5) && baf==0
                IL_eff=IL_lin;

            else if (lin==1 || lin==0.5) && (baf==1||baf==2)
                    IL_eff=IL_lin+IL_baff;

                else if lin==0 && baf==1
                        IL_eff=IL_baff;

                    end
                end
            end
        end
    end
end

xlswrite('/Users/Vivekpc/Dropbox/Research files/Research...
/Thesis compile/Allthings/Results compile/Config 1/Case 3...
/surr4s',[[freq]',[IL_eff]'])
semilogx(freq,IL_eff,'r');
set(gca,'XTick',[63 125 250 500 1000 2000 4000 8000] );
xlim([63 40000])
xlabel('Frequency (Hz)')
ylabel('Insertion Loss (IL)')
hold on;
grid on;

end
```

```
function [IL,freq]=absfs(w,t,l,b,Rf)
crea=5:0.2:15.3;
```

```
freq=2.^crea;

for i=1:1:numel(freq)
    IL(i)=l*2.02097295646691e-6*Rf*freq(i)^2*t^2*2*2/(1...
        .01964682634673 ...
    + 0.00738162549056157*Rf*t + 6.5335952963285e-15*Rf*w...
        ^4*16*freq(i)^5*t^2);

end
end
```

B.2 Sample MATLAB code for surrogate model for airflow

```
function main()
d_w=0.15; %width of duct
d_b=0.15; %breadth of duct
d_h=4*d_w*d_b/(2*(d_w+d_b)); %hydraulic diameter of duct
l=0.8; %length of duct
s_h=2.8; % width/breadth of source/receiver room
r_l=2; % receiver room length
s_hh=s_h; %hydraulic diameter of source room

%%%%%%%%%%%%%%%%%%%%%%%%%%%%%%%%%%%%%%%%%%%%%%%%%%%%
%%%%%%%%%%%%%-from surrogate-%%%%%%%%%%%%%
%%%%%%%%%%%%%%%%%%%%%%%%%%%%%%%%%%%%%%%%%%%%%%%%%%%%

%%%% 2d from FEA

A_s=s_h;
A_d=d_w;

dp1_2d=sc(A_s,A_d,Qin_FEA);
dp2_2d=flw(d_h,s_hh,A_d,l,Qin_FEA);
```

```
dp3_2d=se(A_d,r_l,Qin_FEA);

dp_2d=(dp1_2d+dp2_2d+dp3_2d)

%%%% 3d from FEA

A_s=s_h^2;
A_d=(d_w*d_b);

dp1_3d=se(A_s,A_d,Qin_expt);
dp2_3d=flw(d_h,s_hh,A_d,l,Qin_expt);
dp3_3d=sc2(A_d,r_l,Qin_expt);
dp_3d=dp1_3d+dp2_3d+dp3_3d


%%%error for pressure drop
ver_2d=mean(0.5.*(0.001.*(dp1_2d+dp3_2d)+0.1.*dp2_2d)./dp_2d...
    )
ver_3d=mean(0.5.*(0.001.*(dp1_3d+dp2_3d)+0.1.*dp2_3d)./dp_3d...
    )
%%%%%%

%%%%% optimisation function
[C_d_FEA,C_d_2d,C_d_expt,C_d_3d,Q_error,C,n,C_dev,n_dev,I_y,...
    EOAf_FEA,EOAf_expt,EOAf_expterr,EOAf_surr_2d,EOAf_surr_3d...
    ,SEOA_f_expt ] = optifunc( Qin_FEA,A_d,dp_FEA,dp_2d,...
    dp_expt,Qin_expt,dp_3d );

errorbar(dp_expt,Qin_expt/(d_w*d_b),(Qin_expt-Q_error)/(d_w*...
    d_b),'r-')
hold on;
plot(dp_3d,Qin_expt/(d_w*d_b),'k')
hold on;
plot(dp_2d,Qin_FEA/d_h,'b--')
errorbar(dp_FEA,Qin_FEA/d_h,Qin_FEA/d_h.*ver_2d,'g--')
plot(dp_FEA3d,Qin_FEA3d/(d_w*d_b),'b*')
```

```
xlabel('\Delta p (Pa)','FontSize',10,'FontName','Times New ...
    Roman')
ylabel('u_{d} (m/s) (model-scale)','FontSize',10,'FontName',...
    'Times New Roman')
AX=legend('Experimental','surrogate 3D','surrogate 2D','FEA ...
    2D','FEA 3D','Location','NorthWest')
set(findobj(AX,'type','text'),'FontSize',10)
set(findobj(AX,'type','text'),'FontName','Times New Roman')
grid on;
ax = gca;
xlim([0 50])
set(gca,'GridLineStyle',':');
set(gca,'XTick', 0:5:50);
set(gcf, 'PaperPosition', [0 0 5 4]); %Position plot at left...
    hand corner with width 5 and height 5.
set(gcf, 'PaperSize', [5 4]); %Set the paper to have width 5...
    and height 5.
saveas(gcf, cname, 'pdf') %Save figure
T=[cellstr(cname) EOAf_FEA EOAf_expt EOAf_surr_2d ...
    EOAf_surr_3d C_d_expt C_d_3d C_d_FEA C_d_2d C n C_dev(1) ...
    C_dev(2) n_dev(1) n_dev(2)];
filenamecs = 'configurationcompile.xlsx';
xlwrite(filenamecs,T,1,rowname)

end
```

```
function [ C_d_FEA,C_d_2d,C_d_expt,C_d_3d,Q_error,C,n,C_dev,...
    n_dev,I_y,EOAf_FEA,EOAf_expt,EOAf_expterr,EOAf_surr_2d,...
    EOAf_surr_3d,SEOA_f_expt ] = optifunc( Qin_FEA,A_d,dp_FEA...
    ,dp_2d,dp_expt,Qin_expt,dp_3d )

%%%%% optimisation paramters
C_d_FEA=mean(Qin_FEA./(A_d*(2/1.18*dp_FEA).^0.5))
C_d_2d=mean(Qin_FEA./(A_d*(2/1.18*dp_2d).^0.5));
C_d_expt=mean(Qin_expt./(A_d*(2/1.18*dp_expt).^0.5));
```

```
C_d_3d=mean(Qin_expt./(A_d*(2/1.18*dp_3d).^0.5));

[Q_error,C,n,C_dev,n_dev,I_y]=flowerr(Qin_expt,dp_expt);

EOAf_FEA=mean(((Qin_FEA./(dp_FEA).^0.5)./0.61).*(1.18/2)^0.5...
    );
EOAf_expt=mean((C./0.61).*(1.18/2)^0.5.*dp_expt.^(n-0.5));
EOAf_expterr=exp(I_y);
EOAf_surr_2d=mean(((Qin_FEA./(dp_2d).^0.5)./0.61).*(1.18/2)...
    ^0.5);
EOAf_surr_3d=mean(((Qin_expt./(dp_3d).^0.5)./0.61).*(1.18/2)...
    ^0.5);
SEOA_f_expt=((C./0.61).*(1.18/2)^0.5.*dp_expt.^(n-0.5))/(0...
    .15*0.15);

end
```

```
function [ dp ] = sc( A_s,A_d,Qin )
%%%% Pressure drop due to sudden contraction.
dp=(-0.985+0.896*((A_s/A_d)^2)).*(Qin/A_s).^2;
end
```

```
function [ dp ] = se( A_d,l,Qin )
%%%% Pressure drop due to sudden expansion.
dp=(0.0066+0.05178*l-0.01211*l^2).*(Qin./A_d).^2;
end
```

```
function [dp]= flw(d_h,s_hh,A_d,l,Qin)
dp=(0.013425*l+0.676*(1/(1+exp(-1*(2.092*d_h/(l-0.086)+0...
    .2268*s_hh*l^2/((0.086-l)*d_h))))))).*(Qin./A_d).^2;
end
```

```
function [ Q_error,C,n,C_dev,n_dev,I_y ] = flowerr( Qin_expt...
    ,dp_expt )

x=log(dp_expt);
y=log(Qin_expt);

S_x2=sum(1/(length(Qin_expt)-1).*(x-mean(x)).^2);
S_y2=sum(1/(length(dp_expt)-1).*(y-mean(y)).^2);
S_xy=sum(1/(length(dp_expt)-1).*(x-mean(x)).*(y-mean(y)));

n=S_xy/S_x2;
C=exp(mean(y)-n*(mean(x)));

S_n=((1/S_x2)*((S_y2-n*S_xy)/(length(dp_expt)-2)))^0.5;
S_lnc=S_n*(sum(x.^2)/length(dp_expt))^0.5;

I_lnc = S_lnc*tinv([0.025  0.975],length(dp_expt)-2);
I_n = S_n*tinv([0.025  0.975],length(dp_expt)-2);

n_dev=n+I_n;
C_dev=C.*exp((I_lnc));

S_y_x=S_n*((length(dp_expt)-1)/length(dp_expt)*S_x2+(x-mean(...
    x)).^2).^0.5;
I_y=S_y_x*tinv(0.975,length(dp_expt)-2);

Q_dev_u=Qin_expt.*exp((I_y));
Q_dev_l=Qin_expt.*exp((-I_y));

Q_error=Q_dev_u;
Q_error2=Q_dev_l;

end
```